First-Principles Theory of Scanning Tunneling Microscopy Applied to Transition-Metal Surfaces

Dissertation
zur Erlangung des Doktorgrades
des Fachbereichs Physik
der Universität Hamburg

vorgelegt von
Stefan Heinze
aus Aachen

Hamburg
2000

Gutachter der Dissertation:
    Prof. Dr. R. Wiesendanger
    Priv. Doz. Dr. S. Blügel
Gutachter der Disputation:
    Prof. Dr. R. Wiesendanger
    Prof. Dr. H. P. Oepen
Datum der Disputation:
    16.08.2000
Vorsitzender des Promotionsausschusses:
    Prof. Dr. F.-W. Büßer

Inhaltsangabe

Die Untersuchung von einfachen und lateral strukturierten Übergangsmetalloberflächen spielt eine entscheidende Rolle in der Chemie an Oberflächen, im Nanomagnetismus, im sich zur Zeit entwickelnden Gebiet der Magneto-Elektronik und für entsprechende Anwendungen, z.B. in der Datenspeicherindustrie. Die strukturellen, elektronischen, chemischen und magnetischen Eigenschaften von Übergangsmetalloberflächen auf der nanometer bis zur atomaren Skala zu verstehen, ist eine essentielle Voraussetzung zur Entwicklung neuer Bauelemente. Das Rastertunnelmikroskop (RTM, engl. STM) ist eine starke treibende Kraft auf diesem Gebiet, aber die eindeutige Interpretation der Meßdaten von Übergangsmetalloberflächen auf der atomaren Skala ist erst an seinem Anfang. In den meisten Fällen werden RTM-Bilder auf der Grundlage eines Harte-Kugel-Modells gedeutet. Es wird hier gezeigt, daß dies nicht korrekt ist. Mit der Kombination von modernen ab initio Rechnungen der elektronischen Struktur und dem Tersoff-Hamann Modell für das RTM ergibt sich ein schlagkräftiger und erfolgreicher Ansatz zur Interpretation von RTM-Bildern von Übergangsmetalloberflächen auf der atomaren Skala. In dieser Arbeit wird die erste systematische Untersuchung von RTM-Bildern von Übergangsmetalloberflächen auf der atomaren Skala vorgestellt. Fünf verschiedene Bereiche werden abgedeckt:

(i) Bilder einfacher Oberflächen: Der Einfluß der elektronischen Struktur auf RTM-Bilder selbst im Fall von reinen Übergangsmetalloberflächen wird durch den Effekt der spannungsabhängigen Korrugationsumkehr für bcc-(110) Oberflächen demonstriert. (ii) Chemische Identifikation: Die Schwierigkeit chemisch unterschiedliche Atome an einer Oberfläche zu diskriminieren wird an einem Beispiel dargelegt ($\mathrm{CoSi_2(001)}$), bei dem ein wirkliches Verständnis der experimentellen Daten nur mit der Hilfe der Rechnungen möglich wird. (iii) Vergrabene Grenzflächen: Da das Durchmischen in Multi-Komponenten Systemen nicht auf die Oberflächenlage beschränkt sein muß, wird weiter die Möglichkeit diskutiert, mit dem RTM auch vergrabene Strukturen abzubilden, sogar in Metallsystemen. Die ersten direkten RTM-Bilder einer vergrabenen Übergangsmetallstruktur (Ir) in einem Edelmetallsubstrat (Cu(001)) werden vorgestellt, und der überraschende Effekt wird auf der Grundlage der elektronischen Struktur erklärt und verallgemeinert. (iv) Magnetische Identifikation mit einer nichtmagnetischen Spitze: Es wird untersucht, inwiefern es bei einem komplexen magnetischen System (Cr und Mn auf Fe(001)) möglich ist, verschiedene magnetische Konfigurationen aufgrund von (nicht-spinpolarisierten) RTM Experimenten zu unterscheiden. (v) Magnetische Abbildung mit SP-RTM: Das Potential des spin-polarisierten RTM (SP-RTM), magnetische Strukturen auf der ultimativen, der atomaren Skala abzubilden, wird mittels einer Erweiterung des Tersoff-Hamann Mo-

dells diskutiert. Die Anwendung dieser neuen Idee auf eine Monolage Mn auf W(110) führt zum ersten eindeutigen Nachweis für die Existenz des zwei-dimensionalen Antiferromagnetismus, der bereits 1988 theoretisch vorhergesagt worden ist.

Abstract

The investigation of plain and laterally structured transition-metal surfaces plays a key role in surface chemistry, in nanomagnetism, in the evolving field of magnetoelectronics, and for respective applications, e.g. in the magnetic-storage industry. Understanding the structural, electronic, chemical, and magnetic properties at transition-metal surfaces on the nanometer down to the atomic scale is an essential prerequisite towards the development of new devices. The scanning tunneling microscope (STM) is a strong driving force in this field but the unambiguous interpretation of acquired data of transition metals on the atomic scale is at its infancy. In most cases STM images of transition metals are interpreted on the basis of a hard sphere model. It is shown that this is incorrect. The combination of state-of-the-art first-principles calculations of the electronic structure with the Tersoff-Hamann model of the STM provides a powerful and successful approach to interpret STM images of transition-metals on the atomic scale. In this thesis the first systematic investigation of STM images of transition metals on the atomic scale is presented. We cover five different problems:

(i) Images of plain surfaces: The influence of the electronic structure on STM images even in the simple case of pure transition-metal surfaces is demonstrated by the effect of a bias-voltage dependent corrugation reversal for bcc-(110) surfaces. (ii) Chemical identification: The difficulty of discriminating between different chemical species at a surface is treated with an example ($CoSi_2(001)$) showing how the proper understanding of experimental data can be accomplished by the aid of calculations. (iii) Buried interfaces: Since the intermixing in multi-component systems need not be confined to the surface layer, it is further dealt with the ability of the STM to image also buried structures, even in metal systems. The first direct STM images of buried transition-metal (Ir) structures in a noble-metal surface (Cu(001)) are presented, and the surprising effect is explained and generalized on the basis of the electronic structure. (iv) Magnetic identification using a non-magnetic tip: We explore the feasibility to discriminate different magnetic configurations on the basis of (non-spinpolarized) STM experiments for a complex system (Cr and Mn on Fe(001)). (v) Magnetic imaging with SP-STM: The potential of spin-polarized STM (SP-STM) to image magnetic structures on the ultimate, the atomic scale is discussed with an extension of the Tersoff-Hamann model. Applying this new idea to a Mn monolayer on W(110) leads to the first unambiguous experimental proof of the existence of two-dimensional antiferromagnetism predicted as early as 1988.

Contents

Chapter 1

Introduction

Almost everyone's private and professional life today is influenced by the rapidly increasing importance of computing, information technology and telecommunication. The engine behind this development is the micro-electronics, one of the great intellectual and technological achievements of the 20th century. Micro-electronics has become possible by our understanding of solid state physics through quantum mechanics, the dominating theory in physics during the 20th century[1]. Ongoing refinements of fabrication and production techniques lead to increasingly smaller dimensions of the relevant structures, and we are approaching the nanometer scale, a scale of the order of the electron wave-length in metals. At this limit transport in these structures cannot be treated with semiclassical models anymore and unexpected quantum phenomena have been discovered. At this frontier of physics, a new field of solid state research has evolved in the late 1980's: nano-physics. It is justified to expect it to become the basis of new technology, nano-technology, which might shape the 21st century to an extent micro-technology has shaped the previous one. Only in 1997 for example, IBM presented a commercially available hard-disk drive with a storage density of 2.7 Gbits per square inch which was possible by equipping it with a read head exploiting the recently discovered Giant Magneto Resistance (GMR) effect (1989 by P. Grünberg, see Ref. [1]). This quantum effect on the nanometer scale is a finding of fundamental research. It is but one example of the quick succession of discoveries in basic research and technological applications by the industry in this new area of physics. Applying these new quantum effects requires material engineering with a precision on the nanometer scale. The structuring of metallic and semiconducting materials with such an accuracy has become feasible by the development of sophisticated deposition techniques like molecular-beam epitaxy and remarkable advances in ultra-high vacuum technology.

The ultimate tool to study these nano-structures from the nanometer down to the atomic scale and even to manipulate them atom by atom[2] is the scanning tunneling microscope (STM). Invented by Binnig and Rohrer in 1982 [2], who were awarded the

---

[1] The theory of relativity should certainly not be forgotten.

[2] Some beautiful examples of such structures created by D. Eigler and co-workers, the quantum corrals, are presented on the homepages of IBM, Almaden: http://www.almaden.ibm.com/vis/stm/stm.html.

noble-prize in 1986, it has revolutionized our approach to surface science. Conventional surface characterization techniques like photoemission (PES), inverse photoemission (IPES), low energy electron diffraction (LEED), or Helium scattering provide information in reciprocal space which are averaged over large scales in real-space (on the order of the spot size of the photon beam used in PES, for example). The STM, however, supplies us with real-space images of unprecedented lateral resolution. This new tool allows the formerly unthinkable possibility to study the properties of local structures like individual adsorbed atoms or molecules, step edges, islands, atom chains, domain boundaries, dislocations, and many more. Other scanning probe techniques followed, probing for example atomic forces, magnetic stray-fields or the local capacity, but the STM still provides the highest resolution: atomic resolution[3].

The idea at the heart of the STM is to exploit the *tunnel effect*, a basic result of quantum mechanics taught already in introductory courses [5]. From our experience we know that a particle, for example a ball, is totally reflected by a potential barrier, for example a wall, if its energy is insufficient to overcome it. In the microscopic world this is not true anymore, and there is a finite probability for a particle to *tunnel* through such a barrier. Although the effect is rather simple its technical application in an STM is a scientific challenge. In an STM a sharp metal tip is approached to a distance of a few Ångströms to a conducting sample surface. Now a tunneling current can flow through the vacuum barrier if a bias-voltage is applied between tip and sample. By scanning the tip with piezo-actuators in sub-Ångström steps across the surface and adjusting the vertical position z of the tip with a feed-back loop such that the tunneling current is kept constant a topographic image $z(x, y)$ of the surface is measured. As the tunneling current depends exponentially on the distance between tip and sample a vertical resolution of 1×10^{-3} nm is achieved with the best STMs today. Additionally, energy resolved information on electronic features of local structures can be acquired at the same time with the STM. The correlation of this information with the images provides a powerful approach to study surfaces on the atomic scale. However, interpreting such data in terms of the surface morphology, its electronic and its magnetic properties is by no means trivial. Therefore, great efforts in the development of appropriate models have accompanied the application of the STM from the very beginning [6–14].

There is a variety of effects influencing the tunneling of electrons through a vacuum barrier between two metal electrodes and many approximations have to be made in order to model STM experiments. The nature of the approximations which are required or can be made certainly depends on the specific STM problem addressed. For the interpretation of STM images it is desirable to establish a practicable scheme to model the experiments on the basis of the electronic structure of the sample while taking the STM tip into account by appropriate assumptions. Inelastic effects like the excitation of electron-hole pairs, plasmons, phonons, photons, or spin-flip processes can then be neglected since they present a minor contribution in terms of the STM images. However, these effects do become important when probing the local

---

[3] Quite recently a new technique in atomic force microscopy, the non-contact mode, has also led to atomic resolution [3, 4] but it will take much more research until the same level of sophistication is reached as with the STM.

electronic structure of the sample by scanning tunneling spectroscopy influencing for example the lineshape of electronic features or being essential in order to tunnel into surface states. Further assumptions concerning the vacuum potential barrier, the electric field, the interaction between tip and sample or the description of the tip and sample electronic structure are inevitable. The elastic one-electron-tunneling, i.e. excluding the mutual interaction of the tunneling electrons, can be described exactly, i.e. including tip-sample interaction, by scattering theory which is an approach used by Noguera *et al.* [12], Doyen *et al.* [13], and Corbel *et al.* [15]. In order to use this formalism the electronic structure of the combined system of tip and sample has to be known. For a realistic system the computational effort for an accurate description can be immense and often even unattainable. Since interaction effects can often be ruled out by appropriate tunneling parameters, i.e. if the tip-sample distance is larger than about 4 Å, the pertubative approach proposed by Bardeen [16], neglecting the interaction between tip and sample, is suitable. It provides a straight forward procedure to include the results of full fletched bandstructure calculations as an input. The treatment of the tip is cumbersome in any case and simplifications are needed. Applying the Bardeen approach, Tersoff and Hamann presented an approximation [6] of the tip electronic structure that is both most simple in the implementation and successful. It is the most widely used model and has contributed to the solution of a great variety of problems concerning experiments on semiconductor as well as metal surfaces. In this thesis the Bardeen approach in the treatment of Tersoff and Hamann as well as its extension by Chen [11] is used.

A breakthrough in the understanding of the electronic structure of complex and real condensed matter is due to the development of the density functional theory in the last 20 years [17–19][4]. This theory is an equivalent formulation of the quantum theory of a solid as the many-body wavefunction formalism describing the mutual interaction of electrons within an external potential, e.g. given by the lattice of the nuclei. Today it is *the state-of-the-art* theory to compute the ground-state properties of crystalline solids from first principles and thus a powerful theoretical tool to study the complex relationship between structural, electronic, chemical, and magnetic properties of condensed matter. Even the treatment of low-symmetry systems like surfaces, clusters, and molecules is no obstacle anymore. There is a variety of different density functional theory based methods available each optimized to deal with a limited set of problems. Among these methods the full-potential linearized augmented plane wave (FLAPW) method is one of the most accurate, general, and widely applicable. With its aid one can interpret and understand experimental findings as well as explore and predict trends of new materials leading to such surprising results as the magnetically stabilized c(2 × 2) MnCu/Cu(001) surface alloy [20] and the two-dimensional antiferromagnetism in monolayer transition-metal films on noble-metal surfaces [21] prior to experimental verification. Thus the mutual interaction of this theoretical method with predictive power with new experimental techniques and findings has led to rapid progress in both, theory and experiment. Concerning the simulation of STM experiments in the Bardeen formulation, the FLAPW method in film geometry is the method of choice since the surface electronic structure and the

---

[4] W. Kohn was awarded the noble prize 1998 in chemistry for his contribution to this theory.

vacuum region are described with remarkable precision.

While there have been rather many studies concerning the role of the electronic structure of semiconductor surfaces on STM experiments there has been surprisingly little work on the topic of metals, especially transition metals. While the presence of dangling bond states on semiconductor surfaces supplies a rich basis for the unexpected outcome of STM experiments and the need for theoretical models, conventional wisdom claims that it should be rather simple and uninteresting in the case of metal surfaces [22]. Since electrons screen the nuclear charges in metals much more efficiently than in semiconductors STM images with atomic resolution should simply display the surface atoms as protrusions. Therefore most of the explanations of STM images on the atomic scale for metals have been based on hard sphere models. This is definitely insufficient and mostly wrong as this work clearly demonstrates. Another reason for the lack of STM experiments on metal surfaces in combination with first-principles calculations is the difficulty to achieve atomic resolution on metals compared to the case of semiconductors where many studies also on the bias-voltage dependence have been reported. However, transition-metal surfaces are currently of great interest in fundamental research as well as for the magnetic storage industry due to their astonishing magnetic properties. In the past, the investigation of transition-metal surfaces and ultra-thin films has led to such surprising results as the enhancement of magnetic moments at surfaces, the occurrence of magnetism for metals which are non-magnetic in bulk, two-dimensional antiferromagnetism, non-collinear spin-structures, and the formation of two-dimensional surface and sub-surface alloys. All of these effects occur at the atomic scale making the STM an appropriate tool to study them.

In this work, the first systematic study of the role of the electronic structure in STM experiments on the atomic scale for transition-metal surfaces is presented. It is shown how the combination of first-principles calculations using the FLAPW method, as implemented in the `FLEUR` code, with STM experiments provides new insight into the investigation of this class of materials. In contradiction to conventional wisdom a number of surprising results have been obtained. After an introduction to the basics of density functional theory in chapter 2, the concept and some technical aspects of the FLAPW method are discussed in chapter 3. The procedure of modeling STM experiments on the basis of Bardeen's approach is presented in chapter 4. Further an efficient method to correlate calculated STM images and spectra with the electronic structure is introduced. This approach leads to a selection rule concerning the contribution of states from different parts of the surface Brillouin zone to the possible patterns of the STM images.

The chapters 5 to 9 contain five different applications. We begin in chapter 5 with a study of the most simple case one can think of, pure transition-metal surfaces. It is demonstrated that even in such a situation the interpretation of the acquired experimental data can be difficult. Instead of imaging the atom sites as protrusions as one would expect from conventional wisdom for metals, as a function of the bias-voltage the STM image may display the hollow sites as protrusions. The effect, *bias-voltage dependent corrugation reversal*, prevents one to simply deduce the adsorption sites of deposited atoms from the images.

Further complications are introduced by the presence of different chemical species at a surface which is a frequently encountered situation. To discriminate between different kinds of atoms in such a multi-component system, i.e. to gain *chemical sensitivity* with the STM, is far from trivial and although this has been an open topic for a long time, there is no general recipe available. Chapter 6 gives evidence that sometimes only the combination with first-principles calculations leads to a proper understanding of the experimental results.

In a multi-component system the intermixing between different chemical species need not be limited to the surface layer. Instead, impurities or even two-dimensional alloy layers can be covered by one or more layers of the substrate material. While the direct STM imaging of buried structures in semiconductors has been frequently reported it has previously been impossible for metal systems. The images simply displayed the arrangement of the surface layer atoms, and it had to be concluded indirectly that the formation of a buried structure is taking place. This is consistent with conventional wisdom that the effective screening of electrons in a metal prevents perturbations to be visible for more than about one atomic layer. In chapter 7, we present for the first time *direct STM images of a subsurface alloy.* Aided by the calculations, the unexpected effect can be explained, and its application for a wide class of materials is shown. On the basis of the electronic structure we further explore the feasibility of imaging even deeply buried alloys by the presence of quantum well states in such systems.

After having dealt with the influence of electronic, structural, and chemical properties in the previous chapters, we turn to the currently most important aspect of transition metals in chapters 8 and 9 which are their exceptional magnetic properties. We start in chapter 8 by investigating the influence of different magnetic configurations on the expected (non-spinpolarized) STM experiments. The systems taken under scrutiny, Cr and Mn on Fe(001), display a complex correlation between structure and magnetism on the atomic scale. A real-space probe with atomic resolution like the STM is therefore ideally suited to shed light onto this system. The calculations reveal that the spectroscopic mode of STM should provide a distinction between different magnetic configurations in the case of Cr while it is impossible for the more complicated scenario of Mn. Surprisingly, calculated (atomic resolution) STM images of a Mn-monolayer on Fe(001) display patterns related to the magnetic superstructure rather than to the chemical only the use of spin-polarized STM (SP-STM) [23–28] unit cell. However, due to the variety of competing antiferromagnetic configurations for Mn it can be concluded that will lead to a safe discrimination between the different magnetic configurations.

In chapter 9 a general theoretical discussion of the potential of SP-STM to resolve magnetism on the atomic scale is given by an extension of the Tersoff-Hamann model. With its aid and the selection rule introduced in chapter 4 we can prove that *any magnetic superstructure within an arrangement of chemically equivalent atoms leads to an SP-STM image displaying a pattern corresponding to the magnetic configuration.* There is not just a slight modulation of the non-spinpolarized STM image reflecting the chemical structure but a complete domination of the contrast by the magnetic structure. This general effect is demonstrated experimentally for a Mn monolayer on a W(110)-surface. This system is an example for the occurrence of two-dimensional antiferromagnetism in monolayer films on non-magnetic substrates predicted by S. Blügel *et al.* as early as 1988 [21]. The STM experiment is in excellent agreement with the first-principles calculations and is the first unambiguous proof for the existence of two-dimensional antiferromagnetism. An illustrative image of the achieved magnetic resolution on the atomic scale is given in Fig. 1.1. Instead of providing an explanation posterior to the experiment the calculations were performed in advance and later beautifully verified in the experiment. Predictive power can thus be attributed to the present theoretical approach. Finally, a conclusion and a summary of this work are given in chapter 10.

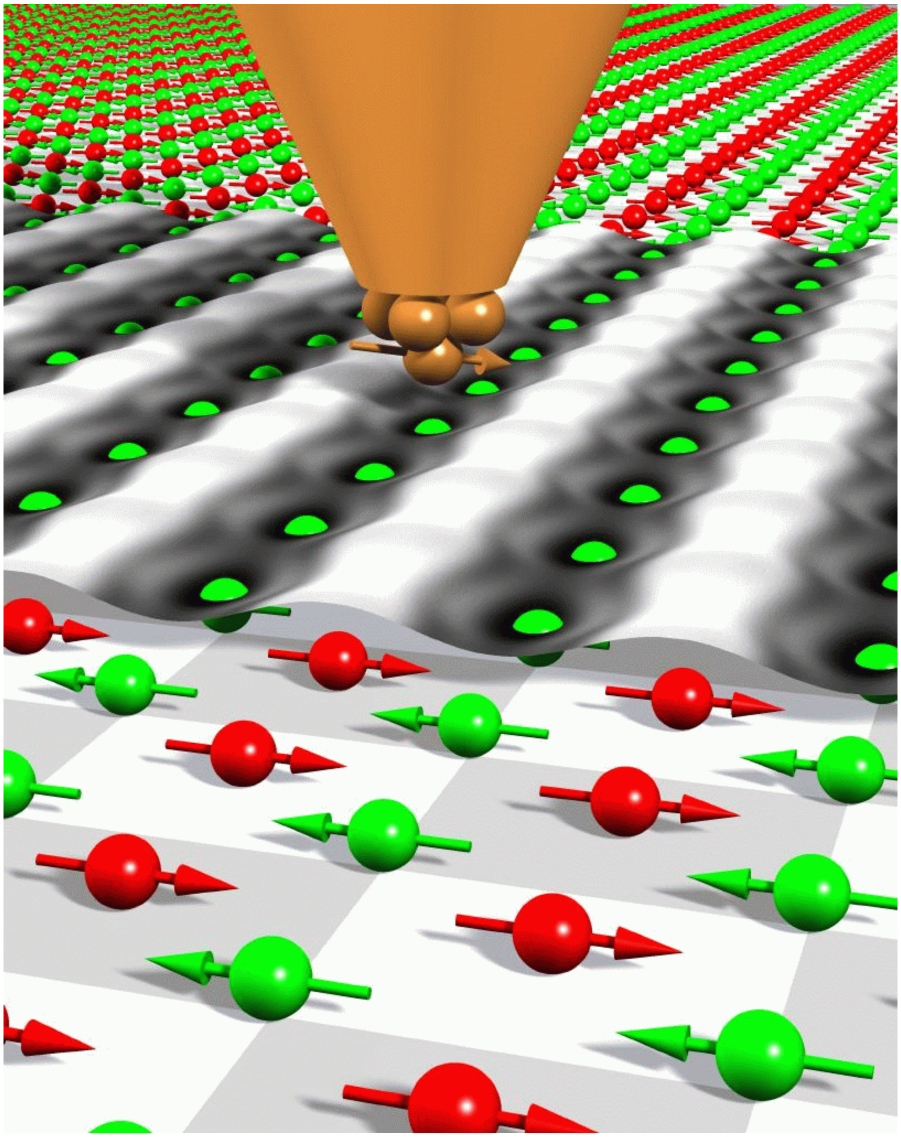

Figure 1.1: Direct observation of the two-dimensional atomic scale antiferromagnetic structure of a monolayer magnetic film by spin-polarized scanning tunneling microscopy (SP-STM). All atoms of the monolayer film (red and green) are of the same chemical species (Mn) and differ only by the orientation of their magnetic moment. Using a magnetic probe tip it is possible to measure an SP-STM image (see the height profile) showing one kind of magnetic atoms (red) as hills and the other kind (green) as valleys, i.e. a direct image of the atomic scale magnetic order within the magnetic film.

Chapter 2

Density Functional Theory

In order to calculate the structural, electronic, and magnetic properties of a solid it is necessary to solve the many-body Schrödinger equation describing the interaction between the electrons and the interaction of the electrons with the nuclei. Thus, one must find the eigenstates $|\Psi\rangle$ and energy eigenvalues E of:

$$H|\Psi\rangle = E|\Psi\rangle, \tag{2.1}$$

where H is the Hamiltonian of the interacting system. It contains the kinetic energy of all particles and the Coulomb interaction between electrons, electrons and nuclei and between the nuclei themselves. Both, the eigenstates $|\Psi\rangle$ and the Hamiltonian H, depend on the positions $\mathbf{r}_i$ and spins σ_i of all electrons as well as on the positions of the nuclei $\mathbf{R}_I$. Since the motion of the electrons is much faster than that of the nuclei one can neglect the atom motion or vibration to a good approximation by fixing their positions. This is called the adiabatic approximation and is common to the majority of electronic structure calculations. In the adiabatic approximation the Hamiltonian can be given explicitly by:

$$H = \sum_{i=1}^{n} -\frac{\hbar^2}{2m}\nabla^2_{\mathbf{r}_i} + \frac{1}{2}\sum_{i,j}\frac{e^2}{|\mathbf{r}_i - \mathbf{r}_j|} - \sum_{i,I}\frac{Z_I e^2}{|\mathbf{r}_i - \mathbf{R}_I|} + \frac{1}{2}\sum_{I,J}\frac{Z_I Z_J e^2}{|\mathbf{R}_I - \mathbf{R}_J|}, \tag{2.2}$$

where Z_I denotes the charge of the nucleus I. Today, there is no analytical or numerical way of finding the solutions, i.e. the many-particle wave functions, to this Hamiltonian if more than a few electrons are considered. Therefore, one has to look for possible reformulations of the problem or to introduce well-justified approximations. In the Hartree-approximation, for example, one treats the electrons independently by writing the many particle wave functions as products of single particle wave functions. Further, the electron interaction term in the Hamiltonian is replaced by the electrostatic Coulomb potential of all electrons, the Hartree potential. Thereby the problem reduces to finding one-particle wave functions in a periodic potential. If, in addition, the requirement of an anti-symmetric many-particle wave function is fulfilled by forming a Slater determinant of single-particle wave functions one can generalize this approach to the Hartree-Fock-approximation. In this way the Pauli-exclusion principle is satisfied keeping any two electrons from occupying the same state. This approach is to a certain extent still successfully applied in quantum chemistry to calculate properties of atoms and molecules, but it is not sufficient for the quantitative description of electrons in bulk or even surface magnetism.

Since one is usually only interested in the expectation values of certain quantum-mechanical operators (the observables), e.g. the total energy, the charge density or the magnetic moment, and not in the enormous amount of information contained in the many-particle wave function it is natural to think about an alternative formulation of the problem. It is the idea of the Thomas-Fermi model to express all properties of a system as a functional of the electron probability density alone. The model turns out to be a rather crude one, as the kinetic energy is described in terms of the density and no electron correlation is included. Therefore, it does not improve the results of Hartree-Fock calculations significantly. Nevertheless in 1964 Hohenberg and Kohn used the idea of this model [17] and derived an equivalent formulation of the many-body Schrödinger equation which is the *density-functional theory*. This theory is the basis of all modern *ab initio* or first-principles (parameter-free) electronic structure calculation methods. The importance of this development was expressed recently by awarding W. Kohn the noble prize 1998 in chemistry for his contributions to this theory[1].

2.1 Theorem of Hohenberg and Kohn

An important limitation of the *density-functional theory* as it has been derived by Hohenberg and Kohn and applied in this work is it being a ground-state theory. Thus it is actually applicable only for temperatures $T \to 0$ K. Rather than the many-electron wave function its central quantity is the probability density n of the electrons given by the expectation value of the density operator:

$$n(\mathbf{r}) \equiv \langle \psi(\mathbf{r}_1, \mathbf{r}_2, ..., \mathbf{r}_N) | \sum_{i=1}^{N} \delta(\mathbf{r} - \mathbf{r}_i) | \psi(\mathbf{r}_1, \mathbf{r}_2, ..., \mathbf{r}_N) \rangle. \tag{2.3}$$

In contrast to the many-electron wave function ψ the probability density n depends on one three-dimensional space coordinate $\mathbf{r}$ instead of 10^{23} for ψ making it easy to handle. The theorem of Hohenberg and Kohn [17] generally applies to any many-electron system with Coulomb interaction in an external potential V_{ext} which is in our case given by the Coulomb interaction with the nuclei located at the lattice sites. It states that the electron density n_0 of the ground-state is uniquely connected with the external potential V_{ext}. Together with the number of electrons N this defines the problem completely. Since an integration in space of the electron density n_0 yields the number of electrons, all properties of the ground-state can be expressed by its electron density n_0. The theorem is twofold:

- All ground-state properties are unique functionals of the ground-state electron

---

[1] The prize was shared with J. A. Pople who implemented the theory most successfully in the field of chemistry in his `GAUSSIAN` code.

density n_0. For example, the total energy can be expressed as

$$E_0 = E[n_0] = F[n_0] + \int n_0(\mathbf{r}) V_{\mathrm{ext}}(\mathbf{r})\, d^3r, \tag{2.4}$$

where $F[n]$ is a functional independent of the specific system as it describes the electron-electron interaction only.

- The total energy functional $E[n]$ obeys a variational principle, i.e. it is minimized for the ground-state electron density n_0:

$$E[n] > E[n_0] = E_0 \;\Rightarrow\; \left.\frac{\delta E[n]}{\delta n}\right|_{n_0} = 0. \tag{2.5}$$

The second part of the theorem provides a way of finding the ground-state density by varying the energy functional with respect to the density. Up to this point the many-body problem has only been reformulated and is hidden in the unknown functional $F[n]$. For the practical applicability of the theory it is essential to find an (approximate) description of this functional. Levy showed [19] that it can formally be written as:

$$F[n] = \min_{\psi \to n} \langle \psi | T + U_{\mathrm{ee}} | \psi \rangle, \tag{2.6}$$

where T is the operator of the kinetic energy, U_{ee} is the Coulomb interaction between electrons and ψ must be an anti-symmetric N-particle wave function, because of the fermionic character of electrons. To my knowledge no practical application of this formulation has been derived so far. Therefore, before one could even think of using the *density functional theory* for practical purposes, it was a further basic step in the theory necessary to construct an energy functional which led to the Kohn-Sham equations [18].

2.2 Kohn-Sham Equations

The idea of Kohn and Sham leading to the practical applicability of *density functional theory* was to map the many-particle problem to an independent particle problem in an effective potential. Thus they have chosen as an ansatz for the energy functional:

$$E[n] = T_{\mathrm{s}}[n] + E_{\mathrm{H}}[n] + E_{\mathrm{ext}}[n] + E_{\mathrm{xc}}[n], \tag{2.7}$$

where $T_{\mathrm{s}}[n]$ is the kinetic energy of non-interacting electrons, i.e. independent particles, and can be given explicitly by using single-electron orbitals $\psi_i(\mathbf{r})$:

$$T_{\mathrm{s}}[n] = 2 \sum_{i=1}^{N} -\frac{\hbar^2}{2m} \int \psi_i^*(\mathbf{r}) \nabla^2 \psi_i(\mathbf{r})\, d^3r, \tag{2.8}$$

where the sum is taken over all occupied states i and the factor 2 accounts for each orbital being occupied with a spin up and a spin down electron. $E_{\mathrm{H}}[n]$ is the Hartree energy describing the Coulomb interaction of the electrons in their electrostatic potential and is given by:

$$E_{\mathrm{H}}[n] = \frac{e^2}{2} \int \frac{n(\mathbf{r})n(\mathbf{r}')}{|\mathbf{r} - \mathbf{r}'|}\, d^3r. \tag{2.9}$$

$E_{\mathrm{ext}}[n]$ is the energy caused by the external potential:

$$E_{\mathrm{ext}}[n] = \int n(\mathbf{r}) V_{\mathrm{ext}}(\mathbf{r})\, d^3r. \tag{2.10}$$

Finally all many-particle interactions and the correction to the kinetic energy due to interacting electrons are contained in the exchange-correlation energy functional $E_{\mathrm{xc}}[n]$. The exchange interaction is caused by the requirement of an anti-symmetric wave function in connection with the Coulomb repulsion of electrons. It is therefore possible to gain energy by aligning electron spins parallel since the orbital wave functions must then be anti-symmetric in the real-space coordinates which reduces the Coulomb energy. It is this mechanism which leads to the magnetic moments of atoms or solids, i.e. a difference in the number of spin up and spin down electrons. The correlation of electron motion on the other hand is a classical many-particle effect caused by their Coulomb interaction.

The great advantage of dividing up the energy functional in the form as written in Eq. (2.7), i.e. into four contributions is motivated by the quite accurate description of the kinetic energy, which is a major contribution to the total energy. Using the kinetic energy of free electrons for this part was a serious drawback of the Thomas-Fermi model. The electron density can now be expressed by the sum over all occupied single-particle orbitals:

$$n(\mathbf{r}) = 2 \sum_{i=1}^{N} |\psi_i(\mathbf{r})|^2. \tag{2.11}$$

Again the factor 2 enters to account for the double occupation of orbitals. In principle, the orbitals $\psi_i(\mathbf{r})$ have not been introduced to be interpreted in the single-particle picture, for example to describe excitations. The main quantity is still the electron density n, but practical applications show the usefulness of the direct interpretation of the ψ_i's as single-electron states. Very often the physics can be understood on the basis of this concept. Further, it can be proved explicitly that the excitations are described by this theory for energies near to the Fermi level.

Instead of varying the energy functional of Eq. (2.7) with respect to the electron density n one can also insert Eq. (2.11) into the energy functional and vary with respect to the single-electron orbitals ψ. The constraint of a constant number of particles can be taken care of by requiring the orbitals to be normed. This introduces Lagrange parameters ϵ_i, which can often be interpreted as excitation energies, and the final result of applying the variational principle are the Kohn-Sham equations:

$$\left(-\frac{\hbar^2}{2m} \nabla^2 + V_{\mathrm{H}}(\mathbf{r}) + V_{\mathrm{ext}}(\mathbf{r}) + V_{\mathrm{xc}}(\mathbf{r}) \right) \psi_i(\mathbf{r}) = \epsilon_i \psi_i(\mathbf{r}). \tag{2.12}$$

This equation is equivalent to a one-particle Schrödinger equation in an effective potential consisting of the Hartree potential V_{H}:

$$V_{\mathrm{H}}(\mathbf{r}) = e^2 \int \frac{n(\mathbf{r}')}{|\mathbf{r}-\mathbf{r}'|}\, d^3r, \tag{2.13}$$

the external potential V_{ext} and the exchange-correlation potential V_{xc}:

$$V_{\mathrm{xc}}(\mathbf{r}) = \frac{\delta E_{\mathrm{xc}}[n]}{\delta n(\mathbf{r})}. \tag{2.14}$$

Both the Hartree and the exchange-correlation potential depend on the electron density and therefore these equations can only be solved self-consistently. By choosing the electron density of the atoms the starting potentials are defined, and by solving Eq. (2.12) and inserting the solutions into Eq. (2.11) an output density is generated. This output density is mixed with the input density[2] to a new starting density and the process is repeated. If the output and input densities differ only marginally the calculation has converged and the ground-state density has been found. It is interesting to note that solving the Kohn-Sham equations is not more demanding than solving the equations of the Hartree-approximation and is far easier than in the Hartree-Fock approximation using non-local potentials.

2.3 Spin Density Functional Theory

In order to describe magnetic properties of atoms, molecules or solids it is necessary to extend the theory to a *spin density functional theory*. This is possible in a straight forward way by introducing in addition to the electron density $n(\mathbf{r})$ the vector of the magnetization density $\mathbf{m}(\mathbf{r})$ which results from the concept of Pauli-spinors accounting for the electron spin. If only collinear spin structures are considered, i.e. ferro- and antiferromagnetic configurations, only a scalar magnetization density $m(\mathbf{r})$ is necessary since the two spinor components can be decoupled. Alternatively, one can operate with majority $n_\uparrow(\mathbf{r})$ and minority $n_\downarrow(\mathbf{r})$ spin densities as independent variables since they are related by:

$$n(\mathbf{r}) = n_\uparrow(\mathbf{r}) + n_\downarrow(\mathbf{r}), \tag{2.15}$$

$$m(\mathbf{r}) = n_\uparrow(\mathbf{r}) - n_\downarrow(\mathbf{r}). \tag{2.16}$$

A theorem equivalent to the one of Hohenberg and Kohn can be proved stating that an unique energy functional of majority and minority spin densities exists which is minimized for their ground-state densities:

$$E[n_\uparrow, n_\downarrow] > E[n_\uparrow^0, n_\downarrow^0] = E_0 \quad \text{for} \quad n_\uparrow \neq n_\uparrow^0 \quad \text{and} \quad n_\downarrow \neq n_\downarrow^0. \tag{2.17}$$

---

[2] Different methods have been developed in order to improve the process of converging a density. Simply using the output density as new starting density usually does not lead to convergence at all.

By introducing an exchange-correlation energy functional $E_{\mathrm{xc}}[n_\uparrow, n_\downarrow]$ depending on both spin densities one obtains a set of Kohn-Sham equations for each spin direction:

$$\left(-\frac{\hbar^2}{2m}\nabla^2 + V_{\mathrm{H}}(\mathbf{r}) + V_{\mathrm{ext}}(\mathbf{r}) + V_{\mathrm{xc}}^{\sigma}(\mathbf{r})\right)\psi_i^{\sigma}(\mathbf{r}) = \epsilon_i^{\sigma}\psi_i^{\sigma}(\mathbf{r}), \tag{2.18}$$

where $\sigma = (\uparrow, \downarrow)$ and the spin-dependent exchange-correlation potential V_{xc}^{σ}:

$$V_{\mathrm{xc}}^{\sigma}(\mathbf{r}) = \frac{\delta E_{\mathrm{xc}}[n_\uparrow, n_\downarrow]}{\delta n_\sigma(\mathbf{r})}. \tag{2.19}$$

The spin densities are given by the spin-dependent orbitals:

$$n_\sigma(\mathbf{r}) = \sum_i |\psi_i^{\sigma}(\mathbf{r})|^2. \tag{2.20}$$

The energetically lowest orbitals are filled until the number of occupied orbitals is equal to the number of electrons (in the unit cell). Thus a difference in the number of majority and minority spin electrons may remain which determines then a finite magnetic moment for the ground-state.

2.4 Local Spin Density Approximation

In the previous two sections it has been shown how the concept of *density functional theory* can be mapped to a practical solvable problem. Still no approximations have been made, and the full many-body problem is contained in the Kohn-Sham equations. All many-particle interactions are described by the exchange-correlation energy functional or, equivalently, the corresponding potential. Since no explicit form can be given for this essential term the value of the whole approach depends on finding an adequate approximation. Most commonly the local spin-density approximation is being used. Its idea is to approximate the exchange-correlation energy locally by that of an homogeneous spin-polarized electron gas with spin-densities as found at a given position $\mathbf{r}$, i.e. by:

$$E_{\mathrm{xc}}[n_\uparrow, n_\downarrow] = \int \epsilon_{\mathrm{xc}}^{\mathrm{homog}}(n_\uparrow(\mathbf{r}), n_\downarrow(\mathbf{r}))\, n(\mathbf{r})\, d^3r. \tag{2.21}$$

Today there are methods of calculating the exchange-correlation energy per electron of an interacting spin-polarized homogeneous electron gas $\epsilon_{\mathrm{xc}}^{\mathrm{homog}}(n_\uparrow, n_\downarrow)$, i.e. with spatially constant spin-densities, with different parameterizations. They result from approximations to the analytical solution of the many-body problem utilizing the random phase approximation [29, 30]. The most accurate ones are derived from numerical Quantum Monte Carlo calculations [31,32]. Although the local spin-density approximation was believed to be accurate only in the limit of slowly varying electron densities the practical application also to very inhomogeneous electron densities, e.g. of transition metals, has been surprisingly successful. The reason for this is seen in the mutual cancellation of different errors inherent to the approximation.

2.5 Stoner Model of Ferromagnetism

Since many of the metal surfaces discussed in this work possess magnetic ground-states it is worthwhile describing the Stoner Model of ferromagnetism to provide a basis for the interpretation of the more complicated systems. In the following we will show how one can derive the model directly from the spin-density functional theory.

In general, the magnetization density $m(\mathbf{r})$ is small compared with the electron density $n(\mathbf{r})$, and therefore one can linearize the exchange-correlation potential V_{xc}^{σ} of the spin-polarized case around the non-spinpolarized case V_{xc}^{0}:

$$V_{\mathrm{xc}}^{\sigma}(\mathbf{r}) \cong V_{\mathrm{xc}}^{0}(\mathbf{r}) \mp \tilde{V}_{\mathrm{xc}}(\mathbf{r}) m(\mathbf{r}), \tag{2.22}$$

where σ denotes the spin direction ($\uparrow, \downarrow$). Higher order terms in the magnetization density $m(\mathbf{r})$ are neglected. Thus there is a decrease of the potential for the majority spin electrons ($\uparrow$) and an increase for the minority spin electrons ($\downarrow$). Stoner introduced a parameter I, the so-called exchange integral, to describe this shift in the potential in a simple manner and Eq. (2.22) becomes:

$$V_{\mathrm{xc}}^{\sigma}(\mathbf{r}) \cong V_{\mathrm{xc}}^{0}(\mathbf{r}) \mp \frac{1}{2} I M, \tag{2.23}$$

where M is the magnetization of an atom in the solid defined by the integral of the magnetization density over the volume of the atom:

$$M = \int\limits_{\mathrm{V_{atom}}} m(\mathbf{r})\, d^3 r. \tag{2.24}$$

Since the potential of the non-spinpolarized case has only been modified by a constant, the eigenstates of the Kohn-Sham equations remain unaltered while the energies are shifted by the constant potential change:

$$\psi_i^{\sigma}(\mathbf{r}) = \psi_i^{0}(\mathbf{r}) \ \text{ with } \ \epsilon_i^{\sigma} = \epsilon_i^{0} \mp \frac{1}{2} I M, \tag{2.25}$$

where ψ_i^0 are the eigenfunctions and ϵ_i^0 the corresponding energy eigenvalues of the non-magnetic problem. Consequently, also the density of states of the majority and minority electrons can be related to the density of states of the non-magnetic one by:

$$n^{\sigma}(\epsilon) = n^{0}(\epsilon \pm \frac{1}{2} I M). \tag{2.26}$$

Given the density of states and the total number of electrons N, we can calculate the Fermi energy E_F of the system:

$$N = \int\limits_{-\infty}^{E_F} \left(n^0(\epsilon + \frac{1}{2} I M) + n^0(\epsilon - \frac{1}{2} I M) \right) d\epsilon. \tag{2.27}$$

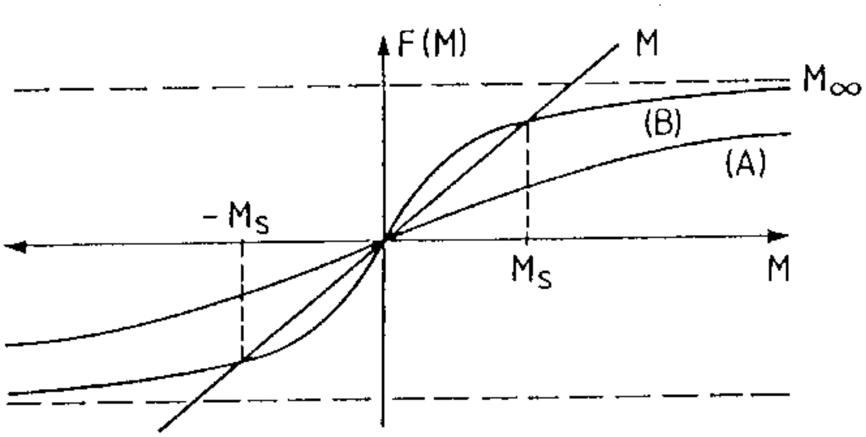

Figure 2.1: Graphical solution of Eq. (2.29). Figure has been taken from Ref. [34].

Analogously, the magnetic moment M is given by:

$$M = \int_{-\infty}^{E_F} (n^0(\epsilon + \frac{1}{2}IM) - n^0(\epsilon - \frac{1}{2}IM))\, d\epsilon. \tag{2.28}$$

From Eq. (2.27) the Fermi energy can be computed as a function of the magnetization, i.e. $E_F = E_F(M)$ and by inserting this into Eq. (2.28) we obtain an equation of the form:

$$M = F(M) \tag{2.29}$$

for the magnetization itself, where $F(M)$ is given by the right-hand side of Eq. (2.28) with $E_F = E_F(M)$. Several characteristics of the function $F(M)$ can be proven:

$$(i)\ F(0) = 0, \quad (ii)\ F'(M) > 0, \quad (iii)\ F(M \to \pm\infty) \to \pm M_\infty, \tag{2.30}$$

$$(iv)\ F(M) = -F(-M). \tag{2.31}$$

In Fig. 2.1 two possible curves for $F(M)$ consistent with the relations (i) to (iv) have been sketched. In case (A) only the solution $M = 0$ is possible while two additional solutions of Eq. (2.29) exist for case (B): $M = \pm M_S$. In (B) the non-magnetic state becomes unstable with respect to the ferromagnetic state. In order to find ferromagnetic solutions to Eq. (2.29) (see case (B)) the function $F(M)$ must increase more than linearly at the origin, i.e. $F'(0) > 1$, which leads to the Stoner criterion of ferromagnetism:

$$In^0(E_F) > 1. \tag{2.32}$$

Thus the occurrence of ferromagnetism depends on the exchange integral I and the density of states n^0 of the non-spinpolarized treatment at the Fermi level E_F. Obviously, $In^0(E_F)$ has to be sufficiently large to fulfill the instability criterion (2.32).

I is basically an atomic quantity and depends on the nuclear number. Within each transition-metal series it varies little. It is typically largest at the end of the series and it holds that $I_{3d} > I_{4d} > I_{5d}$. The density of states n^0 is approximately inversely proportional to the bandwidth W, $n^0 \propto 1/W$. The bandwidth W, on the other hand, depends on the overlap of the wave functions of neighboring atoms and is proportional to the square root of the number of nearest neighbors N, $W \propto \sqrt{N}$. As the number of nodes of the wave functions increases from zero to two from the $3d$ to the $5d$ wave functions, there is also an increased delocalisation and thus an increased overlap. Correspondingly, the bandwidth follows the relationship $W_{3d} < W_{4d} < W_{5d}$ and consequently $n^0_{3d} > n^0_{4d} > n^0_{5d}$. If we choose numbers for these trends based on general arguments, we find that ferromagnetism occurs only for Fe, Co and Ni. With a reduction of the coordination number N from bulk to surfaces, thin films and finally to atoms the tendency towards magnetism increases. Atoms are the limiting case with a bandwidth zero. Thus they always possess a magnetic moment if shells are only partially filled which is expressed in Hund's first rule. The rare-earth metals with their strongly localized f-electrons are related to the case of atoms while the magnetism of the transition metals, i.e. metals with partially filled d-shells, is called band or itinerant magnetism since the same electrons are responsible for transport and magnetism. In the reduced dimensions of a thin film ferromagnetism can occur even for transition metals which are non-magnetic in bulk (for example Ti becomes ferromagnetic as a monolayer film on a noble-metal substrate [33]). Along these lines a whole new class of materials can be created with a variety of new magnetic structures.

The Stoner criterion can be generalized to arbitrary spin configurations, for example antiferromagnetic structures which can be represented by a spin wave with a wave vector $\mathbf{q}$, i.e. a magnetization density that is modulated within the crystal. The generalized Stoner criterion states that

$$I\chi(\mathbf{q}) > 1, \tag{2.33}$$

where $\chi(\mathbf{q})$ is the $\mathbf{q}$-vector dependent susceptibility. The transition metal bulk antiferromagnets are Mn and Cr with complicated ground-states, and especially for Mn the correlation of structure and magnetism is complex. Quite generally one can state that the elements at the beginning or at the end of the $3d, 4d$ and $5d$-row show a tendency towards ferromagnetism while the elements with approximately half-filled d-bands, e.g. Mn and Cr, tend to antiferromagnetism. For a further discussion of antiferromagnetism we refer to the literature (e.g. [34]).

Chapter 3

The FLAPW Method

In the previous chapter the task of computing the properties of a solid has been reduced from a many-body problem of interacting electrons to finding the solutions of a kind of single-particle Schrödinger equation with an effective but density dependent potential, i.e. self-consistently solving the Kohn-Sham equations (Eq. (2.12)). In this chapter we introduce and shortly discuss one specific technique for computing their solutions, the Full-potential Linearized Augmented Plane Wave (FLAPW) method. Describing this powerful, but technically demanding method which has been developed, improved and extended for some 20 years in detail is beyond the scope of this work and for a deeper understanding it can only be referred to a recently published book [35]. Further, Ref. [36, 37] are recommended to learn about the wide field of technical aspects.

A great deal of applications of density functional theory in the field of condensed matter deal with crystalline solids and their surfaces. These possess (external) potentials with translational symmetry. This enables one to apply the Bloch Theorem (see for example [38]) stating that every eigenstate of the Schrödinger equation can be classified by the quantum numbers band index ν and wave vector $\mathbf{k}$. Further, it can be expressed by:

$$\psi_{\mathbf{k}\nu}(\mathbf{r}) = \exp(i\mathbf{kr}) \sum_{\mathbf{G}} c_{\mathbf{k}\nu}^{\mathbf{G}} \exp(i\mathbf{Gr}), \tag{3.1}$$

where $\mathbf{G}$ is a vector of the reciprocal lattice and the $c_{\mathbf{k}\nu}^{\mathbf{G}}$ are Fourier expansion coefficients.

3.1 The Eigenvalue Problem

There are a variety of numerical techniques available today for solving the Kohn-Sham equations all of which – some more, some less – are particularly appropriate for certain classes of materials, structural configurations, or to compute special properties with high accuracy. Most of them share the ansatz of expanding the wave function $\psi_{\mathbf{k}\nu}$ in a set of basis functions ϕ_n:

$$\psi_{\mathbf{k}\nu}(\mathbf{r}) = \sum_{n=1}^{N} c^n_{\mathbf{k}\nu} \phi_{\mathbf{k}n}(\mathbf{r}), \tag{3.2}$$

with the number of basis functions N. Inserting this ansatz into the Kohn-Sham equations (Eq. (2.12)) we arrive at an eigenvalue problem for the eigenvalues $\epsilon_{\mathbf{k}\nu}$ and expansion coefficients $c^n_{\mathbf{k}\nu}$:

$$(\mathbf{H}_\mathbf{k} - \epsilon_{\mathbf{k}\nu}\mathbf{S}_\mathbf{k})\mathbf{c}_{\mathbf{k}\nu} = 0, \tag{3.3}$$

where the Hamiltonian matrix $\mathbf{H}_\mathbf{k}$ is given by:

$$\mathrm{H}^{n,n'}_\mathbf{k} = \int \phi^*_{\mathbf{k}n'}(\mathbf{r}) H \phi_{\mathbf{k}n}(\mathbf{r})\, d^3r, \tag{3.4}$$

and the overlap matrix $\mathbf{S}_\mathbf{k}$ is defined as:

$$\mathrm{S}^{n,n'}_\mathbf{k} = \int \phi^*_{\mathbf{k}n'}(\mathbf{r}) \phi_{\mathbf{k}n}(\mathbf{r})\, d^3r. \tag{3.5}$$

Since the set of basis functions is usually non-orthogonal the overlap matrix differs from the unity matrix, and equation (3.3) is a generalized eigenvalue problem. It can be transformed into a normal eigenvalue problem by decomposing the overlap matrix through a Cholesky factorization. In general $\mathbf{H}_\mathbf{k}$ and $\mathbf{S}_\mathbf{k}$ are hermitian matrices which become symmetric if the crystal has inversion symmetry. It is important to note that the computation time required to solve an eigenvalue problem scales with the order N of the matrix to the third power. Thus it is highly desirable to have an effective basis set, i.e. one which needs only a small number of functions N to describe the electron wave functions accurately. Another aspect important for the choice of a basis is the generation of the Hamiltonian and the overlap matrix which can also be quite time consuming if the basis set is complex.

In spin-density functional theory the effective potential and thereby also the Hamiltonian are spin-dependent. For collinear spin structures the Hamilton matrix becomes block-diagonal which leads to two eigenvalue problems of the form (3.3), one for each spin direction $\sigma \in (\uparrow, \downarrow)$. Correspondingly, the wave functions $\psi^\sigma_{\mathbf{k}\nu}$ gain an extra spin index σ. As the treatment of both spin directions is equivalent and for the sake of simplicity the spin index is neglected in the following but may easily be added in all results.

3.2 Choosing the Basis Functions

The choice of the basis functions together with the approximations made to express the effective potential and the electron density defines different techniques and leads to their names. For example, plane waves are a very natural choice since they fulfill Bloch's theorem (compare Eq. (3.1)) and are easy and efficient to deal with in terms of computing matrix elements of quantum mechanical operators like the Hamiltonian.

Their major drawback is the high number of plane waves needed to express the strong oscillations of electron wave functions near to the atom cores where electrons possess high kinetic energies. Therefore one can either modify the potential in the region near to the nuclei reproducing the correct band energies without finding the right wave functions (this is the concept of the pseudopotential methods) or choose a different set of basis functions for this special region of space. The latter is the concept of the augmented plane wave (APW) based methods and has first been proposed by Slater [39]. Space is partitioned into non-overlapping spheres (so-called muffin-tins) located at the atom sites and the interstitial region in between them. In the interstitial region, where the potential is almost constant, plane waves are still chosen as basis functions. In the spheres, on the other hand, a product of spherical harmonics $Y_{lm}(\hat{\mathbf{r}})$ and solutions $u_l(r)$ of the radial Schrödinger equation with the spherically symmetric part of the effective potential are used:

$$\phi_{\mathbf{G}}(\mathbf{k},\mathbf{r}) = \begin{cases} \frac{1}{\sqrt{\Omega}} \exp\left[i(\mathbf{k}+\mathbf{G})\mathbf{r}\right] & \text{if } \mathbf{r} \in \text{Interstitial}, \\ \sum\limits_{lm} A_{lm}^{\alpha\mathbf{G}}(\mathbf{k}) u_l(r) Y_{lm}(\hat{\mathbf{r}}) & \text{if } \mathbf{r} \in \text{Muffin-Tin Sphere } \alpha, \end{cases} \tag{3.6}$$

where lm are the angular momentum quantum numbers, Ω is the volume of the unit cell and the basis functions are characterized by the wave vector $\mathbf{k}$ and the reciprocal lattice vector $\mathbf{G}$. The coefficients $A_{lm}^{\alpha\mathbf{G}}(\mathbf{k})$ are chosen so that the basis functions are continuous at the sphere boundaries of the atom α. The radial Schrödinger equation[1]:

$$\left(-\frac{\hbar^2}{2m}\frac{d^2}{dr^2} + \frac{\hbar^2}{2m}\frac{l(l+1)}{r^2} + V_{\text{eff}}(r) - E_l\right) r u_l(r) = 0 \tag{3.7}$$

contains the energy E_l of the valence electrons for the angular momentum l. If we insert this ansatz for the basis functions into the Kohn-Sham equations a nonlinear equation for the energy eigenvalues results which is non-trivial to solve. If, on the other hand, the energy E_l would be fixed we would obtain a simple matrix eigenvalue problem which can be solved with standard matrix techniques. However, the practical application shows that this is impossible within the APW idea since the basis functions lack variational freedom if E_l is fixed for all valence electrons of a given l-quantum number and one cannot describe the wave functions and eigen energies of all electrons within a reasonable energy interval with sufficient accuracy. To overcome this difficulty is the point of the linearized augmented plane wave (LAPW) method [40]. One can expand the solution of the radial Schrödinger equation $u_l(r,E)$ in a Taylor series around the solution with energy E_l:

$$u_l(r,E) = u_l(r,E_l) + (E-E_l)\frac{\partial}{\partial E}u_l(r,E)\Big|_{E=E_l} + O((E-E_l)^2). \tag{3.8}$$

The error in the wave functions scales quadratically with the variation $(E - E_l)$ and thus the error in energy is of order 4. Therefore, it becomes possible to describe the

---

[1] In principle one has to deal with the Dirac equation at this point what is actually done in the FLAPW code used in the present work. Since it is not of fundamental importance for the idea of the LAPW method we neglect this further complication here.

Kohn-Sham solutions of the valence bands by a single linearization energy for each orbital character l, e.g. the s-, p-, and d-bands if we include also the energy derivative of u_l into the basis set. The band energy $\epsilon_{\mathbf{k}\nu}$ and expansion coefficients $c_{\mathbf{k}\nu}^{\mathbf{G}}$ of each state are then determined by a single diagonalization of the Hamiltonian matrix. The energy parameters E_l are optimized in each iteration of the self-consistency cycle by setting it to the center of mass of the occupied bands with l-orbital character. The basis functions in the muffin-tin spheres are modified accordingly in the LAPW method:

$$\phi_{\mathbf{G}}(\mathbf{k},\mathbf{r}) = \sum_{lm} \left[A_{lm}^{\alpha\mathbf{G}}(\mathbf{k}) u_l(r,E_l) + B_{lm}^{\alpha\mathbf{G}}(\mathbf{k}) \dot{u}_l(r,E_l) \right] Y_{lm}(\hat{\mathbf{r}}), \tag{3.9}$$

where $\dot{u}_l(r,E_l)$ denotes the partial derivative of $u_l(r,E_l)$ with respect to the energy, and it can be calculated by differentiating Eq. (3.7). The freedom of choosing the coefficients $A_{lm}^{\alpha\mathbf{G}}(\mathbf{k})$ and $B_{lm}^{\alpha\mathbf{G}}(\mathbf{k})$ is exploited to make the basis functions and their derivatives continuous at the sphere boundaries.

By construction the basis functions and thus also the calculated valence states are orthogonal to any function with vanishing amplitude outside the muffin-tin spheres. This makes it possible to treat the core states separately and still calculate the true valence wave functions. As we include all electrons the LAPW method is called an all-electron method. Because spin-orbit effects are of strong influence for the low lying core states the relativistic Dirac equation is applied[2]. From the crystal potential only its spherical symmetric part is used for the core states which presents a minor approximation. Special programs are applied to find the core states but the self-consistency cycle includes core and valence states equally.

In the APW-method we used a spherical potential inside the muffin-tin spheres and a constant potential in the interstitial region. This is certainly a good approximation for metals in close packed structures. However, for materials in open structures such as oxide or nitride materials, the treatment of vacancies, and surfaces or for materials with crystal structures of low symmetry, this approximation can lead to incorrect results. An extension of the LAPW-method capable to deal with these problems is the full-potential LAPW (FLAPW) method, in which no shape approximation is made for the charge density nor the potential. The exact form of the charge density or the potential is described in section 3.4. Being able to include also non-spherical potentials in the spheres is an additional advantage of extending the basis functions by the derivative of the radial solution.

3.3 Describing Surfaces

The approach developed up to this point is sufficient if we limit ourselves to the treatment of bulk crystals. But currently there is a large interest in surfaces and their properties and obviously this is what scanning tunneling microscopy is all about. In

---

[2] The scalar-relativistic approximation to the Dirac equation is used for the valence electrons. Spin-orbit interaction effects like the magnetic anisotropy can still be included in a perturbation treatment.

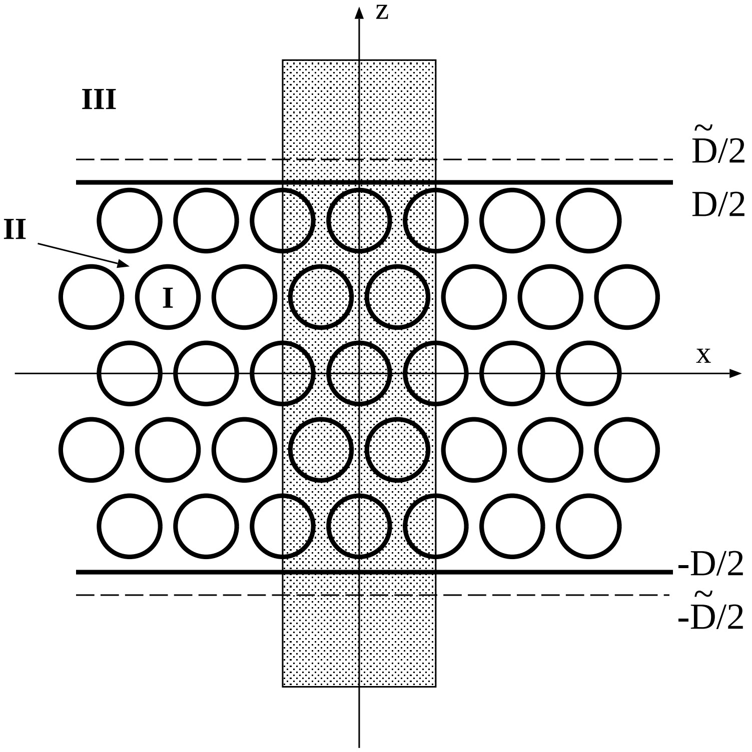

Figure 3.1: Film geometry used in the FLAPW code. The unit cell is sketched. It contains a number of lattice planes with the desired surface orientation and is terminated to both sides by a semi-infinite vacuum region. Space is divided into the three regions: (I) Muffin-Tin Spheres at the atom sites, (II) Interstitial in between, and (III) the semi-infinite Vacuum. At the boundary of two regions the basis functions and their derivatives are fitted continuously.

principle it is still possible to hold onto the previously sketched scheme by simply expanding the unit cell in one direction (commonly the z-direction) without defining any atom positions there. Thereby we create a (perfect) vacuum in between repeated slabs of the crystal. This is called the supercell geometry. The wave functions in the vacuum (which is part of the interstitial region) are expanded in plane waves according to the previous section. At this point we leave the track of Slater who proposed to describe the wave functions by the most appropriate type of basis functions in every region. It is well known from elementary quantum mechanics that wave functions decay exponentially inside a potential barrier given by the vacuum region in our case. Thus a large number of plane waves will be necessary to give an accurate expansion of the wave functions and the charge density in the vacuum region necessary for STM calculations. For practical purposes codes using a plane wave expansion in the vacuum are restricted to distances of about 3 Å from the surface since numerical noise is present at larger distances. An extension of the approach closer to Slater's original motivation of the APW method is realized with the concept of the film geometry [41, 42]. Instead of repeating slabs which are separated by interstitial space[3], a single

---

[3] If the separation between these slabs is too small they can even interact.

film is created by approximating the semi-infinite substrate by a finite number of lattice planes of the desired surface orientation and thickness. The film is terminated on both sides by a semi-infinite region, the vacuum region (see Fig. 3.1). The film thickness are chosen such that the surface properties are converged. In film geometry the FLAPW-method is truly two-dimensional, and we work with two-dimensional Bloch vectors $\mathbf{k}_{\|}$. Further, due to the boundary condition of the potential at infinity ($V(z \to \infty) = 0$), an absolute energy scale is introduced.

The vacuum region present additionally to the muffin-tin spheres and the interstitial is provided with its own basis functions adjusted to the properties of the vacuum:

$$\begin{aligned}\phi_{\mathbf{G}_{\|}\mathbf{G}_{\perp}}(\mathbf{k}_{\|},\mathbf{r}) &= \Big[A_{\mathbf{G}_{\|}\mathbf{G}_{\perp}}(\mathbf{k}_{\|})u_{\mathbf{G}_{\|}}(\mathbf{k}_{\|},z,E_v) + \\ &\quad B_{\mathbf{G}_{\|}\mathbf{G}_{\perp}}(\mathbf{k}_{\|})\dot{u}_{\mathbf{G}_{\|}}(\mathbf{k}_{\|},z,E_v)\Big] \exp\left[i(\mathbf{k}_{\|}+\mathbf{G}_{\|})\mathbf{r}_{\|}\right], \qquad (3.10)\end{aligned}$$

where the reciprocal lattice vector $\mathbf{G} = \mathbf{G}_{\|} + \mathbf{G}_{\perp}$ has been split into its part parallel and perpendicular to the surface. While $\mathbf{G}_{\|}$ is simply an element of the two-dimensional reciprocal lattice the perpendicular contribution is given by:

$$\mathbf{G}_{\perp} = \frac{2\pi q}{\tilde{D}}\hat{\mathbf{n}}, \qquad (3.11)$$

where q is an integer number, $\hat{\mathbf{n}}$ is the unit vector normal to the surface, and $\tilde{D}$ is chosen to be larger than the film thickness D by about twice the muffin-tin radius of the surface layer. The z-dependent part of the basis functions u is a solution of the one-dimensional Schrödinger equation with the laterally averaged part of the vacuum potential $V_{\text{eff}}(z)$:

$$\left(-\frac{\hbar^2}{2m}\frac{d^2}{dz^2} + V_{\text{eff}}(z) + \frac{\hbar^2}{2m}(\mathbf{k}_{\|}+\mathbf{G}_{\|})^2 - E_v\right)u_{\mathbf{G}_{\|}}(\mathbf{k}_{\|},z,E_v) = 0, \qquad (3.12)$$

where E_v is the energy parameter for the linearization of the vacuum basis functions analogous to the E_l's used for the basis in the muffin-tin spheres. As in Eq. (3.9) $\dot{u}$ denotes the energy derivative of u. The basis functions and their derivatives are again matched continuously at the separation surface of the two regions, i.e. to the plane waves of the adjacent interstitial region (see also Fig. 3.1), by the coefficients $A_{\mathbf{G}_{\|}\mathbf{G}_{\perp}}(\mathbf{k}_{\|})$ and $B_{\mathbf{G}_{\|}\mathbf{G}_{\perp}}(\mathbf{k}_{\|})$.

In summary, the basis functions in the vacuum region are composed of two-dimensional plane waves parallel to the surface, which exploits the remaining two-dimensional translational symmetry and of exponentially decaying functions u and $\dot{u}$ in the z-direction. This choice results in a flexible and numerically accurate description of the vacuum wave functions and finally in the possibility to simulate STM measurements performed at distances of 4 to 13 Å from the surface. The accuracy of the film geometry to describe a semi-infinite crystal depends on the extent to which neglecting the interaction between the two surfaces of the film is justified. Further, it has to be checked that the inner film layers possess the electronic structure of the bulk. In order to satisfy these requirements a sufficient number of film layers is needed. In the case of metals 10 to 15 layers have proven to yield good results. This is certainly due to the effective electron screening in metals with screening length of the order of one to two atom layers.

The number of basis functions needed to accurately describe the electronic structure of a surface depends on its constituents as well as the properties to be calculated. A normal starting point is 80 to 100 basis functions per atom in the unit cell. The number is fixed by restricting the reciprocal lattice vectors by:

$$|\mathbf{k}_{\|} + \mathbf{G}| < k_{\text{max}}. \tag{3.13}$$

The accuracy of any calculation is improved by taking more functions into account and it must be checked whether the quantities in question vary on the level of accuracy desired. Thus the number of basis functions is not a parameter in a sense that it imposes a fundamental limit upon the method.

3.4 Representation of Density and Potential

Before we can discuss how the effective potential contained in the Hamiltonian matrix is calculated, a representation of the potential and of the charge density needs to be chosen. In terms of storing both quantities efficiently and treating their strongly varying parts inside the muffin-tin spheres adequately it is natural to apply the threefold representation of the wave functions once more to the potential and the charge density. Thus we use plane waves in the interstitial and vacuum regions[4] and spherical harmonics in the muffin-tin spheres. As the charge density is given by the square of the wave function, the cut-off parameters in the wave function induce natural cut-off parameters for the charge density and potential. These are $G_{\text{max}} = 2k_{\text{max}}$ for the plane wave cut-off and $L_{\text{max}} = 2l_{\text{max}}$ for the cut-off in the angular momentum representation in the atomic spheres. Thus it is reasonable to reduce the number of stored coefficients. This can be done by exploiting the crystal symmetries which must be fulfilled for quantities like the potential and charge density. One can use (i) the operations of the space group for the plane waves of the interstitial and vacuum as well as to reduce the summation over the full Brillouin zone to the irreducible wedge, (ii) the point group operations of atom sites for the spherical harmonics in the muffin-tins, and (iii) restrict the calculation to the non-equivalent atom sites and compute the others by the relating symmetry operations.

Applying the space-group operations $\{\mathbf{R}|\mathbf{t}\}$, each composed of a point operation $\mathbf{R}$ and a translation $\mathbf{t}$, to the plane waves, results in the generation of so-called star functions $\phi_s(\mathbf{r})$, i.e. symmetrized plane waves. They are defined by:

$$\phi_s(\mathbf{r}) = \frac{1}{N_{\text{op}}} \sum_{\mathbf{R}} \exp\left[i\mathbf{R}\mathbf{G}(\mathbf{r} + \mathbf{t})\right], \tag{3.14}$$

where N_{op} is the number of space group operations. By construction these functions are orthogonal and possess the space group symmetries of the crystal. They can be applied to expand any quantity invariant to the corresponding symmetry operations.

---

[4] In the vacuum the Fourier coefficients become z-dependent.

The name star function is due to the fact that each function ϕ_s contains all plane waves with reciprocal vectors which are related by point operations and thereby form a star of vectors. The reciprocal vectors summarized in such a star are all of the same length although not all vectors of the same length need to be contained in one particular star function. Each star function contains a large number of plane waves, while each plane wave is an element of a single star function only. Hence, the number of coefficients which have to be stored decreases tremendously. While the star functions depend on the three-dimensional space coordinate $\mathbf{r}$ in the interstitial they become two-dimensional in the vacuum.

In the muffin-tin spheres we can apply the point-group operations of the atom sites which can and in general are different from site to site. We summarize the spherical harmonics Y_{lm} at site α to so-called lattice harmonics K_ν^α in the form:

$$K_\nu^\alpha(\hat{\mathbf{r}}_\alpha) = \sum_m c_{\nu,m}^\alpha Y_{lm}(\hat{\mathbf{r}}_\alpha) \quad \text{with } \mathbf{r}_\alpha = \mathbf{r} - \mathbf{R}_{\mathrm{MT}}^\alpha, \tag{3.15}$$

where $\mathbf{R}_{\mathrm{MT}}^\alpha$ is the position of atom α and ν is used for numbering the lattice harmonics. Usually a limitation of the angular moment to $l = 8$ is sufficient for the expansion of density and potential in the muffin-tin spheres.

Finally, we can summarize the representation of charge density and potential by giving it explicitly for the density:

$$n(\mathbf{r}) = \begin{cases} \sum_s n_s \phi_s^{3D}(\mathbf{r}) & \mathbf{r} \in \text{Interstitial}, \\ \sum_\nu n_\nu^\alpha(r) K_\nu^\alpha(\hat{\mathbf{r}}_\alpha) & \mathbf{r} \in \text{Muffin-Tin Sphere } \alpha, \\ \sum_s n_s(z) \phi_s^{2D}(\mathbf{r}_\parallel) & \mathbf{r} \in \text{Vacuum}. \end{cases} \tag{3.16}$$

Note that the expansion coefficients $n_\nu^\alpha(r)$ in the muffin-tin spheres have to be calculated on a (exponential) radial mesh r_i and in the vacuum on a (linear) z-mesh, z_i, i.e. perpendicular to the film surface.

3.5 Generating the Potential and Matrices

In order to generate the Hamiltonian matrix entering the eigenvalue problem:

$$H_{\mathbf{G}'\mathbf{G}}(\mathbf{k}) = \int \phi_{\mathbf{G}'}^*(\mathbf{k},\mathbf{r}) \left[-\frac{\hbar^2}{2m}\nabla^2 + V_{\text{eff}}(\mathbf{r}) \right] \phi_{\mathbf{G}}(\mathbf{k},\mathbf{r})\, d^3r, \tag{3.17}$$

we need to calculate the effective potential $V_{\text{eff}}(\mathbf{r})$ consisting of the exchange-correlation potential and the Coulomb potential due to the nucleus and the electron charge. The exchange-correlation potential can be computed rather easily in real space, where it is diagonal. The charge density in the sphere is expressed in real space and the calculation of the exchange-correlation potential is straight forward. The charge density in the interstitial region is stored in reciprocal space and has to be transformed into real space by a discrete Fast-Fourier transform. Then the exchange-correlation potential is calculated and back-transformed into reciprocal space and stored in the representation described in the previous section.

To calculate the Coulomb potential of an arbitrary periodic charge distribution is a non-trivial problem though and for a long time it has simply been treated as in the APW-method discussed before: spherical charge density and potential in the spheres and constant charge density and potential in the interstitial region. As mentioned before this is a major deficiency if open structures like surfaces or molecules are considered where the bonding is highly non-spherical. Fortunately, a solution to the problem has been developed by Weinert [43] and it has been implemented successfully in the present code.

The idea of the method can be sketched as follows. The charge distribution inside the muffin-tin spheres leads to certain multipole moments outside of them, i.e. in the interstitial, which on the other hand do not uniquely define the charge distribution in the spheres. Thus one can construct a new pseudo-charge density distribution in the spheres reproducing the multipole moments of the true charge density in the interstitial region. Further, the freedom of choice can be used to represent this pseudo-charge density by a rapidly converging Fourier expansion. This makes it possible to solve the Poisson equation for this charge density in a trivial way in Fourier space:

$$V_C^{\mathrm{pseudo}}(\mathbf{G}) = \frac{4\pi\rho_{\mathrm{pseudo}}(\mathbf{G})}{G^2}. \tag{3.18}$$

This potential is the true Coulomb potential in the interstitial region including the muffin-tin sphere boundary. The potential inside the muffin-tin spheres can be easily computed by means of a standard Green's function technique (e.g. [44]):

$$V_C^{\mathrm{MT}}(\mathbf{r}) = \int\limits_{\mathrm{MT}} \rho(\mathbf{r}')G_D(\mathbf{r},\mathbf{r}')\,d^3r' - \frac{1}{4\pi}\int\limits_{\delta\mathrm{MT}} V_C^{\mathrm{pseudo}}(\mathbf{r}')\frac{\partial G_D(\mathbf{r},\mathbf{r}')}{\partial n'}da', \tag{3.19}$$

where $G_D(\mathbf{r},\mathbf{r}')$ is the Green's function for Dirichlet boundary conditions and $\frac{\partial G_D}{\partial n'}$ is its normal derivative on the sphere boundary. The first integral includes the true charge density and is over the volume while the second integral is over the surface of the muffin-tin sphere. In the case of the film geometry with a vacuum region the method is extended to take care of the additional vacuum charge.

The synthesis of the Hamiltonian matrix can further be split into three parts:

$$H = H_{\mathrm{FMT}} + \Delta V_{\mathrm{NS}} + \Delta V_{\mathrm{I,V}}, \tag{3.20}$$

where H_{FMT} contains the kinetic energy and the contributions to the potential used for the construction of the film-muffin-tin basis functions (making this part easy to calculate), ΔV_{NS} consists of the non-spherical corrections to the muffin-tin potential and $\Delta V_{\mathrm{I,V}}$ contains the $\mathbf{G} \neq 0$ contribution of the interstitial and vacuum potential, called the warping and corrugation contribution, respectively.

The calculation of the overlap matrix $\mathbf{S}(\mathbf{k})$ is decomposed into the three regions of space defined by the LAPW method:

$$\begin{aligned} S_{\mathbf{G}'\mathbf{G}}(\mathbf{k}) \;&=\; \sum_{\alpha} \int\limits_{\mathrm{MT}\alpha} \phi^*_{\mathbf{G}'}(\mathbf{k},\mathbf{r})\phi_{\mathbf{G}}(\mathbf{k},\mathbf{r})\,d^3r + \int\limits_{\mathrm{cell}} \frac{1}{\Omega}\exp\left[i(\mathbf{G}'-\mathbf{G})\mathbf{r}\right]\Theta(\mathbf{r})\,d^3r \\ & \int\limits_{\mathrm{Vac}} \phi^*_{\mathbf{G}'}(\mathbf{k},\mathbf{r})\phi_{\mathbf{G}}(\mathbf{k},\mathbf{r})\,d^3r, \end{aligned} \tag{3.21}$$

where we have inserted the plane waves in the interstitial explicitly and the step function $\Theta(\mathbf{r})$ cuts out the interstitial region by being zero at positions in the vacuum and inside the muffin-tin spheres and one everywhere else. While the two integrals one and three of Eq. (3.21) can be expressed after some algebra by the matching coefficients and specific values of the basis functions, the second part is equivalent to finding the Fourier expansion of $\Theta(\mathbf{r})$, which is slowly convergent. Since we are using a cut-off for the basis functions the problem is fortunately simplified to finding the appropriate representation of $\Theta(\mathbf{r})$ to integrate functions with a finite Fourier series. It can be shown that for this purpose it is sufficient to truncate the Fourier expansion at the maximum $\mathbf{G}$ of the function to be integrated:

$$\tilde{\Theta}(\mathbf{G}) = \begin{cases} \delta_{\mathbf{G},0} - \sum\limits_{\alpha} \frac{4\pi R_\alpha^3}{\Omega} \frac{j_1(GR_\alpha)}{GR_\alpha} \exp\left(-i\mathbf{G}\mathbf{R}_\alpha\right) & \text{if } G \leq G_{\mathbf{max}}, \\ 0 & \text{if } G > G_{\mathbf{max}}. \end{cases} \tag{3.22}$$

$G_{\mathbf{max}}$ must be twice the number of the cut-off $k_{\mathbf{max}}$ for the basis functions since these enter twice in the calculation of matrix elements. A further simplification for both matrices can be achieved by making use of an inversion symmetry center if present. By placing the origin of the coordinate system at the inversion center the matrices become real and symmetric.

3.6 Brillouin Zone Integrations

In the previous section the generation of the matrices has been discussed. Both, the Hamiltonian and the overlap matrix, depend on the Bloch vector $\mathbf{k}$, and the eigenvalue problem is solved for a chosen set of $\mathbf{k}$ vectors. The electron density n and any other quantity of the crystal are calculated by summing over all occupied states. For a crystal these summations become integrals over the Brillouin zone (BZ):

$$n(\mathbf{r}) = \sum_{\mathbf{k}\nu}^{\text{occ}} |\psi_{\mathbf{k}\nu}(\mathbf{r})|^2 = \sum_{\nu}^{\text{occ}} \int_{\text{BZ}} |\psi_{\mathbf{k}\nu}(\mathbf{r})|^2 \frac{d^3k}{(2\pi)^3}. \tag{3.23}$$

The most common techniques to perform these integrals efficiently are the tetrahedron method [45,46] and the special $\mathbf{k}$-point method [47]. Obviously, it is quite important to restrict the calculations to few $\mathbf{k}$-points since each corresponds to the set-up and the diagonalization of the eigenvalue problem.

The special $\mathbf{k}$-point method applied in the code used in this work, i.e. the `FLEUR` code, is based on the idea that smoothly varying functions can be integrated by the knowledge of their values at specific points chosen to integrate plane waves up to a certain cut-off without error. The integration is then replaced by a weighted summation over these values. The weights do not account for the occupation and problems occur when dealing with metals which possess intersecting bands at the Fermi energy. The problem is solved by smearing out the occupation of the states at the Fermi energy E_F which is done by weighting each state with the Fermi distribution function:

$$\int\limits_{\mathrm{BZ}} |\psi_{\mathbf{k}\nu}(\mathbf{r})|^2 \frac{d^3k}{(2\pi)^3} = \sum_{\mathbf{k}} w(\mathbf{k})|\psi_{\mathbf{k}\nu}(\mathbf{r})|^2 \left[\exp\left(\frac{\epsilon_{\mathbf{k}\nu} - E_F}{k_B T}\right) + 1\right]^{-1}, \tag{3.24}$$

where k_B is the Boltzmann constant, T is the temperature, and $w(\mathbf{k})$ denotes the weight of the special point $\mathbf{k}$. The temperature is chosen according to the density of the mesh of special points and depends also on the energy difference between bands. The Fermi energy is computed iteratively by the requirement that the number of occupied states must be equal to the number of electrons in the crystal.

3.7 Calculating the Total Energy

The total energy is the most important of all ground-state properties since its variation leads to the correct ground-state density. Further, it is an important quantity in terms of the equilibrium configuration of a crystal. For example, it depends on the geometric arrangement of the atoms in the unit cell, the crystal lattice, the lattice constant, the magnetic order, and other constraints externally exposed on the system. By comparing the ground-state energy of different configurations we can find the energetically most favorable one which the system will reach if the thermal energies allow to overcome possible formation barriers. It is thus desirable to find an accurate way of calculating this quantity.

As discussed in Eq. (2.7) we express the total energy of the electrons as a sum of the kinetic energy of non-interacting electrons, the Hartree energy, the energy due to the external potential caused by the nuclei, and the exchange-correlation energy of the interacting electrons. In addition to these terms the Coulomb energy resulting from the mutual interaction of the nuclei E_{ii} enters in the total energy:

$$E[n] = T_s[n] + U_H[n] + E_{\mathrm{ext}}[n] + E_{\mathrm{ii}} + E_{\mathrm{xc}}[n]. \tag{3.25}$$

The large kinetic energy term can be calculated reliably by making explicit use of the Kohn-Sham equations which leads to:

$$T_s[n] = \sum_{\gamma}^{\text{core}} \epsilon_\gamma + \sum_{\mathbf{k}\nu}^{\text{valence}} w(\mathbf{k})\epsilon_{\mathbf{k}\nu} - \int n(\mathbf{r})\left[V_C(\mathbf{r}) + V_{\mathrm{xc}}(\mathbf{r})\right] d^3r, \tag{3.26}$$

where ϵ_γ are the eigenvalues of the core states and n denotes the total electron charge density, i.e. core and valence electron charge. The three next terms of Eq. (3.25) are summarized as the potential energy $U[n]$ and one can rewrite this term in the following way:

$$\begin{aligned} U[n] \;=\; & \frac{e^2}{2}\int\limits_{\text{crystal}} d^3r\, n(\mathbf{r})\left[\int\limits_{\text{crystal}} d^3r' \frac{n(\mathbf{r}')}{|\mathbf{r}-\mathbf{r}'|} - \sum_{\alpha\beta}\frac{Z_\beta^\alpha}{|\mathbf{r}-\mathbf{R}_\beta^\alpha|}\right] - \\ & \frac{e^2}{2}\sum_{\alpha\beta} Z_\beta^\alpha \left[\int\limits_{\text{crystal}} d^3r \frac{n(\mathbf{r})}{|\mathbf{r}-\mathbf{R}_\beta^\alpha|} - \sum_{\alpha'\beta'}^{(\alpha,\beta)\neq(\alpha',\beta')} \frac{Z_\beta^\alpha}{|\mathbf{R}_\beta^\alpha - \mathbf{R}_{\beta'}^{\alpha'}|}\right], \end{aligned} \tag{3.27}$$

where the atom core number α of the basis in unit cell β is located at $\mathbf{R}_\beta^\alpha$ and possesses a nuclear charge of Z_β^α. The term in brackets of the first line of Eq. (3.27) is just the Coulomb potential of the total charge distribution which we have calculated already (see section 3.5). The term in brackets in the bottom line on the other hand is a Madelung term without any divergence and denoted by $V_M(\mathbf{R}_\beta^\alpha)$.

The exchange-correlation energy is given directly by its definition in the local density approximation (Eq. (2.21)) and collecting all terms we receive for the total energy per unit cell of the crystal:

$$\begin{aligned} E[n] &= \sum_{\gamma}^{\text{core}} \epsilon_\gamma + \sum_{\mathbf{k}\nu}^{\text{valence}} w(\mathbf{k})\epsilon_{\mathbf{k}\nu} - \frac{e^2}{2}\sum_\alpha Z^\alpha V_M(\mathbf{R}^\alpha) \\ &\quad - \int n(\mathbf{r})\left[V_{\text{xc}}(\mathbf{r}) - \epsilon_{\text{xc}}^{\text{homog}}(\mathbf{r}) + \frac{1}{2}V_C(\mathbf{r})\right] d^3r. \end{aligned} \tag{3.28}$$

The above equation applies to the non-spinpolarized case. If a spin-polarized calculation is performed the expression is still valid provided $\epsilon_{\text{xc}}^{\text{homog}}$ is the exchange-correlation energy per electron of a spin-polarized homogeneous electron gas and the exchange-correlation potential V_{xc} is replaced by the term $(n_\uparrow V_{\text{xc}}^\uparrow + n_\downarrow V_{\text{xc}}^\downarrow)/n$.

Chapter 4

Model of the STM

4.1 Basics of Scanning Tunneling Microscopy

While the technical realization of the scanning tunneling microscope (STM) is a scientific challenge, its principle, the *quantum mechanical tunnel effect*, is rather simple and discussed already in introductory courses to quantum mechanics [5]. Imagine an electron propagating in the direction of a barrier with a kinetic energy which is lower than the potential energy of the barrier. In classical physics the electron would be totally reflected by the barrier. Quantum mechanics, on the other hand, provides the possibility for the electron to penetrate into the barrier and to be located at the other side of the barrier with a non-vanishing probability, the electron can *tunnel* through the barrier. Therefore a current, a *tunneling current*, can flow even if two metal electrodes are separated by an insulating barrier (for example a vacuum gap). In an STM one exploits this effect by approaching a thin metal wire, the STM-tip, within a distance of 5 to 10 Å to a conducting sample, e.g. a metal surface, while a bias-voltage is applied between tip and sample. The tip is then scanned laterally, in (x, y), above the surface on a sub-Ångström scale with the aid of piezo-elements. At each lateral position, (x, y), the vertical tip position, z, is adjusted so that a predefined constant tunneling current flows. Thereby, a topographic image, $z(x, y)$, of the sample is measured. Since the current depends exponentially on the tip-sample distance as we will see below an enormous vertical resolution of below 1 pm is attainable with the most stable STMs[1].

We can get a more quantitative understanding of the way the tunnel effect is applied in an STM by discussing a one-dimensional model. It is capable of explaining the high sensitivity of STM which opens the fascinating possibility to study (conducting) materials down to the atomic scale. Imagine two metal electrodes, one representing the sample and the other the STM-tip, separated by a vacuum gap of approximately one nanometer. We assume for simplicity that the work functions, i.e. the energy necessary to extract an electron from the surface, of both metals are equal and their electronic states are described in terms of the free-electron-gas model. For the sake of simplicity we choose the temperature T= 0 K leading to a sharp Fermi

---

[1] In order to reach this limit low temperatures and an extremely efficient vibration isolation are required.

edge separating occupied and unoccupied states. The potential scheme is displayed in Fig. 4.1. In equilibrium the two Fermi energies are equal and occupied energy levels of the sample do not match with unoccupied energy levels of the tip and therefore elastic tunneling, i.e. tunneling without change in energy, is impossible. Thus there is no flow of a tunneling current. If we raise the Fermi energy of the sample by applying a small negative bias-voltage with respect to the tip, electrons from occupied levels of the sample can tunnel elastically into unoccupied levels of the tip. A net tunneling current flows. The value of the current can be estimated in the following way. In the vacuum the wave functions of the sample and the tip are solutions of the one-dimensional Schrödinger equation with a constant (vacuum) potential. Since the energy of the electrons is lower than the vacuum potential the wave functions decay exponentially with distance z measured from the surface:

$$\psi(z) = \psi(0)\exp(-\kappa z) \quad , \kappa = \sqrt{2m\phi/\hbar^2}. \tag{4.1}$$

ϕ is the work function, m the electron mass and κ is called the decay constant. The latter depends on the height of the energy barrier faced by the electrons. In the limit of small bias-voltages, i.e. $eV \ll \phi$, all electrons contributing to the tunneling current possess an energy approximately equal to the Fermi energy. Thus they have the same decay constant. The probability density of an electron of the sample to be located at the position of the tip, i.e. at $z = s$ with s being the barrier width, is given by the

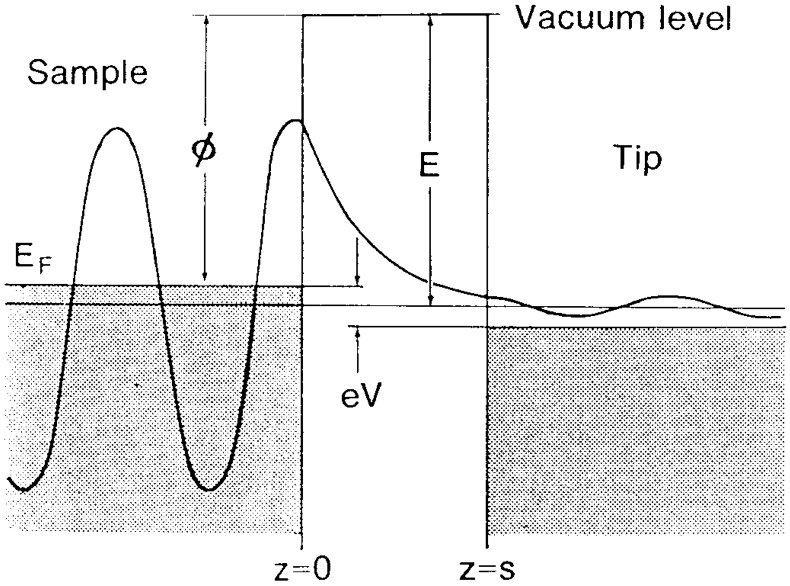

Figure 4.1: Scheme of the potential in a one-dimensional model of STM. Sample and tip are assumed to be simple metals of equal work function ϕ and the temperature is assumed to be 0 K leading to a sharp Fermi edge. The decay of a sample wave function in the vacuum barrier is sketched. Figure is taken from Ref. [11].

square of its wave function:

$$w = |\psi(s)|^2 = |\psi(0)|^2 \exp(-2\kappa s). \tag{4.2}$$

The total tunneling current is proportional to the sum of all electron states available within the energy interval relevant for tunneling. If we assume the same velocity for all states we find:

$$I(s,V) \propto \exp(-2\kappa s) \sum_{E_\mu = E_F - eV}^{E_F} |\psi_\mu(0)|^2. \tag{4.3}$$

The sum is taken over the different electronic states μ of the sample. Equation (4.3) expresses an exponential dependence of the tunneling current I with respect to the vertical separation s between tip and sample. It originates evidently from the decay of the (sample) wave functions. If we choose $\phi = 5$ eV an increase in distance of 1 Å lowers the tunneling current by a factor of 9.8, i.e. one order of magnitude. Thus even smallest changes in distance can be detected, and a vertical resolution on the order of 0.01 Å can be achieved. The *constant-current mode* of STM, mentioned already at the beginning of this section, makes explicit use of this fact. Using an electronic feed-back loop the vertical distance between tip and sample is adjusted to yield a constant tunneling current at each lateral position (x, y) of the sample. Scanning a surface in this mode and recording the changes in vertical distance Δz as a function of the lateral position (x, y) results therefore in a topographic image $\Delta z(x, y)$ of the sample surface. Caution has to be taken when reaching the atomic scale since the electronic structure, hidden in Eq. (4.3) in the sum over states, can then alter the image significantly and it becomes impossible to discuss the images in terms of sample topography. We will discuss this point in detail in chapters 5 to 9.

Another possibility to make use of the distance-dependence of the tunneling current given by Eq. (4.3) is to measure the first derivative of the current with respect to distance, i.e. dI/dz. Experimentally this is accomplished by varying the tip-sample distance with a small ac bias-voltage applied to the z-piezo element of the scanner. Divided by the tunneling current this quantity is a measure of the work function ϕ of the sample. Since its value depends on the material and the crystal orientation it can be used to characterize these properties of a sample surface on a nanometer scale. For example, surface alloying often changes the work function significantly and one can easily separate alloyed and clean parts of a sample.

If we rewrite Eq. (4.3) by replacing the summation over discrete states by an energy integration we arrive at another basic relation:

$$I(s,V) \propto \int_{E_F - eV}^{E_F} dE \sum_\mu \delta(E_\mu - E)|\psi_\mu(s)|^2 = \int_{E_F - eV}^{E_F} n(s,E)\, dE. \tag{4.4}$$

The quantity $n(s, E)$ is denoted as the local density of states (LDOS). Replacing the squares of the wave functions in the summation by *ones* leads to the commonly used density of states [38]. Thus in the LDOS each state receives an extra weight given by its probability density at the position of the tip. Although equation (4.4) has been derived in the limit of $eV \ll \phi$ we will see below that it is applicable also at larger bias-voltages. Therefore, we can mention another important mode of STM at this point, the *spectroscopic mode*. In a spectroscopy experiment the tip position is fixed at a constant height above the surface, and a small ac bias-voltage ΔV is superimposed to the constant bias-voltage V. In this manner the differential conductivity dI/dV can be measured directly. Differentiating the tunneling current in the formulation of Eq. (4.4) with respect to the bias-voltage leads to:

$$\frac{dI}{dV}(s,V) \propto n(s, E_F + eV). \tag{4.5}$$

Hence, the differential conductivity is related directly to the LDOS of the sample at an energy selected by the applied bias-voltage. This fact is exploited in scanning tunneling spectroscopy to correlate topographic features like islands, step edges, defects, adsorbates or surface alloys to their electronic structure contained in the LDOS. Questions addressed are the chemical identity of adsorbates or islands, the depth of defects or even the magnetic state of structures[2]. Note, that this simple result is quite problematic since the influence of the STM-tip has been totally neglected so far. While the three-dimensional extension of the result of equation (4.3) is successfully applied to discuss even subtle problems in the analysis of STM-images, it is often impossible to use equation (4.5) without modification for the interpretation of spectroscopic data. The influence of the STM-tip has been neglected intentionally in the one-dimensional model since basic ideas and results can be presented readily based on these simple assumptions. In the following a three-dimensional model will be derived which enables us to understand the limitations of such an ansatz and provides different levels of sophistication in the simulation of STM experiments.

4.2 The Transfer Hamiltonian Method

In this section we present the Transfer Hamiltonian Method to describe the STM current in three dimensions as it has been derived by Bardeen [16] in general and extended by Tersoff, Hamann and Chen to STM [6, 11]. The Tersoff-Hamann model will be used throughout the present work. A model is naturally limited by its assumptions and it is important to be fully aware of them. In the case of the Transfer Hamiltonian Method, based on time-dependent perturbation theory, the following assumptions enter:

First of all, the electron tunneling is treated as a one-particle process, i.e. it is neglected that electrons can interact while tunneling. In the limit of low tunneling current this is surely reasonable. However, there are cases which cannot be treated within the independent-particle picture, e.g. when tunneling into a superconducting system. Further, we assume elastic tunneling, i.e. no energy loss of the electrons by interaction with quasi-particles of the electrodes, e.g. plasmons or phonons, is considered. The inelastic part of the tunneling current contributes only about 1% of the

---

[2] To establish the latter is the ambitious goal of several groups today. We will return to this point in section 4.5 and in chapter 9.

tunneling current making this a reasonable assumption. Finally, a direct interaction of tip and sample resulting in the formation of coupled electronic states is not taken into account. The validity of the last assumption is directly related to the tip-sample distance. When the tip is brought very close to the surface the assumption will finally cease to be justified. However, a separation of ≥ 4 Å should exclude interaction between tip and sample states. With the above in mind we can start to derive the tunneling current.

Fig. 4.2 displays a schematic view of the system consisting of tip, sample and the vacuum barrier. A bias-voltage is applied shifting the Fermi energies with respect to each other. Since we want to apply perturbation theory a separation of the system into subsystems is convenient. Space is therefore divided into two parts by a fictious separation surface Σ. The potential U of the whole system can then be divided into two parts, one connected with the sample, U_S, and the other with the tip, U_T. Two requirements have to be met: Evidently, the sum of U_S and U_T needs to be the total potential U at every point in space. Second, the product of U_S and U_T should vanish at every point in space. This amounts to one of them being zero where the other is non-vanishing. The second requirement minimizes the second order term in the perturbation expansion [48]. If the separation of tip and sample is large these requirements are fulfilled already by the potentials of the two subsystems unperturbed by the existence of another system. Reducing the tip-sample distance leads to a difference between the free potentials and those constructed along the lines sketched above. This error can be corrected by applying time-independent perturbation theory to the states of the unperturbed subsystems [11] and then using the modified wave functions in the formalism presented below. Often the difference is neglected as in the original Bardeen approach [16]. It remains a good approximation in the limit of small bias-voltages compared to the work functions of tip and sample.

The potentials U_S and U_T are connected with Schrödinger equations of the unperturbed systems:

$$\begin{aligned}(-\frac{\hbar^2}{2m}\nabla^2 + U_S)\psi_\mu &= E^S_\mu \psi_\mu, && (4.6)\\ (-\frac{\hbar^2}{2m}\nabla^2 + U_T)\chi_\nu &= E^T_\nu \chi_\nu. && (4.7)\end{aligned}$$

ψ_μ and χ_ν denote the eigenfunctions of sample and tip and E^S_μ and E^T_ν their eigenvalues. The time-evolution of a state Ψ in the system of tip and sample is governed by a Schrödinger equation containing the full potential:

$$i\hbar\frac{\partial\Psi}{\partial t} = (-\frac{\hbar^2}{2m}\nabla^2 + U_T + U_S)\Psi. \tag{4.8}$$

The time-evolution of states can be treated in perturbation theory. We assume that the tip (potential) was not present at $t \to -\infty$ and an electron is stationary in a state $\Psi = \psi_\mu$ of the sample. Now the tip is approached slowly towards the sample and thereby the tip potential is turned on adiabatically, i.e. gradually. As the time-scale for electrons is femtoseconds this is a reasonable description. We are now interested in the probability of the electron to populate states of the tip per unit time which

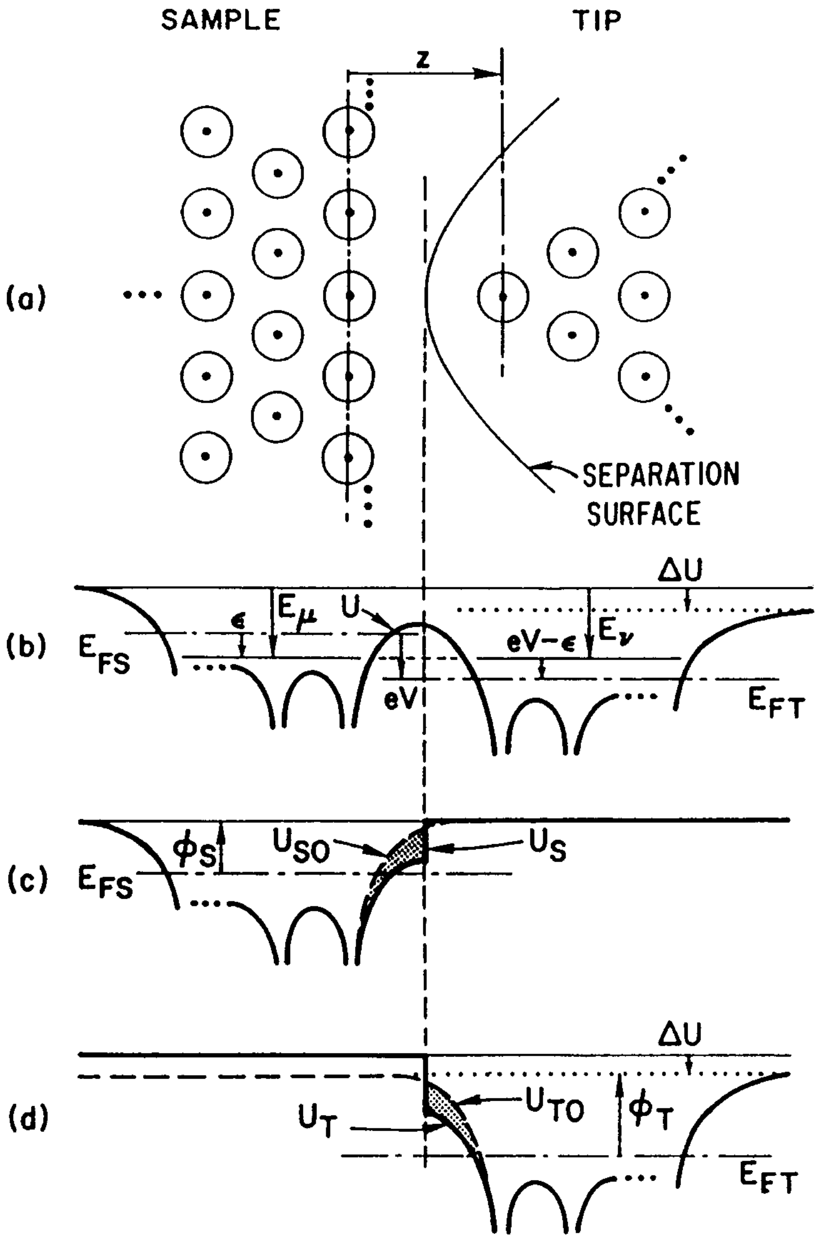

Figure 4.2: Scheme of the potential in a three-dimensional model of STM. (a) Geometry of the tip-sample problem including the separation surface. (b) Potential of the combined system with an applied bias-voltage eV. (c) and (d) Definition of the sample potential U_S and the tip potential U_T. U_{S0} and U_{T0} are the potentials of the free systems. Figure is taken from Ref. [11].

is directly related to the tunneling current. The state Ψ of the whole system can be expanded in a series of tip eigenfunctions, which form an orthogonal and complete basis set:

$$\Psi(t) = \psi_\mu \exp\left(-iE_\mu^S t/\hbar\right) + \sum_\nu c_\nu(t)\chi_\nu \exp\left(-iE_\nu^T t/\hbar\right). \tag{4.9}$$

The initial state is ψ_μ and therefore all coefficients c_ν vanish at $t = 0$. The probability of the electron to be in a state χ_ν of the tip is then given by $|c_\nu|^2$. Inserting the ansatz into equation (4.8) leads to a set of differential equations for the coefficients c_ν. These can be solved iteratively, and to the first order of time-dependent perturbation theory the tunneling probability per unit time $d|c_\nu(t)|^2/dt$ is given by (e.q. [49]):

$$\begin{aligned} \omega_{\mu\nu}^{(1)} &= \frac{2\pi}{\hbar}\delta\left(E_\nu^T - E_\mu^S\right)|M_{\mu\nu}|^2 && (4.10)\\ M_{\mu\nu} &= \langle\chi_\nu\,|U_T|\,\psi_\mu\rangle = \int_{\Omega_T} \chi_\nu^* U_T \psi_\mu \, dV. && (4.11) \end{aligned}$$

This equation is called Fermi's Golden Rule; it is a general result of first-order time-dependent perturbation theory. Elastic tunneling is guaranteed herein by the delta function. $M_{\mu\nu}$ is the tunneling matrix element describing the projection of the initial state ψ_μ per-tubed by the potential U_T onto the final state χ_ν. The integration is limited to the volume of the tip Ω_T since U_T vanishes in the outside by definition. The tunneling matrix element is the central quantity of the Transfer Hamiltonian Method, and in the following sections different approaches to compute it are discussed.

The total tunneling current can be calculated by taking all possible initial and final states of tip and sample into account. Tunneling from a state ψ_μ into a state χ_ν can only occur if the former is occupied and the latter is empty. At zero temperature there is a sharp Fermi edge separating occupied and unoccupied states. At elevated temperatures the Fermi edge is smeared out which is described by the Fermi-Dirac distribution $f(E - E_F) = \{1 + \exp\left[(E - E_F)/k_B T\right]\}^{-1}$. Accounting for the occupation in this manner and assuming an applied bias-voltage V, which shifts the Fermi energies of the tip, E_F^T, and the sample, E_F^S, with respect to each other, we can write the tunneling current from sample to tip, $I_{S\to T}$, and tip to sample, $I_{T\to S}$:

$$\begin{aligned} I_{S\to T} &= \frac{4\pi e}{\hbar}\sum_{\nu\mu} f(E_\mu^S - E_F^S)\left[1 - f(E_\nu^T - E_F^T)\right] \times \\ &\qquad |M_{\mu\nu}|^2\,\delta(E_\nu^T - E_\mu^S - eV) && (4.12)\\ I_{T\to S} &= \frac{4\pi e}{\hbar}\sum_{\nu\mu} f(E_\mu^T - E_F^T)\left[1 - f(E_\nu^S - E_F^S)\right] \times \\ &\qquad |M_{\mu\nu}|^2\,\delta(E_\nu^T - E_\mu^S - eV). && (4.13) \end{aligned}$$

A factor 2 has been introduced accounting for the two possible spin states of each electron. The difference between the current flowing from tip to sample and sample to tip yields the net tunneling current:

$$I = \frac{4\pi e}{\hbar} \sum_{\nu\mu} \left[f(E^S_\mu - E^S_F) - f(E^T_\nu - E^T_F) \right] |M_{\mu\nu}|^2 \, \delta(E^T_\nu - E^S_\mu - eV). \qquad (4.14)$$

The problem left at this stage is to calculate the tunneling matrix element. This problem is discussed in the following sections. One can already guess that only a description of tip and sample in terms of electronic states leads to a satisfactory solution for the tunneling current.

4.3 The Tunneling Matrix Element

In order to compute the tunneling matrix element it is convenient to convert the volume integral into a surface integral. The matrix element from Eq. (4.11) can be transformed by applying the Schrödinger equation for the tip:

$$\begin{aligned} M_{\mu\nu} &= \int_{\Omega_T} \psi_\mu U_T \chi^*_\nu \, dV \\ &= \int_{\Omega_T} \psi_\mu (E^T_\nu - T) \chi^*_\nu \, dV \\ &= \int_{\Omega_T} \psi_\mu (E^S_\mu - T) \chi^*_\nu \, dV. \end{aligned} \qquad (4.15)$$

T is the operator of kinetic energy, i.e. $T = -\hbar^2/2m\nabla^2$. In the last line we made use of energy conservation in the tunneling process, i.e. $E^T_\nu = E^S_\mu$, contained in the delta function of Eq. (4.11). Since the sample potential is zero in the volume of the tip Ω_T we can use the vacuum Schrödinger equation for the sample wave function which results in a form of the integral that can be transformed by Green's theorem into a surface integral:

$$\begin{aligned} M_{\mu\nu} &= \int_{\Omega_T} (\chi^*_\nu T \psi_\mu - \psi_\mu T \chi^*_\nu) \, dV \\ &= -\frac{\hbar^2}{2m} \int_{\Sigma} (\chi^*_\nu \nabla \psi_\mu - \psi_\mu \nabla \chi^*_\nu) \, d\mathbf{S}. \end{aligned} \qquad (4.16)$$

The surface Σ separates the two subsystems tip and sample. Its exact position is arbitrary if the full potential is considered, that is if the wave functions of free tip and sample are modified according to the correction due to interaction [11]. In the original Bardeen approach the error by neglecting the modification of wave functions is minimized if the separation plane is located midway between the two subsystems [12,50].

To use the Transfer Hamiltonian Method in the formulation derived up to this point requires knowledge about the exact electronic structure of tip and sample, i.e. the energy levels and one-particle wave functions. In principle, it is possible to calculate them for both systems within the FLAPW method described in chapter 3, and to compute all tunneling matrix elements to gain the tunneling current. Although this approach is quite elaborate and demanding, it is practicable. However, we face one severe problem: While the atomic structure of the sample surface is usually well-characterized and thus well-known it is mostly unknown for the tip. Consequently, this amounts to a serious limitation of the approach. Therefore it is useful to take a look at model assumptions for the tip. We will see that a large part of STM interpretation can be made successfully on this basis with reasonable effort.

4.4 Approximations for the STM-Tip

The geometric structure and electronic properties of the tip, consisting of tungsten or a platinum-iridium alloy and prepared by electrochemical etching or mechanical ripping from a wire, is albeit its fundamental importance to gain atomic-resolution images or reproducible spectroscopic data commonly unknown. Experimentally, a number of recipes have been reported leading to tips with the desired tunneling properties, and at this point the experimentalist can be (and usually is) quite content. There are still a number of essential questions concerning tip properties. For example, the contribution of electrons with different orbital character, i.e. s, p or d electrons, to the tunneling current is heavily discussed. The answer is important for the possibility of spin-polarized tunneling with ferromagnetic tips. If only s-electrons contribute significantly it may be doubted whether their negligible spin-polarization is sufficient to resolve magnetic structures.

From the viewpoint of theory there have been efforts to include the electronic structure of realistic tips in the simulation of STM experiments to explain unexpected results (e.g. [7, 9, 13, 51]). However, even if the exact geometric structure was known the complicated non-periodic arrangement of atoms at the top of the tip would present a challenging problem to state-of-the-art *ab initio* calculation techniques. Cluster models for the tip have been proposed [52] but they lack the electronic structure of the underlying bulk. Including the electronic structure of the bulk by either a jellium [7] or a W(001) [53] surface has up to now limited the modelling of the tip to a single adsorbed atom on such a surface. Further, there have been no first-principles calculations of the electronic structure of supported magnetic transition-metal STM tips used in spin-polarized STM experiments. In other approaches [13], e.g. based on scattering theory, very simple descriptions of the tip are used. Therefore, it remains an open field, and further efforts have to be made in the future. On the other hand, the exponential distance dependence of the tunneling current as it has been derived in section 4.1 gives a clue that the tunneling current should be dominated by the outermost atom of the tip. Thus there is hope to model the electronic states of a tip successfully by the orbitals of a single atom. This approach is presented below.

At the separation surface Σ the potential of both, tip and sample, have approximately reached the value of the vacuum potential. To compute the matrix element from Eq. (4.16) the wave functions are only needed at the separation surface Σ where they obey the Schrödinger equation for zero potential:

$$(\nabla^2 - \kappa^2)\chi(\mathbf{r}) = 0 \ , \ \kappa^2 = \frac{2m}{\hbar^2}|E|. \tag{4.17}$$

κ is the decay constant which has already been introduced in section 4.1. Keeping in mind the idea of electronic states of a single apex atom we expand the tip wave functions into a series of spherical-harmonic functions $Y_{lm}(\theta, \phi)$ and a radial part $f_{lm}(\kappa\rho)$:

$$\chi(\mathbf{r}) = \sum_{l,m} c_{lm} f_{lm}(\kappa\rho) Y_{lm}(\theta, \phi). \tag{4.18}$$

$\rho = |\mathbf{r} - \mathbf{R}_T|$ is the radial distance from the center $\mathbf{R}_T$ of the outermost tip atom, the apex atom, and (θ, ϕ) defines the direction of $\mathbf{r} - \mathbf{R}_T$. The coefficients c_{lm} contain the information on the electronic structure of the specific tip under consideration. They can be computed by fitting this solution for the vacuum continuously to the wave functions near the apex atom known for example from *ab initio* calculations. Inserting this ansatz into Eq. (4.17) shows that the radial part is independent of m. The differential equation for f_l is of second order and the solutions are known as modified spherical Besselfunctions. Since Eq. (4.17) is of second order there is a regular as well as an irregular solution. Since the irregular solution diverges for large arguments, that is in our context for large distances from the outermost tip atom, it is not a physically relevant solution in the sense of quantum mechanics and is discarded. The regular Besselfunctions are given by:

$$k_l(u) = (-1)^l u^l \, (\frac{1}{u}\frac{d}{du})^l \, \frac{\exp(-u)}{u}. \tag{4.19}$$

On this basis we can discuss two approximations for the electronic states of the tip.

4.4.1 Tersoff-Hamann Model

Tersoff and Hamann proposed the following assumptions for the electronic structure of the tip [6] in order to calculate the tunneling matrix element and thus also the tunneling current. (i) The tip wave function is a spherically symmetric wave function, i.e. an s-wave. (ii) The limit of small bias-voltage and temperature is considered. The second approximation has been dropped in the extension of the Tersoff-Hamann model by Lang [8] to which we are refering here. In order to discuss the tunneling current only in terms of the properties of the sample one further assumes the density of states of the tip to be rather structureless as compared to that of the sample. The resulting model has been successfully applied to a large variety of problems and is still the most commonly used approach to interpret STM data.

The assumptions (i) and (ii) are easily expressed in Eq. (4.18) by replacing the summation by a single term, the spherical symmetric part $l = 0$, with $Y_{00}(\theta, \phi) = 1$:

$$\chi_s(\mathbf{r}) = C\, k_0(\kappa\rho) = C\, \frac{\exp(-\kappa\rho)}{\kappa\rho}. \tag{4.20}$$

Inserting this ansatz for the tip wave function into the expression for the matrix element before transforming it by Green's theorem into a surface integral (upper line of Eq. (4.16)) yields:

$$M_{\mu,s}(\mathbf{R}_T) = -\frac{C\hbar^2}{2m} \int_{\Omega_T} [k_0(\kappa|\mathbf{r}-\mathbf{R}_T|)\,\Delta\,\psi_\mu(\mathbf{r}) - \psi_\mu(\mathbf{r})\,\Delta\,k_0(\kappa|\mathbf{r}-\mathbf{R}_T|)]\,dV. \quad (4.21)$$

Since the sample potential vanishes in the body of the tip we can apply the vacuum Schrödinger equation (Eq. (4.17)) to the first term of the integrand. The second term has a singularity at $\mathbf{r} = \mathbf{R}_T$ similar to $\Delta(\frac{1}{|\mathbf{r}-\mathbf{r}'|})$ and can be simplified by recalling that the 0th Besselfunction k_0 is related to the Green's function of the vacuum Schrödinger equation, i.e. it solves:

$$[\Delta - \kappa^2]G(\mathbf{r}-\mathbf{r}') = -4\pi\delta(\mathbf{r}-\mathbf{r}'). \quad (4.22)$$

Inserting this into Eq. (4.21) gives the final result for the matrix element in the Tersoff-Hamann model:

$$M_{\mu,s}(\mathbf{R}_T) = -\frac{C\hbar^2}{2m} \int_{\Omega_T} 4\pi\delta(\mathbf{r}-\mathbf{R}_T)\psi_\mu(\mathbf{r})\,dV = -\frac{2\pi C\hbar^2}{\kappa m}\psi_\mu(\mathbf{R}_T). \quad (4.23)$$

Hence, the tunneling matrix element is directly proportional to the value of the sample wave function at the position of the apex atom $\mathbf{R}_T$. This result for the matrix element can be inserted into Eq. (4.14). We further replace the delta function by an energy integration over two delta functions:

$$\delta(E^T_\nu - E^S_\mu - eV) = \int \delta(E^T_\nu - eV - \epsilon)\delta(E^S_\mu - \epsilon)\,d\epsilon. \quad (4.24)$$

Note, that including the term eV in the second delta function leads to an equivalent formula for the tunneling current. The chosen form is more convenient in order to discuss the current in terms of sample properties. We arrive at the following expression for the tunneling current in the approximation of an s-wave tip orbital:

$$I(\mathbf{R}_T, V) = \frac{16\pi^3 C^2\hbar^3 e}{\kappa^2 m^2} \int n_T(\epsilon + eV) n_S(\mathbf{R}_T, \epsilon)[f(\epsilon - E^S_F) - f(\epsilon + eV - E^T_F)]\,d\epsilon. \quad (4.25)$$

The current is thus expressed as an energy integral containing the density of states (DOS) of the tip, n_T, and the local density of states (LDOS) of the sample, n_S, at the position of the tip apex atom $\mathbf{R}_T$:

$$n_T(\epsilon) = \sum_\nu \delta(E^T_\nu - \epsilon) \quad \text{and} \quad n_S(\mathbf{R}_T, \epsilon) = \sum_\mu \delta(E^S_\mu - \epsilon)|\psi_\mu(\mathbf{R}_T)|^2. \quad (4.26)$$

At this point our last assumption enters, i.e. the density of states of the tip is chosen to be constant. This reduces the tunneling current to its final result:

$$\begin{aligned} I(\mathbf{R}_T, V) &= \frac{16\pi^3 C^2 \hbar^3 e}{\kappa^2 m^2}\, n_T \int n_S(\mathbf{R}_T, \epsilon)[f(\epsilon - E_F^S) - f(\epsilon + eV - E_F^T)]\, d\epsilon \\ &= \frac{16\pi^3 C^2 \hbar^3 e}{\kappa^2 m^2}\, n_T \int n_S(\mathbf{R}_T, \epsilon) g_{V,T}(\epsilon)\, d\epsilon \qquad (4.27) \\ &\overset{T=0\,\mathrm{K}}{=} \frac{16\pi^3 C^2 \hbar^3 e}{\kappa^2 m^2}\, n_T \int_{E_F}^{E_F+eV} n_S(\mathbf{R}_T, \epsilon)\, d\epsilon. \qquad (4.28) \end{aligned}$$

Eq. (4.28) is the $T = 0$ K limit and expresses that the integral includes all states between the Fermi energy and the Fermi energy shifted by the applied bias voltage: the tunneling current is proportional to an integrated local density of states (ILDOS) of the sample. For elevated temperatures the integral limits are smeared out, and for convenience we have introduced the function $g_{V,T}(\epsilon)$:

$$g_{V,T}(\epsilon) = f(\epsilon - E_F^S) - f(\epsilon + eV - E_F^T), \qquad (4.29)$$

where f is the Fermi distribution function. Note, that Eq. (4.28) is a direct three-dimensional generalization of the result we derived in section 4.1 with rather hand-waving arguments. Since this formula of the tunneling current is widely used – also throughout this work – and led to a variety of successful explanations of STM experiments on the basis of the sample electronic structure we will discuss it in more detail. The first and most important aspect of Eq. (4.28) is the dependence of the tunneling current only on properties of the sample. All electronic effects of the tip have been eliminated. This is on the one hand highly desirable since it is the sample we wish to study, not the tip. At the same time it is a drawback because effects related to special tip states are excluded right from the start. A quantitative interpretation of STM images in terms of a measured tunneling current given in nano-Ampère as a function of the bias voltage, tip-sample distance, and further details of tip and sample is obviously impossible within this model. The great success of the Tersoff-Hamann model rests on the qualitative interpretation of STM images. This justifies the seemingly crude assumptions, and it is an excellent starting point for the interpretation of STM data.

In the low bias-voltage limit the tunneling current reduces to:

$$I(\mathbf{R}_T, V) \propto eV n_S(\mathbf{R}_T, E_F) \qquad (4.30)$$

and (topographic) STM images gained in the constant-current mode represent contours of constant sample LDOS at the Fermi energy. A direct consequence of this result is that there is no one-to-one correspondence between atomically resolved STM images and imaging the atoms as protrusion as would follow naturally for metals if the total charge density was probed. The LDOS at the Fermi energy can and quite often does differ from the charge density which in metals simply screens the positive charge of the nuclei. While the Tersoff-Hamann model agrees often quite well qualitatively with experimental results it cannot explain the values of measured corrugation amplitudes, i.e. the maximum vertical difference as the tip scans the sample surface, for closed-packed metal surfaces. We will see in the following section that an extension of the presented model provides an explanation. Nevertheless, with increasing length scale of the imaged structures the tunneling current becomes independent of the tip orbital considered, and the s-wave model of Tersoff and Hamann becomes a satisfactory description.

As it has been shown explicitly for the one-dimensional model in section 4.1 the exponential dependence of the tunneling current with respect to the tip-sample distance is a direct consequence of the exponential decay of sample wave functions into the vacuum. This result is not altered in the three-dimensional case. Further, the differential conductivity dI/dV measured by scanning tunneling spectroscopy is related to the LDOS of the sample at an energy given by the applied bias-voltage:

$$dI/dV(\mathbf{R}_T, V) \propto n_S(\mathbf{R}_T, E_F + eV). \tag{4.31}$$

By varying the applied bias-voltage, particular electronic states of the sample can thus be observed. Recording these spectra as a function of the lateral tip position (x, y) while simultaneously measuring the topography in the constant-current mode enables one to correlate structural and electronic properties of the sample. Chemical identification of adsorbates is only the simplest application of this technique and many others have been reported. A criticism concerning the validity of this simple expression is the neglect of tip features. They appear in experimental data and complicate matters. Taking the tip fully into account is the only satisfactory solution to this problem. Still, the influence of tip states should only be pronounced at negative sample voltages, i.e. when electrons tunnel from occupied sample to unoccupied tip states[3]. Hence, Eq. (4.31) remains a sensible first order approximation to understand scanning tunneling spectroscopy.

4.4.2 Extension to Arbitrary Tip-Orbitals

The materials commonly used for STM-tips are tungsten and platinum-iridium alloys which belong to the class of transition-metals. Their electronic structure is dominated by d-electrons at the Fermi energy and thus it is reasonable to include other orbital types than the s-wave used in the previous section. This extension of the Tersoff-Hamann model has been proposed by Chen [11], and the derivation presented above has been based on his ideas. The extension leads to a simple rule to account for arbitrary orbital types, the *derivative rule* [11]. In order to calculate matrix elements for orbitals of larger angular momentum higher order Besselfunctions are needed. These can be related to the Green's function of the vacuum Schrödinger equation and its partial derivatives. The calculation is similar to the one demonstrated explicitly in the last section for the simplest case, the s-orbital. There is a relation between the orbital character and the form of the matrix element which led to the name *derivative rule*. It states that the matrix element is given by replacing the notation of orbital

---

[3] The reason is related to the electric field and its influence on the shape of the potential barrier. A nice, detailed discussion of this effect and of further theoretical aspects of the spectroscopic mode is given in [50].

Tip orbital	Tunneling Matrix Element
s	$\frac{2\pi C\hbar^2}{\kappa m}\psi(\mathbf{R}_T)$
p_x	$\frac{2\pi C\hbar^2}{\kappa m}\frac{\partial\psi}{\partial x}(\mathbf{R}_T)$
p_y	$\frac{2\pi C\hbar^2}{\kappa m}\frac{\partial\psi}{\partial y}(\mathbf{R}_T)$
p_z	$\frac{2\pi C\hbar^2}{\kappa m}\frac{\partial\psi}{\partial z}(\mathbf{R}_T)$
d_{zx}	$\frac{2\pi C\hbar^2}{\kappa m}\frac{\partial^2\psi}{\partial z\partial x}(\mathbf{R}_T)$
$d_{z^2-r^2/3}$	$\frac{2\pi C\hbar^2}{\kappa m}\left(\frac{\partial^2\psi}{\partial z^2}(\mathbf{R}_T)-\frac{\kappa^2}{3}\psi(\mathbf{R}_T)\right)$

Table 4.1: Table of tunneling matrix elements according to Chen's *derivative rule*.

characters through partial derivatives of the sample wave function ψ_μ at the position of the tip apex atom $\mathbf{R}_T$ in the following way:

$$\begin{aligned} x &\rightarrow \partial/\partial x \\ y &\rightarrow \partial/\partial y \\ z &\rightarrow \partial/\partial z. \end{aligned} \tag{4.32}$$

For example a p_z-type orbital yields a matrix element proportional to $\partial\psi_\mu/\partial z\ (\mathbf{R}_T)$. Table 4.1 summarizes the matrix elements for arbitrary tip orbitals. In principle it is possible to expand the states of a realistic tip, calculated for example by *ab initio* techniques, in these orbitals and to compute the matrix element by adding the contributions according to their weight. Whether this approach is convenient depends on the applied *ab initio* method and its basis function set.

The extension by Chen provides an explanation of the high corrugation amplitudes Δz measured on close-packed metal surfaces contradictory to the low corrugation amplitudes due to their local density of states n. Applying the derivative rule to the p_z- and d_{z^2}-orbital leads to a large enhancement of the calculated corrugation amplitude in much better agreement with experimental values. Since the p_z- and d_{z^2}-orbitals possess charge densities stretching out further from the tip apex atom into the vacuum than that of an s-wave they act similar to an s-wave at a reduced distance from the sample surface. As the local density of states and also the corrugation amplitude decrease exponentially with distance this leads to an enormous enhancement in the measured corrugation amplitude which can be expressed by an enhancement factor. This factor is given for a d_{z^2}-orbital by:

$$f_{d_{z^2}} = (1+3q^2/2\kappa^2)^2 \text{ with } q = G_\parallel/2. \tag{4.33}$$

$G_\parallel$ is the length of the reciprocal lattice vector corresponding to the Fourier component of the STM image (in section 4.6 this connection is discussed in more detail). In the case of a square lattice with lattice constant $a_\parallel$ of the surface unit cell of the sample we get $G_\parallel = 2\pi/a_\parallel$ for an image showing the lattice sites. Assuming a typical close-packed surface with $\phi = 4.5$ eV and $a_\parallel = 2.87$ Å leads to a factor of 6.5 for a d_{z^2}-type tip. From Eq. (4.33) we find the enhancement factor to be reduced with increasing lattice constant $a_\parallel$ or equivalently with increasing length scale of the structure. In the limit of large length scales the model becomes independent of the type of the tip orbital. This is in accordance with experiments performed on reconstructions of the Au(111)-surface [54]. The fact that atomic-resolution on close-packed metal surfaces cannot be achieved with every tip is a further experimental clue in favor of this explanation relying on special tip configurations.

On the other hand, orbitals of $m \neq 0$ like the d_{xy} and $d_{xz,yz}$ are expected to produce a large tunneling current not with the tip apex atom located on top of a surface atom but rather at a hollow site of the surface. Due to their particular charge density distribution a large overlap with sample orbitals occurs in this configuration. These orbitals thus explain STM-images showing anti-corrugation, i.e. imaging atoms as depressions (low tunneling current) and hollow sites as protrusions (high tunneling current). In chapter 5 we will see that it is also quite often possible to find anti-corrugation for transition-metal samples as a result of their electronic properties.

We have implemented the derivative rule in the `FLEUR` code for p_z- and d_{z^2}-orbitals (see section 4.6.1) and tested the importance of these orbitals for the example of W(110) (see chapter 5).

4.5 The Spin-Polarized Tunneling Current

In the derivation of the tunneling current presented in the previous sections we have taken the spin of the electron into account only by the double occupation of single-particle states. However, in order to describe the tunneling in the set-up of the spin-polarized STM (SP-STM) (Fig. 4.3) we need to take the spin-polarized electronic structure of both tip and sample explicitly into account. The SP-STM can be realized by coating a common STM tip with a magnetic material, for example Fe or Gd have been successfully used [27, 132], and using this spin-sensitive probe to scan the surface of the magnetic sample. In the following we assume the coated tip to be ferromagnetic with a spin-polarized bandstructure of spin-up (↑) and spin-down (↓) states with respect to a quantization axis given by the magnetization axis $\mathbf{M}_T$ of the tip. With the concept of Pauli-spinors we can write electronic states of the tip as:

$$\Psi^T_{\nu\uparrow}(\mathbf{r}) = \psi^T_{\nu\uparrow}(\mathbf{r}) \begin{pmatrix} 1 \\ 0 \end{pmatrix} \quad \text{and} \quad \Psi^T_{\nu\downarrow}(\mathbf{r}) = \psi^T_{\nu\downarrow}(\mathbf{r}) \begin{pmatrix} 0 \\ 1 \end{pmatrix}. \tag{4.34}$$

The orientation of the magnetization axis $\mathbf{M}_T$ of the tip with respect to the geometric axis of the tip depends on the material and the geometric structure, and it is called the magnetic anisotropy. It results from a competition between the crystal anisotropy energy, a consequence of spin-orbit interaction, and the shape anisotropy energy, accounting for magnetic dipole interaction.

The sample, on the other hand, may possess a variety of different magnetic structures. A ferromagnetic, antiferromagnetic, or ferrimagnetic configuration as well as a commensurate or incommensurate spin-density wave or a non-collinear spin-structure

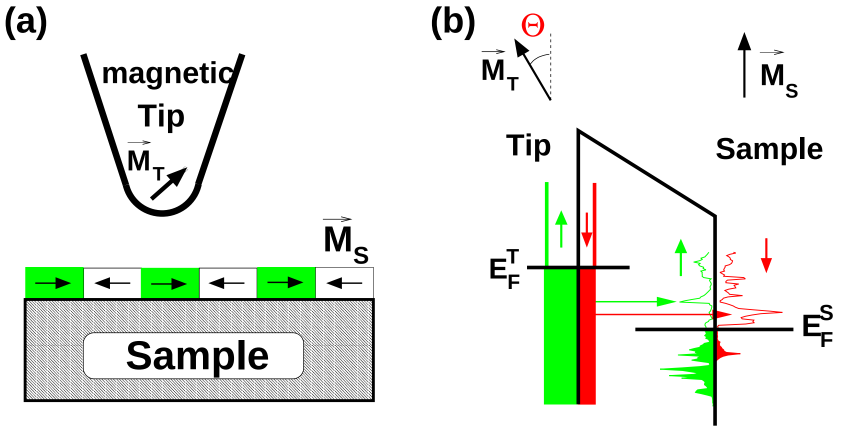

Figure 4.3: Schematics of spin-polarized STM (SP-STM) using a magnetically coated STM tip. (a) shows the geometry of the experimental set-up including the magnetization axes of tip $\mathbf{M}_T$ and sample $\mathbf{M}_S$. In general a non-collinear orientation of the two magnetization axes occurs. (b) displays the situation in terms of the electronic structure of tip and sample. In the case of a perfect parallel alignment of $\mathbf{M}_T$ and $\mathbf{M}_S$ only majority electrons can tunnel into unoccupied majority states and only minority electrons into unoccupied minority states.

is possible. The magnetization axis of the sample $\mathbf{M}_S$ is in general non-collinear with respect to the magnetization axis of the tip $\mathbf{M}_T$. Therefore a transformation into a global reference system for the spin must be performed for the calculation of the matrix elements. We work with the assumption that the spin is conserved within the global reference system during the tunneling process. A loss of spin information can occur by scattering processes connected with a spin-flip in the tunneling barrier. For the vacuum tunneling of STM these can be excluded to a high degree since the only scattering processes are given by many-particle processes which seem to play a minor role in most cases.

For the sake of simplicity, we derive the spin-polarized tunneling current for a collinear magnetic structure of the sample. Nevertheless, we will be able to give a direct generalization of the obtained result for an arbitrary spin-structure of the sample. In the case of a collinear spin configuration of the sample, i.e. when we can discuss spin in terms of majority or spin-up (↑) and minority or spin-down (↓) single-particle states, each state can be decomposed into its real-space and spin-space part similar to the tip states:

$$\Psi^S_{\mu\uparrow}(\mathbf{r}) = \psi^S_{\mu\uparrow}(\mathbf{r}) \begin{pmatrix} 1 \\ 0 \end{pmatrix} \quad \text{and} \quad \Psi^S_{\mu\downarrow}(\mathbf{r}) = \psi^S_{\mu\downarrow}(\mathbf{r}) \begin{pmatrix} 0 \\ 1 \end{pmatrix} . \tag{4.35}$$

Since in general, tip and sample do not share the same quantization axis, we define a global magnetization axis of tip and sample, which in many cases is either the magnetization axis of the tip or of the sample. The spin states, defined such that the expectation value of the z-component of the spin S_z is diagonal with respect to the local quantization axis, are transformed to the global quantization system. This is accomplished by means of the rotation matrix $U(\theta)$:

$$U(\theta) = \begin{pmatrix} \cos(\theta/2) & -\sin(\theta/2) \\ \sin(\theta/2) & \cos(\theta/2) \end{pmatrix}, \tag{4.36}$$

where θ is the angle between the magnetization axes of tip and sample. The tunneling matrix element for the tunneling from a state $|\mu\sigma\rangle$ of the sample into a state $|\nu\sigma'\rangle$ of the tip (Eq. 4.11) can be separated accordingly into a part depending only on the rotation in spin-space and a part depending on the real-space tip position:

$$\begin{aligned} M^{\sigma\sigma'}_{\mu\nu}(\mathbf{R}_T, \theta(\mathbf{R}_T)) &= \langle \Psi^T_{\nu\sigma'} | U_T | U(\theta(\mathbf{R}_T)) \Psi^S_{\mu\sigma} \rangle \\ &= \int_{\Omega_T} \psi^{T*}_{\nu\sigma'} \left(\delta_{\uparrow\sigma'}\,,\, \delta_{\downarrow\sigma'}\right) U_T U(\theta(\mathbf{R}_T)) \psi^S_{\mu\sigma} \begin{pmatrix} \delta_{\uparrow\sigma} \\ \delta_{\downarrow\sigma} \end{pmatrix} dV \\ &= \left(\delta_{\uparrow\sigma'}\,,\, \delta_{\downarrow\sigma'}\right) U(\theta(\mathbf{R}_T)) \begin{pmatrix} \delta_{\uparrow\sigma} \\ \delta_{\downarrow\sigma} \end{pmatrix} \int_{\Omega_T} \psi^{T*}_{\nu\sigma'} U_T \psi_{\mu\sigma} dV \\ &= U_{\sigma\sigma'}(\theta(\mathbf{R}_T))\, M^{\sigma\sigma'}_{\mu\nu}(\mathbf{R}_T). \end{aligned} \tag{4.37}$$

σ and σ' denote the spin of the sample and tip state, respectively, and can be of values $\uparrow$ or $\downarrow$. The real-space dependent part of the matrix element is calculated as derived in the previous sections (in the chosen approximation) using the real-space part of the wave functions for the desired spin direction. Note, that the angle θ between the magnetization axes of tip and sample depends in general on the position of the tip $\mathbf{R}_T$. Inserting this expression of the matrix element into the formula for the tunneling current (Eq. (4.14)) yields:

$$\begin{aligned} I(\mathbf{R}_T, V, \theta(\mathbf{R}_T)) &= \frac{2\pi}{\hbar} \sum_{\sigma\sigma'} |U_{\sigma\sigma'}(\theta(\mathbf{R}_T))|^2 \sum_{\mu\nu} |M^{\sigma\sigma'}_{\mu\nu}(\mathbf{R}_T)|^2 \delta(E^T_{\nu\sigma'} - E^S_{\mu\sigma} - eV) \\ &= \sum_{\sigma\sigma'} |U_{\sigma\sigma'}(\theta(\mathbf{R}_T))|^2 I_{\sigma\sigma'}(\mathbf{R}_T, V). \end{aligned} \tag{4.38}$$

For the sake of simplicity, the $T = 0$ K approximation has been used in the upper line but the second line still holds for arbitrary temperatures. From Eq. (4.38) we conclude that the total tunneling current $I(\mathbf{R}_T, V, \theta(\mathbf{R}_T))$ is given by a sum over the tunneling currents $I_{\sigma\sigma'}(\mathbf{R}_T, V)$ for the different possible spin channels $\sigma \to \sigma'$ weighted by the squares of the rotation matrix $U_{\sigma\sigma'}(\theta(\mathbf{R}_T))$.

The decomposition of the spin-polarized tunneling current in Eq. (4.38) allows a convenient discussion in terms of the different spin channels. Three particular cases are of special interest: $\theta = 0, \pi$ and $\pi/2$. The related tunneling currents can be expressed by:

$$I(\mathbf{R}_T, 0) = I_{\uparrow\uparrow}(\mathbf{R}_T) + I_{\downarrow\downarrow}(\mathbf{R}_T) = I_P(\mathbf{R}_T) \tag{4.39}$$

$$I(\mathbf{R}_T, \pi) = I_{\uparrow\downarrow}(\mathbf{R}_T) + I_{\downarrow\uparrow}(\mathbf{R}_T) = I_{AP}(\mathbf{R}_T) \tag{4.40}$$

$$\begin{aligned} I(\mathbf{R}_T, \pi/2) &= \frac{1}{2}\left[I_{\uparrow\uparrow}(\mathbf{R}_T) + I_{\downarrow\downarrow}(\mathbf{R}_T) + I_{\uparrow\downarrow}(\mathbf{R}_T) + I_{\downarrow\uparrow}(\mathbf{R}_T)\right] \\ &= \left[I_P(\mathbf{R}_T) + I_{AP}(\mathbf{R}_T)\right]/2. \end{aligned} \tag{4.41}$$

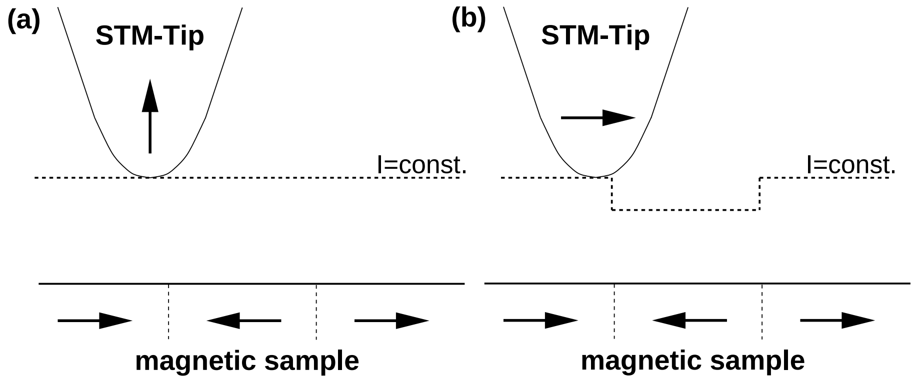

Figure 4.4: Scheme of spin-polarized STM with ferromagnetic tips. In (a) the magnetization axes of tip and sample are perpendicular to each other and scanning domains of opposite magnetization direction does not result in a change of the tunneling current. On the other hand (b) displays the case of a collinear alignment of magnetization axes and the tunneling current between different domains changes from I_P to I_{AP} leading to an image of the magnetic structure.

For convenience, we have neglected the bias-voltage in the notation above. We observe that in the case of $\theta = \pi/2$ all possible channels contribute equally. Hence it is impossible to measure a different tunneling current on magnetic domains of antiparallel magnetization axes if the magnetization is in-plane for the sample and out-of plane for the tip or *vice versa*. This is sketched in Fig. 4.4.

In order to analyze STM-experiments in terms of sample properties we generalize the Tersoff-Hamann model to the case of a spin-polarized STM by assuming a magnetic tip which has a constant DOS for each spin direction of unequal values, $n_T^{\uparrow}$ =const. and $n_T^{\downarrow}$ =const. but $n_T^{\uparrow} \neq n_T^{\downarrow}$. Further, we use the same s-wave function for both spin directions, i.e. $C = C_{\uparrow} = C_{\downarrow}$ and $\kappa = \kappa_{\uparrow} = \kappa_{\downarrow}$. Analogously to Eq. (4.28) we find the spin-polarized generalization of the tunneling current:

$$
\begin{aligned}
I(\mathbf{R}_{T}, V, \theta(\mathbf{R}_{T})) &= \frac{8\pi^3 C^2 \hbar^3 e}{\kappa^2 m^2} \sum_{\sigma\sigma'} |U_{\sigma\sigma'}(\theta(\mathbf{R}_{T}))|^2 n_T^{\sigma'} \int g_{V,T}(\epsilon) n_S^{\sigma}(\mathbf{R}_{T}, \epsilon)\, d\epsilon \qquad (4.42)\\
&= \frac{8\pi^3 C^2 \hbar^3 e}{\kappa^2 m^2} \sum_{\sigma\sigma'} |U_{\sigma\sigma'}(\theta(\mathbf{R}_{T}))|^2 n_T^{\sigma'} \tilde{n}_S^{\sigma}(\mathbf{R}_{T}, V) \qquad (4.43)\\
&= \frac{4\pi^3 C^2 \hbar^3 e}{\kappa^2 m^2} \Big(\underbrace{n_T\, \tilde{n}_S(\mathbf{R}_{T}, V)}_{non-spinpolarized} + \underbrace{m_T\, \tilde{m}_S(\mathbf{R}_{T}, V) \cos\theta(\mathbf{R}_{T})}_{spin-polarized} \Big), \qquad (4.44)
\end{aligned}
$$

where $n_S^{\sigma}(\mathbf{R}_{T}, \epsilon)$ is the spin-dependent local density of states of the sample at the position of the tip and $\tilde{n}_S^{\sigma}(\mathbf{R}_{T}, V)$ denotes the integrated spin-resolved local density of states (ILDOS) of the sample for an applied bias-voltage V:

$$
\tilde{n}_S^{\sigma}(\mathbf{R}_{T}, V) = \int g_{V,T}(\epsilon) n_S^{\sigma}(\mathbf{R}_{T}, \epsilon)\, d\epsilon. \qquad (4.45)
$$

n_T is defined as the sum of the constant majority and minority DOS of the tip, $n_T = n_T^{\uparrow} + n_T^{\downarrow}$, and m_T is the difference of these, $m_T = n_T^{\uparrow} - n_T^{\downarrow}$. An analogous definition is used for the sample, but the quantities depend on the tip position and on the applied bias-voltage:

$$\tilde{n}_S(\mathbf{R}_T, V) = \tilde{n}_S^{\uparrow}(\mathbf{R}_T, V) + \tilde{n}_S^{\downarrow}(\mathbf{R}_T, V) \tag{4.46}$$

and

$$\tilde{m}_S(\mathbf{R}_T, V) = \tilde{n}_S^{\uparrow}(\mathbf{R}_T, V) - \tilde{n}_S^{\downarrow}(\mathbf{R}_T, V), \tag{4.47}$$

where $\tilde{n}_S(\mathbf{R}_T, V)$ is the integrated local density of states of the sample and $\tilde{m}_S(\mathbf{R}_T, V)$ is the integrated local spin density of states. Eq. (4.43) expresses a weighting of the majority and minority spin parts of the LDOS by the tip DOS, while we have rewritten the result in Eq. (4.43) into a decomposition of the non-spinpolarized and spin-polarized part. In the case of an arbitrary spin-structure of the sample Eq. (4.44) can be generalized in the form (see Appendix A for the derivation):

$$I(\mathbf{R}_T, V, \theta, \phi) = \frac{4\pi^3 C^2 \hbar^3 e}{\kappa^2 m^2} \left[n_T\, \tilde{n}_S(\mathbf{R}_T, V) + \mathbf{m}_T\, \tilde{\mathbf{m}}_S(\mathbf{R}_T, V) \right], \tag{4.48}$$

where $\mathbf{m}_T = m_T(\cos\phi \sin\theta, \sin\phi \sin\theta, \cos\theta)$ is the magnetization vector of the tip and $\tilde{\mathbf{m}}_S(\mathbf{R}_T, V)$ is the vector of the integrated local spin density of states of the sample defined by:

$$\tilde{\mathbf{m}}_S(\mathbf{R}_T, V) = \int g_{V,T}(\epsilon) \sum_{\mu} \delta(\epsilon_\mu - \epsilon) \Psi_\mu^\dagger(\mathbf{R}_T) \boldsymbol{\sigma} \Psi_\mu(\mathbf{R}_T)\, d\epsilon. \tag{4.49}$$

$\boldsymbol{\sigma}$ is given by the Pauli spin-matrices, i.e. $\boldsymbol{\sigma} = (\sigma_1, \sigma_2, \sigma_3)$.

The consequences of Eq. (4.44) shall be illustrated by two examples. The first natural application of SP-STM is to image directly, i.e. in the constant-current mode, the difference of the tunneling current above adjacent domains. This kind of experiment has been performed by Wiesendanger *et al.* [23] to prove the topological antiferromagnetism between adjacent terraces of the Cr(001) surface predicted by Blügel *et al.* [55]. In order to estimate the height difference achievable in the constant-current mode we assume a perfect collinear alignment between the magnetization axes of tip and sample, i.e. $\theta = 0, \pi$ for adjacent magnetic domains. Requiring the tunneling current to be equal above two magnetic 180° domains leads to:

$$n_T \tilde{n}_S(z_1, V)(1 + P_T \tilde{P}_S(z_1, V)) = n_T \tilde{n}_S(z_2, V)(1 - P_T \tilde{P}_S(z_2, V)), \tag{4.50}$$

where $P_T = m_T / n_T$ is the spin-polarization of the tip and $\tilde{P}_S(z, V) = \tilde{m}_S(z, V)/\tilde{n}_S(z, V)$ is the integrated local spin-polarization of the sample. From the one-dimensional model we know already that the local density of states decays exponentially with distance z (see Eq. (4.3)). In a first approximation the spin-polarization of the sample is thus constant with respect to z. After some elementary transformations we arrive at the final result for the corrugation amplitude $\Delta z = z_2 - z_1$:

$$\Delta z = \frac{1}{2\kappa} \ln \left(\frac{1 + P_T \tilde{P}_S(V)}{1 - P_T \tilde{P}_S(V)} \right). \tag{4.51}$$

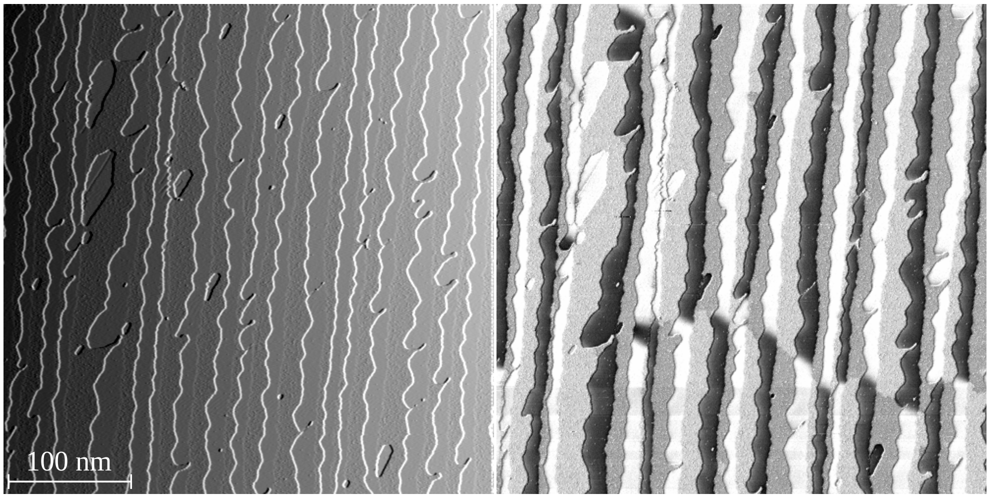

Figure 4.5: Spin-polarized STM-measurements of 1.3 ML Fe on W(110) using a Gd-coated tungsten tip. The left image shows the surface topography, i.e. the constant-current image, while the right image is a map of the differential conductivity dI/dV at a bias-voltage of +0.7 V. At the chosen coverage and growth conditions a closed monolayer of Fe decorates the W-substrate plus double layer thick Fe-nanowires along the step edges of the substrate which appear black and white in the right image. The magnetization axis of the double layer is out-of-plane while it is in-plane for the monolayer [56]. There is domain contrast observable on both, the monolayer and the double layer areas, hinting at a canted magnetization axis of the Gd-coated tungsten tip. Figure by courtesy of M. Bode.

$\Delta z = 0$ in the case of vanishing spin-polarization $P_T\tilde{P}_S(V) = 0$ and for a perfect spin-polarization of both systems, i.e. $P_T\tilde{P}_S = 1$, the corrugation amplitude becomes infinite since there is no current above one domain. For reasonable values of the tip spin-polarization, $P_T = 0.4$ and $P_T = 0.8$, and a sample with a work function of about 4.5 eV we compute maximum corrugation amplitudes, i.e. if $\tilde{P}_S(V) = 1$, of 0.4 Å and 1.0 Å, respectively. In the literature there is only one report of a successful application of this mode to a magnetic surface [23] where corrugation differences of 0.2 Å have been reported. This is connected with an effective spin-polarization $P_T\tilde{P}_S(V)$ of 0.2. A disadvantage of this approach, making it difficult to apply in general, is given by $\tilde{P}_S(V)$ entering Eq. (4.51). $\tilde{P}_S(V)$ depends on the bias voltage. With increasing voltage the number of states between E_F and $E_F + eV$ is monotonically increasing while the difference between spin-up and down electrons may be constant. Thus $\tilde{P}_S(V)$ may be a decreasing function of the bias voltage. Nevertheless, one can circumvent this problem quite elegantly by using the spectroscopy mode of STM and mapping the value of the measured differential conductivity $dI/dV(V)$ for a specific bias-voltage V as a function of the lateral tip position. This map can be correlated directly to the topography of the surface which is measured simultaneously. The advantage of this contrast mechanism can be understood if we differentiate Eq. (4.44) with respect to V:

$$dI/dV(V) \propto n_T n_S(\mathbf{R}_T, E_F + eV)\big[1 + \cos(\theta(\mathbf{R}_T))P_T P_S(\mathbf{R}_T, V)\big], \qquad (4.52)$$

where $P_S(\mathbf{R}_T, V) = m_S(\mathbf{R}_T, E_F + eV)/n_S(\mathbf{R}_T, E_F + eV)$. Since the differential conductivity is proportional to the (local) spin-polarization of the sample at a certain bias-voltage V one can select a special feature in the DOS of the sample which shows a high spin-polarization and thereby leads to a large contrast for the dI/dV-maps. Recently, applications of this mode have been very successful in the study of Fe-nanowires on W(110) [27]. An example of such a measurement is shown in Fig. 4.5.

Although the constant-current (topography) mode is clearly unfavorable in the imaging of domain structures of magnetic surfaces it provides a great potential in the resolution of magnetic structures on the atomic scale. This aspect of SP-STM will be discussed in chapter 9 along with a presentation of the first measurement on this scale.

4.6 Applying the FLAPW Method

The basis of the simulation of STM experiments has been presented in the previous sections. This section deals with some technical aspects of applying the results. Further consequences concerning the connection between electronic structure and bias-voltage dependent STM images are discussed. This leads naturally to a method for the analysis of STM images on the basis of the electronic structure. Results discussed in chapters 5 to 9 refer to this method.

Under normal tunneling conditions the distance between the outermost tip and surface atom is estimated to be between 4 and 10 Å. Due to the exponential decay of the wave function into the vacuum the reliable representation of the wave functions in this region of the vacuum is a non-trivial problem. For example in supercell calculations using a plane-wave basis, it is difficult to go beyond 3 to 4 Å. Therefore, it is especially useful that we apply the full-potential linearized augmented plane wave method in film geometry as it has been described in chapter 3 to calculate the electronic structure. We recall that it is a truly two-dimensional method consisting of a semi-infinite vacuum region, which is solved in real space, and of a finite number of atomic layers to describe the substrate. The vacuum wave function $\psi_{\mathbf{k}_\parallel \nu}$, characterized on the basis of Blochs Theorem (e.g. [38]) by a band index ν and a wave vector $\mathbf{k}_\parallel$ of the two-dimensional (2D) Brillouin zone, is expanded into basis functions:

$$\psi_{\mathbf{k}_\parallel \nu}(\mathbf{r}_\parallel, z) = \sum_n c^n_{\mathbf{k}_\parallel \nu} d^n_{\mathbf{k}_\parallel}(z) \exp\left[i(\mathbf{k}_\parallel + \mathbf{G}^n_\parallel)\mathbf{r}_\parallel\right], \tag{4.53}$$

which are 2D plane waves parallel to the surface and linearized z-dependent basis functions $d^n_{\mathbf{k}_\parallel}(z)$ with

$$d^n_{\mathbf{k}_\parallel}(z) = a^n_{\mathbf{k}_\parallel} u^n_{\mathbf{k}_\parallel}(\epsilon_v, z) + b^n_{\mathbf{k}_\parallel} \dot{u}^n_{\mathbf{k}_\parallel}(\epsilon_v, z). \tag{4.54}$$

$a^n_{\mathbf{k}_\parallel}$ and $b^n_{\mathbf{k}_\parallel}$ are determined by the continuity of the basis function and its derivative at the vacuum boundary to the film interstitial. The vacuum energy parameter ϵ_v, for which the wave functions are solved is usually positioned in the vicinity of the Fermi energy. The function $u^n_{\mathbf{k}_\parallel}(\epsilon_v, z)$ (and analogously its energy derivative $\dot{u}^n_{\mathbf{k}_\parallel}(\epsilon_v, z)$; see also section (3.3)) is the exact numerical solution of the one-dimensional Schrödinger equation to the laterally averaged z-dependent part of the effective vacuum potential $V_{\text{eff}}(z)$:

$$\left[-\frac{\hbar^2}{2m}\frac{d^2}{dz^2} + V_{\text{eff}}(z) - \epsilon_v + \frac{\hbar^2}{2m}(\mathbf{k}_\parallel + \mathbf{G}^n_\parallel)^2\right] u^n_{\mathbf{k}_\parallel}(\epsilon_v, z) = 0. \tag{4.55}$$

This choice of the basis functions is ideally suited to describe the vacuum region as it already includes the exponential decay of the wave functions with respect to the correct potential. The maximum distance in z-direction we have taken into account, was about 13 Å. Thus we were able to calculate the tunneling current at realistic tip-to-sample separations.

4.6.1 The 2D Star Functions

In general, quantities possessing the crystal symmetry of the lattice can be expanded into a set of symmetrized functions. The local density of states $n(\mathbf{r}_\parallel, z \,|\, \epsilon)$, needed in the Tersoff-Hamann model to compute the tunneling current, is invariant with respect to the 2D symmetry operations of the surface structure. Thus, we use the rotational part of the 2D space group operations to form out of plane waves symmetrized plane waves, so-called star functions $\phi^{2D}_s(\mathbf{r}_\parallel)$. A star function corresponds to a representative reciprocal lattice vector $\mathbf{G}^s_\parallel$, which is equivalent with respect to symmetry operations to a star of reciprocal lattice vectors $\mathbf{G}^n_\parallel$. This allows the restriction of the Brillouin-zone summation over the irreducible part of the 2D Brillouin zone (I2BZ).

The LDOS n in the vacuum region determining the tunneling current in the Tersoff-Hamann model is written as:

$$n(\mathbf{r}_\parallel, z \,|\, \epsilon) = \sum_s n^s(z \,|\, \epsilon)\, \phi^{2D}_s(\mathbf{r}_\parallel) \tag{4.56}$$

with

$$n^s(z \,|\, \epsilon) = \sum_{\mathbf{k}_\parallel \nu} \delta(\epsilon - \epsilon_{\mathbf{k}_\parallel \nu})\, n^s_{\mathbf{k}_\parallel \nu}(z) \tag{4.57}$$

and

$$n^s_{\mathbf{k}_\parallel \nu}(z) = \sum_{n,n'} c^n_{\mathbf{k}_\parallel \nu} c^{n'*}_{\mathbf{k}_\parallel \nu} d^n_{\mathbf{k}_\parallel}(z) d^{n'*}_{\mathbf{k}_\parallel}(z) \delta(\mathbf{G}^n_\parallel - \mathbf{G}^{n'}_\parallel, \mathbf{G}^s_\parallel). \tag{4.58}$$

For arbitrary tip orbitals, $d^n_{\mathbf{k}_\parallel}(z)$ in Eq. (4.58) is replaced by derivatives of $d^n_{\mathbf{k}_\parallel}(z)$ with respect to z according to the *derivative rule* of Chen (section 4.4.2). The expansion coefficients $n^s(z \,|\, \epsilon)$ are called star coefficients.

As an example for star functions $\phi^{2D}_s(\mathbf{r}_\parallel)$, we show the first three of them corresponding to the three smallest stars (s=1,2,3) of reciprocal lattice vectors for a square lattice (see Fig. 4.6) (e.g. representing the bcc- and fcc-(001) surfaces): $\mathbf{G}^s_\parallel$, $\mathbf{G}^{(1)}_\parallel = (0, 0)$, $\mathbf{G}^{(2)}_\parallel = (1, 0)$, $\mathbf{G}^{(3)}_\parallel = (1, 1)$, expressed in units of $2\pi/a$, with a being

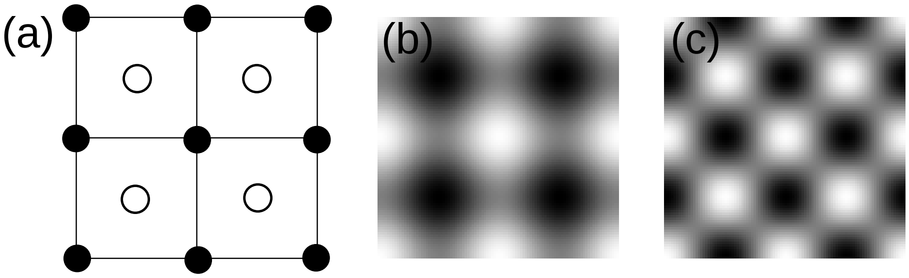

Figure 4.6: Star functions for a square lattice. (a) unit cell of a square lattice with a two atom basis, i.e. representing a c(2 × 2) checkerboard structure typical of a surface alloy. The first star function is a constant. (b) corresponding second star function displaying the black atoms as protrusions and the white ones as depressions. Note, that the sign of the expansion coefficient can be negative leading to an inversion of this image. (c) third star function showing both types of atoms.

the lattice constant:

$$\phi_1^{2D}(\mathbf{r}_\|) = 1 \tag{4.59}$$

$$\phi_2^{2D}(\mathbf{r}_\|) = \frac{1}{2}[\cos(\mathbf{G}_{\|,1}\mathbf{r}_\|) + \cos(\mathbf{G}_{\|,2}\mathbf{r}_\|)] \tag{4.60}$$

$$\phi_3^{2D}(\mathbf{r}_\|) = \cos[(\mathbf{G}_{\|,1} + \mathbf{G}_{\|,2})\,\mathbf{r}_\|]. \tag{4.61}$$

$\mathbf{G}_{\|,1}$ and $\mathbf{G}_{\|,2}$ are the two-dimensional reciprocal lattice vectors:

$$\mathbf{G}_{\|,1} = \frac{2\pi}{a}(1,0) \quad \text{and} \quad \mathbf{G}_{\|,2} = \frac{2\pi}{a}(0,1). \tag{4.62}$$

In Fig. 4.6 the star functions are displayed together with the 2D unit cell for a checkerboard structure of two different atom types. The first star function is a constant and represents the lateral constant part of the LDOS and thereby also of the tunneling current in the Tersoff-Hamann model. Its expansion coefficient $n^1(z|\epsilon)$ (see Eq. (4.56)) must be positive as it corresponds to a local charge density if we integrate the LDOS over the 2D unit cell and energy. Higher star coefficients can be of both signs. In our example of a square lattice and a checkerboard arrangement of two different atoms the second star function distinguishes between the two kinds of atoms. Only one type is shown as a protrusion while the other corresponds to a depression. If the star coefficient is positive the black atoms can be seen in the LDOS (or correspondingly in the STM image). The image is inverted for a negative coefficient, and the white atoms are observed as protrusions. The third star function does not distinguish between the two kinds of atoms, i.e. there is no chemical sensitivity in this part of the LDOS. If the corresponding star coefficient is positive atoms are shown as protrusion if it becomes negative the hollow sites appear as protrusions and the atoms as depressions (this is denoted as anti-corrugation).

4.6.2 The $\mathbf{k}_\|$-Selection for Star Coefficients

In order to analyze our first-principles results in terms of a simplified model we follow Sacks *et al.* [57] by approximating the z-dependent part of the vacuum wavefunction $d^n_{\mathbf{k}_\parallel}(z)$, Eq. (4.54), by its simplified tail. The vacuum is described by a barrier $V(z) = 0$. Then, the vacuum wave-function can be solved exactly and the wave function of energy ϵ will decay inside the barrier as:

$$d^n_{\mathbf{k}_\parallel}(z) = \exp\left(-\kappa^n_{\mathbf{k}_\parallel} z\right) \tag{4.63}$$

with z pointing into the barrier and with the decay constant:

$$\kappa^n_{\mathbf{k}_\parallel}(\epsilon) = \sqrt{2m|\epsilon|/\hbar^2 + (\mathbf{k}_\parallel + \mathbf{G}^n_\parallel)^2}. \tag{4.64}$$

The energy ϵ is measured with respect to the vacuum potential at large distance from the surface, which is zero in our case. We can write the $\mathbf{k}_\parallel$- and $\mathbf{G}^s_\parallel$-resolved contribution to the LDOS for the eigenstate $|\mathbf{k}_\parallel\nu\rangle$ at the energy $\epsilon_{\mathbf{k}_\parallel\nu}$ in the form:

$$n^s_{\mathbf{k}_\parallel\nu}(z) = \sum_{n,n'} c^n_{\mathbf{k}_\parallel\nu} c^{n'*}_{\mathbf{k}_\parallel\nu} \exp\left[-(\kappa^n_{\mathbf{k}_\parallel\nu} + \kappa^{n'}_{\mathbf{k}_\parallel\nu})z\right] \delta(\mathbf{G}^n_\parallel - \mathbf{G}^{n'}_\parallel, \mathbf{G}^s_\parallel). \tag{4.65}$$

where ϵ of Eq. (4.64) is replaced by $\epsilon_{\mathbf{k}_\parallel\nu}$. In this model the electronic structure is contained in the coefficients $c^n_{\mathbf{k}_\parallel\nu}$ and the exponential z-dependent decay into the vacuum is now seen explicitly.

In order to find those states, which contribute most to the different patterns of STM-images we take a look at the z-dependence of the wave functions at different points in reciprocal space. From our simplified model we can see, that the $\mathbf{k}_\parallel$- and $\mathbf{G}^s_\parallel$-resolved contribution to the surface topography at the surface plane $z = 0$ is detected at the distance z after $\mathbf{k}_\parallel$- and $\mathbf{G}^s_\parallel$-dependent weighting expressed by Eq. (4.63). Consequently, waves with the smallest lattice vectors $\mathbf{G}^s_\parallel$ and the highest energy ϵ will reach out furthest into the vacuum and contribute most to the STM image. Thus a $\mathbf{k}_\parallel$- and $\mathbf{G}^s_\parallel$-dependent filtering of the available electronic states takes place.

For a selected reciprocal lattice vector $\mathbf{G}^s_\parallel$ those reciprocal lattice vectors $\mathbf{G}^n_\parallel$ of the wave function contribute most which are the smallest. Additionally, the Bloch vector $\mathbf{k}_\parallel$ of the states plays a role in the selection of the largest contributions from the Brillouin zone. For $\mathbf{G}^s_\parallel = 0$ the highest contributions are thus expected for $n = n' = 0$ and $\mathbf{k}_\parallel = 0$, i.e. the Γ-point of the 2D Brillouin zone. Analogously we find for the smallest non-vanishing representative reciprocal lattice vector, i.e. $\mathbf{G}^s_\parallel = \mathbf{G}^{(1)}_\parallel$, $n = 1$ and $n' = 0$ (and all symmetry related combinations) and $\mathbf{k}_\parallel = -\mathbf{G}^{(1)}_\parallel/2$ (and all symmetry related points of the 2D BZ).

The $\mathbf{k}_\parallel$-dependent filtering effect in Eq. (4.65) on $n^s_{\mathbf{k}_\parallel\nu}(z)$ is analyzed graphically in Fig. 4.7a-c for the three smallest stars (s=1,2,3) of reciprocal lattice vectors $\mathbf{G}^s_\parallel$ of a square lattice. Fig. 4.7a-c display the exponential decay of $n^s_{\mathbf{k}_\parallel}(z_0 \,|\, E_F)$ in terms of grey scale plots over the 2D Brillouin-zone calculated for the Fermi energy, $\epsilon = E_F$, at a tip-sample distance of $z_0 = 5$ Å. In these plots the electronic structure has been explicitly ignored by replacing in Eq. (4.65) all coefficients $c^n_{\mathbf{k}_\parallel\nu}$ by a constant and replacing $\kappa^n_{\mathbf{k}_\parallel\nu}$ by $\kappa^n_{\mathbf{k}_\parallel}(E_F)$. We used $E_F = -4.5$ eV as calculated for a Fe(001)-surface. There is only a minor dependence on the exact Fermi energy which is usually

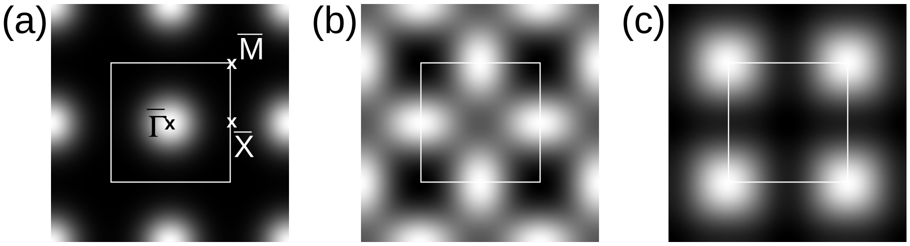

Figure 4.7: Grey-scale plots showing the decay of star coefficients in $\mathbf{k}_\parallel$-space for the case of a square lattice. The white square denotes the boundaries of the 2D Brillouin zone. (a) displays the $\mathbf{k}_\parallel$-dependence for the first star coefficient. Clearly states from the $\bar{\Gamma}$-point contribute most significantly. (b) and (c) show the same for the second and third star coefficient. Again high symmetry points of the 2D Brillouin zone contribute most to the different star coefficients.

around 4 to 5 eV. On the basis of Fig. 4.7 we can discuss the importance of various contributions to the tunneling current over the $\mathbf{k}_\parallel$-space.

The first term $n^{(1)}_{\mathbf{k}_\parallel}$ corresponding to $\mathbf{G}^{(1)}_\parallel = \mathbf{0}$ leads to an $\mathbf{r}_\parallel$ independent, i.e. laterally constant contribution to the tunneling current (cf. Eq. (4.59)). $n^{(1)}_{\mathbf{k}_\parallel}$ is always positive. It does not make any contribution to the corrugation pattern but it adds to the total tunneling current (total LDOS) and becomes important in scanning tunneling spectroscopy. By Fig. 4.7a one concludes that this star coefficient is dominated by states near the center of the BZ, i.e. the $\bar{\Gamma}$-point.

The decay of the second star coefficient $n^{(2)}_{\mathbf{k}_\parallel}$ of the LDOS is displayed in Fig. 4.7b. The STM topography pattern resulting from the second star function (see Eq. (4.60)) depends on the sign of the star coefficient and contributes to imaging either one or the other atom type in our example. One finds that in this case the main contribution results from states around the $\bar{X}$-point.

Finally the third star coefficient is plotted in Fig. 4.7c. The z-dependent $\mathbf{k}_\parallel$-point filtering shown in Fig. 4.7c projects out states near the $\bar{M}$–point. The third star coefficient can become positive or negative, and shows either both atom kinds or all hollow sites of the lattice. The relation between the second and third star coefficient thus decides whether chemical resolution is possible. In chapter 6 we will see how we can exploit this in realistic electronic structure calculations. The influence of the electronic structure on the STM-images can then be clarified by taking the coefficients $c^n_{\mathbf{k}_\parallel\nu}$ explicitly into account.

Because the average values of the star coefficients n^s decrease exponentially with the length of the star vector as can be concluded from equation (4.65) higher star functions can be neglected (see also Table 4.2). This cut-off depends on the scale of the 2D unit cell since, if the lattice constant increases, the difference in reciprocal lattice vectors decreases. To illustrate the different orders of magnitude, we present in Table 4.2 a comparison of the decay factors at the high symmetry points contributing most significantly to each star coefficient. The values are given relative to the decay of the lateral constant part of the LDOS, i.e. the first star. We have taken the Fe(001)-surface as an example. The p(1×1) unit cell corresponds to a clean surface, a c(2×2)

Unit cell	(γ_2/γ_1) (4 Å)	(γ_3/γ_1) (4 Å)	(γ_4/γ_1) (4 Å)
p(1×1)	0.026	0.002	$2 \cdot 10^{-5}$
	$f = 6.5$	$f = 16.7$	$f = 50.6$
	$\times f = 0.17$	$\times f = 0.03$	$\times f = 0.001$
c(2×2)	0.136	0.026	0.002
	$f = 3.1$	$f = 6.5$	$f = 16.6$
	$\times f = 0.43$	$\times f = 0.17$	$\times f = 0.03$
p(2×2)	0.351	0.136	0.026
	$f = 1.9$	$f = 3.1$	$f = 6.5$
	$\times f = 0.67$	$\times f = 0.43$	$\times f = 0.17$

Table 4.2: Table showing a comparison of decay factors $\gamma_s(z)/\gamma_1(z) = \exp[-2z((\kappa^2 + (\mathbf{G}_\parallel^s/2)^2)^{1/2} - \kappa)]$ for the leading contributions to star s. As an example we have chosen different superstructures based on the square unit cell of Fe(001) with $\phi = 4.5$ eV, $a_0 = 2.87$ Å and a tip-sample distance of $z = 4$ Å. The second line for each superstructure displays the corresponding enhancement factors for a d_{z^2} orbital as given by Eq. (4.33) and the third line shows the product of decay and enhancement factor.

to the checkerboard structure of a surface alloy with every second Fe atom replaced by another kind (see Fig. 4.6), and a p(2×2) cell can be used to model a single impurity atom incorporated in a surface. In the second line of each superstructure we have given the enhancement factor for a d_{z^2} orbital (Eq. (4.33)) to this star function, i.e. Fourier component, of the image. The Table quite clearly expresses that for a clean surface only the second star coefficient should be significant. Even if we take an enhancement factor into account the third star coefficient values are negligible. This is also physically reasonable since the third star function possesses maxima at both the atom and hollow sites of the surface unit cell. As we have pointed out earlier (see Fig. 4.6) this is different for a c(2×2) structure. The second star function then shows maxima at only one atom position of the unit cell while the third star function now shows maxima at every atom site. Accordingly, the difference of the decay factors is less significant and taking the enhancement factor into account leads to a factor of 2.5 between the decay factors of second and third star coefficient. Again we find this in agreement with our intuition. Experimental STM images of the CuAu/Au(001) surface alloy actually show contributions of both the second and third star function [58]. The sketched trend is continued for the p(2×2) unit cell. We also recognize that the enhancement factors are considerably lower in accordance with the statement that the STM images become independent of tip orbitals with increasing scale of the structure.

4.6.3 Calculating the Corrugation Amplitude

The star function method is also valuable in calculating the corrugation amplitudes, as will be shown next. The corrugation amplitude Δz, defined as the maximum difference in tip height as the surface is scanned, is calculated making use of the observation that the corrugation is of the order of typically $\Delta z \simeq 0.10$ Å for all $\mathbf{r}_\|$ within the entire unit cell, which is tiny compared to the average tip–sample distance z_0 of about $z_0 \simeq 5$ Å. We write

$$z(\mathbf{r}_\|) = z_0 + \Delta z(\mathbf{r}_\|) \tag{4.66}$$

and linearize the tunneling current $I(\mathbf{r}_\|, z(\mathbf{r}_\|) \,|\, V) = I(\mathbf{r}_\|, z_0 + \Delta z(\mathbf{r}_\|) \,|\, V)$ around z_0,

$$\begin{aligned} I(\mathbf{r}_\|, z(\mathbf{r}_\|) \,|\, V) &\approx I(\mathbf{r}_\|, z_0 \,|\, V) + \frac{\partial I}{\partial z}\Big|_{(\mathbf{r}_\|, z_0 \,|\, V)} \Delta z(\mathbf{r}_\|) & (4.67)\\ &\approx I_0(V) + dI(\mathbf{r}_\| \,|\, V) & (4.68) \end{aligned}$$

with

$$dI(\mathbf{r}_\|) = \nabla_{\mathbf{r}_\|} I|_{(\mathbf{r}_\|, z_0)} d\mathbf{r}_\| + \frac{\partial I}{\partial z}\Big|_{(\mathbf{r}_\|, z_0)} dz(\mathbf{r}_\|) \tag{4.69}$$

The explicit V dependence in Eq. (4.69) was dropped for convenience. In the constant current mode the tunneling current (and in the Tersoff-Hamann model the ILDOS $\tilde{n}$) is kept constant

$$I(\mathbf{r}_\|, z(\mathbf{r}_\|) \,|\, V) = \int_{-\infty}^{+\infty} g_{V,T}(\epsilon) n(\mathbf{r}_\|, z(\mathbf{r}_\|) \,|\, \epsilon)\, d\epsilon = \tilde{n}(\mathbf{r}_\|, z(\mathbf{r}_\|), V) = const(V) \tag{4.70}$$

and thus $dI(\mathbf{r}_\|) = 0$. Taking Eq. (4.69) and integrating the local change $dz(\mathbf{r}_\|)$ from the position of minimal ILDOS $\mathbf{r}_\|^{min}$ to the position of maximal ILDOS $\mathbf{r}_\|^{max}$ we obtain the maximum corrugation amplitude:

$$\Delta z = \int_{z(\mathbf{r}_\|^{min})}^{z(\mathbf{r}_\|^{max})} dz(\mathbf{r}_\|) = \int_{\mathbf{r}_\|^{min}}^{\mathbf{r}_\|^{max}} -\left(\frac{\partial I}{\partial z}\right)^{-1}_{(\mathbf{r}_\|, z_0)} \nabla_{\mathbf{r}_\|} I(\mathbf{r}_\|, z_0)\, d\mathbf{r}_\| . \tag{4.71}$$

We can now replace the tunneling current I by the ILDOS according to Eq. (4.70) using the expansion of the LDOS $n(\mathbf{r}_\|, z)$ in terms of star functions $\phi_s^{2D}(\mathbf{r}_\|)$ (Eq. (4.56)). Since higher star coefficients become quickly negligible (see also Table 4.2), the summation over the stars can be approximated by the leading star contributions. This is $s = 1$ for $\partial I / \partial z$, i.e. we replace $\partial I / \partial z$ at $(\mathbf{r}_\|, z_0)$ by an $\mathbf{r}_\|$ independent $\partial I / \partial z$ at (z_0) for all $\mathbf{r}_\|$ and pull this term in front of the integral, and $s > 1$ for $\nabla_{\mathbf{r}_\|} I$. With this we arrive at our final result for the corrugation amplitude:

$$\begin{aligned} \Delta z(z_0, V) &\approx S \, \frac{\sum\limits_{s>1} \Delta\phi_s^{2D} \int\limits_{-\infty}^{+\infty} g_{V,T}(\epsilon) n^s(z_0 \,|\, \epsilon)\, d\epsilon}{\int\limits_{-\infty}^{+\infty} g_{V,T}(\epsilon) 2\kappa^{(1)}_{\mathbf{k}_\|=\mathbf{0}}(\epsilon) n^{(1)}(z_0 \,|\, \epsilon)\, d\epsilon} \\ &= S \, \frac{\sum\limits_{s>1} \Delta\phi_s^{2D}\, \tilde{n}^s(z_0, V)}{\tilde{n}^{(1)}_\kappa(z_0, V)} . \end{aligned} \tag{4.72}$$

In this equation, $\Delta\phi_s^{2D}$ is the difference of the star function at the location of the maximum and the minimum ILDOS $I(\mathbf{r}_\parallel, z(\mathbf{r}_\parallel)\,|\,V)$:

$$\Delta\phi_s^{2D} = \phi_s^{2D}(\mathbf{r}_\parallel^{max}) - \phi_s^{2D}(\mathbf{r}_\parallel^{min}). \tag{4.73}$$

In order to calculate the derivative with respect to z in Eq. (4.72) the z-dependence of the 1st star coefficient $n^{(1)}(z\,|\,\epsilon)$ has been approximated by $n^{(1)}(z\,|\,\epsilon) \propto \exp\left(-2\kappa^{(1)}_{\mathbf{k}_\parallel=\mathbf{0}} z\right)$. κ is the energy-dependent decay length: $\kappa^{(1)}_{\mathbf{k}_\parallel=\mathbf{0}} = [2m|\epsilon|/\hbar^2]^{-1/2}$. The $\mathbf{k}_\parallel$ dependence of κ has been approximated by $\mathbf{k}_\parallel = \mathbf{0}$, since $\mathbf{k}_\parallel = \mathbf{0}$ dominates the $n^{(1)}$ contribution to the tunneling current as has been pointed out in the previous section.

In Eq. (4.72) a factor S has been introduced that needs to be explained. The origin of the coordinate system for the $\mathbf{r}_\parallel$ integration is usually located at the position of a surface atom, and $\mathbf{r}_\parallel^{max}$ and $\mathbf{r}_\parallel^{min}$ are taken from the positive quadrant of the 2D surface unit cell. In connection with the star functions of a square lattice (Fig. 4.6) we have discussed the possibility to image either one or the other kind of atoms in a checkerboard structure. It is convenient to define a sign S for the corrugation amplitude allowing us to express the two possible STM patterns. Let us call the corrugation amplitude positive if the tip–sample distance at the position of the black atom in Fig. 4.6 is larger than at the white atom site. We can do this by introducing S defined as follows:

$$S = \text{sign}\left[\int_{-\infty}^{+\infty} g_{V,T}(\epsilon) n^{(2)}(z_0\,|\,\epsilon)\, d\epsilon\right]. \tag{4.74}$$

S is thus the sign of the integrated second star coefficient. This definition makes use of the fact that the second star function has a maximum at the site of the black atom and a minimum at the site of the white atom taken the definition of star functions (Eq. (4.60)). A negative sign of the second star coefficient turns the maximum to a minimum and *vice versa*.

The quality of Eq. (4.72) has been tested calculating $n(\mathbf{r}_\parallel, z)$ on a fine z grid in real space and evaluating Δz directly from the condition that $n(\mathbf{r}_\parallel, z(\mathbf{r}_\parallel)) = const.$ The two different approaches are in good agreement although the evaluation of Eq. (4.72) is much faster.

4.6.4 Distance-Dependence of the Corrugation Amplitude

Using the result for the corrugation amplitude from the previous section and our analysis of leading contributions to the star coefficients we can estimate the distance-dependence of the corrugation amplitude. Let's assume that the image is dominated by the second star coefficient and that we can neglect higher order terms (this is usually the case). Taking the low bias-voltage limit we can then write the corrugation amplitude as:

$$\Delta z(z,V) = \Delta z(z_0|V) \exp\left[-2(z-z_0)\left(\sqrt{\kappa^2 + (\mathbf{G}_\parallel^{(2)}/2)^2} - \kappa\right)\right] \tag{4.75}$$

The distance-dependence of the first and second star coefficient has been approximated by the most significant contributions from the Brillouin-zone. Since the value of $(\mathbf{G}_{\|}^{(2)}/2)^2$ decreases with increasing unit cell size the decay of the corrugation amplitude, given by $(\kappa^2 + (\mathbf{G}_{\|}^{(2)}/2)^2)^{1/2} - \kappa$, decreases as well. This is in accordance with the experimental observation of STM images becoming nearly independent of tunneling parameters (by varying the constant current at a given bias-voltage the distance between tip and sample can be altered) [54].

4.6.5 Corrugation Amplitude for Magnetic Surfaces

A point of importance in the case of magnetic surfaces is the contribution of the two spin directions to the total corrugation amplitude. Additionally, the possibility of applying spin-polarized STM on the atomic-scale can be discussed in this context. The generalization of Eq. (4.72) for a sample with a spin-polarized electronic structure and an STM-Tip with a non-vanishing spin-polarization $P_T = m_T/n_T$ yields:

$$\Delta z(z_0, V) \quad \approx \quad S \, \frac{\sum\limits_{s>1} \Delta\phi_s^{2D} \left[n_T \, \tilde{n}^s(z_0, V) + m_T \, \tilde{m}^s(z_0, V) \cos\theta \right]}{n_T \, \tilde{n}_\kappa^{(1)}(z_0, V) + m_T \, \tilde{m}_\kappa^{(1)}(z_0, V) \cos\theta}, \tag{4.76}$$

where we have used the definitions introduced in section (4.5) and the spin-polarized generalization of the Tersoff-Hamann model as discussed there. The sign S, discussed previously, is now used in the modified form:

$$S = \operatorname{sign} \left[\int\limits_{-\infty}^{+\infty} g_{V,T}(\epsilon) \left(n_T \, n^{(2)}(z, \epsilon) + m_T \, m^{(2)}(z, \epsilon) \cos\theta \right) \, d\epsilon \right]. \tag{4.77}$$

In the nominator as well as the denominator of Eq. (4.76) we find the decomposition into non-magnetic and magnetic contributions to the ILDOS, i.e. the tunneling current in the applied model. While we can neglect the magnetic contribution in the denominator since the charge density is usually much larger than the magnetization density and the first star coefficient is related to these quantities, care has to be taken in the nominator. In general, the chemical and the magnetic unit cell are not the same and therefore also the star functions that apply are different. In the previous sections we have demonstrated the strong dependence of the decay of different contributions to the STM image on the length of their representative reciprocal lattice vector $\mathbf{G}_{\|}$. A magnetic superstructure for example has a larger lattice constant than the chemical unit cell and thus smaller reciprocal lattice vectors. According to what has been said before the contribution of the magnetic superstructure to the STM image will thus decay more slowly into the vacuum. This argument does not change the denominator as it is determined by the $\mathbf{G}_{\|} = 0$ terms which are independent of the size of the unit cell. Thus the second term in the nominator may very well dominate depending on the magnetic superstructure. An example of this effect will be discussed in more detail in chapter 9. In the definition of the sign S the lowest non-vanishing star function of the chemical and the magnetic unit cell has to be used accordingly.

Even in a non-spinpolarized experiment, $P_T = 0 \to m_T = 0$, the total corrugation is in general neither the average nor the sum of the corrugation amplitudes

$$\Delta z_\uparrow(z_0, V) = S_\uparrow \, \frac{\sum\limits_{s>1} \Delta\phi_s^{2D} \, \tilde{n}_\uparrow^s(z_0, V)}{\tilde{n}_{\kappa,\uparrow}^{(1)}(z_0, V)} \tag{4.78}$$

for majority and

$$\Delta z_\downarrow(z_0, V) = S_\downarrow \, \frac{\sum\limits_{s>1} \Delta\phi_s^{2D} \, \tilde{n}_\downarrow^s(z_0, V)}{\tilde{n}_{\kappa,\downarrow}^{(1)}(z_0, V)} \tag{4.79}$$

for minority electrons. There are two limiting cases. First, if $\tilde{n}_{\kappa,\uparrow}^{(1)}(z_0, V) \gg \tilde{n}_{\kappa,\downarrow}^{(1)}(z_0, V)$ then the total corrugation amplitude is approximately given by $\Delta z_\uparrow(z_0, V)$ and *vice versa*. Second, if $\tilde{n}_{\kappa,\uparrow}^{(1)}(z_0, V) \approx \tilde{n}_{\kappa,\downarrow}^{(1)}(z_0, V)$ then the total corrugation amplitude is approximately equal to the average of up and down corrugation amplitudes. In both cases the weighted integral over the lateral constant part of the LDOS $\tilde{n}_{\kappa,\sigma}^{(1)}(z_0, \epsilon)$ decides about the contribution of the different spin directions. In chapter 8 we will present an application of these arguments.

Chapter 5

Bias-Voltage Dependent Corrugation Reversal

In this chapter we explore the interpretation of STM images with atomic resolution of pure transition-metal surfaces. Being able to image a surface on the atomic scale has but recently[1] been the speciality of the STM. To interpret these STM images unambiguously is of great importance for the studies of new materials since the exact atomic structure is critical for many surface properties. Experience over the past 10 years has proven that the knowledge of the electronic structure is particularly important for the interpretation of atomically resolved topography images for surfaces of covalently bonded semiconductors [59–64], which show spatially oriented occupied and unoccupied dangling bonds. In this case the STM image may differ drastically from a surface topography. A crucial experimental clue for the interpretation of images on the basis of the electronic structure is provided by the dependence of the image upon tunnel voltage. The combination of voltage dependent images with theoretical electronic structure calculations developed to a successful approach for the analysis of atomically resolved images [62–67].

On the other hand for metals the conventional wisdom [22] says, that the interpretation of metal surfaces is fairly straight forward and rather simple: In metals, electrons screen the nuclear charge and thus follow to a good approximation the atomic structure. Thus areas of high and low tunneling current should be assigned to protruding atoms or atomic interstices, respectively. The STM image may correspond quite closely to a topography of the surface, even on the atomic scale. This type of interpretation has been widely used for atomically resolved STM-images of metal surfaces [68–70]. Although this argument might be true for simple metals such as Au, Al, or Cu, theoretical evidence is given here that for transition-metal surfaces and in the following chapters also for transition-metals in semiconductor (chapter 6) and noble-metal surfaces (chapter 7) the interpretation of STM images is far from being trivial.

In this chapter we discuss the (110)-surfaces of transition-metals with a bcc bulk lattice structure as an example of one-component transition-metal systems. Although

---

[1] By using the dynamic mode of the atomic force microscope true atomic resolution was demonstrated for the first time with another scanning probe microscope [3, 4]

we are limiting our analysis to these systems the presented effect, a bias-voltage dependent change of the STM-image for bcc-(110) surfaces leading to images where protrusions relate to the hollow and not the atom sites, was found also for other surface orientations. This is contradictory to common wisdom a rather probable effect (see also section 8.5). We performed the detailed analysis for the W(110) surface and comment on other materials, also ferromagnetic ones, in the last two sections.

5.1 Computational Details

A film consisting of 11 layers has been chosen to simulate the W(110)-surface using the experimental W lattice constant (a_0 = 5.972 a.u.). No vertical relaxation of the surface has been included, since it is experimentally known to be less than 2% [71]. For the exchange-correlation potential the local density approximation in the parametrization by Moruzzi, Janak, and Williams [72] has been applied. The basis set used for the valence states consists of about 100 augmented plane waves per atom in the unit cell. Non-spherical terms in the potential, charge density and wave functions are expanded within the muffin-tin spheres with radius R_{MT} = 2.456 a.u. up to $l_{max} \leq 8$. The self-consistent electronic structure was determined with 36 $\mathbf{k}_{\|}$-points in the irreducible part of the two-dimensional Brillouin zone (I2BZ). The integrated local density of states (ILDOS) resolved over the 2D-BZ has been analyzed using 630 $\mathbf{k}_{\|}$-points in the I2BZ. All star coefficients and by this also the STM-images and corrugation amplitudes were calculated on this $\mathbf{k}_{\|}$-point basis.

Calculations of Ta(110) were performed with the same parameters as in the case of W(110) using the experimental lattice constant of Ta (a_0 = 6.25 a.u.) and a muffin-tin radius of R_{MT} = 2.65 a.u.

Calculations of ferromagnetic bcc Fe(110) were carried out employing the local spin density approximation. The Fe(110)-surface was described by a 15 layer Fe film and the theoretically determined lattice constant of a_0 = 5.23 a.u., determined by minimization of the total energy with respect to the lattice constant. A muffin-tin radius of R_{MT} = 2.151 a.u. was chosen. All other parameters are identical to those of the W(110) calculation.

The vacuum energy-parameter ϵ_v was set close to the Fermi energy E_F. We tested the influence of the energy parameter on the LDOS at the position of the tip (z_0 = 5 Å). Setting ϵ_v to the Fermi energy E_F did not change the LDOS significantly.

5.2 STM-Images of W(110)

The experimental data were measured with a commercial ultra-high vacuum (UHV)-compatible scanning tunneling microscope (Micro-STM, Omicron) operated in a home-built UHV chamber with a base pressure in the low 10^{-11} torr range. The chamber was equipped with facilities for substrate heating by electron bombardment and a combined LEED/Auger-optic for checking surface crystallographic order and cleanliness of the sample prior to imaging with the STM. We prepared the W(110) single crystal by cycles of heating in an oxygen atmosphere ($p_{\mathrm{Ox}} = 1 \times 10^{-7}$ torr) for 30 min and subsequent flashing up to 2600 K [73]. Imaging was carried out in constant current mode at room temperature. Typically, when trying to obtain atomic resolution images we took 50 Å scans with a 0.1 Å per pixel increment. The piezo-tube scanner was calibrated on highly–orientated pyrolytical graphite (HOPG) and Si(111)-7 × 7 *ex-* and *in situ*, respectively.

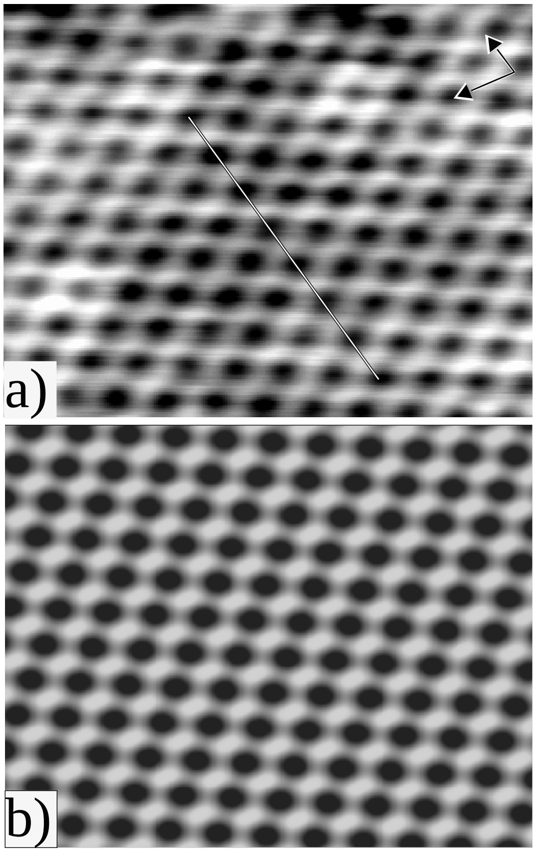

Figure 5.1: Comparison of experimental and calculated STM-image. a) Atomically resolved clean W(110)-surface at a bias voltage of about 40 mV and a tunneling current of about 10 nA. The scan area is 33 Å × 25 Å. b) Calculated ILDOS at a distance of 5 Å above the surface atoms in an energy range equivalent to a). Line-section as indicated in a) is presented in Fig.5.3.

Figure 5.1a shows a 33×25 Å^2 constant current topography of the W(110)-surface taken at a bias voltage of about +40 mV and a tunneling current of 10 nA. This image shows atomic scale corrugation appearing as an equidistant array of black interstices and nets of protrusions. The length scale and orientation of the arrays are consistent with a p(1 × 1) unit cell of W(110), which suggests that the observed corrugations are associated with the positions of the W atoms. The features of this image where typical of those taken at different locations on the surface.

Fig. 5.1b displays the calculated ILDOS at a distance of 5 Å from the surface atoms in the energy range of $(E_F, E_F + 50$ meV). This tip-surface distance is a typical value for which little tip-surface interactions is expected. We find a good agreement between experiment and theory. Both images show a pattern of dark spots with the symmetry of the 2D surface unit cell. Looking more carefully one finds also a pattern of bright spots, with the same symmetry, which are connected by feeble fuzzy-lines. Although the atomic resolution of the STM-image can already be deduced by the symmetry and lateral scale of the pattern, it is *a priori* not clear whether the bright or the dark spots or none of them correspond to the atomic sites. From the calculated image we find that at this particular bias voltage the interpretation of the STM image is indeed in line with the intuitive assumption that large tunnel current (bright spots) corresponds to the atomic sites. The dark spots correspond to the hollow sites of the (110)-surface unit cell. To our knowledge the presented STM-image is the only experimental evidence of an atomically resolved STM-image of the W(110)-surface to date. Images at other particularly negative bias voltages could not be obtained in this experiment and other results are not known to us.

5.3 Voltage Dependent Corrugation Reversal

On the other hand, STM images were recalculated for different bias voltages. We found a surprising result: depending on the bias voltage we predict that sites of high tunneling current correspond to the hollow sites or interstitial sites, respectively, and sites of low tunneling current correspond to the atom positions, e.g. *vice versa* to the results of Fig. 5.1.

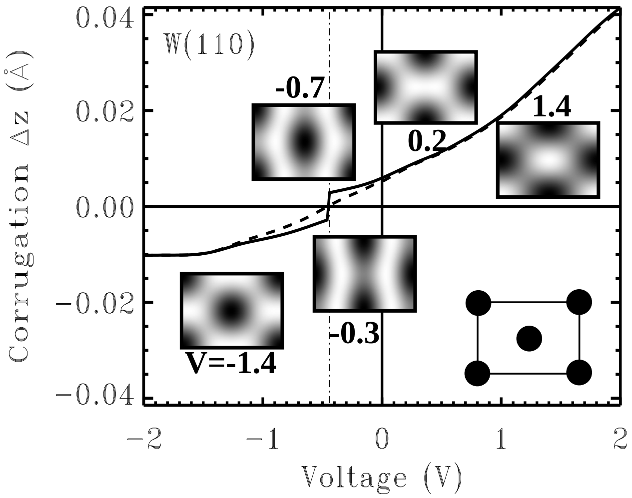

Figure 5.2: Dependence of the corrugation amplitude Δz, on the bias voltage of the calculated STM-image of W(110). Insets show the surface unit-cell (bottom right) with atomic sites marked by dots and typical STM-images calculated for different bias voltages V. The full line displays $\Delta z = z_{max} - z_{min}$, calculated by Eq. (4.72), between the lateral points $\mathbf{r}_{\|}$ of maximum and minimum corrugation within the unit cell. The dashed line displays $\Delta z = z_{atom} - z_{hollow}$, the corrugation measured between the position of the atom and the hollow site. All results are calculated at a distance of $z_0 = 4.6$ Å. Area of dark grey scale means small tunneling current.

This corrugation reversal is documented in Fig. 5.2 at a distance $z_0 = 4.6$ Å from the surface. The maximum corrugation amplitude $\Delta z = z_{max} - z_{min}$ between the lateral points $\mathbf{r}_{\|}^{max}$ and $\mathbf{r}_{\|}^{min}$ of maximum and minimum tip–sample distances is plotted as function of the applied bias voltage V together with the corrugation amplitude

$\Delta z = z_{atom} - z_{hollow}$ measured as difference between the tip–sample distances at the position of the atom and the hollow site.

In the case of $V > 0$, corresponding to the bias voltage in Fig. 5.1, we determined a positive corrugation amplitude of the order of 0.01 Å, which rises at higher voltages up to 0.04 Å. The positive sign of the corrugation amplitude means that atoms are imaged as protrusions (normal image) and representative topography images of the rectangular surface unit cell are shown in Fig. 5.2 as insets for voltages of 0.2 and 1.4 V. In the case of high negative voltages ($V < -0.9$ V) we find that the image is reversed and hence the sign of the corrugation amplitude is negative. The absolute value is of the same order as in the positive voltage regime. A typical image is shown as an inset in Fig. 5.2 ($V = -1.4$ V). Comparing the insets at positive voltage and high negative voltage, the effect of image-reversal is quite apparent (see the 2D unit cell as reference).

In the intermediate voltage regime, in which the corrugation reversal occurs, the images display a pattern of bent stripes parallel to the short side of the rectangular unit cell. Starting from a voltage with a normal image (i.e. +1.4 V) and reducing the bias voltage continuously there is a gradual change and absolute maxima change to local maxima at the positions of the atoms in the intermediate voltage regime. At a voltage of about $V = -0.4$ V even the local maxima have disappeared. The change is also pointed out by the dashed line in Fig. 5.2, which shows the difference Δz between an atom position and a hollow site of the unit cell and does not coincide with the corrugation amplitude. The analogous discussion occurs starting with a reversed image at large negative voltages, but in this case absolute maxima change to local maxima at the hollow position (see inset in Fig. 5.2 for $V = -1.4$ V and $V = -0.7$ V).

The voltage, which can be identified as the border between normal and reversed image, is about −0.4 V. However, this is not an absolute number since it changes with the distance z_0, which corresponds experimentally to the chosen constant current. The trend is, that for separations larger than $z_0 = 4.6$ Å the critical voltage rises linearly. At a distance of 7.2 Å it is equal to 0 V.

Obviously, these observations are in contradiction to conventional wisdom that on metal surfaces there is a one to one correspondence between high tunnel current and atom positions. The effect of image reversal makes the determination of atomic sites by the STM image rather difficult. Finally we would like to stress one more point: In the transition regime of image-reversal at bias voltages between −0.7 V and 0 V, the corrugation amplitude becomes extremely small and we speculate that this might be the origin of the experimental difficulties in resolving the W(110)-surface with atomic resolution at negative bias voltage.

5.4 Corrugation Amplitude

Figure 5.3 shows a typical corrugation profile taken along the [001] direction of the W(110)-surface as indicated by a straight line in Fig. 5.1a. The experimental value for the corrugation amplitude is about 0.13 Å. This is about one order of magnitude

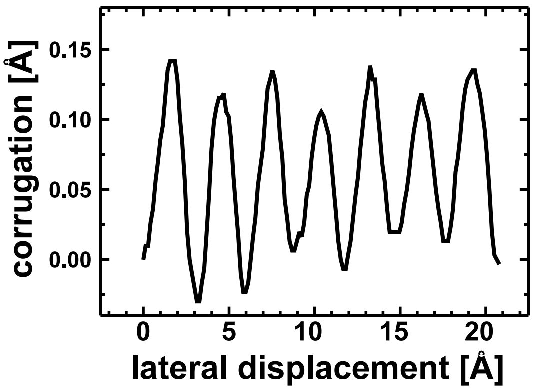

Figure 5.3: A corrugation profile taken by a line scan along the [001] direction of the W(110) surface as indicated by a straight line in Fig.5.1a using scanning parameters as given in Fig.5.1.

larger than the theoretically determined corrugation in Fig. 5.2, which is on the order of 0.01 Å at a distance z_0 from the surface of 4.6 Å.

We attribute this tiny and in reality by STM non-detectable corrugation amplitude to the application of the Tersoff-Hamann model [6], which is based on s-like tip wave-functions (see section (4.4.1)). As also described in chapter 4, Chen [11] has extended this model to arbitrary tip orbitals. We have applied the *derivative rule* (section (4.4.2)) to the calculated STM-image of Fig. 5.1b and extracted new corrugation amplitudes, using the same procedure as before. In addition to the s-orbital, which corresponds to the description of Tersoff and Hamann, the tip-states with p_z- and d_{z^2}-character are considered.

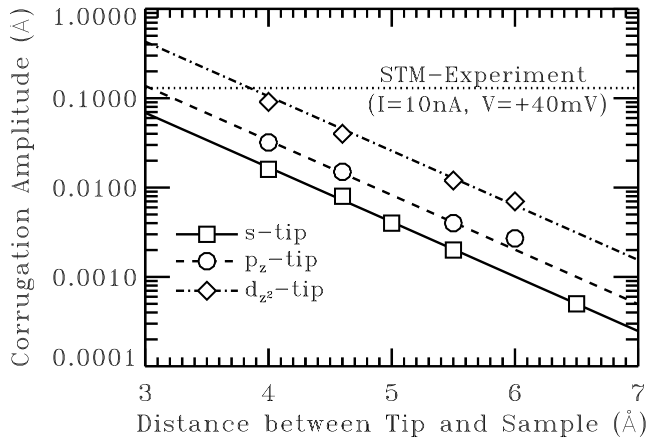

Figure 5.4: Corrugation amplitude as function of the tip-sample distance for three different orbital symmetries of the tip state. Using Chen's derivative rule [10] the corrugation amplitudes for s, p_z and d_{z^2} type tip-orbitals have been calculated at a bias voltage of +0.1 V. The experimental corrugation amplitude obtained from the STM-image of Fig.5.1a is given by the horizontal dotted line. Symbols indicate calculated values. The full line is a linear interpolation of the values calculated for an s type tip. The dashed and dotted-dashed lines are given by the interpolated values of the s-type tip multiplied by Chen's enhancement factors [10] for a p_z- and d_{z^2}-tip, respectively.

Fig. 5.4 shows the corrugation amplitude as function of the tip-sample distance for the three different tip orbitals. The corrugation amplitudes were calculated at different tip-sample distances for a fixed bias voltage of +0.1 V. The linear scaling of the corrugation amplitudes as function of the tip-sample distance in the semi-logarithmic plots describes the exponential decay of the tunneling current with the distance. Comparing the corrugation amplitudes of a p_z- or d_{z^2}-state tip with that of an s-state one, the amplitudes are larger by factors of 2 or 6.25, respectively, as predicted by Chen's derivative rule [11]. These results are consistent with the experimentally measured corrugation amplitude (cf. Fig. 5.3) of 0.13 Å, added in Fig. 5.4 as dotted horizontal line, for a tip-sample separation of about 4 Å. This distance is already quite small, but it is consistent with an estimation of the experimental tip-sample separation by means of the tunnel conductance:

$$G = \frac{I}{U} = \frac{2e^2}{h} \exp\left[-2\kappa(z - z_{contact})\right]. \tag{5.1}$$

In Eq. (5.1) we make the assumption that the tunnel conductance becomes equal to the conductance quantum at (single atom) contact $z = z_{contact}$ and that it decreases exponentially with increasing distance from the surface. Applied to the tunneling conditions of Fig. 5.1a, this leads to a value of $z - z_{contact} = 2.4$ Å. Taking $z_{contact}$ as the lattice plane separation in tungsten of 1.6 Å [$\langle 100\rangle$-directions] to 2.2 Å [$\langle 110\rangle$-directions] one ends up with a tip-sample separation of $4.0 - 4.6$ Å. This result is in accordance to our estimation comparing the calculated and measured corrugation amplitude.

The orbital character of the tip-state depends much on the tip material used. Experiments discussed in section (5.2) have been carried out with W tips. For W tip atoms the tunneling is mostly due to d-electrons at the Fermi energy. This has also been confirmed by electronic structure calculations of Ohnishi et al. [52] on W clusters, which makes the assumption of d_{z^2} rather realistic.

We may draw one important conclusion from this investigation: The corrugation reversal shown in Fig. 5.2, and calculated for an s-state tip, should be also scaled-up by the enhancement factor [11] and thus should be detectable by STM-experiments.

Although more realistic tip-orbitals magnify the corrugation amplitude we found, however, that the STM-images obtained from p_z- or d_{z^2}-state tip orbitals do not differ qualitatively from the s-tip images. Therefore, we can safely restrict the further discussion and analysis on the corrugation reversal to the model of Tersoff and Hamann.

5.5 Analysis of Corrugation Reversal

To give an explanation of the image-reversal on the basis of the electronic structure we start with the Fermi surface of W(110) as displayed in Fig. 5.5. Fig. 5.5a shows the centered rectangular 2D-BZ of the bcc-(110)-surface and in Fig. 5.5b calculated electronic states at the Fermi energy are marked. Small open circles distinguish bulk-like states from surface localized states represented by full dots. One finds three surface resonance bands and a surface-state band which have also been studied experimentally by photoemission [74]. The experimentally observed surface resonances and surface state at the Fermi surface were explicitly mapped [74] over the 2D-BZ and a comparison shows a good agreement to our calculation (cf. Fig. 5.5).

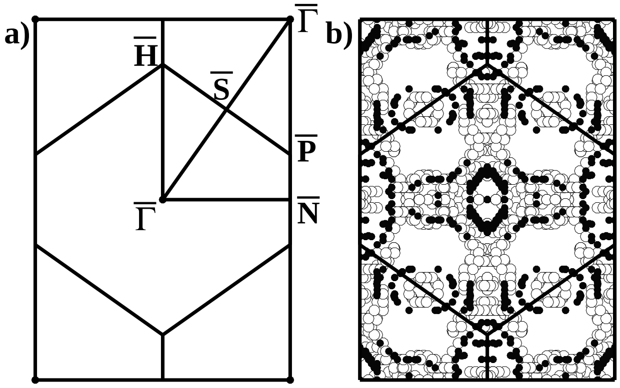

Figure 5.5: Fermi surface of W(110). a) 2D-Brillouin zone corresponding to the centered rectangular unit cell of bcc transition-metal (110) surfaces (e.g. W(110)). b) States of W(110) at the Fermi energy. Open circles mark bulk states while filled circles represent surface states or resonances with a localization (expectation value) of either more than 10% within the vacuum region or more than 45% within the muffin-tin spheres of the surface atoms including the vacuum region or more than 65% within the surface atoms, subsurface atoms and the vacuum region.

The surface state surrounds the $\bar{S}$ point of the Brillouin-zone while one resonance is around $\bar{\Gamma}$, and around $\bar{N}$, and a third one is stretching along the axes $\bar{\Gamma}\bar{H}$ and $\bar{\Gamma}\bar{N}$. In order to see the dispersion of these different surface localized states Fig. 5.6 shows the bandstructure in $\bar{\Gamma}\bar{S}$-direction. One recognizes the surface state located in an energetic gap of bulk bands as well as two types of resonances. The surface-state band has its energetic minimum at -1.3 eV and from a more detailed analysis it can be concluded that its character changes from predominantly d-character at the minimum to a p-type state at the zone boundary. This change occurs gradually and states near the Fermi energy have comparable contributions of both types with a small admixture of s-electrons. While the resonance around $\bar{\Gamma}$ exhibits a rather flat dispersion, the resonance crossing the Fermi energy approximately half way to $\bar{S}$, rises quite steeply. Thus, there is a considerable number of possible electronic states responsible for the observed phenomena and one has to understand the relative importance of these states as well as their quantitative contribution to the corrugation inversion. In order to find those states, which contribute most to the corrugation in STM-images we are looking at the z-dependence of the wave functions at different points in reciprocal space. Following Sacks et al. [57] we begin the analysis in terms of the simplified model introduced by Eqs. (4.63–4.65). In this model we can see, that the $\mathbf{k}_{\|}$- and $\mathbf{G}_{\|}^{s}$-resolved contribution to the surface topography at the surface plane $z = 0$ is detected at the distance z after $\mathbf{k}_{\|}$- and $\mathbf{G}_{\|}^{s}$-dependent weighting expressed by Eq. (4.63). Consequently, waves with the smallest lattice vectors $\mathbf{G}_{\|}^{s}$ and the highest energy ϵ will reach out furthest into the vacuum and contribute most to the STM image. In Fig. 5.7 the first three star functions $\phi_{s}^{2D}(\mathbf{r}_{\|})$ are explicitly shown

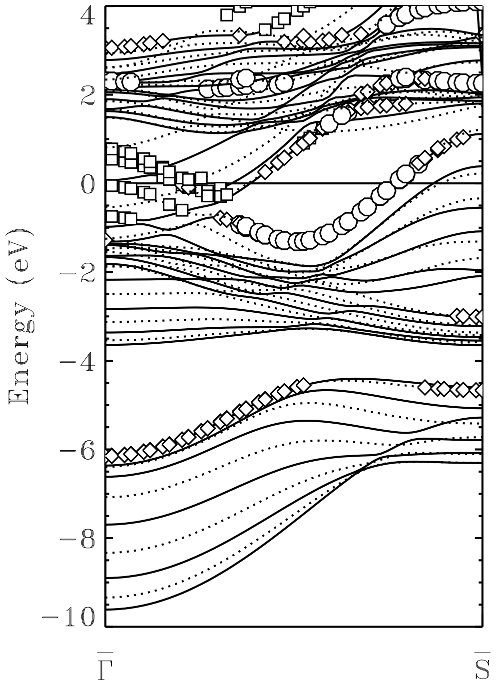

Figure 5.6: Calculated surface bandstructure of W(110) along the $\bar{\Gamma}\bar{S}$-direction of the Brillouin zone. States marked with square, dot or diamond are localized with more than 5% in the vacuum, more than 60% within the vacuum plus the muffin-tin sphere of the surface atom, or more than 70% within the vacuum plus the muffin-tin spheres of the surface and subsurface atoms, respectively. The Fermi energy E_F defines the energy zero.

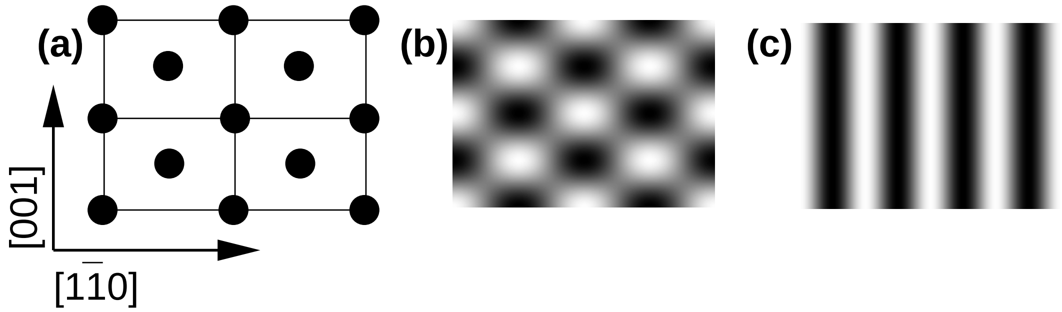

Figure 5.7: Star functions for a bcc (110) surface, i.e. a rectangular-centered two-dimensional unit cell. (a) 2D unit cell. The first star function is a constant. (b) corresponding second star function displaying the atoms as protrusions. Note, that the sign of the expansion (star) coefficient can be negative leading to an inversion of this image. (c) third star function showing parallel stripes along the short axis of the rectangular cell.

for a bcc-(110) surface lattice, corresponding to the three smallest stars (s=1,2,3) of reciprocal lattice vectors $\mathbf{G}_\parallel^s$, $\mathbf{G}_\parallel^{(1)} = (0,0)$, $\mathbf{G}_\parallel^{(2)} = (1,\sqrt{2})$, $\mathbf{G}_\parallel^{(3)} = (2,0)$, expressed in units of $\sqrt{2}\pi/a_0$, with a_0 being the lattice constant:

$$\phi_1^{2D}(\mathbf{r}_\parallel) = 1 \tag{5.2}$$

$$\phi_2^{2D}(\mathbf{r}_\parallel) = \frac{1}{2}[\cos(\mathbf{G}_{\parallel,1}\mathbf{r}_\parallel) + \cos(\mathbf{G}_{\parallel,2}\mathbf{r}_\parallel)] \tag{5.3}$$

$$\phi_3^{2D}(\mathbf{r}_\parallel) = \cos[(\mathbf{G}_{\parallel,1} + \mathbf{G}_{\parallel,2})\,\mathbf{r}_\parallel]. \tag{5.4}$$

$\mathbf{G}_{\|,1}$ and $\mathbf{G}_{\|,2}$ are the two-dimensional reciprocal lattice vectors

$$\mathbf{G}_{\|,1} = \frac{\sqrt{2}\pi}{a_0}(1,\sqrt{2}) \quad \text{and} \quad \mathbf{G}_{\|,2} = \frac{\sqrt{2}\pi}{a_0}(1,-\sqrt{2}). \tag{5.5}$$

The $\mathbf{k}_\|$-dependent filtering effect of $\exp\left(-\kappa^n_{\mathbf{k}_\|} z\right)$ on $n^s_{\nu\mathbf{k}_\|}(z)$ is analyzed graphically in Fig. 5.8a-c for these three smallest stars. Fig. 5.8a-c display the exponential decay of $n^s_{\mathbf{k}_\|}(z_0\,|\,E_F)$ in terms of grey scale plots over the 2D Brillouin-zone calculated for the Fermi energy, $\epsilon = E_F$, at a tip-sample distance of $z_0 = 4.6$ Å. In these plots the electronic structure has been explicitly ignored by replacing in Eq. (4.65) all coefficients $c^n_{\nu\mathbf{k}_\|}$ by a constant and replacing $\kappa^n_{\nu\mathbf{k}_\|}$ by $\kappa^n_{\mathbf{k}_\|}(E_F)$. We used $E_F = -5.69$ eV as calculated for our W(110)-film. These results need to be compared to Fig. 5.8d-f, which show the actual coefficients $n^s_{\nu\mathbf{k}_\|}(z_0)$ for the first three stars, including the electronic structure, calculated according to Eq. (4.58) by FLAPW calculations in the energy interval (E_F−0.2 eV,E_F). On the basis of Fig. 5.8 we can discuss the importance of various contributions to the tunneling current over the $\mathbf{k}_\|$-space.

The first term $n^{(1)}_{\mathbf{k}_\|}$ corresponding to $\mathbf{G}^{(1)}_\| = \mathbf{0}$ leads to an $\mathbf{r}_\|$ independent, i.e. laterally constant contribution to the tunneling current (cf. Eq. (5.2)). $n^{(1)}_{\mathbf{k}_\|}$ is always positive. It does not make any contribution to the corrugation pattern but it adds to the total tunneling current (total LDOS) and thus it is important in scanning tunneling spectroscopy. By Fig. 5.8a one concludes that this star coefficient is dominated by states near the center of the BZ as is commonly accepted. Comparing Fig. 5.8a to Fig. 5.8d, it is clear, that the particular electronic structure of the surface still leads to some deviation of the simple picture. One can recognize the surface resonance around $\bar{\Gamma}$ as well as a part of the resonance which stretches along the axes of $\mathbf{k}_\|$-space (see Fig. 5.5 for comparison). The area in the BZ which is of importance for $n^{(1)}_{\mathbf{k}_\|}$ is thus still influenced by the particular electronic structure.

The decay of the second star coefficient $n^{(2)}_{\mathbf{k}_\|}$ of the LDOS is displayed in Fig. 5.8b. The STM topography pattern resulting from the second star function (see Eq. (5.3)) depends on the sign of the star coefficient and contributes to corrugation or anti-corrugation as seen in Fig. 5.2 for voltages $V = +1.4$ V or $V = -1.4$ V, respectively. One finds that in this case the main contribution results from states around $\bar{\mathrm{S}}$. From Fig. 5.8e we analyze the contribution to the STM-image made by different states in the BZ. Fig. 5.8e displays positive $n^{(2)}_{\mathbf{k}_\|}$ coefficients in yellow color and red for coefficients with negative sign. Now one can easily understand the different role of the surface resonance and the surface state on the corrugation. We find that all bulk states and all surface resonances have positive $n^{(2)}_{\mathbf{k}_\|}$ coefficients and contribute to a normal STM image, consistent with the general wisdom for metal surfaces that electrons try to screen the positive charge of the nucleus and the STM topography and the atom position should coincide. The surface states located around $\bar{\mathrm{S}}$ are the only states with negative $n^{(2)}_{\mathbf{k}_\|}$ and are the single source of the anti-corrugation of the STM image. In addition the negative $n^{(2)}_{\mathbf{k}_\|}$ contributes to the total $n^{(2)}$ by a large weighting factor because of its position close to $\bar{\mathrm{S}}$ while the resonances are of rather

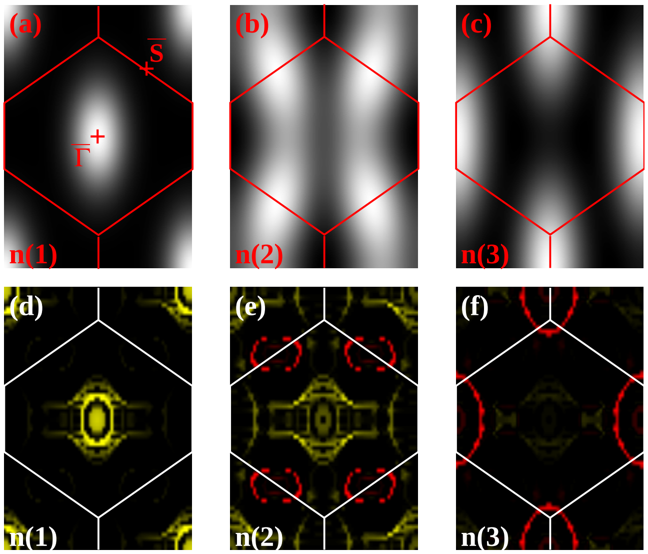

Figure 5.8: Star coefficients in $\mathbf{k}_{\|}$-space at a tip-sample distance z_0 of 4.6 Å. Panels a) to c) show the first three star coefficients decay function as calculated by equation (4.65) with $E_F = -5.69$ eV and d) to f) first three star coefficients of the FLAPW-calculation for W(110) in the energy range $(E_F - 0.2\text{ eV}, E_F)$. Images d) to f) have been calculated using 630 $\mathbf{k}_{\|}$-points in the I2BZ. Yellow shows positive coefficient values while red marks negative values.

small value due to the little weight of $n^{(2)}_{\mathbf{k}_{\|}}$ at the $\bar{\Gamma}$ or $\bar{\text{H}}$-point. The resonance along the axes $\bar{\Gamma}\bar{\text{H}}$ and $\bar{\Gamma}\bar{\text{N}}$ contributes the highest values among the normal states.

The actual STM-image for a chosen bias voltage depends upon the integral value of the second star coefficient of the LDOS over the 2D-BZ. This quantity, $n^s(z_0 \,|\, \epsilon)$, is displayed in Fig. 5.9 for the first three star coefficients as a function of energy at a tip-sample distance of $z_0 = 4.6$ Å. We see $n^{(1)}(\epsilon)$ is always positive, since it represents the total charge density integrated over the 2D unit cell. The second star coefficient of the LDOS $n^{(2)}(\epsilon)$ is three orders of magnitude smaller than $n^{(1)}(\epsilon)$ and changes sign at an energy of about -0.2 eV. Thus for energies below -0.2 eV the negative contribution of the surface states is higher in absolute value than the contribution of all other states, which is positive. Since the tunneling current at a certain bias voltage V is given by an energy integral of the LDOS between E_F and $E_F + eV$ (Eq. (4.28)), the corrugation does not change its sign until a voltage of -0.4 V is reached (see Fig. 5.2). Then the positive values of $n^{(2)}$ states between $E_F - 0.2$ eV and E_F are compensated by negative values between $E_F - 0.4$ eV and $E_F - 0.2$ eV. Reducing the applied voltage below -0.4 V results then in an image reversal. A maximal negative value of $n^{(2)}(z \,|\, \epsilon)$ is reached at -1.3 V, which is the minimum of the surface state band (Fig. 5.6) consistent with the interpretation that the surface state is responsible for the anti-corrugation. The change in sign of the second star coefficient and its rise for energies above E_F is due to the competition between the surface state and the resonance.

Finally the third star coefficient is plotted in Fig. 5.8c and f. The z-dependent $\mathbf{k}_{\|}$-

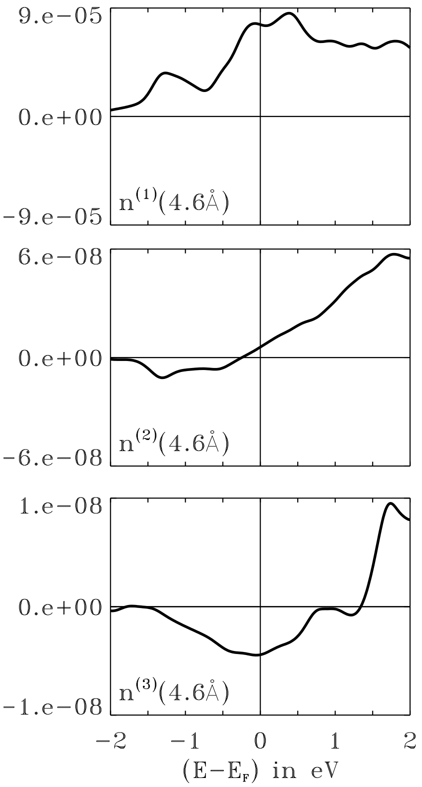

Figure 5.9: Star coefficients integrated over the 2D Brillouinzone as a function of energy at $z_0 = 4.6$ Å. a) $n^{(1)}(z|\epsilon)$, b) $n^{(2)}(z|\epsilon)$ and c) $n^{(3)}(z|\epsilon)$. $n^{(1)}(z|\epsilon)$ is always positive since it resembles the LDOS. The sign of $n^{(2)}(z|\epsilon)$ decides whether the STM-image displays a corrugation or anti-corrugation pattern. The value of $n^{(3)}(z|\epsilon)$ is non-neglectable only in the energy range that shows the change of sign for $n^{(2)}(z|\epsilon)$. Compare Fig.5.2.

point filtering shown in Fig. 5.8c projects out states near the $\bar{\mathrm{N}}$–point. The emphasis on these states becomes also evident in the plots including the electronic structure (Fig. 5.8f). One observes the strong influence of the resonance around the $\bar{\mathrm{N}}$–point on this star coefficient of the LDOS. The third star coefficient can become positive or negative, but the third star function (see Eq. (5.4) and Fig. 5.7) is simply a cosine function in the $[1\bar{1}0]$-direction of the surface and hence it is not responsible for the effect of corrugation reversal. Nevertheless, the actual FLAPW calculation demonstrates that $n^{(2)}$ and $n^{(3)}$ can be of comparable value. This happens for the energy regime between -0.4 eV and 0 eV, when the second star coefficient becomes quite small (see Fig. 5.9) or zero due to the compensation between the surface state and the resonance. In this regime the superposition of the star function $\phi_2^{2D}(\mathbf{r}_\parallel)$ and $\phi_3^{2D}(\mathbf{r}_\parallel)$ leads to new images exhibiting patterns of bent stripes from the cosine function $\phi_3^{2D}(\mathbf{r}_\parallel)$ (see patterns in Fig. 5.2 at the voltages -0.7 V and -0.3 V). Stars of even higher order do not contribute significantly anymore because the average value of the star coefficients n^s decreases exponentially with the length of the star vector as can be concluded from equation (4.65) and is also evident from Fig. 5.9.

In Fig. 5.10 the charge density contours in real space of typical surface states and surface resonances along the $\bar{\Gamma}\bar{\mathrm{H}}$ and $\bar{\Gamma}\bar{\mathrm{N}}$ lines are displayed. Fig. 5.10a and b show cross sections through the W(110)-film of states lying on the surface-state band. One finds a charge density between surface atoms which spills into the vacuum and causes the anti-corrugated image. The behavior of the resonance states shown in Fig. 5.10c and d is quite different. The d_{xz}- and d_{z^2}-type states lead to vacuum LDOS located at the atom and thus to a normal STM-imaging of atomic sites.

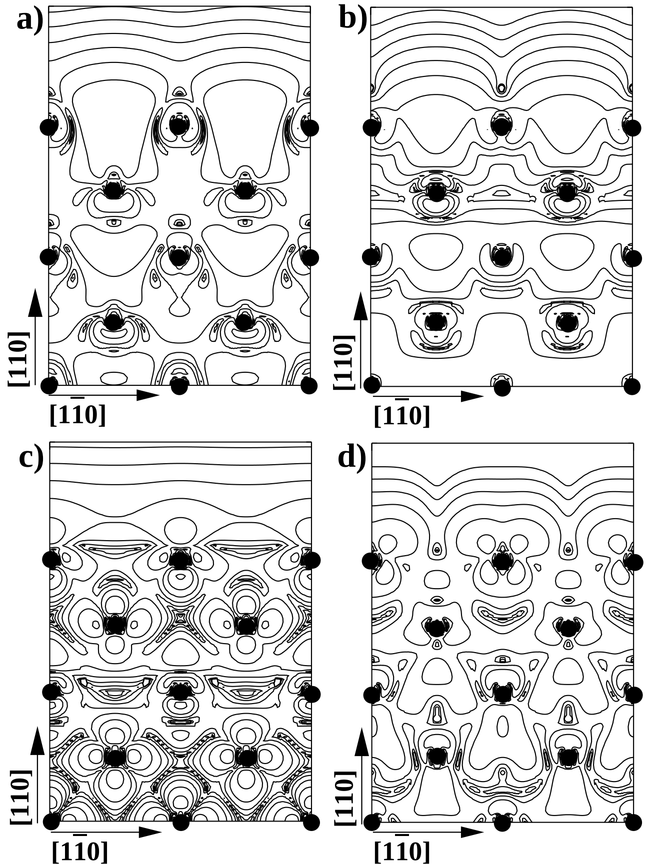

Figure 5.10: Single-state valence charge-density contour maps, $n_{\mathbf{k}_{\parallel}\nu}(\mathbf{r})$ for W(110) on the (001) plane. Contours start from 10^{-7} electrons/(a.u.)^3 and increase by a factor 4. Panels a) and b) show plots for states on the surface-state band at $\mathbf{k}_{\parallel} = (0.35, 0.39\sqrt{2})\pi/a\sqrt{2}$, $\epsilon_\nu = -0.05$ eV and $\mathbf{k}_{\parallel} = (0.58, 0.38\sqrt{2})\pi/a\sqrt{2}$, $\epsilon_\nu = -0.11$ eV, respectively. Panels c) and d) show plots for states on the surface-resonance bands at $\mathbf{k}_{\parallel} = (0.15, 0.18\sqrt{2})\pi/a\sqrt{2}$, $\epsilon_\nu = +0.04$ eV and $\mathbf{k}_{\parallel} = (0.15, 0.61\sqrt{2})\pi/a\sqrt{2}$, $\epsilon_\nu = +0.04$ eV, respectively. Atom positions are marked by filled circles.

In order to understand the formation of the charge density contour of the surface state as exhibited in Fig. 5.10a or b and the surface state itself from the bulk bands we follow the formation of the W(110)-surface from the bulk by pulling apart the W bulk in discrete steps long the [110]-direction. We have chosen a (110) unit cell of 4 (110)-planes in z-direction and increased the separation between these unit cells by 0.5 Å, 1.0 Å and 2.5 Å along the z-direction starting from the bulk separation. At each separation we calculated the projected bandstructure and confirmed that the surface-state band described above is a split-off state from binding bulk states and is lifted in energy. The evolution of the charge density contour associated with a particular surface state along with the formation of the surface is shown in Fig. 5.11 for the different unit-cell separations. In the bulk, the state under discussion is a bonding state with bonding charges between the atoms along the short side of the centered rectangular [the $\langle 001\rangle$-directions] unit cell of the bcc-(110) surface. Along the long side of the unit cell [the $\langle 1\bar{1}0\rangle$-directions] there are charge density zeros between the atoms and it is thus an anti-bonding state along the long side of the unit cell and perpendicular to the surface. As the surface is formed, the bond strength between atoms at the forming surface is increased, the symmetry of the forming surface state changes, the hybridization of this state with the underlying substrate decreases und leads to a de-hybridization of subsurface charge, the charge density of the so formed surface state releases energy by spilling out into the vacuum and causes the anti-corrugation. The behavior of the surface state reminds at the formation of dangling bond states of covalently bonded semiconductors with directed sp^3 hybrids, which are also responsible for anti-corrugation. For the surface resonance states displayed in Fig. 5.12 the picture is quite different. The charge density is located at the atom and the symmetry does not change by the formation of the surface and a resonance state supports a normal image.

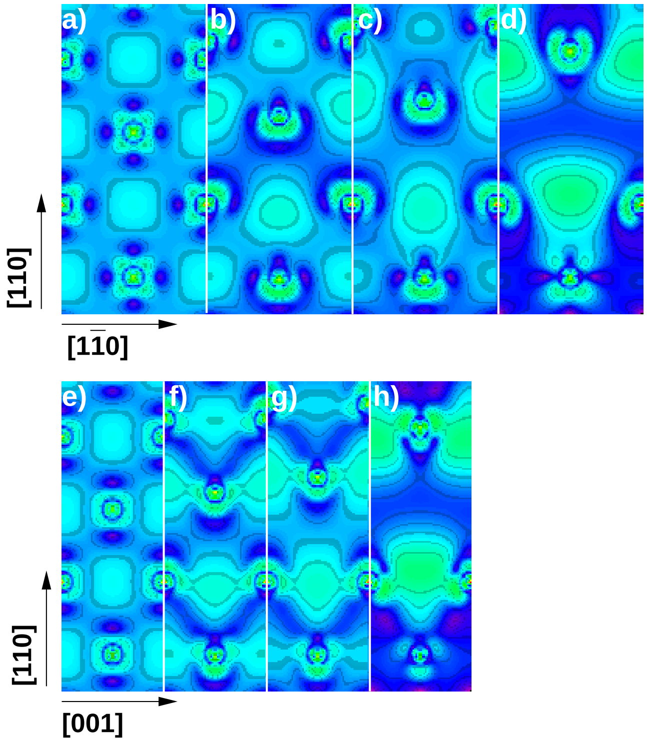

Figure 5.11: Change of the surface state charge density when a W(110)-surface is created from a bulk calculation. A single state of the band at $\mathbf{k} = \sqrt{2}\pi/a_0\,(0.35, 0.35\sqrt{2}, 0.35)$ with energy $\epsilon_{\mathbf{k}\nu} = E_F - 1.2$ eV is displayed. a)-d) in [1$\bar{1}$0]-direction: a) bulk, b) +0.5 Å, c) +1.0 Å and d) +2.5 Å. e)-h) in [001]-direction: e) bulk, f) +0.5 Å, g) +1.0 Å and h) +2.5 Å.

In order to confirm our interpretation of the formation of the surface-state band as being partly due to the de-hybridization of subsurface states in favour to the surface state, which gives the characteristic charge density features leading to anti-corrugation in STM-images, we also calculated a free monolayer of W(110). In that case we expect to find no states which exhibit an anti-corrugation image since there is no subsurface layer. The bandstructure of the monolayer is presented in Fig. 5.13.

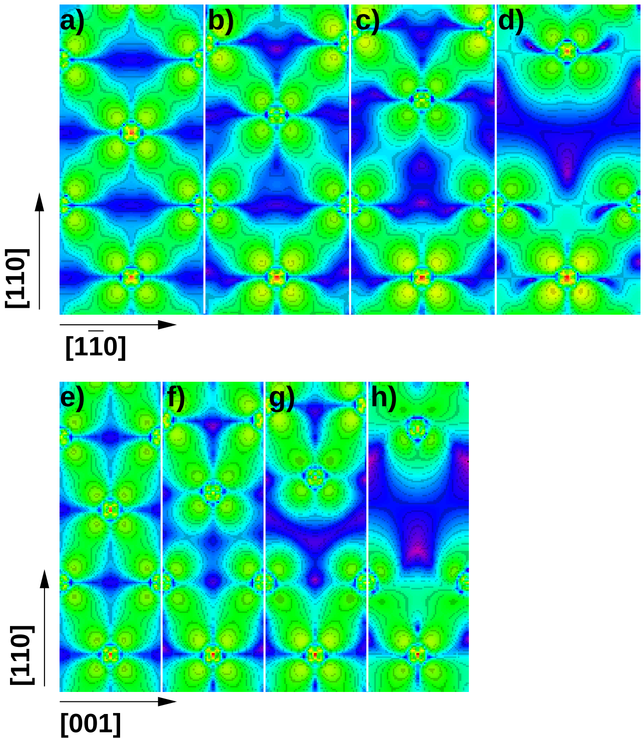

Figure 5.12: Change of the surface resonance charge density when a W(110)-surface is created from a bulk calculation. A single state of the band at $\mathbf{k} = \sqrt{2}\pi/a_0\,(0, 0.35\sqrt{2}, 0.3)$ with energy $\epsilon_{\mathbf{k}\nu} = E_F + 1.4$ eV is displayed. a)-d) in [1$\bar{1}$0]-direction: a) bulk, b) +0.5 Å, c) +1.0 Å and d) +2.5 Å. e)-h) in [001]-direction: e) bulk, f) +0.5 Å, g) +1.0 Å and h) +2.5 Å.

Comparing this bandstructure with the 11 layer calculation of Fig. 5.6 one notices that the surface-state band with its characteristic energy minimum in the middle of the $\bar{\Gamma}\bar{S}$-direction is missing. There is a band in the monolayer bandstructure with a behavior near $\bar{S}$-point (at +0.5 eV, see Fig. 5.13) similar to the surface-state band of the W(110)-surface but the calculation of the second star coefficient displays no sign reversal (not shown here). We have thus analyzed that the surface-state band, which leads to anti-corrugation in STM-images, originates from a hybridisation of surface and subsurface states. This concludes the analysis of the electronic structure with respect to the phenomena of image-reversal.

5.6 Other Transition-Metals: Nb, Mo, and Ta

It is well-known [75] that the overall form and structure of the LDOS and of the bandstructure depend on the crystal symmetry, while the actual peak positions relative to the Fermi energy, peak heights or energy dispersions depend on the crystal potential or chemical element, respectively. Thus, we speculate that the image-reversal,

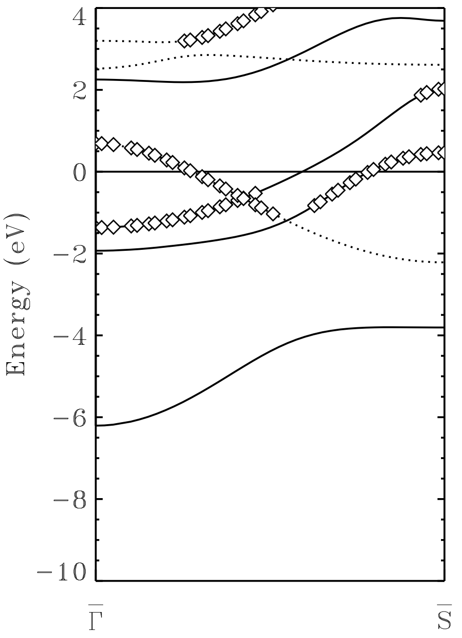

Figure 5.13: Calculated surface bandstructure of a free monolayer of W(110) along the $\bar{\Gamma}\bar{\mathrm{S}}$-direction of the Brillouin zone. States marked with a diamond are localized with more than 20% in the vacuum. The Fermi energy E_F defines the energy zero.

predicted for W(110), is a rather general phenomenon for all bcc-(110)-transition-metal surfaces although the image change may occur at different voltages depending on the metal. Therefore, we have calculated Ta(110) as an additional example of non-magnetic bcc-(110)-transition-metal surfaces. The corrugation amplitude at a distance of $z_0 = 4.6$ Å is displayed in Fig. 5.14. As for W(110) there is a corrugation reversal which in this case occurs at $V = +1.3$ V. Thus in a wide voltage regime around 0 V only anti-corrugation images will be observed. Also the change from one corrugation type to the other takes place on a much smaller voltage scale (i.e. the curve is much steeper near the critical voltage). The surface-state band responsible for the effect has its band minimum at an energy of 0.6 eV below E_F. It has shifted up by 0.7 eV compared to W, which is due to the fact that Ta has one electron less.

Mo, as another possible candidate, is isoelectronic to W and hence we expect for the Mo(110)-surface an image-reversal around E_F. Nb is isoelectronic to Ta and we estimate that the bottom of the surface-state band should be also around 0.6 eV below E_F and an image-reversal should occur around $V = +1.3$ V.

5.7 Magnetic Systems: Fe(110)

A more complicated scenario may develop for the (110)-surfaces of the magnetic bcc 3*d* transition metals Cr, Mn, and Fe. The electronic structure is spin-split by an exchange splitting, whose size is proportional to the local magnetic moment. Therefore, the image-reversal should occur twice, once for the majority states and once for the minority states. If the majority states are located below E_F and the minority states are located above E_F or a magnetic tip is used, then the observation of both anti-corrugations should become possible. In general, however, non-magnetic tips are used and electrons of one spin character dominate the tunneling current. In this case

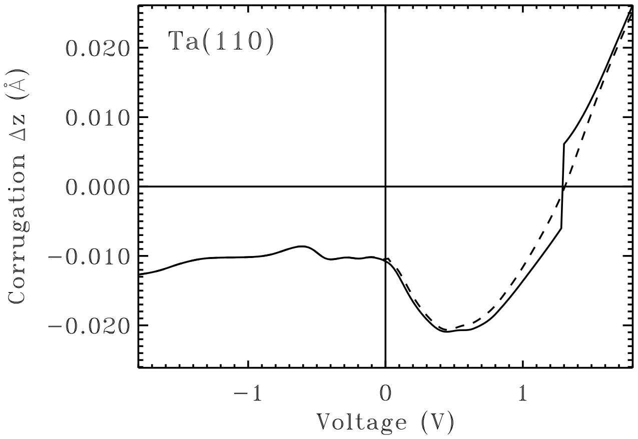

Figure 5.14: Dependence of the corrugation amplitude Δz of the Ta(110)-surface on the bias voltage. The full line displays $\Delta z = z_{max} - z_{min}$, calculated by Eq. (4.72), between the lateral points $\mathbf{r}_{\|}$ of maximum and minimum corrugation within the surface unit cell. The dashed line displays $\Delta z = z_{atom} - z_{hollow}$, the corrugation measured between the position of the atom and the hollow site. The distance from the surface was $z_0 = 4.6$ Å.

one expects only the anti-corrugation of the leading vacuum spin character. The minor vacuum spin character, which is not necessarily identical to the minority states, may contribute to a small intensity variation of the tunneling current.

To explore this further we have investigated ferromagnetic Fe(110) as a typical example of a magnetic bcc transition metal in more detail. Fe has two valence electrons more than W. Since ferromagnetic Fe has a moment of about 2 μ_B, both additional electrons occupy majority states and the number of Fe minority electrons and of W valence electrons per spin state are about the same. Therefore, similar to W, Fe minority spin states should drive the anti-corrugation effect at energies close to the Fermi energy, e.g. small bias voltage, and thus should be accessible by STM-experiments. The anti-corrugation effect driven by the majority electrons may be well below E_F and probably not accessible by STM-experiments.

We have calculated the electronic structure of ferromagnetic Fe(110). The bulk magnetic moment was determined to 2.06 μ_B in good agreement with the experimental value of 2.12 μ_B. The surface magnetic moment was enhanced to 2.35 μ_B. As expected we found a spin-split electronic structure. Looking at the LDOS of a surface Fe atom displayed in Fig. 5.15 we find an exchange splitting of about 2 eV for a surface atom. The minority spin states are the dominating spin character in the vicinity of the Fermi energy. Moreover, at E_F the majority states are mostly bulk states and the minority states are mostly surface states located in the typical bcc bonding-antibonding gap dominating the tunneling current through the vacuum barrier (cf. Fig. 5.15).

Figure 5.16 exhibits the surface bandstructures of the Fe(110) minority and majority states along $\bar{\Gamma}\bar{S}$ direction. Both are similar to the bandstructure of the W(110)-surface (cf. Fig. 5.6). In particular the surface-state band, responsible for the anti-

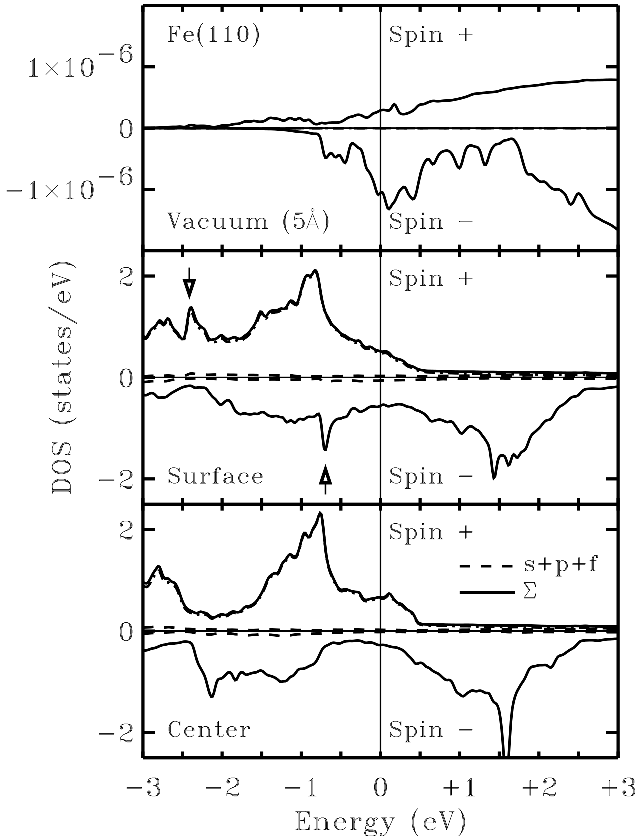

Figure 5.15: Spin-resolved density of states of ferromagnetic Fe(110) as a function of energy. Upper part of each panel displays majority states (spin +), lower part minority states (spin −). Top panel contains the DOS in the vacuum at a tip-sample distance of $z_0 = 5$ Å in a volume determined by $\delta z_0 = 1.3$ Å. Middle and bottom panel show the angular momentum decomposed density of states projected in muffin-tin spheres for surface atom and center atom, respectively. The latter corresponds to the bulk LDOS. Full line represents the total contribution while the broken line represents the insignificant amount of $s + p + f$ contribution. Arrows indicate the minimum of the surface state band. The Fermi energy is the origin of energy zero.

corrugated images of the W(110)-surface, can be found for both spin characters. For the Fe minority state, the bottom of the surface-state band is located at about −0.7 eV [76], indeed close to the value of −1.3 eV for W(110). For majority states, the bottom of the surface-state band is located at −2.4 eV [76]. The zero curvature at the bottom of the surface-state bands lead to narrow peaks in the LDOS of the surface Fe atom and the vacuum exhibited in Fig. 5.15.

Corresponding to the minority-state surface-band starting at −0.7 eV we determined the corrugation-reversal from the anti-corrugated image to the normal STM-image in the minority-state-channel at a voltage of about +0.7 V, shown in Fig. 5.17. Since in general the STM-tip is not sensitive to the spin direction of tunneling electrons, majority spin states will also contribute to an image taken at this energy.

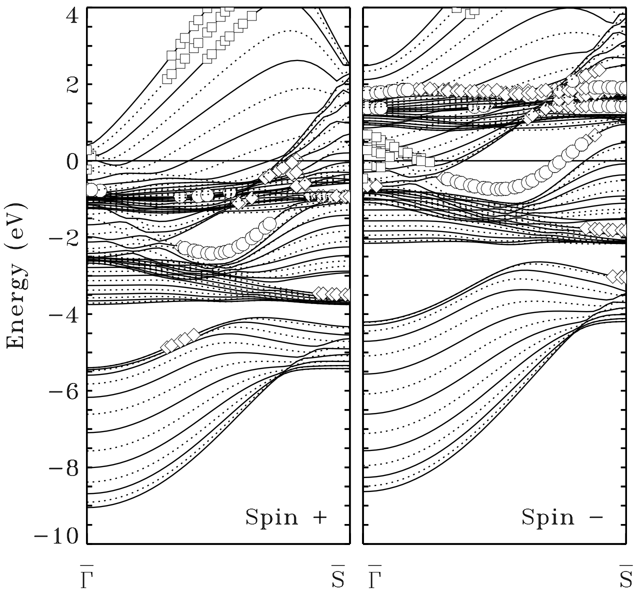

Figure 5.16: Calculated surface bandstructure of Fe(110) majority (left) and minority (right) states along the $\bar{\Gamma}\bar{S}$-direction of the 2D BZ. States marked with a square, dot or diamond are localized with more than 5% in the vacuum, more than 60% within the vacuum plus the muffin-tin sphere of the surface atom, or more than 70% within the vacuum plus the muffin-tin spheres of the surface and subsurface atoms, respectively. The Fermi energy E_F defines the energy zero.

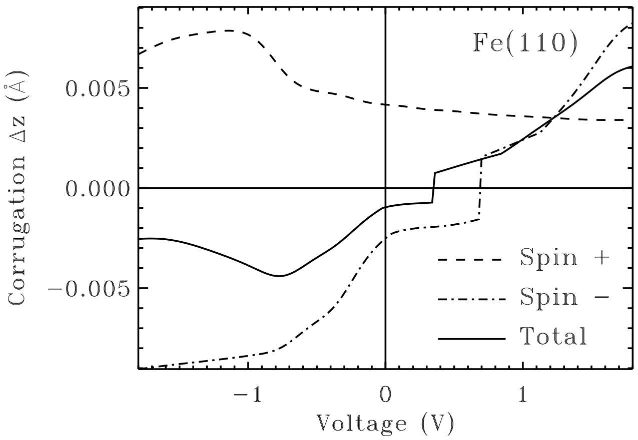

Figure 5.17: Dependence of the corrugation amplitude on the bias voltage of the ferromagnetic Fe(110)-surface. The full line displays $\Delta z = z_{max} - z_{min}$, calculated by Eq. (4.72), between the lateral points $\mathbf{r}_{\|}$ of maximum and minimum corrugation within the unit cell at a distance of $z_0 = 4.5$ Å. The sign of corrugation amplitude has been defined by the sign of the (integrated) second star coefficient. The dashed and dotted-dashed lines display the contributions of majority and minority electrons, respectively. Notice that the total corrugation amplitude is not simply the sum of majority and minority contributions.

From Fig. 5.17 we see, that for this energy range, majority electrons always lead to a normal corrugation pattern and work against the corrugation reversal caused by the minority surface state. However, their contribution to the tunneling current is much smaller than that of the minority states and the image-reversal will take place. The critical voltage at which the reversal takes place is shifted to +0.4 V. Since the contributions of majority and minority states to the corrugation amplitude are of different sign the total amplitude becomes extremely small (compare to W(110), Fig. 5.2). Thus one might not be able to gain atomic resolution on the Fe(110)-surface at all.

Chapter 6

Chemical Sensitivity in Multi-Component Systems

In the previous chapter we have demonstrated that even in the simple case of pure metal surfaces the interpretation of the STM images may not be unambiguous. As we will see in this chapter, it can even be essential to perform electronic structure calculations in order to verify structural models of surfaces with two or more chemical species on the basis of STM images. Although we are not dealing with a pure metal system in this case but with a silicide, $CoSi_2$, the influence of the transition-metal atom (Co) and the type of analysis is rather typical also for pure metal surface alloys, for example MnCu/Cu(001) [20, 77]. In one-component systems, the STM has given valuable information on the atomic structure of semiconductor surfaces [78]. In multi-component systems, where two or more different chemical species are expected at the surface, the chemical identification on the atomic scale turned out to be more difficult. For some binary systems like GaAs [79] or Al on Si(111) [80] STM measurements at different bias-voltages or spectroscopic measurements proved to be successful. However, for other systems like Ge/Si, the silicides or the perovskites, the chemical identification atom by atom is an open problem.

The surface of $CoSi_2$ presents a case study for this type of problem. Due to the specific requirements of growing flat silicide layers [81–83] or growing silicide islands [84] on Si(100), for applications of silicides in microelectronic devices, a detailed knowledge of growth and structure is desirable. $CoSi_2$ is the best investigated silicide surface of all, but no clear conclusion on the chemical nature of the surface structure exists. $CoSi_2$ crystallizes in the CaF_2 lattice structure, characterized by adjacent (100) lattice planes stacked along the [001] direction alternately occupied with 8 Si or 4 Co atoms. Correspondingly, two different bulk terminated surface structures exist: a Si and a Co terminated one. Experimentally it was found, that both surfaces reconstruct. The Co rich surface (C-surface) was found to be $(\sqrt{2}\times\sqrt{2})R45^\circ$ reconstructed. In models reported for this C-surface, one monolayer of Si resides on top of the Co layer [83, 85–87]. A structural model of the C-surface is shown in the top

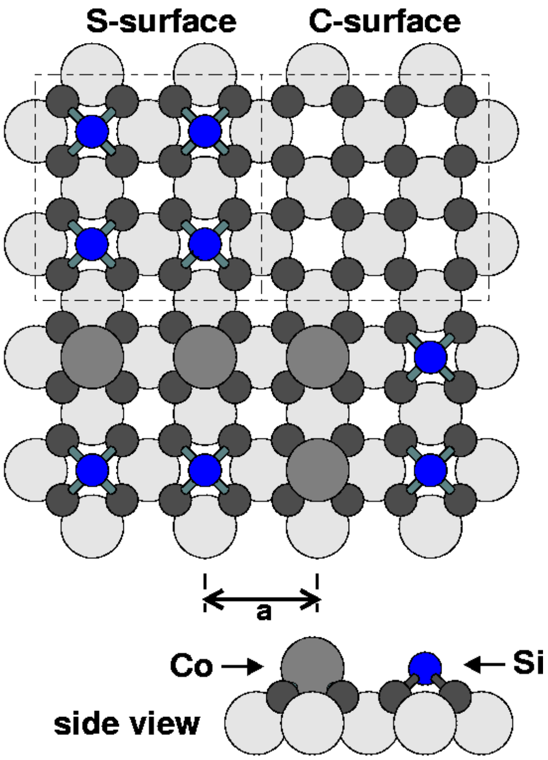

Figure 6.1: Structural models of different terminations of $CoSi_2(100)$. Models for the S- and C-terminated surfaces are shown in the left and right dashed squares in the top, respectively. In the lower part of the top view a model of a mixed surface termination is shown. Part of the surface is S-terminated, in the other part of the surface the top Si atom is replaced by a Co atom (cf. side view).

right part of Fig. 6.1[1]. The Si rich surface (S-surface [2]) shows also a $(\sqrt{2}\times\sqrt{2})R45°$ reconstruction with 1.5 ML Si on top of the upper Co layer illustrated in the top left part of Fig. 6.1 [83,86]. A recent STM study shows that the C- surface has a complete occupation of the lattice sites and only the S-surface has an incomplete one [83].

In this chapter, we interpret atomically resolved STM images of $CoSi_2$ islands, taken at different tunneling voltages, on the basis of the electronic structure calculated with the FLAPW-method and the analysis of STM images introduced in chapter 4. We find that the comparison of experimental and theoretical images resolves the chemical nature of the protrusions observed in the STM images. When we image the surface applying a sample bias voltage U_B larger than $\sim$+0.5 V above the Fermi energy (E_F), the observed protrusions can be assigned to Co atoms. On the other hand, when we image with bias voltages lower than $\sim$+0.5 V, the observed protrusions can be assigned to Si atoms. This is exactly opposite to simple arguments based on the bulk density of states of Co and Si. These results show, (i) that the combination of voltage dependent STM measurements and *ab initio* electronic structure calculations open the possibility to identify the chemical nature of the atoms observed in STM images, and (ii) we propose a new model with an inhomogeneous occupation of the surface lattice sites by Co or Si atoms.

---

[1] The model of the C-surface shown in Fig. 6.1 is (1x1) terminated. For the sake of simplicity the relaxations towards the $(\sqrt{2}\times\sqrt{2})R45°$ reconstruction are not shown.

[2] It should be pointed out that although the terminology "C- and the S-surface" is widely used and we refer to this terminology here, it is misleading, because both, the C- and the S-surface are known to be Si terminated, the C-surface with 1 ML Si and the S-surface with 1.5 ML Si.

6.1 Experimental Details

The STM experiments were performed at room temperature in the constant current mode with a tunneling current of several 100 pA and typical bias voltages between -2 V and +2 V, applied to the sample. To study the bias voltage dependence of the STM images, we use the following procedure: Each scan line is recorded up to six times with up to six different sample bias voltages. This way, we scan six images simultaneously with six different bias voltages. Here we used: 0.3 V, 0.6 V, 0.9 V, 1.2 V, 1.5 V and 1.8 V. For the negative polarities we took another six images.

The silicide films were prepared by reactive deposition epitaxy, i.e. depositing 1.5 ML of Co with the Si(100) sample held at a temperature of 500°C. It was shown earlier, that under such conditions formation of $CoSi_2$ occurs [87]. We observe formation of (3D) islands with aspect ratios (length /width) of 3...5 and heights of ~ 15 Å [88]. The morphology of these 3D islands is described in detail in Ref. [88]. Some of these silicide islands have flat tops. In the following, we will concentrate on the structure of the top facets of these islands.

6.2 Bias-Voltage Dependent STM-Images

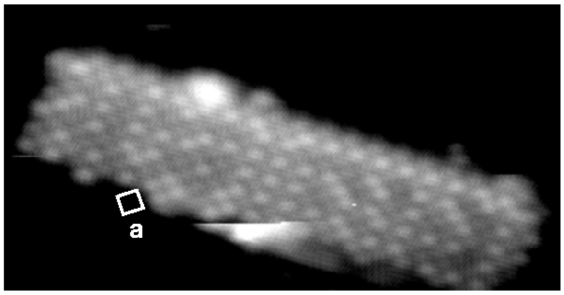

Figure 6.2: Atomically resolved image of the top facet of a silicide island. (1.5 ML Co deposited, T_{Si} = 500°C, $U_B = +1.2$ V, I=200 pA). The surface unit cell is indicated corresponding to a $(\sqrt{2}\times\sqrt{2})$R45° reconstruction. Only 50% of the lattice sites are occupied by atomic protrusions shown as bright dots.

Figure 6.2 shows an atomically resolved STM image of the plateau of an 3D island (U_B=+1.2 V). The atomic protrusions shown as bright spots are located on a square lattice with a periodicity of 5.5 Å along the $\langle 110 \rangle$ directions of the substrate. The unit cell of this reconstructed surface is $\sqrt{2}$ times longer in linear dimension and rotated by 45° relative to the underlying Si substrate. This shows, that experimentally a $(\sqrt{2}\times\sqrt{2})$R45° reconstructed lattice is observed by STM. However, this reconstruction lattice seems not to be occupied completely. For about 50% of the lattice positions in Fig. 6.2, no atomic protrusions are observed. Stalder et al. [83] observed a similar behavior. They interpreted the incomplete occupation of the lattice sites as vacancy defects.

To analyze the reason for this incomplete occupation of the lattice sites in detail, we performed voltage dependent STM measurements. In Fig. 6.3(a) we show another atomically resolved STM image of the top plateau of a silicide island (U_B=+1.2 V). Also on this island a $(\sqrt{2}\times\sqrt{2})$R45° reconstruction lattice is present. In Fig. 6.3(a) 25% of the lattice positions are occupied by bright protrusions. When we change the sample bias voltage from +1.2 V in Fig. 6.3(a) to +0.3 V in Fig. 6.3(b), we observe that different lattice sites are displayed as bright protrusions. A detailed comparison of the images shown in Fig. 6.3(a) and (b) shows, that both images are complementary in the sense that the lattice sites, on which bright protrusions are present at a $U_B = +1.2\,V$, have no protrusions at $U_B = +0.3\,V$ and *vice versa.*

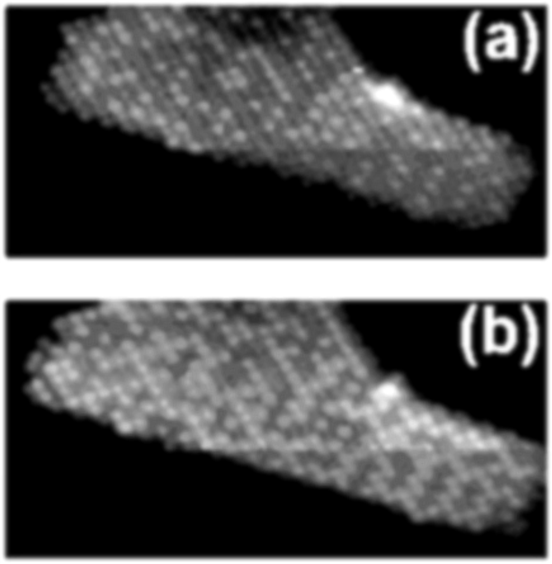

Figure 6.3: The top facet of a silicide island is shown in (a) and (b) imaged at +1.2 V and +0.3 V sample bias voltage, respectively (I=150 pA). Complementary sets of lattice positions are imaged as bright protrusions at the different bias voltages.

The general trend with respect to the voltage dependence of the images is as follows: At bias voltages of +0.6 V and higher always the same lattice sites show bright protrusions, and for bias voltages of +0.3 V and lower (and for negative bias voltages) the complementary set of lattice positions is imaged as bright protrusions. This voltage dependence of the observed corrugation at different lattice sites precludes a purely morphologic nature of the observed image contrast. Therefore, vacancy defects are excluded as a reason for the observed incomplete occupation of the lattice sites and we propose a new model with an inhomogeneous occupation of the surface lattice sites by Co and Si atoms. The model is based on the S-surface, which has 1.5 ML Si on top of $CoSi_2(100)$. In our model a certain amount of the top Si atoms are replaced by top Co atoms (cf. bottom of Fig. 6.1). In order to prove our model, we aim to relate the voltage dependent behavior of the STM images to the chemical identity at the $CoSi_2(100)$ surface by performing *ab initio* calculations based on the method described in chapter 4.

6.3 Computational Details

Electronic structure calculations are carried out within the local-density approximation using the parametrization of Moruzzi, Janak, and Williams [72]. *Ab initio* calculations for an inhomogeneous distribution of Co and Si surface atoms as proposed in our model are at present unattainable. To simulate a mixed termination, with Co and Si atoms randomly distributed at the lattice positions of the $(\sqrt{2}\times\sqrt{2})$R45° reconstructed surface, we use a c(2×2) unit cell shown in Fig. 4 (d) with an equal amount of Si and Co at the surface. We think that this is a good structural model

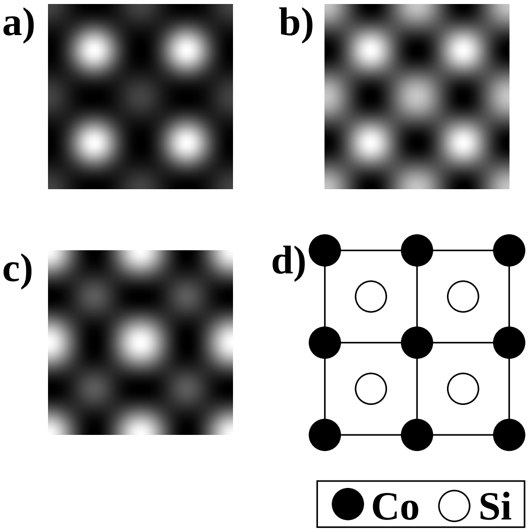

Figure 6.4: Calculated lateral distribution $\boldsymbol{r}_{\|}$ of the ILDOS $\int n(\boldsymbol{r}_{\|}, z_0|E)dE$ at a distance of $z_0 = 7$Å from the center of the surface atoms. The panels show integrals over different energy ranges: a): -1.0 to 0 eV, b): 0 to 0.5 eV, c): 0 to 1.0 eV. d) shows the surface unit cell with Co shown as solid circles and Si as open circles.

since the STM images show little difference in the brightness when nearest neighbor atoms are of the same kind. We have chosen a 9 layer film consisting of 7 layers bulk CoSi_2 made up of an alternating sequence of 4 Co or 8 Si atoms per layer. We have chosen the experimental lattice constant of 5.356Å. Structural relaxation are not taken into account.

6.4 Understanding the STM-Images

Theoretical STM images have been calculated based on the Tersoff Hamann model [6] and are thus directly related to the energy integrated LDOS (ILDOS). Thus the energy integrated LDOS (ILDOS) of occupied ($U_B < 0$) or unoccupied ($U_B > 0$) states in the energy range (E_F, $E_F + eU_B$) contribute to the tunneling current, $I(\boldsymbol{r}_0) \propto \int_{E_F}^{E_F+eU_B} n(\boldsymbol{r}_0|E)dE$, and can be directly compared with the grey scale plots of constant current STM images.

Figure 6.4 shows grey scale plots of the LDOS integrated over energy intervals characteristic for different STM images observed. For energies corresponding to tunneling voltages probing the occupied states, the image is dominated by large ILDOS located at the position of the Si atoms. The ILDOS does not change much for bias voltages in the range between -1.5 eV and E_F and Fig. 6.4(a) provides a typical example at $U_B = -1.0$eV. Even for tunneling voltages probing the unoccupied states till close to $+0.5$ eV the ILDOS remains nearly unchanged. At about $+0.5$ eV above the Fermi level, an approximately equal amplitude of the ILDOS is calculated at the positions of the Co and the Si atoms (Fig. 6.4 (b)). For higher energies, $E > +0.75$ eV, a contrast reversal is observed and the largest ILDOS is observed at the positions of the Co atoms (Fig. 6.4 (c)). This type of image remains nearly unchanged up to an energy of about $+1.2$ eV, then the ILDOS located at the Si site recovers partly leading to a smaller corrugation between Si and Co atoms.

Comparing these results with the STM images, we find that the theoretically predicted and experimentally observed contrast reversal at a tunneling voltage of about

+0.5 V agree very well. Combining the STM results with the *ab initio* calculations, we assign the protrusions observed for tunneling voltages below ∼+0.5V to Si atoms and the ones observed above ∼+0.5V to Co atoms.

This assignment is in opposite to the intuition based on the simple arguments derived from the LDOS of bulk Co and Si [72]. For Co we find a large LDOS within ±0.5eV, i.e. within the vicinity of E_F while Si shows a band-gap in this region. Therefore, it is expected that mainly Co states contribute to STM images at energies below +0.5eV and the observed STM image is thought of probing the Co states rather than the Si ones. An understanding of the STM images on the basis of the electronic structure is provided by the comparison of the LDOS of the surface Si and Co atoms and the bandstructure with the star coefficients show in Fig. 6.5.

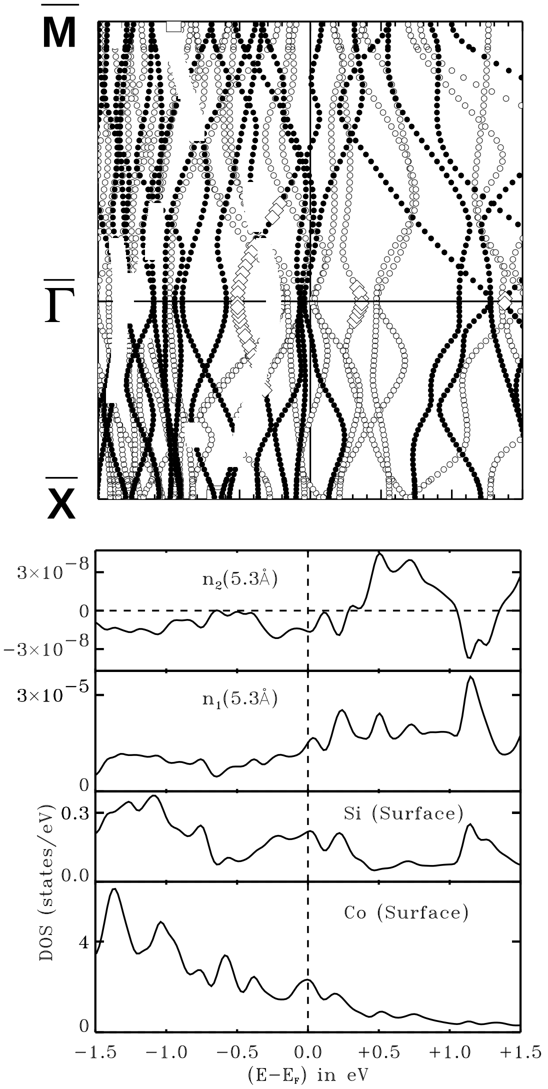

Figure 6.5: Comparison of the electronic structure, in terms of the bandstructure and density of states of the surface Si and Co atoms, with the STM images, in terms of the first and second star coefficient. A positive (negative) value of the second star coefficient corresponds to an STM image where the Co (Si) atoms are observed as protrusions. Note, that there is a sign reversal in the second star coefficient at about +0.3 eV. Filled (open) circles in the bandstructure denote states of odd (even) symmetry with respect to a mirror plane along the high symmetry direction. Further, states located at the Co surface atom and the vacuum with more than 50 % are marked by open squares while states located at the Si surface and the vacuum with more than 20 % are marked by open squares.

Although for $E < E_F$ the DOS is clearly dominated by Co, the constant part of the vacuum LDOS given by the first star coefficient follows the Si LDOS. Also the second star coefficient, representing the corrugated part of the vacuum LDOS which discriminates between the Co and Si surface atom, is negative defined as showing the Si surface atom as a protrusion in the STM image. This is due to the orbital character for the different atoms. For an energy interval between about -1eV and E_F the Si states are of p_z character and extent further into the vacuum than the Co d_{zx} and d_{zy} states. We can see two bands marked by squares and diamonds just below the Fermi energy corresponding to these states. Also at positive energies we find a peak at about +0.2 eV in the vacuum, the Si and the Co surface LDOS, which is due to p_z and $d_{zx,y}$ states localized at the Si and Co surface atoms, respectively, leading to the same ILDOS as for the occupied states. This interpretation is verified by the negative second star coefficient. At about +0.3 eV above the Fermi energy a sign reversal occurs accompanied by a decrease of the Si surface LDOS. For energies between 0.4eV and 1.0eV the LDOS of Si is very small but the constant part of the vacuum LDOS, the first star coefficient, shows several bumps. These are due to Co states and the states between +0.5 eV and +0.75 eV are responsible for the contrast reversal. In this energy range there are flat bands to be found near the $\bar{\mathrm{X}}$-point of the 2D-BZ. The energy integrated (0.5eV< E <0.75eV) LDOS $n(\mathrm{r})$ shows that these states are of d_{z^2} character and dominate the STM image. At +1.2 eV we find a peak in the vacuum LDOS causing a negative second star coefficient which is basically of Si-sp character reducing the corrugation in the STM image at larger bias voltages. There is no further reversal of the image though.

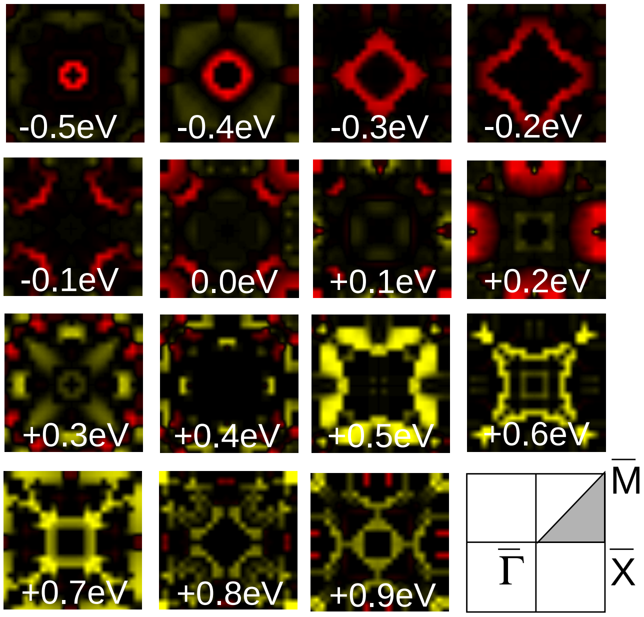

Figure 6.6: The second star coefficient is plotted as a function of the wave vector $\mathbf{k}_{\|}$ in the 2D-BZ. Positive (negative) values of the second star coefficient are marked by yellow (red). The sign reversal at +0.3 eV can be readily seen from the plots and one can identify the responsible bands.

In order to find out which bands contribute most significantly to the different STM images and finally cause the image reversal Fig. 6.6 displays the second star coefficient as a function of the wave vector $\mathbf{k}_{\|}$. From these plots we can easily deduce the responsible states. At an energy of -0.5 eV below the Fermi energy there is only a small negative contribution from bands near the $\bar{\Gamma}$-point of the BZ[3]. With increasing energy we see how the band spreads in the BZ and just above the Fermi energy it vanishes from the plots. Comparing with Fig. 6.5 we can relate this band to the one marked by diamonds in the bandstructure, i.e. which is highly located at the Si surface atom. At an energy of +0.3 eV we find the first positive contributions to the second star coefficient becoming dominant at +0.5 eV. This corresponds to the peak position seen in Fig. 6.5. Again a correlation with bands from the bandstructure plot is possible. With the aid of these plots we can finally choose states responsible for imaging the Si or the Co surface atoms and decide on their orbital character.

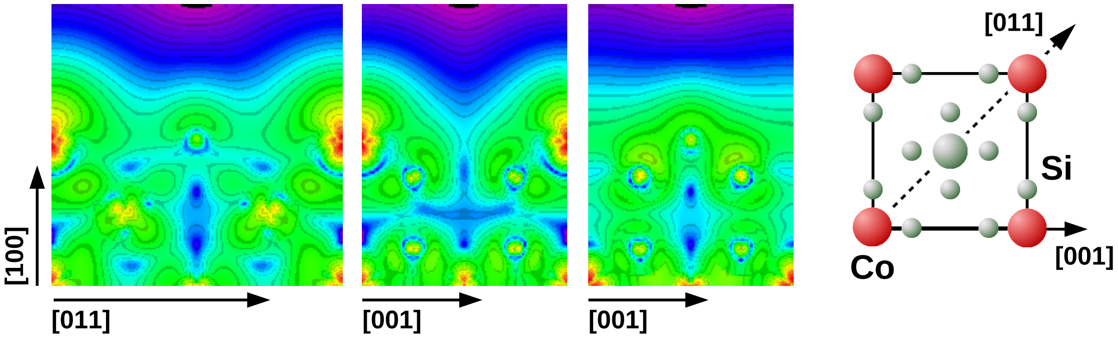

Figure 6.7: Single eigenstate at $\mathbf{k}_{\|} = (0.375, 0.125)\pi/a$ responsible for the imaging of Co as a protrusion at bias-voltages above +0.5 V. At the far right the surface unit cell is displayed. Small light circles denote subsurface Si atoms. Large light (dark) circles denote Si (Co) surface atoms. The left (right) cross-section in [001]-direction intersects the Co (Si) surface atoms. Note, that the d_{z^2}-orbital character at the Co atom is clearly visible.

Fig. 6.7 and Fig. 6.8 display cross-sections of specific states with a local density of states leading to an STM image with the Co surface atoms as protrusions and with the Si surface atoms as protrusions, respectively. The orbital character at the Co atom changes from d_{z^2} for the Co imaging states to $d_{xz,yz}$ for the Si imaging states. For the Si surface atom a significant p_z-type contribution can be seen in Fig. 6.8. Both plots lead to gigantic corrugation amplitudes of up to 1 Å.

---

[3] Notice, that the two-dimensional unit cell is quite large and correspondingly the BZ rather small in this calculation. Therefore, the $\mathbf{k}_{\|}$-selection rule discussed in chapter 4 does not rule out large contributions also from other than the most favorable high symmetry points, which is the $\bar{X}$-point in this case.

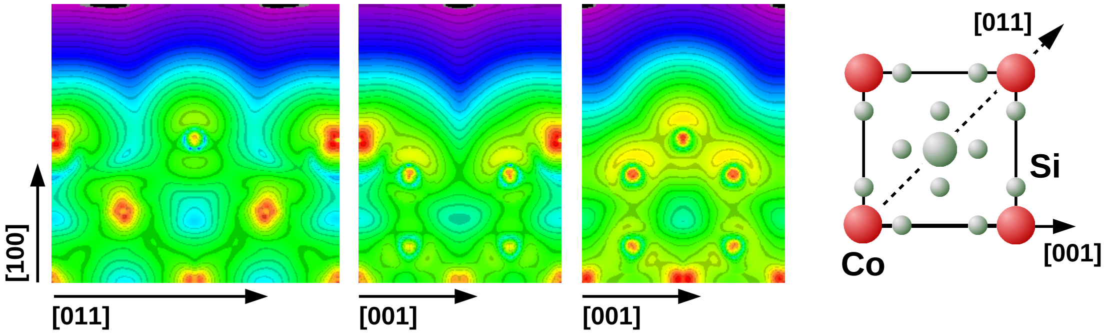

Figure 6.8: Eigenstates in the energy range $[E_F - 0.2\text{ eV}, E_F]$ showing the Si surface atoms as protrusions in the STM-image. At the far right the surface unit cell is displayed. Small light circles denote subsurface Si atoms. Large light (dark) circles denote Si (Co) surface atoms. The left (right) cross-section in [001]-direction intersects the Co (Si) surface atoms. Notice, that the character of the state is $d_{xz,yz}$ at the Co surface atoms and of s, p_z-type at the Si surface atoms.

Chapter 7

Imaging Buried Transition-Metal Structures

Structural, catalytic, magnetic, and electronic properties of metal surfaces and ultrathin films are strongly altered upon alloying. Novel ordered and disordered alloys are formed at the surface or surface near region due to surface segregation of bulk alloys or upon metal-on-metal growth, where intermixing takes place between deposited and substrate metals, even between metals, which are immiscible in bulk. Over the past few years, the scanning tunneling microscopy (STM) developed to a very powerful real-space probe providing an unprecedented wealth of new insight into this field [20, 58, 89–95]. It permitted i.e. the correlation between the surface compositional structure of the alloy on an atomic level and macroscopic properties. Two key issues in this context are (i) the chemical sensitivity of the STM, necessary to discern different chemical components of the alloy which we have treated in the last chapter, and (ii) the depth sensitivity of the STM, the capability to image alloys below the surface layer or to discern alloy components at different layers below the surface. While it is quite often possible to achieve chemical resolution, no evidence for imaging more than the surface layer exists although sub-surface growth of Pd on Cu(110) and Ag(110) has been studied by STM [93]. This seems to be in accordance with the conventional wisdom of effective screening of impurities below the surface by the nearly free electrons of the metals and that the STM tip follows the surface topography of surface atoms. In the case of semiconductors screening is weaker and imaging even of uncharged impurities down to the third layer below the surface has been reported [96].

In this chapter it is demonstrated that transition-metal structures buried below a metal surface can be imaged by STM. The experiments have been performed[1] combining STM, Ion Scattering Spectroscopy (ISS), X-ray Photoelectron Spectroscopy (XPS) and Low-Energy Electron Diffraction (LEED) [97]. With the aid of the *ab initio* calculations the imaging of buried structures is shown explicitly for the subsurface alloy formed after deposition of Ir on Cu(001). Arguments and results are provided showing that this is not particular to the Ir/Cu(001) system but applies

---

[1] The experiments are part of the PhD Thesis of G. Gilarowski, carried out at the Humboldt University in Berlin.

to a wide class of transition-metals buried in noble-metal substrates. Further, the calculations reveal that impurities are detectable by STM for a few layers below the surface, while two-dimensionally ordered structures develop quantum-well states and are therefore detectable to much larger depth.

7.1 STM and ISS Experiments

STM images were taken at room temperature with an OMICRON combined STM/AFM operated in constant-current mode. Fig. 7.1(a) shows a typical STM image with atomic resolution for Ir deposited on a Cu(001) surface at low coverage. It exhibits a regular array of white dots and reveals disordered star-like defects as depressions. As carefully checked by the *ab initio* calculations no bias-voltage-dependent corrugation reversal as discussed in chapter 5 occurs on Cu(001) and the regular array of dots is interpreted as Cu atoms. The apparent depth of the star-like depressions is about 0.3 Å and is assigned to single Ir atoms. Note that the center of gravity of these defects is not located on regular Cu sites in the surface lattice, but instead at the fourfold-hollow sites. Excluding interstitial positions for Ir due to the large radius of the atom, Ir must be located below or on top of the surface. The latter can be discarded on the basis of He^+ ISS measurements, which are known to be sensitive to the topmost surface layer only [98]. No Ir signal was detected by ISS.

A closer inspection of the image further reveals that sometimes the star-like defects overlap when two Ir atoms are located at nearest-neighbor sites. As a consequence dark lines start to form along the [011] directions (c.f. dark line in the lower right part of Fig. 7.1(a)). After direct deposition of Ir (0.5-0.6 ML) at elevated temperatures long range ordering occurs which is indicated by a (2×1) LEED superstructure exposing two domains. The amount of Ir visible in ISS is then below 1%, whereas XPS results show that Ir is segregated into the surface but remains in a surface near region, e.g. in the second layer. The corresponding STM image of the ordered surface exhibits a distinct chain like structure orientated along the two equivalent [011] directions (Fig. 7.1(b)). The distance between adjacent chains of the same kind is measured to about 5 Å (i.e. twice the nearest-neighbor distance) in agreement with a (2×1) LEED structure. The ordered alloy shows an apparent corrugation of 0.3 Å as measured by STM. Successful imaging of the sub-surface alloy was only possible for negative bias voltages U_{sample} (occupied sample states) in a range between -0.2 V and -0.5 V, indicating electronic effects as the origin of the measured corrugation. Summarizing the experimental findings from the STM, LEED, ISS, and XPS measurements we propose the following structural model: 0.5 ML of Ir deposited on Cu(001) leads to the formation of an ordered (2×1) CuIr alloy layer of adjacent Cu and Ir chains along the [011] directions buried under one monolayer of Cu.

Although above experimental findings lead to a consistent structural model of an ordered CuIr sub-surface alloy, (i) the result is quite surprising as Ir and Cu exhibit a large miscibility gap in the bulk phase diagram [99], and (ii) the model relies on the assumption that STM is able to image Ir impurities and chains buried in the substrate, for which there is no experimental evidence so far and disputed by the

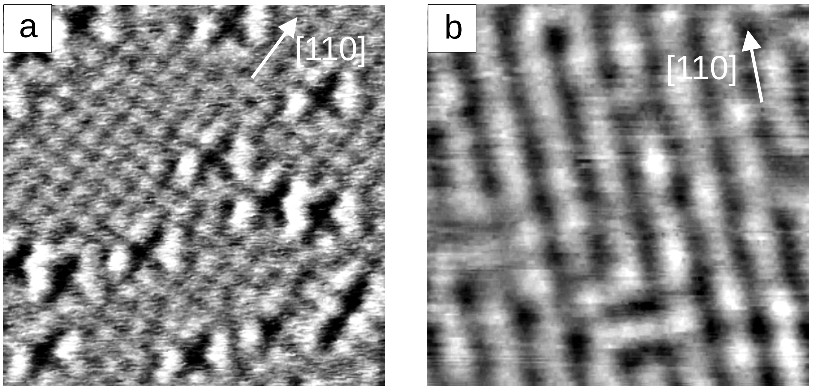

Figure 7.1: STM images of the Cu-Ir surface: a) Low Ir coverage. 0.05 ML of Ir deposited at 200 K and annealed at 650 K ($U_{sample} = 0.02$ V, $I = 2.1$ nA). b) Ordered CuIr/Cu(100) sub-surface alloy. 0.6 ML of Ir deposited at 620 K ($U_{sample} = -0.3$ V, $I = 0.5$ nA). Image sizes: 40 Å × 40 Å. Tip-to-sample distance $z \approx 6 - 9$ Å.

conventional school of thought that STM follow the topography of surface atoms. In order to shed light onto the question of detectibility of buried Ir structures, and to interpret and understand STM images of Ir point defects and CuIr adjacent chains STM images were calculated on the basis of the method introduced in section 4.6.

7.2 Computational Details

Electronic structure, total energy, and force calculations are carried out within the local-density approximation using the parametrization of Vosko, Wilk, and Nusair [100]. The surface and surface near region are modeled by eleven-layer (001) films, at the experimental lattice constant of Cu ($a_{Cu} = 3.616$ Å), consisting of nine layers of Cu and one layer containing Cu and Ir atoms placed on both sides of the film at the surface (S), sub-surface (S$-$1) or deeper (S$-$2, S$-$3) layers. The Ir impurity is modeled using a p(2×2) surface unit cell containing three Cu atoms and one Ir atom per impurity layer which leads to 44 atoms in the film unit cell. Similarly the CuIr chain structure is treated in a p(2×1) unit cell with 2 atoms per layer. To investigate the energetic competition with a checkerboard arrangement of Cu and Ir atoms we performed also calculations for two-dimensional (2D) c(2×2) CuIr alloys. For the system with the p(2×1)-CuIr chains at S$-$1 all atom positions are fully relaxed, minimizing the total energy by force calculations. We found a buckling of the Ir and Cu atom at the S$-$1 layer of $\Delta Z/d = 2.9$ % of the interlayer distance $d = a_{Cu}/2$ between two (001) plains. This increases the corrugation amplitudes of STM-images presented below by $\Delta z \simeq 0.05$ Å, which is a minor contribution in the context of the effect discussed in the following sections and the relaxation is therefore not considered any further. For the self-consistency calculations 36, 32 and 10 $\mathbf{k}_{\|}$-points were used in the irreducible wedge of the 2D Brillouin zone (I2BZ) for the c(2×2), p(2×1) and p(2×2) structure, respectively. The STM images were analyzed using 465, 288 and

66 $\mathbf{k}_{\parallel}$-points in the I2BZ, respectively.

For the deeply buried 2D chains a 23 layer film was used additionally in the p(2 × 1) unit cell. A test calculation has been performed with an asymmetric 13 layer film where the 2D CuIr alloy layer was covered by one Cu layer with respect to one vacuum region and by 11 Cu layers with respect to the other inequivalent vacuum region.

7.3 Energetic Stability of Buried CuIr Alloys

Ir site	p(2×2)	c(2×2)	p(2×1)	c(2×2)−p(2×1)
Surface	750	721	374	433
(S−1)	±0	±0	±0	86
(S−2)	33	20	49	57

Table 7.1: Total energy differences in meV/Ir-atom for calculated 2D CuIr alloy structures placed at layer S, S−1, and S−2. Energies are given relative to the configuration S−1. The last column shows the energy difference between the c(2 × 2) checkerboard and the $p(2 \times 1)$ chain structure where a positive sign favors the chain structure.

In Table 7.1 we summarize the total-energy differences of the 2D CuIr layer in the p(2 × 2) impurity, the c(2 × 2) checkerboard, and in the p(2 × 1) chain structure located in the layer S, S−1, and sub-sub-surface layer (S−2). The results show, Ir being at the surface is the most unfavorable configuration. This is consistent with the argument that the surface free-energy for Ir is higher than for Cu and the energy is lowered when Cu terminates the surface. In accordance with the STM analysis, Ir located in the sub-surface layer is the energetically most stable configuration. This can be understood in terms of bond-strength arguments: The bond strength increases with the reduction of nearest neighbors. Thus, among all Cu atoms, the Cu atoms at the surface form the strongest bonds to Ir atoms in the sub-surface layer. The energy of 49 meV for Ir in the p(2 × 1) CuIr structure to diffuse to deeper layers can be overcome by temperature T and indeed, it is experimentally found, that Ir diffuses into the bulk for $T > 650$ K. The p(2 × 1) chain structure at S−1 is 86 meV more favorable than the checkerboard arrangement of Ir and Cu atoms, which is due to the direct $d-d$ hybridization between Ir atoms along the chains, which is missing in the c(2 × 2) structure.

7.4 Calculated STM-Images

The theoretically determined STM images for the Ir impurity (p(2 × 2)) and chain (p(2 × 1)) structure buried in the sub-surface layer S−1 (Fig. 7.2) calculated for the bias-voltage $U = -0.6$ V clearly reproduces the experimental images of star- and chain-like patterns.

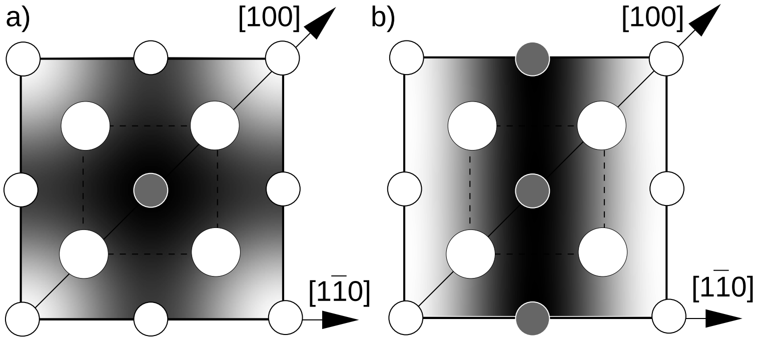

Figure 7.2: Calculated STM images at $U = -0.6$ V, $z = 5$ Å for Ir impurity (a) and chain (b) located at S$-$1. Open (full) circles represent Cu (Ir) atoms, big (small) circles represent atoms at S (S$-$1).

A wide range of the bias-voltage dependence of STM-images is covered in Fig. 7.3 in terms of calculated corrugation amplitudes for Ir impurities and chains at the Cu(001) surface layer S or buried in the sub-surface layer S$-$1. From Fig. 7.3 it can be concluded that Ir atoms and chains in the surface should be imaged as protrusions ($\Delta z > 0$) while depressions ($\Delta z < 0$) should be found for the buried structures, and vice versa for Cu atoms. Strikingly the absolute corrugation amplitudes are of comparable values, irrespective whether Ir is in the surface or sub-surface layer. Note the distinct bias-voltage dependence for the buried structures. The maximum corrugation amplitudes for the buried structures were found around -0.5 eV and an atomic resolution becomes possible only at negative bias voltages, i.e. occupied sample states, which is in perfect agreement with the experimental observation.

Since the corrugation amplitudes for CuIr chains buried at different layers are very similar, and from Fig. 7.1(b) it is *a priori* unknown whether Cu or Ir is imaged as protrusion it is impossible to conclude from Fig. 7.1(b) at which layer the CuIr alloy is located. On the other hand in the low coverage limit, single defects (Fig. 7.1(a)) are clearly related to single Ir atoms. Since they appear as depressions with a similar corrugation amplitude as the chains we conclude that Ir is located in the sub-surface layer.

7.5 Correlation with the Electronic Structure

In order to correlate the bias-voltage dependence of the corrugation amplitude to the underlying electronic structure of the p(2$\times$1)-CuIr chain structure buried in S$-$1, we present in Fig. 7.4 a comparison of the bandstructure with the first and second star coefficient of the vacuum LDOS and the DOS in the muffin-tin spheres of the surface Cu and sub-surface Ir atoms. We recall from the discussion of section 4.6.1 that the corrugation pattern is determined by n_2. For a perfect Cu(001) surface, the two Cu atoms in a p(2$\times$1) surface cell are indistinguishable, the difference in the corrugation between Cu atom 1 and 2 is zero and thus n_2 is identically zero.

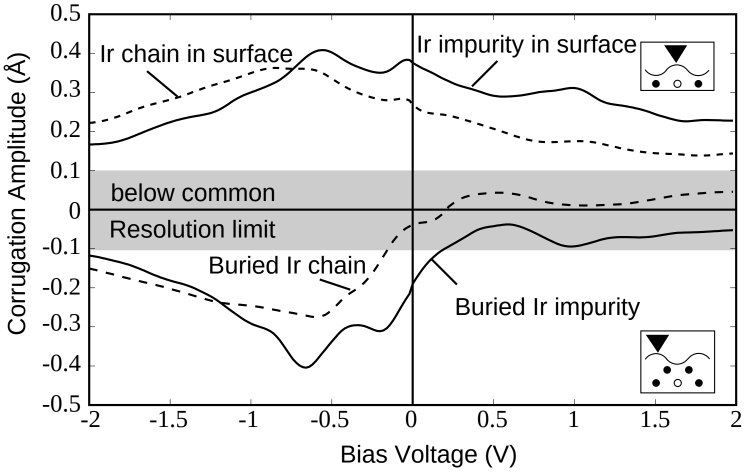

Figure 7.3: Calculated corrugation amplitudes of a tip at $z = 5.3$ Å, as a function of the applied bias-voltage U for the Ir impurity and the Ir chain. In the insets at the upper and lower right corners, filled (open) circles denote Cu (Ir) atoms. Positive (negative) corrugation amplitudes are defined as imaging the Ir site as a protrusion (depression).

Replacing one chain of Cu atoms by Ir atoms breaks the symmetry and n_2 will be non-zero. In Fig. 7.4 we find, n_2 is basically zero over a large energy range, except around -0.5 eV, where n_2 shows a negative peak. According to our definition, a negative value of n_2 means Ir is imaged as depression and Cu as protrusion. The fact that n_2 is zero for positive bias voltages explains why no resolution of the chain structure was found in the experiment at $U > 0$.

The peak of n_2 is a consequence of electronic states (see dashed vertical line) close to the $\bar{\mathrm{X}}$-point and along the $\bar{\Gamma}\bar{\mathrm{M}}^*$ direction of the 2D BZ. These are marked by open circles in the band structure by the criterion that they are localized at Ir atoms at S-1 as well as the Cu atoms at S, and possess a large weight in the vacuum. The hybridization of the state between the buried Ir and surface Cu atom is also visible in the DOS shown in the bottom panel of Fig. 7.4 where peaks appear in both panels close to -0.5 eV below the Fermi energy.

For the Ir chain system buried at S-1, a real space view of a typical state at the energy of the peak of n_2 is shown in Fig. 7.5 in terms of a charge-density contour-plot. Fig. 7.5 displays that the hybridization of the Ir d-states [largest charge density in Fig. 7.5] with the Cu sp-states results in tilted pd-orbitals at the Cu surface atoms (and of the Cu atoms below the Ir atoms, S-2). The bond between the Cu surface atom and the Ir atom is of antibonding nature and the tilted pd-orbitals form a bond charge above the Cu sub-surface atom, which implies that the charge density maximum, which is for a plain Cu(001) surface above the Cu surface atom, shifts to the position above the Cu sub-surface atom. Depending on the structural symmetry this results in the star-like or stripe-like pattern observed in experiment (Fig. 7.1) and theory (Fig. 7.2) for the CuIr impurity and chain structure at S-1.

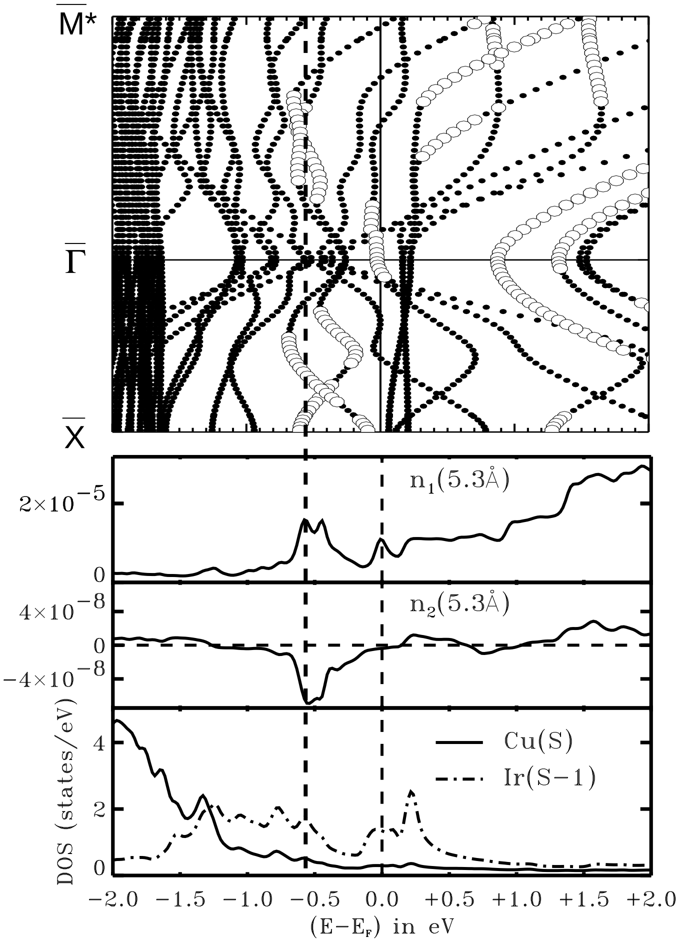

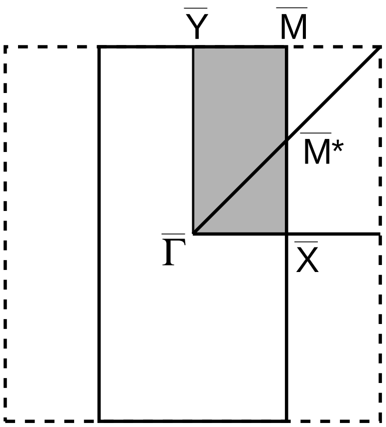

Figure 7.4: Comparison of band structure, star coefficients n_1 and n_2 and density of states for the Cu-ML/p(2 × 1) IrCu/Cu(001) structure. In the bandstructure states marked by an open square are characterized by a localization of more than 45% at the buried Ir and surface Cu atoms and of more than 5% in the vacuum. The 2D-BZ of the p(2 × 1) unit cell is also displayed above.

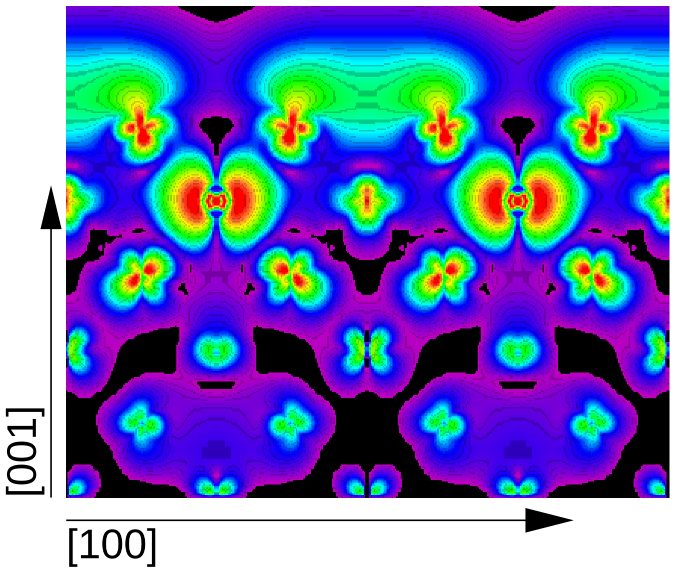

Figure 7.5: Cross section along the [100] direction through the charge density of a typical state ($\mathbf{k}_{\|} = \pi/a * (0.325, 0.325)$) in the 2D BZ at an energy $E_F - 0.6$ eV for Ir chains at S−1.

7.6 Generalization for 4*d*- and 5*d*-Metals

The arguments based on the hybridization of the Cu *sp*- and Ir *d*-states are rather general and the visibility of buried transition-metal atoms should also hold for other

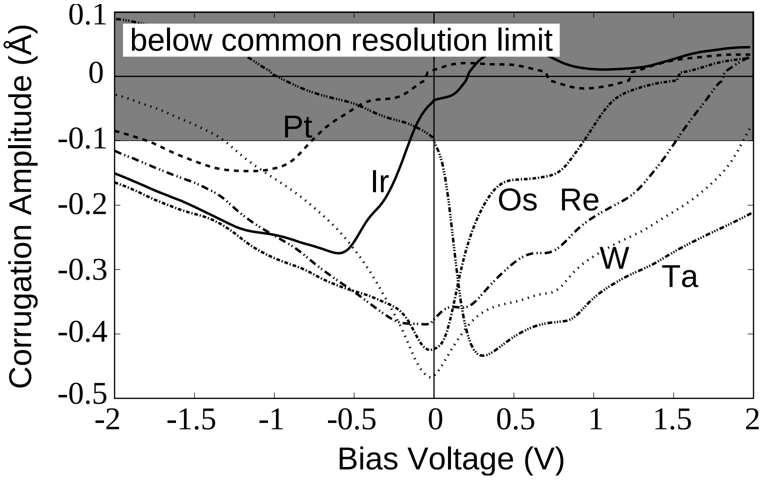

Figure 7.6: Comparison of corrugation amplitudes at a distance of $z_0 = 5.3$ Å for the $5d$-elements in the chain structure, i.e. p(2×1), buried beneath one monolayer of Cu(001) (S-1). The plots for Pd, isoelectronic to Pt, and Rh, isoelectronic to Ir, do not differ qualitatively except for a small ($< 10\%$) decrease in absolute values due to a stronger localization of the $4d$-states.

transition-metal atoms. First candidate is Rh, isoelectronic to Ir. As expected there is only a neglectable difference between the two corrugation amplitude plots. Still, the maximum is slightly smaller for Rh which is probably due to the more localized $4d$-states influencing the Cu sp-states a little less. The same holds for the comparison of Pt and Pd. With increasing number of d-electrons (Ir, Pt, Au) we expect that the d-band energy lowers with respect to the Fermi energy and thus the tunneling barrier of the state seen in STM becomes higher. This increases the decay of the wavefunction into the vacuum and the corrugation amplitudes should drop. In addition a lower d-band energy reduces the symmetry breaking between Cu and the $3d$ metal, n_2 approaches zero and again the corrugation amplitudes should drop. For elements with decreasing number of d electrons (Ir, Os, Re, $\cdots$), the opposite trend is expected. This picture is confirmed by the calculations for Ta, W, Re, Os, Pt, and Ag chains in Cu(001) at S$-$1 presented in Fig. 7.6. For Pt, the corrugation amplitude drops to a maximum value of 0.15 Å at $U = -1.2$ V and an amplitude lower than 0.05 Å within an energy of $U = \pm 0.5$ V. We conclude it is most likely impossible to image buried Pt. We speculate that this is the reason why the sub-surface growth of Pd, isoelectronic to Pt, in Cu(110) [93] was impossible to image with STM. For Ag buried in Cu(001), we found corrugation amplitudes of 0.03 Å, which will hardly be measurable by STM. For Os, Re, W, and Ta, on the other hand, corrugation amplitudes of ~ 0.4 Å are found in a bias-voltage interval of $U = \pm 0.5$ V. The maximum corrugation amplitude increases in energy with decreasing number of d electrons and the buried Ta chains can only be detected for $U > 0$.

7.7 Profile of Corrugation Amplitude Plots

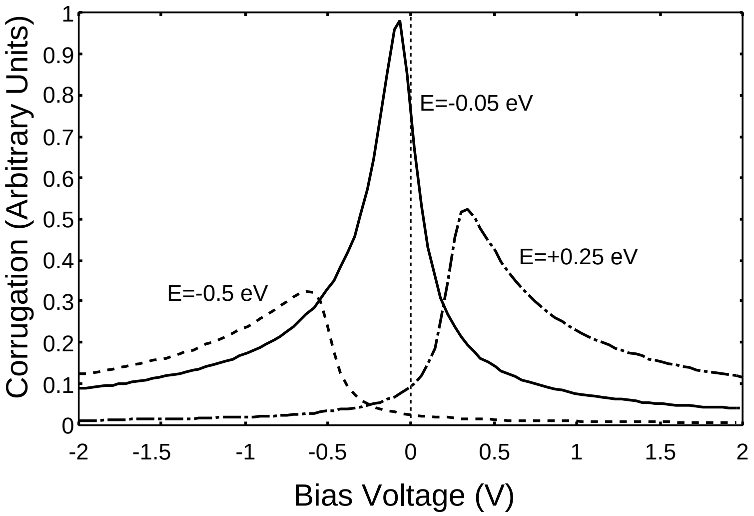

Figure 7.7: Comparison of theoretical corrugation amplitudes calculated on the basis of Eq. (7.1) for three different values of the energy position of the peak in the second star coefficient. The peak positions are given relative to the Fermi energy and an energy width $\Gamma = 0.15$ eV has been chosen. An increase of the latter results in a decrease of the corrugation amplitude.

Before we continue the discussion on the depth dependence of the corrugation amplitude for the buried Ir chains, we shall present a simple model to faciliate the understanding of the corrugation amplitude plots. As we have seen in Fig. 7.4 the second star coefficient is zero almost everywhere except for one peak at an energy $E_0 = E_F + \Delta E_0$, which we can describe by a Lorentzian function of energy width Γ. We further approximate the first star coefficient $n_1(E)$ by a constant n_1. If we insert these assumptions into Eq. (4.72) and neglect higher order stars, we find:

$$\begin{aligned}\Delta z(V) &\approx \frac{\int\limits_{E_F}^{E_F+eV} \Gamma/(\Gamma^2 + (E-E_0)^2)\, dE}{\int\limits_{E_F}^{E_F+eV} 2\kappa(E) n_1(E)} \\ &\approx \frac{\arctan\left[\frac{2}{\Gamma}(eV - \Delta E_0)\right] - \arctan\left[\frac{2}{\Gamma}(-\Delta E_0)\right]}{2\kappa(E_F) n_1 eV}. \end{aligned} \tag{7.1}$$

The energy dependence in $\kappa(E)$ has been neglected by taking the value at the Fermi energy E_F. Fig. 7.7 displays the result of this bias-voltage dependence for three different values of E_0. Two features of the calculations presented so far can be readily explained with this plot. First of all, the overall form of the calculated corrugation curves (see Fig. 7.3 and 7.6, compare Ir, Re and Ta) resembles the curves of the model of Fig. 7.7 very well. The second more important aspect concerns the maximum value of the corrugation amplitude. It is obvious from the graphs that the value is greatly increased if the peak is located closer to the Fermi energy. This is due to the denominator of Eq. (7.1) which increases linearly with the voltage and therefore the corrugation amplitude $\Delta z(V)$ is inversely proportional to the bias-voltage. This effect is also visible in the calculation for the $5d$-elements (Fig. 7.6) and becomes important in connection with the imaging of quantum-well states, investigated in the following sections. In Fig. 7.7 the energy width Γ which depends on the dispersion of the bands responsible for the peak in the second star coefficient is equal for all plots. An increase of the width leads to a decrease in the corrugation amplitude.

7.8 Depth-Dependence of STM-Images

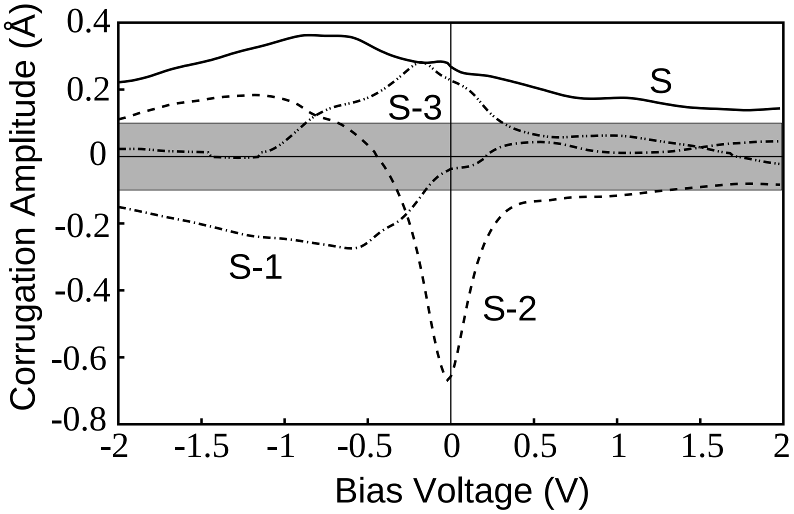

Figure 7.8: Comparison of corrugation amplitudes at a distance of $z_0 = 5.3$ Å for the Ir chains, i.e. in the p(2×1) unit cell, at different Cu coverage. Coverages of zero (S), one (S$-$1), two (S$-$2), and three (S$-$3) monolayers of Cu are displayed. The enormous increase of the corrugation amplitude for (S$-$2) is due to the peak location near to the Fermi energy (compare with Fig. 7.7).

Since it has been shown in the previous sections that it is after all possible to image transition-metal atoms and structures beneath a monolayer of Cu, it is natural to ask whether the buried structure can also be resolved at a higher Cu coverage. This question is explored in the following for the buried Ir chains in the p(2×1) unit cell. Fig. 7.8 displays the resulting corrugation amplitudes where the sign convention is the same as before. If the Cu coverage is increased in steps of additional monolayers from one, such that the Ir chains are located in the subsurface layer (S$-$1), to two monolayers (S$-$2) Cu(001) the maximum corrugation amplitude does not decrease as one might expect but instead it increases enormously. This increase is due to a shift of the peak in the second star coefficient closer to the Fermi energy connected with an enhancement of the corrugation amplitude as discussed at the end of the previous section. Further, the profile is very symmetric in agreement with the model (Fig. 7.7). An additional layer of Cu (S−3) leads to a decrease of the amplitude but still a value above 0.15 Å is reached in a broad energy interval around zero bias-voltage. The expectation of an exponential decrease of the signal due to screening is thus not satisfied at all. On the other hand, the calculations for the Ir impurities in the p(2 × 2) unit cell showed a significant decrease for a location at (S−2) and (S−3) with a maximum corrugation amplitude of 0.15 Å (see Fig. 7.9). A coverage of five monolayers reduces the corrugation below 0.1 Å which fulfills our expectation that the perturbation caused by an impurity should become unobservable rather quickly. However, the Ir impurity calculation has been performed in a p(2 × 2) unit cell and there is actually a two-dimensional periodic array of Ir impurities. Therefore, it is impossible to find the limit of an exponential decay from such a calculation. We can conclude that a periodic structure does not show a decrease of the corrugation amplitude by screening of nearly free Cu electrons while an impurity does. The reason is connected with the development of quantum-well states in the covering Cu layers as we can see from the following section.

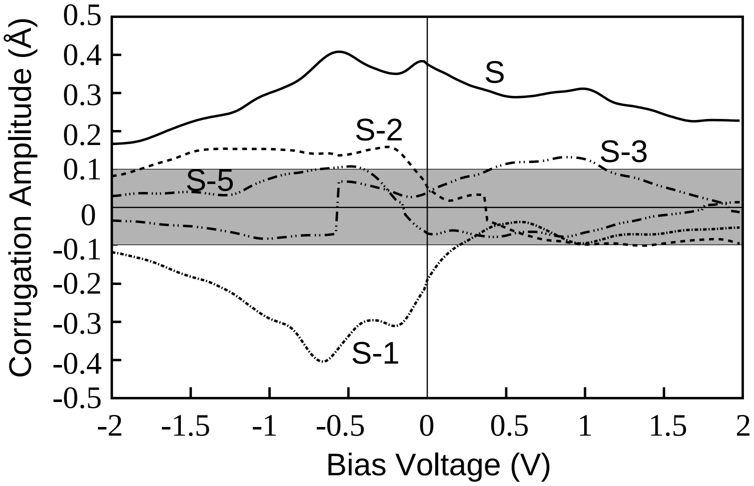

Figure 7.9: Comparison of corrugation amplitudes at a distance of $z_0 = 5.3$ Å for Ir impurities in Cu(001) calculated in the p(2×2) unit cell at different Cu coverage. Coverages of zero (S), one (S−1), two (S−2), three (S−3), and five (S−5) monolayers Cu are presented. Note, that the corrugation amplitude does not exceed a value of 0.1 Å for a coverage of five monolayers Cu.

7.9 Imaging Quantum-Well States

Already in elementary quantum mechanics the problem of a particle in a box is treated [5]. It is known that the energy eigenvalue spectrum is discrete and the eigenfunctions are standing waves. A similar situation occurs if a noble-metal, like Cu, with nearly free *sp*-electrons is grown pseudomorphically on a transition-metal substrate, like Co[2] or Ir. While the electrons of the noble-metal are still free in the lateral film direction they are confined in the direction perpendicular to the surface by the vacuum on one side and the transition-metal substrate on the other side which also produces a potential shift. For example, the $5d$-bands of Ir are located in the same energy range as the Cu sp-electrons resulting in a barrier for these Cu electrons. As a result a discrete set of nearly free electron bands develops which can be characterized by a wave vector k_z of values:

$$k_z = \frac{2\pi}{d}(n - \frac{1}{2}) \quad \text{with } n = 1, 2, 3, ..., \tag{7.2}$$

where d denotes the thickness of the film. The situation is a little bit more complicated in our case though. First of all, we do not have a crystal substrate but only one two-dimensional alloy layer (of Cu and Ir atoms) which is covered on both sides with monolayers of Cu(001) in the film calculation. Thus this barrier will not be as strong as that of a substrate. Still, a potential shift occurs at this layer possessing the lateral periodicity of the alloy layer. Since we are interested in changes of the corrugation amplitude the wave vector dependent selection rule discussed in section 4.6.2 requires that states near the $\bar{\text{X}}$-point and not near the $\bar{\Gamma}$-point of the 2D-BZ have to be investigated.

One technical aspect of the film calculations becomes important in these investigations, and it is necessary to rule out any influence on the results from the beginning. Every system described within the film geometry is actually a quantum well confined by vacuum barriers on both sides. Thus we find discrete bands in the 2D bandstructure where a continuous energy spectrum should occur from a projection of the bulk bandstructure. However, if the film thickness is increased the bands become denser and denser and the semi-infinite crystal is approximated better and better. Even though the bandstructure differs from the projection of the bulk bandstructure quantities calculated by Brillouin zone integrations describe the surface properties very well since the additional (bulk) bands are very similar to the ones included. For the present treatment of quantum-well states within our intrinsic film quantum wells, care has still to be taken that the observed effects are not caused by our particular geometry. This problem has been checked quite extensively in Ref. [77] for c(2 × 2) MnAg alloys in Ag(001). It was concluded there [77] that the film calculations provide the correct physics if a symmetric geometry of the buried layer is chosen [3] which we usually do in order to minimize the computational effort. To test the conclusion of Ref. [77] for the present system, i.e. Ir chains in Cu(001), we performed a calculation using an asymmetric 13 layer film where the p(2 × 1) CuIr alloy was covered by a monolayer of Cu(001) on one side and eleven monolayers Cu(001) on the other side. Thereby two inequivalent vacuum regions are created. Comparing the results for the star coefficients and corrugation amplitude plots of each vacuum region with the one from a symmetric film calculation with the same Cu coverage gave no qualitative dif-

---

[2] Co has been chosen as an example because it has become very famous in connection with spin-polarized quantum well states and was investigated thoroughly by photoemission [101].

[3] In the case of a coverage of five or more monolayers only one alloy layer is needed in order to create a sufficiently thick film. The alloy layer is then located at the center of the film.

ference. Thus, we can safely use our setup of a symmetric film to study the influence of quantum-well states on the STM images.

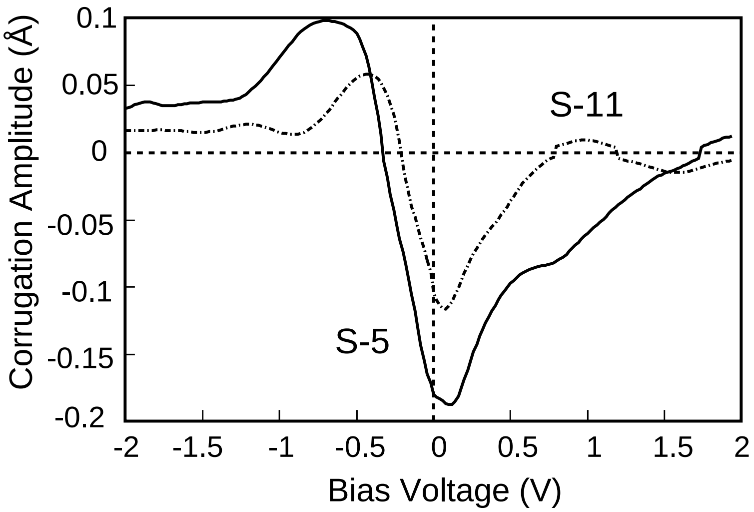

Figure 7.10: Comparison of the corrugation amplitudes as a function of the applied bias-voltage at a distance of $z_0 = 5.3$ Å for Ir chains buried beneath five (S−5) and eleven monolayers (S−11) of Cu(001). In both cases only one layer of the chain structure has been used which was located in the center of the film. There is a distinct increase in oscillations for the corrugation amplitude at a coverage of 11 monolayers caused by an increase of available quantum well states in the covering Cu layers. The sign convention from the previous sections has been used, i.e. a positive (negative) sign is related to imaging the Ir (Cu) chains as protrusions.

Fig. 7.10 displays the corrugation amplitudes for a coverage of five and eleven monolayers of Cu on the p(2 × 1) CuIr chain structure. Both curves show oscillations as a function of the bias-voltage leading several times to a sign reversal. For the five monolayer coverage the amplitude is well above 0.1 Å in a voltage regime of −0.2 V to +0.5 V, which is very large compared to the case of an Ir impurity atom (see Fig. 7.9). For the higher coverage there is a strong reduction of the amplitude but it is still justified to expect the possibility to observe the stripe pattern of the chains located at such an enormous depth. The overall similarity of the two curves is also quite striking although the number of oscillations increases for the larger coverage. This is related to an increased number of available quantum-well states in the thicker Cu film as we shall see in the following. The enhancement of the corrugation amplitude in the vicinity of zero bias-voltage can again be explained on the basis of the simple model discussed in section 7.7. This point is of importance, as in the end, it is responsible for the expectation of being able to observe the presence of the quantum-well states with an STM.

In order to understand the corrugation amplitudes shown in Fig. 7.10, it is again necessary to correlate the electronic structure, given by the energy bands and the density of states, with the calculated STM images, contained in the second star coefficient. The correlation is presented in Fig. 7.11 for the 11 layer (L) Cu(001)/p(2 × 1)

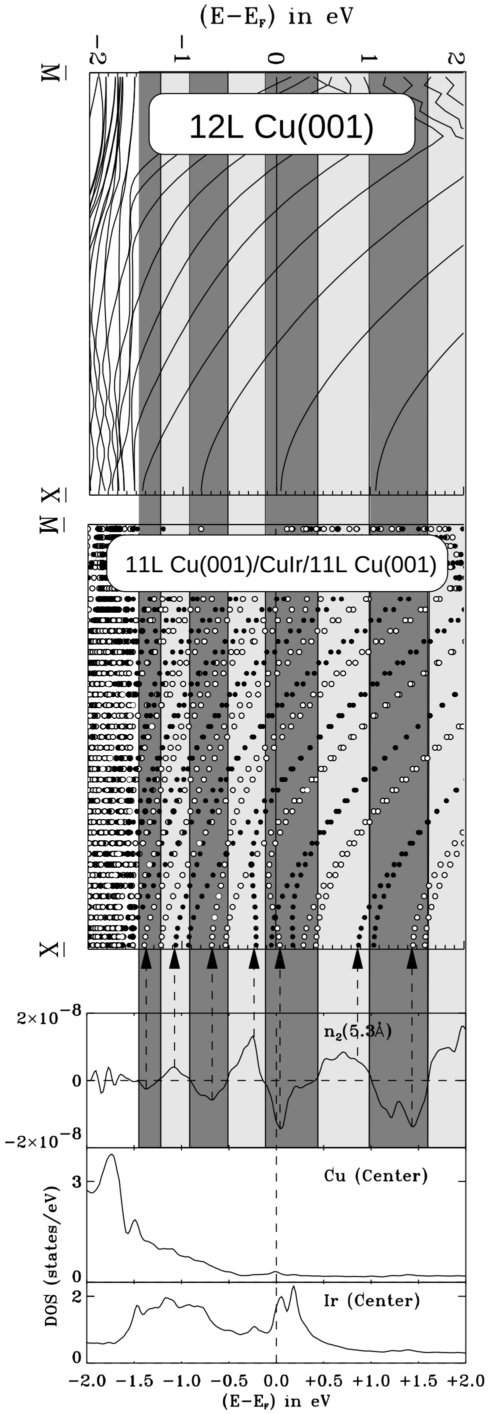

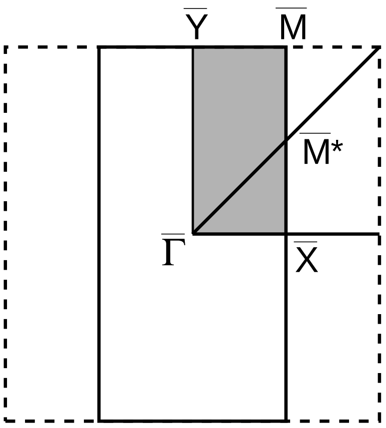

Figure 7.11: Comparison of band structure (middle panel), second star coefficient n_2 , and density of states (DOS) for the inner layer of the 11ML-Cu(001)/p(2 × 1) IrCu/11ML-Cu(001) structure with the bandstructure of a 12L-Cu(001) film (upper bandstructure). Shaded boxes mark energy ranges of positive and negative second star coefficient. The arrows indicate the correlation between the maxima in n_2 and bands at the $\bar{X}$-point of the 2D-BZ. Note, that the energy width of the sum of adjacent positive and negative boxes are equal to the energy differences between bands at the $\bar{X}$-point of the 12L Cu(001) film. Open (full) circles correspond to bands with an even (odd) symmetry with respect to a mirror plane perpendicular to the surface along the $\bar{X}\bar{M}$ direction.

CuIr/11L Cu(001) film calculation. The plot additionally includes the bandstructure of a pure 12L Cu(001) film in order to explain the creation of the quantum-well states[4]. Focus on the panel for the second star coefficient first. Starting at about $E_F - 1.5$ eV oscillations are setting in with an increasing period length and oscillation

---

[4] We will explain later why we are using a 12 layer film instead of 11 layers which seems more obvious.

amplitude as the energy increases. In the energy range of the oscillations Ir $5d$-bands are present while the Cu $3d$-bands end at the starting point of the oscillations (see the Cu and Ir DOS in the two lower panels). In the bandstructure of the 12L Cu(001) film we also notice the dense Cu $3d$-bands at the far left almost lacking any dispersion. At higher energies strongly dispersing Cu sp-bands appear with an increasing energy difference between adjacent bands (easily seen at the $\bar{\mathrm{X}}$-point of the upper panel). In the p(2 × 1) surface unit cell all of these bands are degenerate for the 12L Cu(001) film. The corresponding energy eigenstates possess charge densities of the same type but showing one or the other of the two atoms of the p(2 × 1) unit cell. Since these states are degenerate their contribution to a p(2 × 1) pattern cancels out and the STM-image shows all Cu atoms equally as required by symmetry for a pure Cu(001)-surface. That means n_2 is identical zero. However, if we replace one Cu atom of the center layer by an Ir atom creating a real p(2 × 1)-unit cell the degeneracy is lifted (see lower bandstructure plot) with bands splitting into a branch favoring the Ir atom position and another favoring the Cu atom position. Furthermore, the two states do not possess the same strength anymore since the Ir atom produces a shift in the potential. Thus the p(1 × 1) symmetry of the local charge density in the vacuum is broken and non-zero contributions to the second star coefficient, i.e. the p(2 × 1) pattern, are possible. The energy splitting is easily seen at the $\bar{\mathrm{X}}$-point of the bandstructure of the 11L Cu(001)/p(2 × 1) CuIr/11L Cu(001) film and its value amounts to about 0.15 eV. The band edge of one branch is always located inside a shaded area coinciding with a maximum or a minimum of the second star coefficient (see the arrows; note that there is one exception from this rule). The band edge of the other branch correlates with the sign reversals of the second star coefficient (see the boundaries of the shaded boxes). The energy splitting of bands is largest at the $\bar{\mathrm{X}}$-point and reduces to zero for the higher bands shown in the plot along the $\bar{\mathrm{X}}\bar{\mathrm{M}}$-line of the 2D-BZ. The oscillation period grows with increasing energy which is due to the larger energy differences between adjacent bands of the 12L Cu(001) film and the period length is in good agreement with these differences.

In a similar case of buried c(2 × 2) MnAg alloy layers in Ag(001) it has been demonstrated [77] that the energies of the sign reversals in the star coefficient are given by the band edges of the degenerate bands of the covering Ag(001)-film and the center between two adjacent ones. This is nearly fulfilled for the 11L Cu(001)/p(2 × 1) IrCu/ 11L Cu(001) if we choose a 12 layer Cu(001) for comparison. Using an 11L Cu(001) film leads to an even worse agreement which may be caused by the fact that the reflection of electron waves confined in the covering Cu-film takes place rather beneath the two-dimensional CuIr alloy layer than above it. Another reason why the sign reversals do not correlate as nicely as for the MnAg case is connected to the wide spread of the bands in the 2D-BZ. This makes the attempt of using a single high symmetry line for the correlation inappropriate. Thus it is necessary to take a look at the star coefficient as a function of the wave vector $\mathbf{k}_{\|}$ which is done in the following.

Fig. 7.12 and Fig. 7.13 show the plots of the first and second star coefficient, respectively, in the 2D-BZ in an energy range of (−1.4 eV,+1.4 eV) around the Fermi energy. Let us start with the first star coefficient which is limited to positive

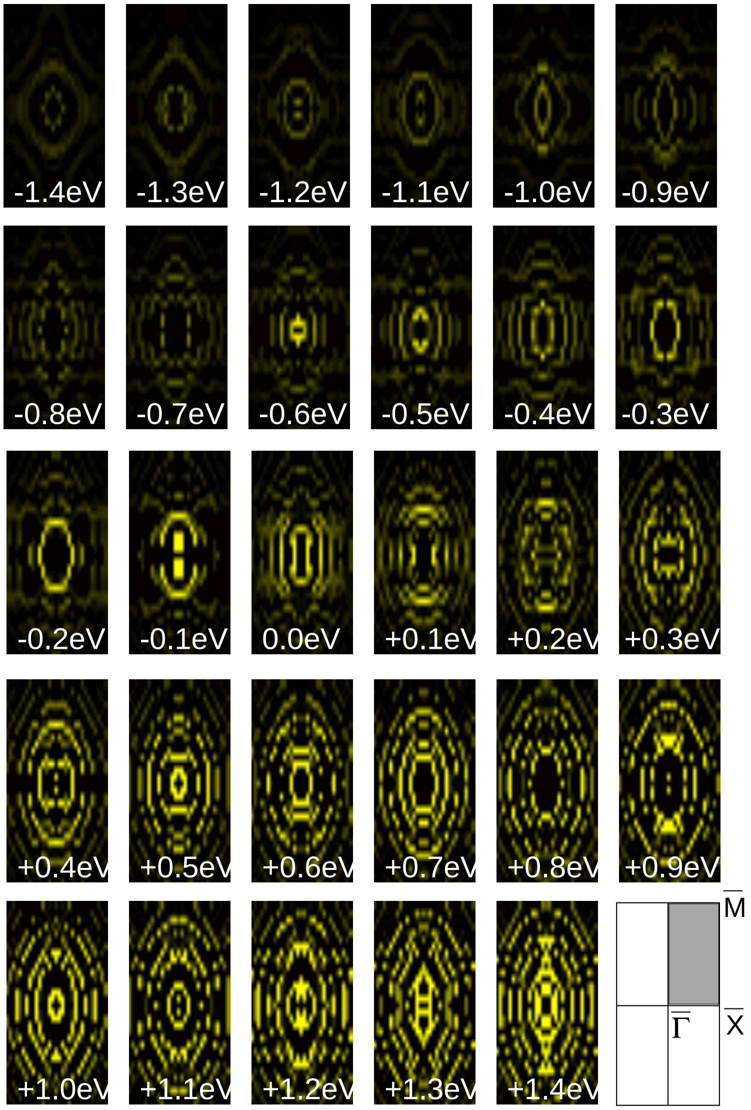

Figure 7.12: First star coefficient of the 11L Cu(001)/p(2×1) CuIr/11L Cu(001) film at a distance of $z_0 = 5.3$ Å from the surface as a function of the wave vector $\mathbf{k}_{\|}$ in the 2D-BZ at different energies relative to the Fermi energy. Intervals of 0.1 eV and a mesh of 512 $\mathbf{k}_{\|}$-points have been chosen. The scaling is the same for all plots which is the reason that the plots at higher energies give the impression of equally important contributions from the entire BZ. At low energies the focusing to states near the $\bar{\Gamma}$-point is clearly visible.

values as it is related to the lateral constant part of the local charge density in the vacuum (see section 4.6.1). As expected the highest contribution results from states near the $\bar{\Gamma}$-point of the BZ and we can observe the different parabolic *sp*-bands as ellipses. These plots give an impression of the bandstructure.

Now we turn to the plots for the second star coefficient, presented in Fig. 7.13, where positive and negative values are possible which are marked by yellow and red scales while black areas denote a zero value. Again, our expectation of high contributions from a high symmetry point is fulfilled which is the $\bar{\mathrm{X}}$-point in this case. We can correlate these plots once more with the oscillations of the second star coefficient as a function of energy shown before. We start with a negative BZ-integrated value at $E_F - 1.4$ eV due to bands close to the $\bar{\mathrm{X}}$-point. Because of their dispersion they move away from the $\bar{\mathrm{X}}$-point with increasing energy and new bands with a positive contribution appear at the $\bar{\mathrm{X}}$-point. These shift as well and new bands with negative values are seen. In this manner oscillations of the second star coefficient are created. Thus our interpretation of the bandstructure which did not contain the

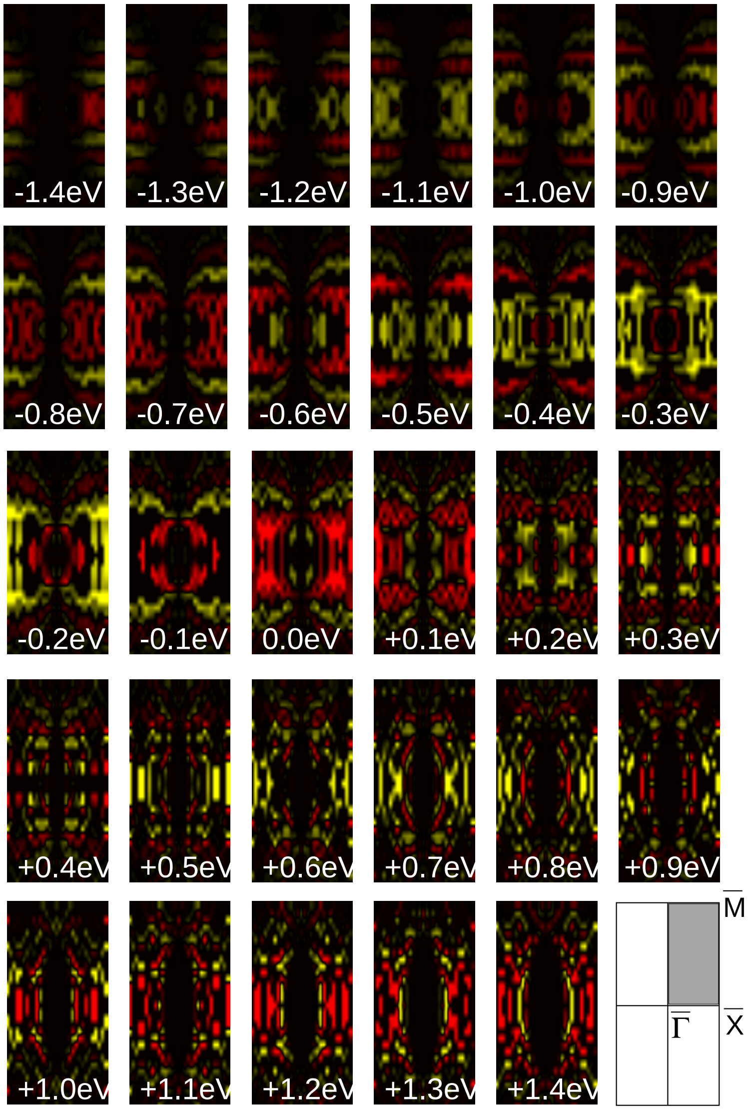

Figure 7.13: Second star coefficient of the 11L Cu(001)/p(2×1) CuIr/11L Cu(001) film at a distance of $z_0 = 5.3$ Å from the surface as a function of the wave vector $\mathbf{k}_\parallel$ in the 2D-BZ at different energies relative to the Fermi energy. Yellow corresponds to positive and red to negative contributions while black areas denote the zero. Intervals of 0.1 eV and a mesh of 512 $\mathbf{k}_\parallel$-points have been chosen. The scaling is the same for all plots which is the reason that the plots at higher energies give the impression of equally important contributions from the entire BZ. At low energies the focusing to states near the $\bar{\mathrm{X}}$-point is clearly visible.

information of the second star coefficient for specific bands is justified by these plots. It is also possible to observe the reduced splitting as bands move to the $\bar{\mathrm{M}}$-point since there are almost no contributions from this area. On the other hand, we do find major contributions in quite a large area around the $\bar{\mathrm{X}}$-point making it necessary to go beyond the discussion of one high symmetry line of the BZ only. Especially at the high absolute values of the second star coefficient at about $E_F - 0.2$ eV and $E_F + 0.05$ eV one needs to take the entire BZ into account in order to find the responsible states.

At the end of the discussion, after having related the origin of the oscillations to the formation of quantum-well states with the covering 11 layers of Cu(001), we can plot the responsible states in real space to get an impression of their appearance. The states shown here are representative for all energies at the $\bar{\mathrm{X}}$-point. Fig. 7.14 shows two cross-sections through the film for the two branches of a split band at the $\bar{\mathrm{X}}$-point. We can nicely see the close relation between the two states if we compare Fig. 7.14(b) and Fig. 7.14(d), which show the sections with only Cu atoms. There

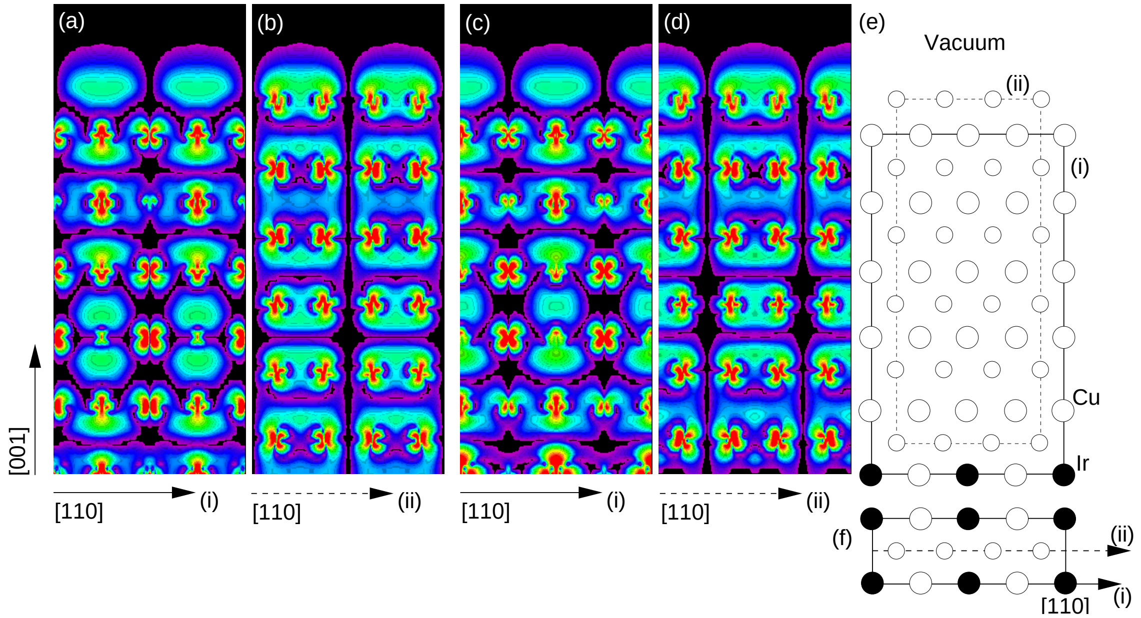

Figure 7.14: Quantum well states at the $\bar{X}$-point of the 2D-BZ for the Ir chains covered by 11 monolayers of Cu(001). (a) and (b): Cross-sections (i) and (ii) through the 2D unit cell (see also (e) and (f)) for the quantum well state with an energy of $E_F - 0.7$ eV, and (c) and (d): the same for $E_F - 0.5$ eV. (e) and (f) show the film unit cell. Note, that the two states possess an opposite second star cofficient, i.e. at an energy $E_F - 0.7$ eV the Cu chains are seen as protrusions while the Ir chains are visible at $E_F - 0.5$ eV.

is a canting of sp-orbitals, as discussed for the STM images of the Ir chains buried beneath only one Cu layer, and the two states differ only by a shift of half a lattice vector of the p(2 × 1) unit cell. A similarity can also be seen for the two other cross-sections, Fig. 7.14(a) and Fig. 7.14(c). Along the z-direction two different types of orbitals occur, one being a d_{xz}- and the other a d_{z^2}-type. Thus the quantum-well states are not exclusively of sp-character but hybridize also with d-states. If the state possesses a d_{z^2}-orbital at the Ir (Cu) atom of the inner layer the STM image displays a protrusion above the Ir (Cu) atom. The characteristic oscillations of quantum-well states along the axis of confinement, the [001]-axis in our case, can also be seen in Fig. 7.14(a) and Fig. 7.14(c) but with a phase shift between the oscillations above the Ir and Cu atom. This phase shift is due to the corrugated potential of the confining inner layer.

Although the experimental verification of imaging the quantum-well states of buried Ir chains in Cu(001) is still missing, there is justified hope that it will be achieved soon. On one hand, it seems to be possible to prepare these structures since the Ir chain alloy in the subsurface position is quite stable and one may thus grow additional layers of Cu without destroying the alloy underneath. On the other hand, there has been an analogous work by Altfeder *et al.* [102] where Pb has been deposited on the famous Si(111) (7 × 7)-reconstruction. The unit cell of the buried Si-structure was still observable at a coverage of 100 Å of Pb. Even a contrast inversion of the images as a function of the applied bias-voltage were reported in accordance with the expectations from the present study.

Chapter 8

Influence of Thin Film Magnetism on STM and STS

In the field of low-dimensional magnetism there is a huge current interest in the development of well-defined nanomagnets, laterally and vertically structured ultra-thin films, or magnetic nanowires [103]. These systems are expected to open new vistas for magneto-electronics and magneto-optics. Thus, there is a great demand to investigate magnetic properties in real space on the nanometer and even down to the atomic scale. Ideally suited to cope with these demands is a spin-polarized scanning tunneling microscope (SP-STM) combining the high resolution of common STM with magnetic sensitivity. In order to achieve magnetic sensitivity several approaches have been proposed [23–28]. Recently, the coating of the STM tips with a thin film of a ferromagnetic material like Fe or Gd has proved to be very successful [26, 27]. A recent highlight of this method will be discussed in chapter 9.

In the future, this approach will doubtlessly lead to new insight into the field of nano-magnetism but it is still quite sophisticated and not yet commonly applicable. Therefore, we take a different theoretical route in this chapter, which is to explore the feasibility to distinguish different magnetic configurations by probing the local electronic structure applying non-spinpolarized STM and scanning tunneling spectroscopy (STS). Very recently STS combined with *ab initio* electronic structure calculations was successfully applied for bcc-(001) transition-metal surfaces. For Cr(001) and Fe(001) [66] characteristic STS peaks were identified as d_{z^2}-surface resonances and were used to distinguish between Cr and Fe on the atomic scale, which is otherwise impossible. This form of chemical identification was applied to investigate the growth of Cr on Fe(001) [94]. It led to the experimental evidence of the formation of a two-dimensional CrFe surface alloy with random occupation of substitutional Cr atoms with repulsive Cr-Cr interaction and a local c(2×2) order. Until now, STS on metal surfaces and particularly on magnetic surfaces is not widely applied. In this chapter we investigate cases where STM and STS makes the discrimination of magnetic configurations possible. Further we point out the additional benefit of SP-STM for these systems.

We take Cr on Fe(001) and Mn on Fe(001) under close scrutiny. Both systems present case studies for this type of problem. For example theoretical investigations on Cr and Mn monolayers on Fe(001) [104] show several magnetic states in close energetic vicinity. Particularly Mn/Fe(001) [105–111] draws a large attention and several recent experiments report on partly contradictory magnetic couplings of Mn with Fe as a function of the coverage, growth mode and temperature, which ranges from non-magnetic to ferromagnetic and antiferromagnetic configurations. This indicates a complicated relationship between growth condition, electronic structure, and magnetic coupling, which is ideal to be tackled by a real space probe. The magnetism of 1 ML Cr and Mn on Fe(001) [105] as well as the surface alloy formation of a c(2×2) CrFe/Fe(001) and MnFe surface alloy has been investigated theoretically [112]. The different considered magnetic configurations for these systems are presented in Fig. 8.1, and the corresponding ground-state configurations for the 3*d*-elements are displayed in Fig. 8.2.

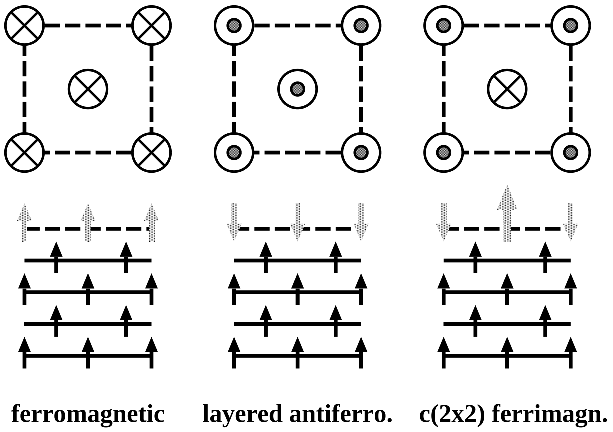

Figure 8.1: Schematic representation of a ferromagnetic, a layered antiferromagnetic, and a c(2×2) (anti)ferrimagnetic superstructure of a monolayer film (broken line) grown as overlayer on a magnetic substrate (full line). Upper panel is a view onto the surface, lower panel shows sideviews. Arrows indicate the relative spin direction at the positions of the atoms. Figure has been taken from Ref. [104].

In the case of Cr monolayers the layered antiferromagnetic state is found to be the ground-state although it is nearly degenerate to the c(2×2) (anti)ferrimagnetic solution (see Fig. 8.2). As a consequence of the small energetic difference it cannot be excluded that there is a transition from one magnetic state to the other during the monolayer formation from islands [113]. Experimentally it was observed that conditions normally used for layer-by-layer growth lead to a surface alloy formation in the case of Cr [94]. Cr monolayers have not been stabilized experimentally yet, although such temperature regimes might exist. For Mn the monolayer ground-state, as calculated by *ab initio* methods (see Fig. 8.2), is the c(2×2) (anti)ferrimagnetic configuration. The tendency to alloying has not yet been investigated with a real space probe for Mn. *Ab initio* calculations predict a behavior similar to Cr [112, 114] in contrast to recent experiments which claim to find growth of perfect monolayers [108, 110]. In the first part of this chapter we focus on the relationship between magnetic configurations and scanning tunneling spectra and answer the question

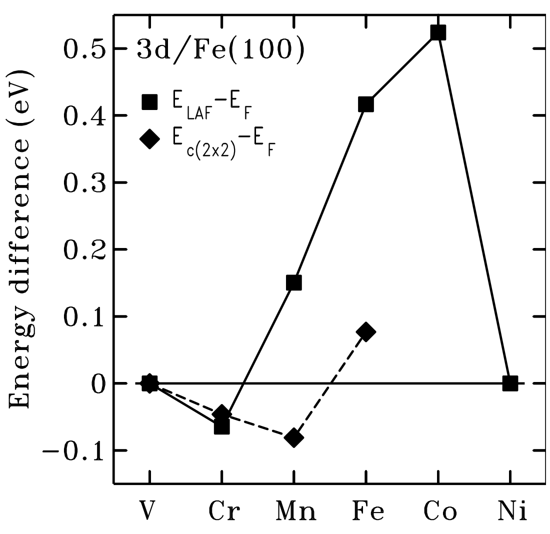

Figure 8.2: Total energy difference $\Delta E_1 = E_{LAF} - E_F$ between the p(1×1) layered antiferromagnetic and the ferromagnetic coupling (solid squares connected by solid lines) and $\Delta E_2 = E_{c(2\times2)} - E_F$ between the c(2×2) ferrimagnetic and the p(1×1) ferromagnetic coupling (solid diamonds connect by dashed lines) of 3*d* transition–metal monolayers with Fe(001). The ferromagnetic (layered antiferromagnetic or ferrimagnetic) coupling is energetically preferred for $\Delta E > 0$ (< 0). The layered antiferromagnetic coupling is preferred over the ferrimagnetic one if $\Delta E_1 < \Delta E_2$. Figure has been taken from Ref. [104].

whether different magnetic configurations can be distinguished by STS for these systems. The excellent agreement we find between calculated and measured ST-spectra in the case of the CrFe surface alloy as well as that of earlier *ab initio* calculations for the Fe(001)-surface [66,67] gives us the confidence to carry on to a system which has not been studied by STM up to now, i.e. Mn on Fe(001).

In the second part the influence of the magnetic configuration on the expected STM image is investigated and consequences of using a spin-polarized STM are pointed out. Since we are using a ferromagnetic substrate, Fe(001), the electronic structure of the two 3*d*-atoms in the c(2×2) antiferrimagnetic structure is not equivalent and thus even with non-spinpolarized STM an image differing from the chemical p(1 × 1) unit cell might occur. If on the other hand a non-magnetic substrate is used the two antiferromagnetic coupling atoms of the monolayer are indistinguishable by common STM as we will discuss in the following chapter.

8.1 Computational Details

The calculations of the electronic structure were performed using the local spin-density approximation of Barth and Hedin [29] in the parameterization by Moruzzi, Janak and Williams [72]. The films consisted of 7 layers Fe(001) in the c(2×2) two-dimensional (2D) unit cell covered by one layer of the monolayer or surface alloy on each side giving a total of 9 layers. The theoretical lattice constant of Fe has been used ($a_0^{Fe} = 5.23$ a.u.), and for the monolayers the relaxed interlayer distances according to Ref. [104] were taken, while the surface alloys were calculated in the perfect geometry.

The basis set used for the valence states consisted of about 80 augmented plane waves per atom. Non-spherical terms in the potential, charge density, and wave functions are expanded within the muffin-tin spheres with radii $R_{MT}^{Fe,Cr} = 2.151$ a.u. and $R_{MT}^{Mn} = 2.171$ a.u. up to $l_{max} \leq 8$. The self-consistent electronic structure was determined with 10 special $\mathbf{k}_{\|}$-points in the irreducible wedge of the 2D-BZ (I2BZ).

System	M (μ_B)	ϕ (eV)	d_{surf} (%)	ΔE (meV)
Cr-ML				
F	$+1.01$	5.2	-5.0	$+110$
LAF	-1.40	5.1	-7.3	0
c(2×2) AF	$+0.64/-1.83$	5.3	$-5.0/-5.0$	$+53$
c(2×2) AF	$-0.02/-1.59$	5.3	$-5.0/-7.3$	$+37$
Mn-ML				
F	$+3.28$	4.7	$+5.40$	$+100$
LAF	-3.03	4.7	-0.25	$+228$
c(2×2) AF	$+2.95/-3.26$	5.0	-0.25	0
c(2×2) AF	$+3.09/-3.26$	4.9	$+5.40/-0.25$	$+27$
CrFe				
AF	$-2.54/+2.50$	5.4	0/0	$+16$
AF	$-2.33/+2.48$	5.5	$-6.9/0$	0

Table 8.1: Table of calculated moments M, work functions ϕ, interlayer distances d_{surf} and relative energies of all presented systems on Fe(001) (notice that the c(2×2) AF configuration has been calculated in two geometries). The moments are given for the Cr and Mn atoms. For the surface alloys the second value is that of the Fe surface atom. Notice that positive values indicate ferromagnetic alignment with respect to the Fe-substrate, and in the case of the c(2×2) AF configuration of the ML there are two inequivalent atoms. The interlayer distance is given relative to the unrelaxed value of 2.615 a.u. . The energies are given in meV per surface atom relative to the ground state. Work function measurements usually provide chemical sensitivity in STM on a large scale. The calculated work function of the pure Fe(001)-surface is 4.5 eV which should be kept in mind as a reference value.

The LDOS has been analyzed using 465 $\mathbf{k}_{\|}$-points in the I2BZ.

8.2 The Fe(001)-Surface

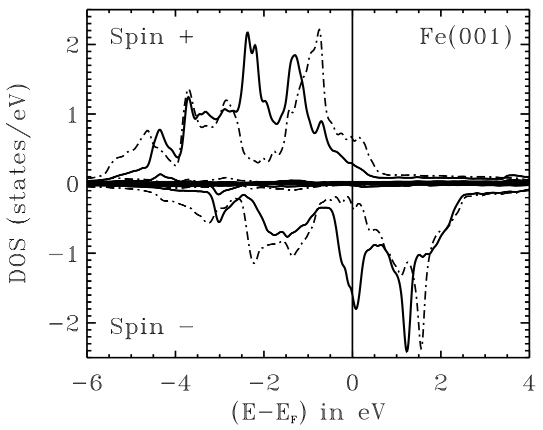

Figure 8.3: Calculated spin-resolved muffin-tin density of states for bulk (dashed-dotted line) and surface atoms (full line) of the ferromagnetic Fe(001)-surface. A surface state is clearly visible in the majority and minority surface DOS at an energy $E_F - 2.4$ eV and $E_F + 0.19$ eV, respectively. The calculation has been performed using a 31 layer thick film, a lattice constant of a= 5.205 a.u. and the parametrization of the local density approximation of Vosko, Wilk, and Nusair [32].

As an introduction to the field of STS in combination with *ab initio* calculations we discuss the clean Fe(001)-surface in this section. The results computed for the monolayers and surface alloys possess a lot of similarities with this case because of the geometrical and chemical relationship. The Fe(001)-surface has been studied by Stroscio *et al.* [66] in connection with STS and was the first example of a metal surface with a characteristic d-band related feature in scanning tunneling spectroscopy. Fig. 8.3 displays the density of states (DOS) calculated for the surface and bulk atoms. In the pseudo gap between bonding and antibonding states of the majority and minority bulk DOS, shifted against each other by the exchange splitting, the surface DOS has a sharp peak. This feature is located slightly above the Fermi energy (+0.19 eV) in the minority spin channel and is caused by a surface resonance state of d_{z^2} character at the $\bar{\Gamma}$ point of the 2D-BZ [66].

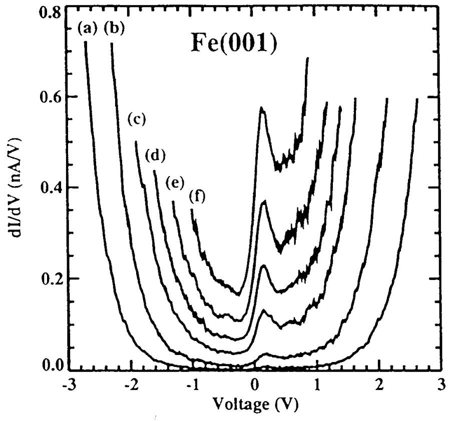

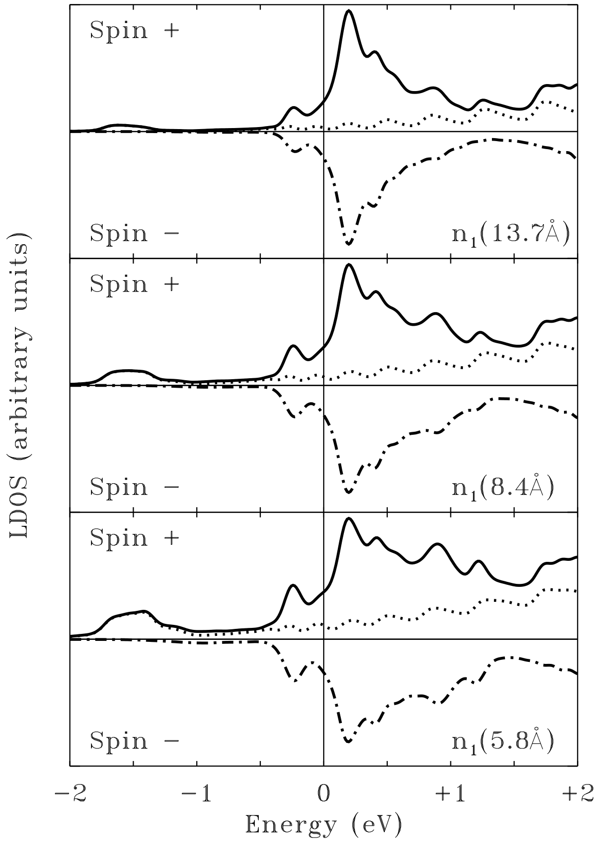

Figure 8.4: Lateral constant part of the LDOS in the vacuum, $n_1(z)$, of the Fe(001)-surface calculated at three different distances z from the surface. The dotted (dashed-dotted) curve represents the majority (minority) electron contribution while the full line is the sum of both. The d_{z^2}-surface state peak in the minority channel is clearly visible at an energy of about +0.19 eV which decays much slower than all other states. The experimentally measured spectrum, taken from Ref. [66], is shown for comparison above. Curves (a)-(f) correspond to decreasing distances between tip and sample obtained with different stabilizing conditions.

Being located at the center of the 2D-BZ this state decays rather slowly into the vacuum (see section 4.6.2). Thus, it is also present in the calculated lateral constant part of the local DOS (LDOS) in the vacuum given by the first star coefficient

$n_1(z)$[1] (Fig. 8.4). The displayed LDOS is directly comparable to the measured spectrum of STS within the Tersoff-Hamann model (see Eq. (4.31)), and one finds an excellent agreement with the experiment (see Fig. 8.4). A similar state is found for the Cr(001)-surface located at -0.05 eV (see Fig. 8.5). This d_{z^2} surface resonance, characteristic for bcc-(001) transition metal surfaces, encouraged the idea of gaining chemical sensitivity by scanning tunneling spectroscopy. In the following sections, we check on the applicability of this method when several structural and magnetic configurations become possible. It is difficult to decide upon such a situation only from experiment. On the other hand, this state is also promising for the imaging of magnetic domains by SP-STS (see section 4.5) due to the high spin-polarization of the LDOS at its energy (see Fig. 8.4).

8.3 The c(2×2) CrFe Surface Alloy

The experimental situation of Cr on Fe(001) as described in Ref. [94] shows the tendency of Cr atoms to change places with Fe atoms of the substrate. These lifted Fe atoms form islands on the surface while the Cr atoms are incorporated into the surface layer and some diffuse into deeper layers of the Fe-substrate. The Cr atoms in the surface layer do not cluster but exist as single impurities at low coverage and form a disordered surface alloy at higher coverage. Locally, this surface alloy possesses a c(2×2) symmetry which has therefore been chosen as the 2D-unit cell of the calculation. Cr impurities are also incorporated into the newly formed Fe-islands but no islands consisting mainly of Cr have been observed. These conclusions upon the growth of Cr on Fe(001) have been drawn on the basis of STS-experiments. Fig. 8.5 displays the ST-spectra of this experiment in comparison with our calculation of the LDOS above the CrFe surface alloy. The scanning tunneling spectroscopy on this system revealed the above facts in the following manner. If the STM-tip is positioned above the original surface or the formed islands far away from any impurity, which are clearly visible in the topography mode, the measured spectrum is identical to that of the clean Fe(001)-surface (see Fig. 8.5), i.e. it shows the known d_{z^2} surface resonance peak (see section on Fe(001)). On the other hand, near to any impurity, in islands as well as in the substrate, the spectrum displays two small features at about -0.3 V and $+0.25$ V (see Fig. 8.5). Thereby it was concluded that the islands consist of Fe atoms lifted to the surface by exchange processes with adsorbed Cr atoms while all impurities are of the same chemical species, namely Cr.

To verify these conclusions, we compare the calculated LDOS on top of the Cr atom in the surface alloy with the experimental spectrum (see Fig. 8.5). One finds two peaks in the LDOS near the Fermi energy located at -0.5 eV and $+0.15$ eV. The energy difference is thus 0.65 eV which is in good agreement with the measured difference of 0.55 V. The shift of about 0.1 V with respect to the experiment is within the accuracy of the calculation since the theoretical lattice constant has been used. Notice also that the occupied state is a rather broad feature while the unoccupied

---

[1] As STS measurements on the Fe(001)-surface are not performed with atomic resolution one does not need to consider higher star coefficient contributions related to a lateral variation of the LDOS.

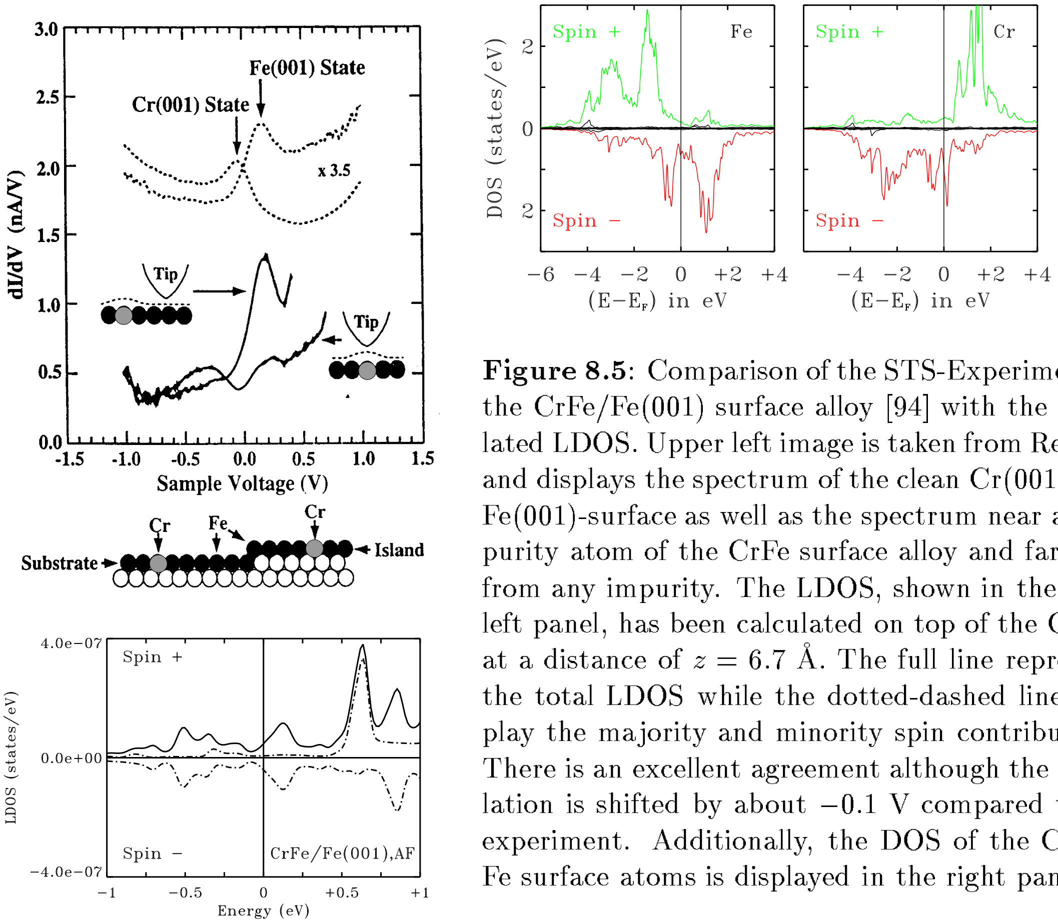

Figure 8.5: Comparison of the STS-Experiment on the CrFe/Fe(001) surface alloy [94] with the calculated LDOS. Upper left image is taken from Ref. [94] and displays the spectrum of the clean Cr(001)- and Fe(001)-surface as well as the spectrum near an impurity atom of the CrFe surface alloy and far away from any impurity. The LDOS, shown in the lower left panel, has been calculated on top of the Cr site at a distance of $z = 6.7$ Å. The full line represents the total LDOS while the dotted-dashed lines display the majority and minority spin contributions. There is an excellent agreement although the calculation is shifted by about −0.1 V compared to the experiment. Additionally, the DOS of the Cr and Fe surface atoms is displayed in the right panel.

state is quite sharp. This is in accordance with the experimental observation (see Fig. 8.5). In conclusion, one can be confident that these states are the origin of the STS peaks. Still, one must keep in mind that the result is based on an ordered c(2 × 2) surface alloy and not a true impurity calculation. There might thus be changes which need to be investigated in the future.

Since the unoccupied state is close in energy to the original d_{z^2} surface resonance of Fe(001) it was speculated in Ref. [94] that it is closely related to it. Our calculations reveal that this state is indeed a strongly localized d_{z^2} surface state although with origin at the Cr, not the Fe atom. It lies at the $\bar{\mathrm{X}}$ point of the 2D-BZ and therefore even atomic resolution should be possible in STM at a small positive bias voltage using this state. The charge density of this state (Fig. 8.6) further illustrates these statements.

The occupied state, appearing in the ST-spectrum, on the other hand, results from a state with strong hybridisation between the Cr and Fe surface atoms. This can be concluded from the DOS (Fig. 8.5) and also from the charge density maps (Fig. 8.6). In contrast to the localized unoccupied d_{z^2}-state it displays a considerable dispersion in the $\bar{\Gamma}\bar{\mathrm{X}}$ and $\bar{\Gamma}\bar{\mathrm{M}}$ direction of the 2D-BZ. As a result it appears broader in the LDOS of the atoms and in the vacuum also (see Fig. 8.5).

We have studied the effect of buckling on the calculated LDOS by relaxing the Cr atom to the interlayer distance of the relaxed antiferromagnetic Cr monolayer

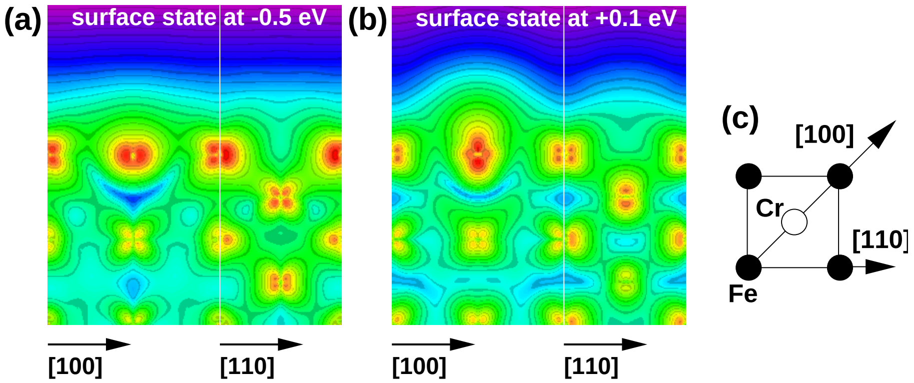

Figure 8.6: Charge density plots of the two surface localized states in the c(2 × 2) CrFe surface alloy on Fe(001) responsible for the peaks in the calculated LDOS (see Fig. 8.5). (a) shows the occupied state which is evenly localized in the alloy layer and (b) the unoccupied state which is strongly localized and of d_{z^2}-type at the Cr site. (c) displays the surface unit cell of the c(2 × 2) for orientation.

and found no significant change neither in the position nor the charge density of the discussed states. The small difference in moment of the Cr atom ($0.2\,\mu_B$, see Table 8.1) has no influence on these states.

8.4 STS of Cr and Mn Monolayers on Fe(001)

In this section we present calculations on the lateral constant part[2] of the LDOS in the vacuum $n_1(z)$, which are equivalent to ST-spectra within the Tersoff-Hamann model (see Eq. (4.31)), for the different magnetic configurations of the Cr and Mn monolayers on Fe(001). On one hand, the aim is to point out difficulties and possibilities in distinction between the magnetic configurations on the basis of STS. On the other hand, we check whether peaks in the LDOS remain characteristic for a certain chemical species when different structural and magnetic configurations may occur that cannot be deduced from other findings.

Fig. 8.7 displays the calculated spectra, i.e. the first star coefficient $n_1(z)$, and the DOS of the two atoms of the c(2 × 2) unit cell of the calculation for a Cr-monolayer on Fe(001). For the p(1 × 1) ferromagnetic and p(1 × 1) layered antiferromagnetic the two atoms are equivalent and the c(2 × 2) unit cell[3] becomes superficial but for the c(2 × 2) antiferrimagnetic configuration the two atoms are inequivalent. The DOS of the Cr atoms has been displayed for a wide energy range ($E_F - 6$ eV to $E_F + 4$ eV) in order to get an impression of the whole bandstructure. The LDOS in the vacuum has

---

[2] Strictly speaking the restriction to the lateral constant part applies only if the STS measurements are taken without atomic resolution which is the case for such small 2D unit cells. In the following we will for brevity always use LDOS meaning only its lateral constant part.

[3] In order to compare the total energies one must calculate all magnetic configurations within the same 2D unit cell.

only been plotted in an interval of ±1 eV around E_F since this is the energy range accessible with STS.

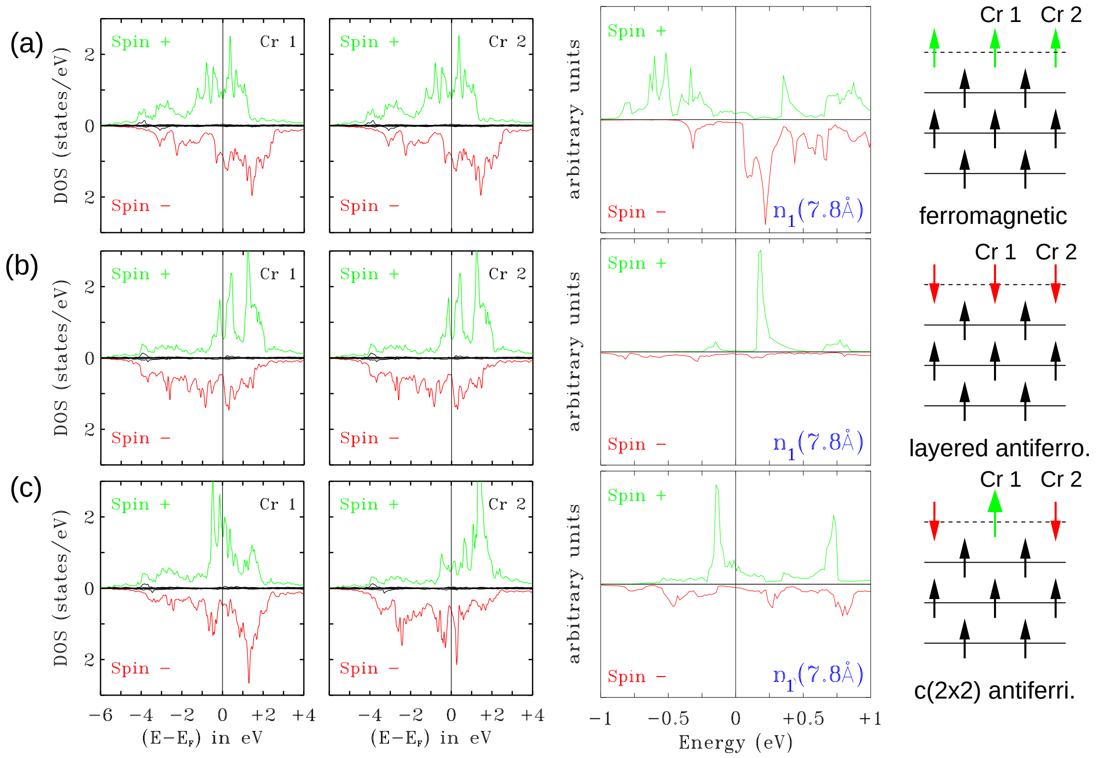

Figure 8.7: Density of states of the two surface Cr atoms of the c(2 × 2) surface unit cell used in the calculation and the lateral constant part of the LDOS in the vacuum given by the first star coefficient $n_1(z)$ at $z = 7.8$ Å for the different magnetic configurations of a Cr monolayer on Fe(001). Plots show the majority (Spin +) and minority (Spin −) contributions. (a) displays the p(1 × 1) ferromagnetic, (b) the p(1 × 1) layered antiferromagnetic, and (c) the c(2 × 2) antiferrimagnetic configuration. The corresponding magnetic configurations are sketched at the far right. Note, that the two surface Cr atoms are equivalent for (a) and (b) but different in (c). The energy range of the LDOS in the vacuum has been restricted to $E_F \pm 1$ eV since this is the experimentally important energy range in STS.

We observe a highly structured spectrum for the ferromagnetic configuration (Fig. 8.7a) with a dominating minority state peak at about +0.2 eV. This state is situated at the same energy as the known d_{z^2}-surface resonance of the clean Fe(001)-surface (see section 8.2) and also results from minority states with d_{z^2}-character at the $\bar{\Gamma}$-point of the 2D-Brillouin zone. Since the other strong features lie quite high in energy and may in practise not be available it is impossible to distinguish the ferromagnetic Cr monolayer from the pure Fe(001)-surface on the basis of STS (non-spinpolarized as well as spin-polarized). The layered antiferromagnetic configuration (Fig. 8.7b) which is the ground state configuration for Cr (see Fig. 8.2) displays once more a feature at an energy of +0.2 eV but resulting from the majority and not the minority states. The peak lies in the pseudo gap between the Fe-majority states which are fully occupied (compare Fig. 8.3) and the Cr-majority states which are almost fully unoccupied (Fig. 8.7b). It results from a state located at the $\bar{\Gamma}$ point of the 2D-BZ which possesses d_{z^2}-character. As this state lies at the same energy as the Fe(001)-surface resonance the indistinguishability between the monolayer and the pure Fe(001)-surface still holds for this magnetic configuration on the basis of non-spinpolarized STS. However, spin-polarized STS should lead to a difference because the feature of the Cr-monolayer originates from majority states while the d_{z^2}-surface resonance of the Fe(001)-surface is a minority spin state. By mapping the dI/dV-signal of a spin-polarized STS measurement (see section 4.5) a clear contrast between areas of the Cr-monolayer and the Fe(001)-surface should thus be observed. An important remark has to be made concerning the experiment of Davies *et al.* [94] discussed in the previous section. The islands which formed on the surface after Cr deposition were identified to consist of Fe atoms on the basis of the ST-spectrum displaying a sharp peak at +0.2 V. However, this feature appears also in our calculation for the layered antiferromagnetic Cr monolayer as discussed above. Thus it should be impossible to tell the chemical difference by STS. Fortunately, their interpretation of intermixing has been verified by a different technique, Auger-electron spectroscopy [110], and need not be regarded with doubt. For future studies it should be kept in mind though that such interpretations based on STS can be misleading if materials of very similar electronic structure are present and the structural differences are small.

Finally, there are two majority state peaks for the c(2×2) (anti)ferrimagnetic configuration (Fig. 8.7c) at −0.15 eV (d_{z^2}) and +0.7 eV resulting from the ferromagnetic and antiferromagnetic coupling Cr atom, respectively, as can be seen by comparing to the DOS. These two significant peaks should provide a possibility to distinguish this magnetic state from the layered antiferromagnetic and ferromagnetic situation as well as from the pure Fe(001)-surface. Two further remarks are worth being made. First, there are two minority state features appearing at −0.5 eV and +0.2 eV caused by states localized at the antiferromagnetic Cr atom, which have no impact on the total spectrum since the mentioned occupied majority state is of a much larger value. However, it is these states which dominated the CrFe-surface alloy as has been discussed in the previous section. Since they appear also for the monolayer we conclude that their occurrence is only due to the antiferromagnetic coupling of one Cr atom to the Fe substrate. Second, one can find a spin split partner of the majority state at +0.7 eV connected to the ferromagnetically coupled Cr atom with only slightly higher energy. Therefore it does not produce an extra peak in the total spectrum. This is altered for the Mn-monolayer as we will learn below.

The influence of buckling turns out to be of more importance for the c(2×2) (anti)ferrimagnetic configuration of the Cr monolayer than it was for the CrFe surface alloy. Relaxing the antiferromagnetically coupled Cr atom inward by another 2 % (see Table 8.1) results in a damping of all peaks mentioned above relative to the occupied d_{z^2} surface state. This is due to the fact that all these damped states originate from the (antiferromagnetic) inward relaxed Cr atom increasing their vacuum barrier relative to that of the d_{z^2} state. The dominating role of the d_{z^2} state is hence strengthened. Further, it shifts in energy to a value of −0.05 eV and is now located at the same energy as the d_{z^2} surface resonance of the pure Cr(001)-surface [66]. One is

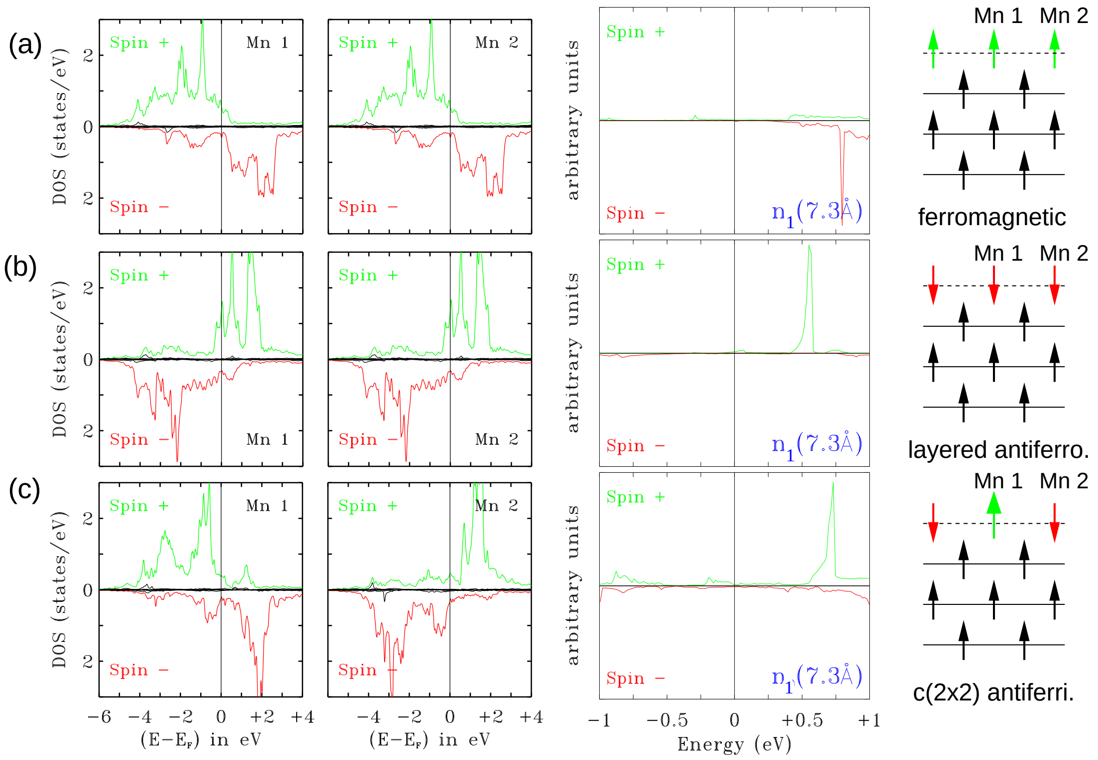

Figure 8.8: Density of states of the two surface Mn atoms of the c(2 × 2) surface unit cell used in the calculation and the lateral constant part of the LDOS in the vacuum given by the first star coefficient $n_1(z)$ at $z = 7.3$ Å for the different magnetic configurations of a Mn monolayer on Fe(001). Plots show the majority (Spin +) and minority (Spin −) contributions. (a) displays the p(1 × 1) ferromagnetic, (b) the p(1 × 1) layered antiferromagnetic, and (c) the c(2 × 2) antiferrimagnetic configuration. The corresponding magnetic configurations are sketched at the far right. Note, that the two surface Cr atoms are equivalent for (a) and (b) but different in (c). The energy range of the LDOS in the vacuum has been restricted to $E_F \pm 1$ eV since this is the experimentally important energy range in STS.

not able to tell the difference between both morphologies anymore on the basis of STS. To measure the buckling of the monolayer is also difficult since it amounts to only 0.05 Å lying below the commonly achieved resolution in STM. Electronic effects may yet strongly enhance the measured buckling (see e.g. [77]), and thereby solve the problem of distinction between the Cr(001)-surface and the c(2×2) (anti)ferrimagnetic Cr monolayer on Fe(001). This is one topic of the following section.

Let us now analyze the results for the Mn monolayers on Fe(001) presented in Fig. 8.8 in terms of the calculated LDOS and the DOS in the muffin-tin spheres of the two Mn atoms of the monolayer. In the LDOS of the ferromagnetic configuration (Fig. 8.8a) we observe only a single feature located at an energy of +0.8 eV and caused by minority states. This peak is still in the minority state pseudo gap of the Fe(001)-surface and of d_{z^2} type as in the case of Cr but located at a higher energy because of the increased magnetic moment of Mn (compare table 8.1 and also the muffin-tin DOS in Fig. 8.7 and Fig. 8.8). Thus, a confusion with the surface resonance peak of

Fe(001) can be excluded. In the layered antiferromagnetic configuration (Fig. 8.8b) we find a high qualitative resemblance of the Mn and Cr LDOS the only difference being a shift of the d_{z^2} majority state peak to an energy of +0.5 eV. This similarity is caused by the fact that the enhanced moment of Mn is connected with a shift of the minority state bands to lower energies while the majority states are only slightly influenced (see Fig. 8.8b). In the c(2×2) (anti)ferrimagnetic configuration, on the other hand, the difference to Cr is quite apparent. First of all the occupied majority state feature of the ferromagnetic atom has disappeared while the peak at +0.7 eV is still present. As for the layered antiferromagnetic configuration the majority band is influenced only little by the gain in magnetic moment. The spin split partner of the majority state at +0.7 eV is located at +1.1 eV and results in a further peak of the total LDOS. It is also important to notice that the minority states which were present for Cr near the Fermi level have disappeared. In the calculated spectra of all magnetic configurations the appearing features are energetically far from the position of the Fe(001)-surface resonance (+0.2 eV). A distinction on the basis of STS is thus easily possible.

Since the two magnetic configurations closest in energy for Mn are the ferromagnetic and the c(2 × 2) antiferrimagnetic configuration (see Fig. 8.2) it would be desirable to distinguish between them on the basis of the spectra. This is impossible as can be concluded from the calculation because both display a sharp peak at an energy of about +0.75 eV. Thus a different technique must be applied. Spin-polarized STS might be applicable since the peak is located in the minority spin states for the ferromagnetic and in the majority spin states for the c(2 × 2) antiferrimagnetic configuration. Using the known minority surface resonance of the Fe(001)-surface as a reference may then provide a distinction. In the next section we will discuss a different much simpler method which is measuring non-spinpolarized STM images with atomic resolution. Additionally, it will be shown that the magnetism of a Mn monolayer on Fe(001) is even more complicated than discussed up to now, and other competing configurations need to be taken into account.

8.5 Imaging Cr and Mn Monolayers on Fe(001)

In this section the calculated STM images will be discussed qualitatively, i.e. by the expected pattern of the images, and quantitatively, i.e. in terms of the corrugation amplitudes. In relation to the following chapter we will also point out the information gain when spin-polarized STM is applied to these systems. Concerning the expected patterns we recall the method of the star function expansion for a square lattice presented in section 4.6.1. In Fig. 4.6 the appearance of the lowest star functions were given for the example of a square lattice with a two atom basis. This is exactly what is needed for the system of 3*d*-monolayers on Fe(001) since for the c(2 × 2) antiferrimagnetic configuration the two atoms of the monolayer are electronically inequivalent due to the ferromagnetism of the Fe(001)-substrate. Thus a c(2 × 2) pattern, i.e. Fig. 4.6b, is possible. In the ferromagnetic and layered antiferromagnetic case, on the other hand, this is ruled out by symmetry since the two atoms are equivalent and the use of a c(2×2) unit cell is superficial[4].

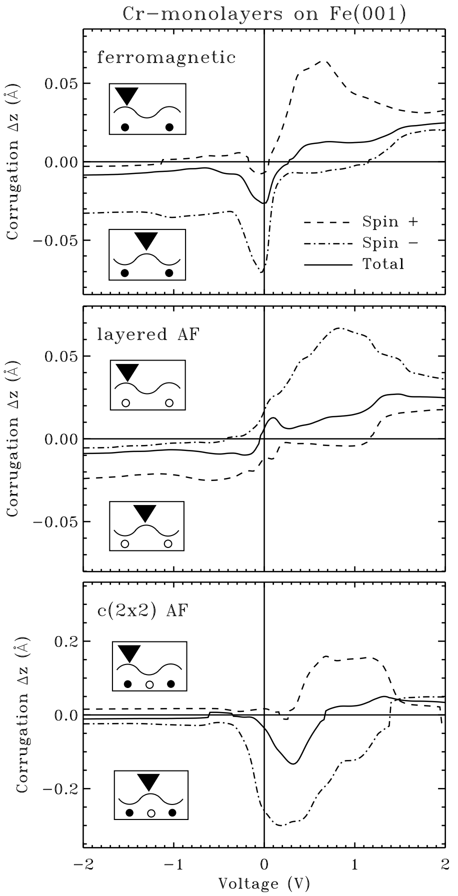

Figure 8.9: Calculated corrugation amplitudes for an *s*-type tip as a function of the bias voltage for Cr-monolayers on Fe(001) for different magnetic configurations: ferromagnetic (F), layered antiferromagnetic (LAF) and c(2×2) (anti)ferrimagnetic (AF) at a distance of $z_0 = 5.1$ Å above the surface. Full and open circles in the inset indicate ferromagnetic and antiferromagnetic spin alignment relative to the Fe-substrate. The sign convention of the corrugation amplitude is defined by the scan lines displayed in the insets of each plot. For the p(1×1) ferromagnetic and p(1×1) layered antiferromagnetic configuration a positive (negative) corrugation amplitude corresponds to a normal (anti-corrugated) image. For the c(2×2) (anti)ferrimagnetic configuration a positive (negative) corrugation amplitude corresponds to imaging the ferromagnetically (antiferromagnetically) coupled Cr atoms as protrusions.

In Fig. 8.9 the calculated corrugation amplitudes as a function of the applied bias-voltage are presented for the Cr monolayer on Fe(001). In the ferromagnetic and layered antiferromagnetic case the corrugation pattern resembles the chemical p(1×1) unit cell as required by symmetry. A negative sign of the corrugation amplitude is accordingly defined as anti-corrugation, an effect which has already been extensively investigated in chapter 5. In the case of the c(2×2) (anti)ferrimagnetic configuration the STM image shows the magnetic c(2×2) unit cell, i.e. one of the Cr-atoms is imaged as a protrusion while the other appears as a depression (see also Fig. 4.6b). The different signs in the corrugation amplitude then denote imaging either the ferromagnetic or the antiferromagnetic coupling Cr atom with respect to the Fe(001)-surface (see the insets in Fig. 8.9). The pattern of the image can deviate from the c(2×2) pattern due to the specific electronic structure of the Cr monolayer. This is actually the case at some bias voltages which are characterized by extremely small corrugation amplitudes. It is at these voltages that the pattern changes from the c(2×2) type, characteristic of the magnetic unit cell, to the p(1×1) pattern corresponding to the chemical unit cell. This effect of a qualitative change in the

---

[4] In order to compare the total energies one must calculate all magnetic configurations within the same 2D unit cell.

STM image has also been pointed out in chapter 5 where it occurred during the corrugation reversal (see Fig. 5.2). From the discussion of section 4.6.5 we recall that the contribution of the majority and minority spin states to the total corrugation amplitude depends on their first star coefficient $n_1^\sigma(z)$, i.e. the lateral constant part of the LDOS in the vacuum ($n_1^\sigma(z)$ has already been displayed in Fig. 8.7 and Fig. 8.8). If $n_1^\uparrow(z) \gg n_1^\downarrow(z)$ the total corrugation amplitude is almost identical to that of the majority spin and vice versa. If $n_1^\uparrow(z) = n_1^\downarrow(z)$ then the total corrugation amplitude is the average of both spin directions.

The absolute values of the calculated corrugation amplitudes are rather small for the p(1 × 1) unit cell while it is of a value comparable to experimental resolution for the c(2 × 2) unit cell. This behavior results from the bigger 2D lattice constant for the latter unit cell. The tip-dependent enhancement factors suggested by Chen [11] possess an inverse dependence on the 2D lattice constant (see section 4.4.2). For a d_{z^2}-tip state and our system ($a_0^{Fe} = 2.77$ Å, $\phi \approx 5$ eV) the factors would be 6.2 and 3.0 for the p(1 × 1) and c(2 × 2) unit cell, respectively. The presented corrugation amplitudes in all figures do not include these factors.

For the ferromagnetic configuration a small total corrugation amplitude is observed. The contribution of the majority spin displays a pronounced maximum around +0.5 V of positive corrugation, i.e. imaging of atom sites, which is explainable by an extended surface state band in the $\bar{\Gamma}\bar{M}$ direction of the c(2 × 2) 2D-BZ. Of more importance is the peculiar minimum in the minority states near 0 V which contributes to anti-corrugated STM images. This state is equivalent to the one held responsible for the experimentally observed anti-corrugation on the Fe(001) and Cr(001) surface [115,116]. Its charge density shows the same characteristics, i.e. (directed) $d_{xz,yz}$-orbitals, and it also produces the same features in the 2D-BZ. In the layered antiferromagnetic configuration the roles of majority and minority states are exchanged as compared to the ferromagnetic case. This is reasonable since the majority bands are now mainly unoccupied and the minority bands are about half occupied (see Fig. 8.7). Again a change from anti-corrugation to corrugation with applied voltage can be observed.

Finally, the c(2 × 2) (anti)ferrimagnetic configuration is of special interest because the two Cr atoms of the c(2 × 2) surface unit cell are inequivalent due to the different magnetic coupling to the substrate. The situation is therefore related to that of chemically different atoms. The calculation displays a maximum corrugation at a voltage of +0.3 V where the antiferromagnetic atom is imaged as a protrusion while the ferromagnetic atom appears as a depression. The STM image shows a c(2 × 2) pattern, i.e. a square arrangement of protrusions with a lattice constant of $\sqrt{2}a$. The feature responsible for the maximum in the corrugation amplitude originates from minority spin states. However, the total corrugation amplitude is significantly weakened by the majority spin contribution. This hints at a large first star coefficient of the majority spin states which is verified by taking a look at Fig. 8.7. The minority spin state causing the maximum in the corrugation amplitude is of d_{z^2} character at the antiferromagnetic Cr atom and highly localized there. It is the same state which is experimentally measured by STS on the CrFe/Fe(001) surface alloy [94]. It should enable one to distinguish between the c(2 × 2) (anti)ferrimagnetic configuration and the two other magnetic configurations, since it produces a pattern with the symmetry of the magnetic c(2×2) rather than that of the chemical p(1×1) unit cell. There is no clear possibility to distinguish the ferromagnetic from the layered antiferromagnetic configuration by the images. However, one could argue that they display an opposite pattern at the Fermi energy (anti-corrugation in the ferromagnetic and corrugation in the layered antiferromagnetic case) which might be detectable by adsorbates of known site. This effect is quite significant for the minority states and might be exploitable by applying SP-STM.

Already from this first discussion on the influence of the spin-polarized electronic structure on the STM-images and their corrugation amplitudes it is evident that selecting one or the other spin direction can greatly enhance the measured contrast, since the two spin contributions tend to cancel each other. The experimentally achieved resolution of magnetic superstructures on magnetite with Fe-tips [24] may very well be explained by this effect. Another example will be presented in chapter 9.

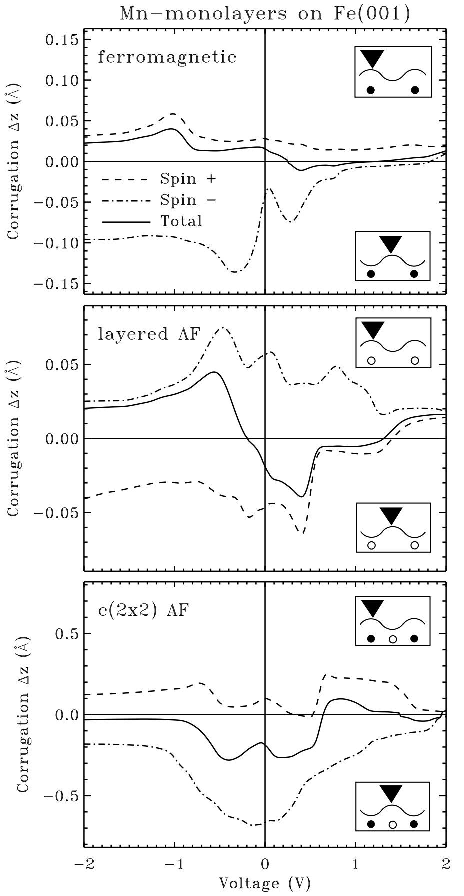

Figure 8.10: Calculated corrugation amplitudes for an s-type tip as a function of the bias voltage for Mn monolayers on Fe(001) for different magnetic configurations: ferromagnetic (F), layered antiferromagnetic (LAF) and c(2×2) (anti)ferrimagnetic (AF) at a distance of z_0 = 4.8 Å above the surface. Full and open circles in the inset indicate ferromagnetic and antiferromagnetic spin alignment relative to the Fe-substrate. The sign convention of the corrugation amplitude is defined by the scan lines displayed in the insets of each plot. For the p(1×1) ferromagnetic and p(1×1) layered antiferromagnetic configuration a positive (negative) corrugation amplitude corresponds to a normal (anti-corrugated) image. For the c(2×2) (anti)ferrimagnetic configuration a positive (negative) corrugation amplitude corresponds to imaging the ferromagnetically (antiferromagnetically) coupled Mn atoms as protrusions.

Switching to the Mn monolayers on Fe(001) now (see Fig. 8.10), we recall that the magnetic moments have increased considerably compared to Cr (see table 8.1) which is the main reason for all changes in the corrugation amplitude plots discussed in the following. For the ferromagnetic configuration the maximum in the majority corrugation amplitude has shifted to −1.0 V and has become less pronounced. The minority contribution on the other hand has split into two anti-corrugation peaks resulting from states of similar character as for Cr. In the layered antiferromagnetic configuration a significant change is observed resulting from a rather big difference in magnetic moment compared to the case of Cr. This corrugation dependence is a nice example of the special cases discussed in section 4.6.5. The occupied part of the corrugation is dominated by minority electrons and accordingly we find a high minority LDOS in this energy range (see Fig. 8.8b). At positive bias-voltages, i.e. for unoccupied sample states, the total corrugation amplitude follows the majority spin contribution which is related to a high majority LDOS (see Fig. 8.8b). For the c(2×2) (anti)ferrimagnetic configuration of the Mn monolayer we observe a similar behavior as for Cr. Again the minority state corrugation amplitude displays a maximum near 0 V which also appears in the total amplitude. However, it is considerably damped due to the majority states. Still a value of about 0.2 Å remains which is clearly above the common resolution limit of STM of 0.1 Å. Thus it is possible to answer the important question whether the Mn monolayer couples (anti)ferrimagnetically to the Fe(001) surface as has been predicted on the basis of *ab initio* calculations [104] directly by STM even though the buckling is expected to be only on the order of 0.06 Å [117]. By using a spin-polarized STM one may greatly enhance the measured corrugation amplitude if the magnetically coated tip favors the minority spin states which depends on the orientation of the relative magnetization axes as well as on the sign of the spin-polarization of the tip (see section 4.5).

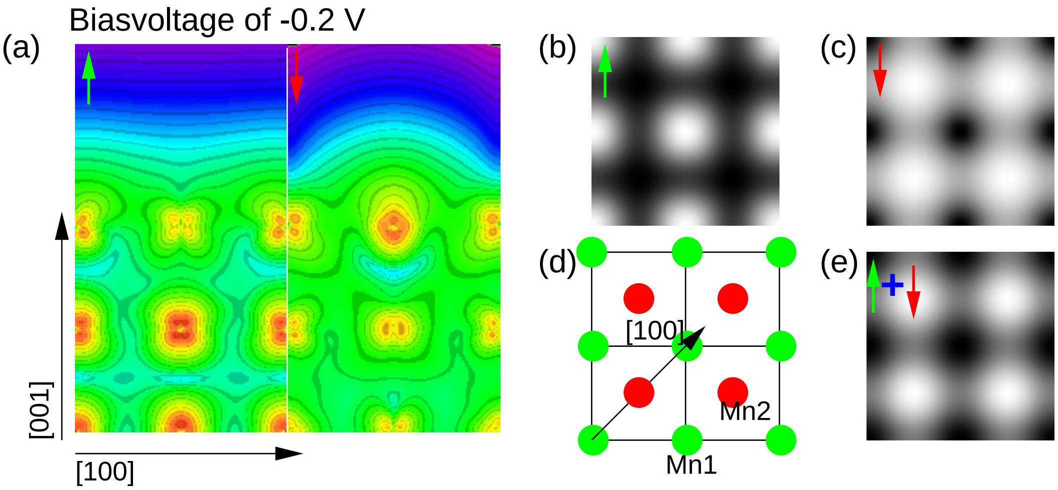

Figure 8.11: Calculated STM images and cross-sections of the integrated local density of states (ILDOS) for the Mn-monolayer on Fe(001) in the c(2 × 2) antiferrimagnetic configuration for a bias-voltage of −0.2 V. (a) shows the cross-section of the ILDOS for the majority (left) and minority (right) electrons. The corresponding STM images of the (b) majority, (c) minority, and (e) the spin-summed ILDOS. (d) displays the surface unit cell with the ferromagnetic (light) and antiferromagnetic (dark) coupling Mn atom of the monolayer. (b) and (c) show the ferro- and antiferromagnetic coupling Mn atoms with respect to the Fe(001)-substrate as protrusions, respectively. However, also in the spin-summed ILDOS corresponding to a non-spinpolarized STM image the antiferromagnetic Mn atoms appear as protrusions, i.e. the magnetic c(2 × 2) unit cell is observed.

In Fig. 8.11 the states contributing to the calculated STM image for the c(2 × 2) (anti)ferrimagnetic configuration at a bias-voltage of −0.2 V are displayed in real-space as well as the corresponding STM-images. We observe a d_{z^2}-type orbital at the antiferromagnetic coupling Mn atom leading to the protrusions in the (non-spinpolarized) STM image. Comparing this plot with the one of the CrFe surface alloy on Fe(001), Fig. 8.6, a close resemblance can be seen.

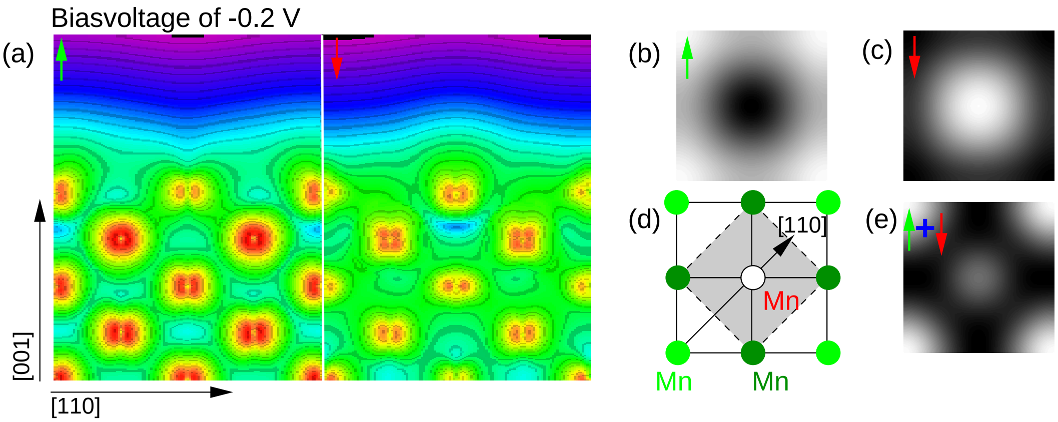

Figure 8.12: Calculated STM images and cross-sections of the integrated local density of states (ILDOS) for the Mn-monolayer on Fe(001) in the p(2 × 2) ferromagnetic configuration for a bias-voltage of −0.2 V. (a) shows the cross-section of the ILDOS for the majority (left) and minority (right) electrons. The corresponding STM images of the (b) majority, (c) minority, and (e) the spin-summed ILDOS. (d) displays the surface unit cell consisting of two ferromagnetic (light and dark dots) and one antiferromagnetic coupling (white dot) Mn atom of the monolayer. The c(2 × 2) unit cell is also included by the shaded box for comparison with Fig. 8.11. (b) and (c) show one of the ferro- and the antiferromagnetic coupling Mn atoms with respect to the Fe(001)-substrate as protrusions, respectively. However, in the spin-summed ILDOS corresponding to a non-spinpolarized STM image a pattern of a c(2 × 2) unit cell is observed. The contrast between the two protrusions is quite faint as can also be concluded from the corrugation amplitudes (see Fig. 8.13).

Although there is actually an infinite number of possible antiferromagnetic configurations we have only considered the three magnetic configurations of Fig. 8.1 up to now. This is reasonable if we can assume the nearest neighbor exchange interaction to be strongest and neglect the interaction with further neighbors. In order to establish this assumption one can use the next larger 2D unit cell, which is p(2 × 2), and calculate the energetic differences between all possible configurations on such a lattice. Recently, this has been done with our FLAPW-code [118] and contradictory to the expectation that further magnetic configurations are considerably higher in energy than the c(2 × 2) antiferrimagnetic configuration, which was assumed to be the ground-state, there is a ferrimagnetic p(2 × 2) configuration that is favorable by the tiny energy difference[5] of 6.4 meV per Mn atom. In this configuration two Mn

---

[5] The common energy differences between competing magnetic configurations are in the range of 50 to 100 meV per atom (see for example table 8.1) while energy differences of several meV are

atoms couple ferromagnetically and one couples antiferromagnetically with respect to the Fe(001)-substrate. At low temperatures this configuration is expected but considering the very small energy difference with respect to the c(2 × 2) antiferrimagnetic configuration even a coexistence in separated domains seems possible. It is thus extremely interesting to distinguish unambiguously between the two.

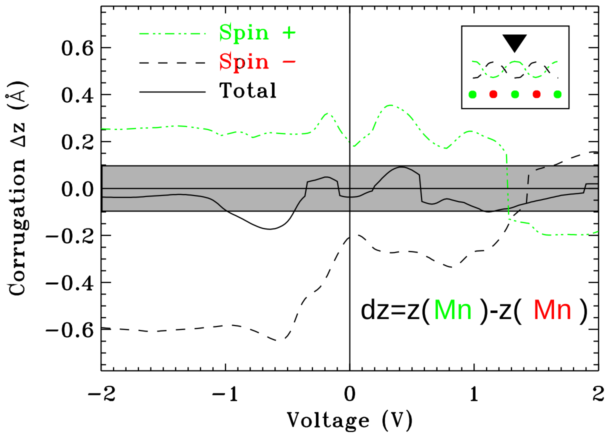

Figure 8.13: Calculated corrugation amplitudes for an s-type tip as a function of the bias voltage for the Mn-monolayer on Fe(001) in the p(2 × 2) ferromagnetic configuration. Dark and light circles in the inset indicates the corner ferromagnetic and the antiferromagnetic coupling Mn atom with respect to the Fe-substrate. The two curves define positive and negative corrugation amplitudes correponding to imaging either the corner ferromagnetic Mn atom or the antiferromagnetic Mn atom as a protrusion.

Therefore, STM-images have also been calculated for the ferrimagnetic p(2 × 2) configuration as a function of the bias voltage, and an example is presented in Fig. 8.12 in a similar form as in Fig. 8.11. While the contribution of majority states (Fig. 8.12b) to the image shows one type of the ferromagnetically coupled Mn atoms as protrusions, the minority states (Fig. 8.12c) result in protrusions on top of the antiferromagnetically coupled Mn atoms. Thus the images of the two spin directions considered separately display the magnetic p(2 × 2) unit cell. However, two local maxima appear in the spin-summed, i.e. non-spinpolarized, STM image (Fig. 8.12e). If the slight height difference between the local maxima is experimentally unresolvable a c(2×2) pattern must be deduced from the image. In order to decide upon the height difference between these two maxima we have plotted the calculated corrugation amplitude as a function of the applied bias-voltage in Fig. 8.13. The amplitude denotes the height difference between the maximum and the minimum in the unit cell. While the contributions from only the majority or only the minority states lead to values of 0.2 to 0.6 Å with the images inverted as exemplified in Fig. 8.12b and Fig. 8.12c, the total corrugation amplitude is quite small and below 0.1 Å. From the corresponding images it is impossible to deduce a difference to the c(2 × 2) pattern since the height difference between the two maxima is even lower than the total corrugation amplitude. Thus with a non-spinpolarized STM one may not discriminate the two competing magnetic configurations, i.e. the c(2×2) antiferrimagnetic from the p(2 × 2) ferrimagnetic one. Because of the extremely high corrugation amplitudes occurring for the two spin directions it is rather obvious that spin-polarized STM favoring one of the two spin directions is a promising method to experimentally

---

typical for the magnetic anisotropy energy.

identify the magnetic ground-state configuration. The feasibility of such an approach is demonstrated in the next chapter for a different system.

Chapter 9

Resolving Magnetic Structures on the Atomic Scale by SP-STM

The magnetism of nanostructures such as ultrathin films made out of magnetic transition metals of a thickness down to one monolayer deposited on a non-magnetic, ferromagnetic, or antiferromagnetic substrate has recently attracted enormous attention. Novel magnetic properties have been observed in these systems which are of interest for both, fundamental research as well as for applications in the magnetic storage technology [119] and the arising field of magneto-electronics [120]. An example for a potential application is to exploit the exchange-bias effect [121] to tune the characteristics of giant-magneto resistance devices, like read-heads in hard disk drives. In order to do so one must understand the origin of this complicated effect which occurs when ferromagnetic films are in contact with antiferromagnetic ones. The magnetism in such structures can be very complex, and phenomena such as antiferromagnetism, ferrimagnetism, commensurate and incommensurate spin-density waves, and non-collinear spin structures can occur. Currently strong efforts are being undertaken to study these systems [122–124].

In this chapter we introduce an approach to image complicated magnetic structures of surfaces directly on the atomic scale by spin-polarized STM (SP-STM). By generalizing the Tersoff-Hamann model to the case of SP-STM and applying the expansion of the STM image into star functions developed in sections 4.6.1 and 4.6.2 we prove that in general the SP-STM image of *any magnetic superstructure within an arrangement of chemically equivalent atoms leads to an SP-STM image displaying a pattern corresponding to the magnetic configuration.* This is in contradiction to the intuitive expectation that the non-spinpolarized STM image reflecting the chemical structure is only slightly modulated in the SP-STM experiment. This approach extends the use of STM from the exploration of the topological, chemical, and ferromagnetic structure of surfaces to the inherently much more difficult investigation of antiferromagnetic surfaces with ultimate, atomic resolution. It may even be possible to reveal more complicated non-collinear spin structures in the future (see Fig. 10.1).

The method of imaging magnetic structures on the atomic scale directly by SP-STM is applied to the problem of two-dimensional antiferromagnetism in monolayer-thick transition metal films on non-magnetic substrates. The existence of two-dimensional antiferromagnetism in such ultrathin films has been predicted already in 1988 by S. Blügel *et al.* [21] but unambiguous experimental proof is still missing. The proof of the two-dimensional antiferromagnetism would provide an understanding of the magnetic interaction in these films and confirm and extend the predictive power of the density functional theory towards two-dimensional systems. By using SP-STM with atomic resolution the predicted antiferromagnetic ground-state configuration can be observed in real-space providing a direct proof of the magnetic structure. Thereby the missing proof for the existence of two-dimensional antiferromagnetism is given in this chapter.

9.1 Imaging 2D Antiferromagnetism of Ultrathin Films

Two-dimensional antiferromagnetism is poorly understood. The investigations suffer from the problem that no adequate experimental technique combining high-spatial resolution in real-space with a sufficient degree of surface and magnetic sensitivity has been routinely available. The ultimate limit of a two-dimensional antiferromagnet is a magnetic monolayer of chemically equivalent atoms, where adjacent atoms at nearest-neighbor sites have magnetic moments with opposite directions, deposited on a non-magnetic substrate. More than 10 years ago, Blügel *et al.* predicted the existence of such antiferromagnets, i.e. V, Cr, and Mn on (100) oriented Pd substrates [21] and later also on noble-metal substrates [125] on the basis of first-principles calculations. From these calculations one can conclude that the hybridisation between the monolayer and the noble-metal substrate is negligible and the monolayer film behaves as if it were a perfect two-dimensional system. There have been several attempts to verify the existence of two-dimensional antiferromagnetism and some evidence has been given [126, 127], but unambiguous proof is still missing. The experimental difficulties are numerous. First of all, one needs to control the growth of the film to be sure of the required perfect pseudomorphic structure. Surface alloying has to be safely excluded. Further, the Néel temperature at which magnetic ordering occurs is unknown and is probably very low. Finally, an experiment providing an unambiguous evidence of the antiferromagnetic configuration is needed which is far from being trivial since the total magnetization vanishes and the order is on the atomic scale.

Especially, surface alloying has been a serious problem in many experiments. It is caused by the fact that transition-metals quite generally possess larger surface free energies than noble-metals, and thus it is favorable for an adsorbed transition-metal atom to change places with a substrate atom. One of the best studied examples is the c(2×2) MnCu surface alloy [20]. To prevent the occurrence of alloying one may choose a more stable substrate like W(110) which has become a very popular substrate for the growth of thin magnetic films, e.g. Fe on W(110) [128]. The drawback is a strong hybridization of the monolayer with such a $5d$-substrate influencing the magnetic properties. The $3d$-bands of the transition-metal broaden which reduces the possible exchange-splitting and thereby also the magnetic moment. Nevertheless, the two-dimensional antiferromagnetism within the monolayer film should not be destroyed since it does not depend on a high density of states at the Fermi energy as in the case of ferromagnetism but rather on a low density of states in the center of the d-band which becomes sometimes even larger due to the hybridization with the substrate. We have therefore chosen this system to demonstrate the potential of spin-polarized STM (SP-STM) [23,24] to give a direct proof of two-dimensional antiferromagnetism within an ultrathin film.

9.2 Computational Details

The calculations have been performed in the c(2×2) two-dimensional unit cell with two atoms per layer and using films consisting of 11 layers, i.e. 9 layers of the W(110)-substrate and a monolayer of a $3d$-transition metal on both sides. The interlayer distance between the Cr, Mn, Fe, or Co monolayer and the W(110)-surface has been relaxed by total energy minimization[1]. For tungsten we worked with the theoretical lattice constant of $a_0 = 5.928$ a.u. which is 1% smaller than the experimental lattice constant. The exchange-correlation potential has been applied in the local density approximation of von Barth and Hedin [29] using the parametrization by Moruzzi, Janak, and Williams [72]. The basis set used for the valence states consisted of about 80 augmented plane waves per atom in the unit cell. Non-spherical terms in the potential, charge density, and wave functions are expanded within the muffin-tin spheres with radius $R^{W}_{MT} = 2.456$ a.u. and $R^{3d}_{MT} = 2.1$ a.u. up to $l_{max} \leq 8$. The self-consistent electronic structure was determined with 35 $\mathbf{k}_{\|}$-points in the irreducible part of the two-dimensional Brillouin zone (I2BZ). The integrated local density of states (ILDOS) resolved over the 2D-BZ has been analyzed using 176 $\mathbf{k}_{\|}$-points in the I2BZ. All star coefficients and by this also the STM images and corrugation amplitudes were calculated on this $\mathbf{k}_{\|}$-point set.

9.3 Magnetism of $3d$-Monolayers on W(110)

Before we demonstrate the feasibility to image the magnetic ground-state of a $3d$-ML/W(110) with SP-STM, the magnetism in such a system shall be discussed. Although we are dealing with a transition-metal substrate, W(110), instead of a noble-metal substrate, like Ag(001) or Cu(001) often used in the past [125], most of the results are very similar. However, some effects are reduced due to the strong hybridization between the substrate and the monolayer. Fig. 9.1 shows the different considered magnetic configurations for a monolayer film placed perfectly pseudomorphic on the W(110)-substrate. In Fig. 9.1(a) the non-magnetic film is depicted along with the chemical p(1×1) unit cell while Fig. 9.1(b) displays the ferromagnetic configuration with a parallel alignment of all Mn moments. The simplest possible antiferromagnetic configuration is given in Fig. 9.1(c) which displays antiparallel magnetic moments of nearest-neighbor atoms. This configuration is analogous to the c(2×2) antiferromagnetic structure on a square substrate lattice, like Ag(001), and we denote it as a checkerboard structure accordingly.

---

[1] All results for these systems refer to the relaxed interlayer distances.

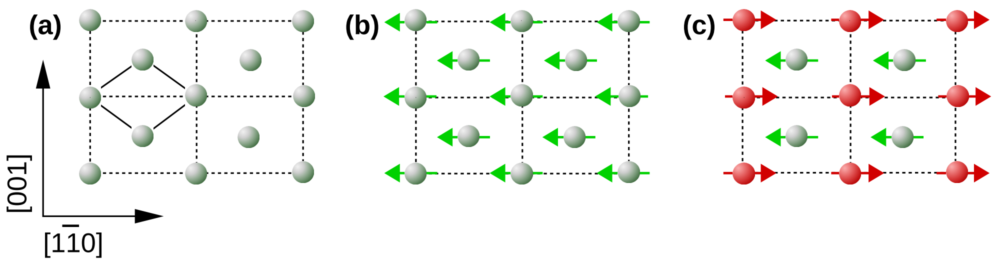

Figure 9.1: Magnetic configurations taken into account for the determination of the magnetic ground-state configuration of a $3d$-transition metal monolayer on W(110). (a) shows the non-magnetic film, (b) the ferromagnetic configuration, and (c) the c(2×2) antiferromagnetic structure, a checkerboard arrangement of up and down spins. The chemical p(1×1) unit cell has been marked in (a) by the full line.

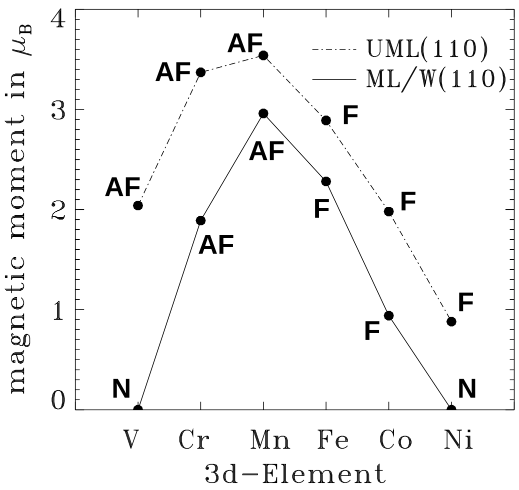

Figure 9.2: The magnetic moments of the calculated ground-state configuration for (110) oriented unsupported $3d$-monolayers on the LDA lattice constant of W (UML) and for the $3d$-monolayer on the W(110)-surface (ML/W(110)). The magnetic ground-state is denoted by: ferromagnetic (F), c(2×2) antiferromagnetic (AF), or non-magnetic (N). There is a large reduction of magnetic moments between the perfect two-dimensional system of the UML and the ML on W(110) due to the strong hybridization with the substrate. For Cr, Mn, Fe, and Co the relaxed interlayer distances have been used for the ML/W(110), i.e. 3.79 a.u. , 3.91 a.u. , 3.66 a.u. , and 3.58 a.u. , respectively.

Fig. 9.2 displays the magnetic moments and the ground-state configuration for the $3d$-monolayers on the W(110)-substrate as well as without substrate as unsupported monolayers. The latter calculation provides information on the significance of the substrate hybridisation on the electronic and magnetic properties. We investigated for all transition metals both, the ferromagnetic and the c(2×2) antiferromagnetic spin structure. For most systems we found both magnetic states to be stable. A total energy analysis reveals that for the unsupported monolayers the early $3d$'s, i.e. V, Cr, and Mn, are antiferromagnetic and the late $3d$'s, i.e. Fe, Co, and Ni, are ferromagnetic. For a noble-metal substrate the trend is analogous [125] to the unsupported monolayers indicating a neglectable hybridisation. In the case of a W(110) substrate, on the other hand, where a strong hybridization with the 2D-film occurs, V and Ni become non-magnetic while for Cr the ferromagnetic solution does not exist anymore. Still, the trend of the magnetic ground-state throughout the 3*d*-row remains unchanged while the magnetic moments are reduced considerably. Thus the substrate strongly alters the monolayer properties, and the system is not a perfect two-dimensional system in this sense. The antiferromagnetic order of Cr and Mn, however, is still two-dimensional and the magnetic moments are significant. Fortunately, the growth of Mn on W(110) has been studied experimentally in the past and perfect pseudomorphic growth without intermixing has been observed for a coverage of $\Theta < 3$ ML [131]. Thus a direct comparison with the calculations is possible.

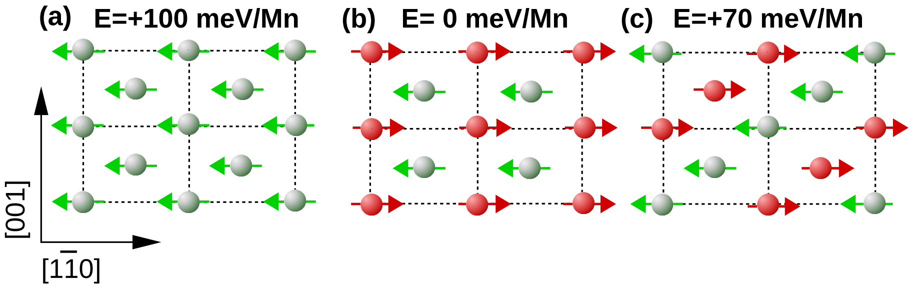

Figure 9.3: Comparison of different magnetic configurations of the Mn monolayer on W(110): (a) the p(1×1) ferromagnetic structure, (b) the c(2×2) antiferromagnetic structure and (c) the p(2 × 1) antiferromagnetic structure. The calculated magnetic moments are $2.40\,\mu_\mathrm{B}$, $\pm 2.96\,\mu_\mathrm{B}$ and $\pm 2.79\,\mu_\mathrm{B}$, respectively. The total energies are given with respect to configuration (b).

Mn possesses an untypically large bulk unit cell of 29 atoms at room temperature hinting at its complicated magnetic properties. Thus different competing antiferromagnetic structures might occur in this complex case, and additional configuration has been taken into account. The three possible magnetic configurations considered here are schematically represented in Fig. 9.3: (a) ferromagnetic, (b) c(2 × 2)-antiferromagnetic with antiferromagnetic coupling of all nearest neighbor atoms, and additionally (c) p(2 × 1)-antiferromagnetic where two nearest neighbors couple ferromagnetically while the other two couple antiferromagnetically. For all configurations the equilibrium interlayer distance between Mn and W was determined by total energy minimization (Fig. 9.4). By comparing the total energies of the three magnetic structures we conclude that the c(2 × 2)-AFM configuration (b) is the magnetic ground-state structure, i.e. at low temperatures a checkerboard arrangement of magnetic moments occurs. The energy of the c(2 × 2)-AFM configuration is 100 meV and 70 meV per Mn atom lower than the ferromagnetic (a) or p(2 × 1)-AFM (c) state, respectively. By including the spin-orbit interaction into the calculations one can even compute the easy axis of the magnetization. From these calculations [129] we conclude that the magnetic moments of the c(2 × 2)-antiferromagnetic structure have an in-plane orientation along the [1$\bar{1}$0] direction (long side of the surface unit-cell). The energy difference between the in-plane and out-of-plane orientation of the magnetic moment, known as the magnetocrystalline anisotropy energy, amounts to about 1.3 meV per atom [129].

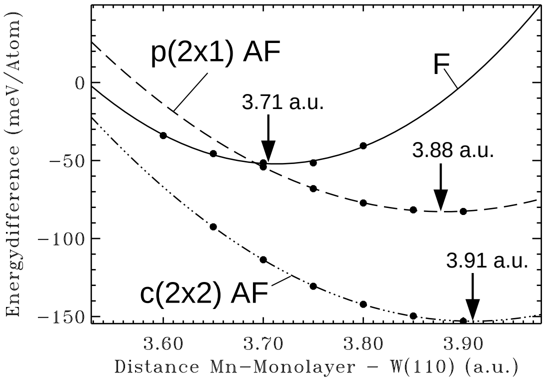

Figure 9.4: The interlayer distance of the Mn monolayer on W(110) by energy minimization for the different magnetic configurations of Fig. 9.3. The large difference between the interlayer distance of the ferromagnetic and the two antiferromagnetic configurations is probably due the much smaller magnetic moment in the ferromagnetic state ($2.40\mu_B$ compared to $\pm2.96\mu_B$ and $\pm2.79\mu_B$).

9.4 Principle of SP-STM on the Atomic Scale

In this section we will apply the principle of SP-STM which has already been introduced in section 4.5 to the special case of a magnetic superstructure on the atomic scale. The effect exploited in order to image the magnetic ground-state configuration of a Mn-monolayer on W(110) is of general validity, and it may lead to the understanding of many more magnetic structures on this lowest possible scale in the future. The first applications of the SP-STM have been demonstrated by Wiesendanger *et al.* [23, 24]. The working principle is sketched in Fig. 9.5. The electronic structure of Mn is therein expressed in terms of spin-dependent local density of states (DOS) $n_{\uparrow(\downarrow)}$. Since a Mn atom is magnetic, the DOS of majority, $n_\uparrow$, and minority, $n_\downarrow$, electrons (insets in Fig. 9.5) around the Fermi energy, E_F, which is relevant for the tunneling of electrons, is different, and the spin-polarization $P = (n_\uparrow - n_\downarrow)/(n_\uparrow + n_\downarrow)$ is non-zero. However, the sum of both, $n_o = n_\uparrow + n_\downarrow$, is identical above any Mn atom, so a non-spin-polarized STM measurement will only be sensitive to the chemical unit cell. If the STM tip can be made sensitive to the spins of the tunneling electrons, for example by coating the STM-tip with Fe or Gd, the tunneling current I depends on the angle θ of the relative orientation between the magnetization axes of tip and sample as well as on the electronic structure and on the spin-polarization P_S and P_T of the sample (Mn) and the tip states, respectively (see Eq. (4.43)). The tunneling current can be decomposed into two contributions, $I(\theta) = I_o + I_P \cos\theta$ (see Eq. (4.44)), the conventional tunneling current of non-spin-polarized electrons I_o, and the additional contribution I_P due to the tunneling of spin-polarized electrons, $I_P \sim P_S\, P_T$ (in the limit of small applied bias voltage V). Obviously, the highest effect is expected for tip and sample magnetization being either parallel or antiparallel while the effect vanishes for a perpendicular geometry.

According to conventional wisdom spin-polarization is a small effect, and one might expect normal STM images to be slightly modulated due to magnetism. Instead, it is quite different. The STM-image of a periodic surface, i.e. the change ΔI of the tunneling current I as a function of the lateral position $\mathbf{r}_\parallel$ of the tip, can be

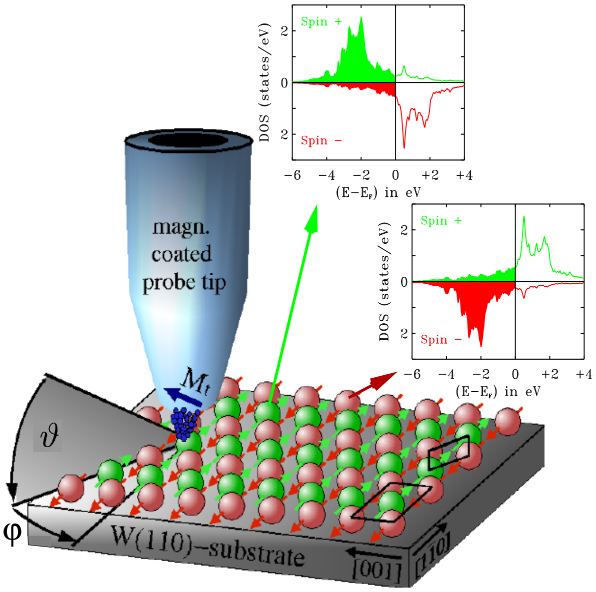

Figure 9.5: Principle of spin-polarized scanning tunneling microscopy using a ferromagnetically coated probe tip which is scanned across a Mn monolayer film on W(110). The magnetic ground state configuration is shown (cf. Fig. 9.3) and the corresponding DOS of the ferro- and antiferromagnetic Mn atoms. The angle θ between the magnetization axes of tip and sample can be related to ϑ and φ by $\cos\theta = \cos\varphi\cos\vartheta$. Additionally, the diamond-shaped chemical and the rectangular magnetic unit cells are displayed.

written in terms of a two-dimensional Fourier expansion:

$$\Delta I(\mathbf{r}_\|, z, \theta, V) = \sum_{n\neq 0} I_{\mathbf{G}_\|^n}(z, \theta, V) \exp\left(i\mathbf{G}_\|^n \mathbf{r}_\|\right). \tag{9.1}$$

$\mathbf{G}_\|^n$ denotes the reciprocal lattice vectors, and $I_{\mathbf{G}_\|^n}(z, \theta, V)$ is the tip-sample distance (z), angle (θ), and bias-voltage (V) dependent expansion coefficient. As we have described in detail in section 4.6.1 the plane waves of symmetry related reciprocal lattice vectors $\mathbf{G}_\|^n$ can be summarized to a two-dimensional star function $\phi_s^{2D}(\mathbf{r}_\|)$. Thus we can rewrite Eq. (9.1) to:

$$\Delta I(\mathbf{r}_\|, z, \theta, V) = \sum_{s>1} I_s(z, \theta, V)\phi_s^{2D}(\mathbf{r}_\|), \tag{9.2}$$

with a representative vector $\mathbf{G}_\|^s$. Due to the tunneling of electrons through the vacuum barrier these coefficients decrease exponentially with increasing length $G_\|^s$ (see the $\mathbf{k}_\|$-selection rule of section 4.6.2), and to a good approximation the topographic STM image or, to be more precise, the constant current STM image, is determined by the lowest star function which is laterally non-constant, i.e. $\phi_2^{2D}(\mathbf{r}_\|)$[2] (see section 4.6.1):

$$\Delta I(\mathbf{r}_\|, z, \theta, V) \approx I_2(\theta, V)\phi_2^{2D}(\mathbf{r}_\|) \exp\left[-2z\sqrt{2m/\hbar^2|E_F + eV| + (G_\|^{(2)}/2)^2}\right]. \tag{9.3}$$

Since we are only interested in the dependence of the exponential decrease on the representative reciprocal lattice vector $G_\|^s$ in this context the exponential term has been approximated by the highest contribution resulting from the corresponding high symmetry point of the 2D Brillouin zone, i.e. $\mathbf{k}_\| = -\mathbf{G}_\|^{(2)}/2$. If we image Mn on W(110)

---

[2] In our definition, introduced in section 4.6.1, $\phi_1^{2D}(\mathbf{r}_\|) = 1$.

with a non-magnetic tip, $I = I_o$, all atoms are equivalent, and the chemical unit cell is diamond shaped (Fig. 9.6(a)). The four smallest reciprocal lattice vectors of this cell, all related by symmetry operations, are displayed in Fig. 9.6(b). The corresponding 2D star function resulting from the superposition of the four corresponding plane waves represents the expected STM topography (Fig. 9.6(c)).

An antiferromagnetic superstructure lowers the translational symmetry, and the additional tunneling current due to spin-polarized electrons, I_P, is sensitive to the unit cell of the superstructure (Fig. 9.6(d)). Therefore, smaller reciprocal lattice vectors become accessible (Fig. 9.6(e)). Since these possess exponentially larger coefficients they dominate the STM-image, $\Delta I \approx \Delta I_P$, even in the case of small effective spin-polarization $P_S P_T \cos\theta$, for example if the angle θ is close to 90°. Thus the corrugation amplitude Δz (the maximum difference in tip height while it scans the surface) is directly proportional to the spin-polarization, $\Delta z(z_0) \sim P_S\, P_T\, \cos\theta$, where z_0 is the average tip-sample distance. A stripe pattern (Fig. 9.6(f)) without any chemical background is expected to be seen in the experiment due to the smallest reciprocal superlattice vector. Correspondingly, we expect a diagonal stripe pattern for the p(2 × 1)-AFM state (Fig. 9.3(c)).

These arguments are quite general and in principle applicable to any magnetic superstructure. The electronic structure, contained in $I_{s>1}(\theta, V)$ of Eq. (9.3), of a specific surface can still compete with this effect, and first-principles calculations need to be performed in order to interpret the experiments unambiguously. STM images were calculated on the basis of the Tersoff-Hamann model [6] as described in chapter 4. The spin-polarized measurements utilizing a ferromagnetic tip were simulated by assuming different values for the spin-polarization P_T of the tip states.

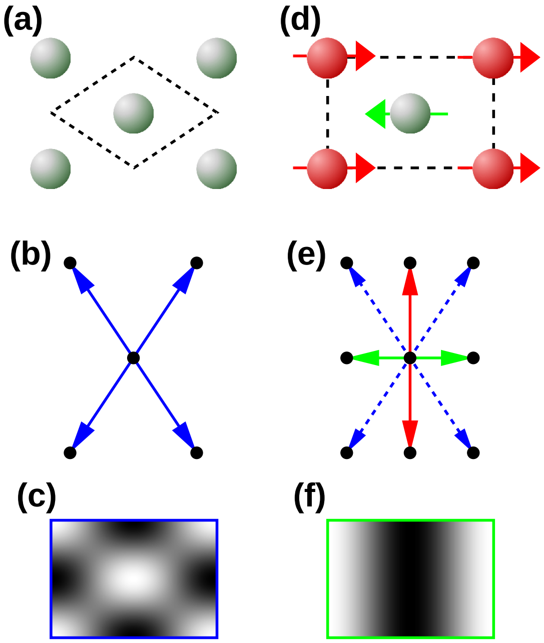

Figure 9.6: Lattice (a), (d), shortest reciprocal lattice vectors (b), (e), and the 2D starfunction, i.e. the expected STM images (c) and (f), associated to the shortest reciprocal lattice vectors of the chemical and the magnetic unit cell of a Mn monolayer on W(110). Note that (e) contains the shortest vectors of the chemical unit cell (dashed) and the two inequivalent pairs of additional vectors due to the magnetic superstructure.

9.5 Experimental Details

The SP-STM experiments[3] were performed in a cryogenic ultra-high vacuum (UHV) system equipped with a 2.5 T magnet [130] and separate chambers for substrate preparation, sample transfer, metal vapor deposition (MVD) and surface analysis. The sample preparation procedure is described in detail in Refs. [130, 131]. We used etched W-tips which were flashed *in-vacuo* to remove oxide layers. In the MVD-chamber the tips were magnetically coated with Fe or Gd while held at 300 K, subsequently annealed at $T \approx 550$ K for 4 min, and then transfered into the cryogenic STM. During the measurement tip and sample were at a temperature $T = 16$ K.

9.6 SP-STM Images of Mn/W(110)

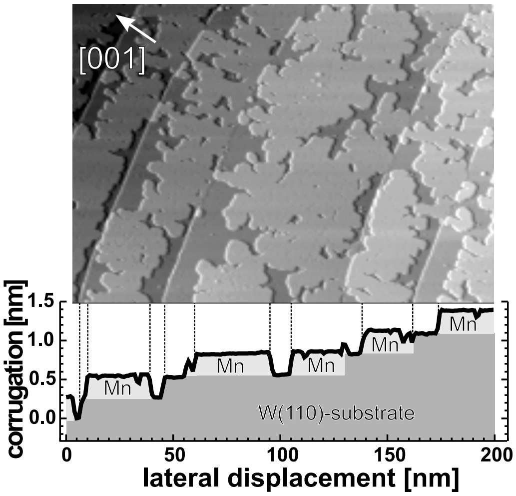

Figure 9.7: Topography of 0.75 ML Mn grown on a stepped W(110) substrate. A line-section (bottom panel) was drawn at the bottom edge of the image. The structure of the sample is schematically represented by different grey levels. The image size is 200 nm × 200 nm.

The growth of Mn on W(110) has previously been studied [131]. It was found that a monolayer (ML) Mn grows atomically flat and pseudomorphically on W(110), i.e. Mn has the same in-plane lattice constant as the underlying W substrate. No hints of alloying could be observed. Fig. 9.7 shows the topography of 0.75 ML Mn/W(110) grown at a substrate temperature $T_{\mathrm{sub}} \approx 400$ K. Atomically flat Mn islands as well as parts of the uncovered tungsten substrate are visible.

Using a clean tungsten tip atomic resolution was achieved on the Mn-islands as shown in Fig. 9.8(a). The diamond-shaped unit cell of the pseudomorphic (1×1) Mn-monolayer is clearly visible. The line-section drawn along the dense-packed $[1\bar{1}1]$-direction exhibits a periodicity of 0.27 ± 0.01 nm which almost perfectly fits the expected nearest-neighbor distance of 0.274 nm. The measured corrugation amplitude amounts to 15 pm. In the inset a calculated STM-image for a conventional tip without spin-polarization, i.e. $P_T = 0$, is given for comparison. Obviously, the qualitative agreement between theory and experiment is excellent. However, the theoretically

---

[3] The experiments have been performed by M. Bode, A. Kubetzka, and O. Pietzsch, and it is my pleasure to thank them for their fabulous work.

determined corrugation amplitude is by far too small. This deficiency of the Tersoff-Hamann model in predicting the correct corrugation in atomically resolved STM-images of close-packed metal surfaces is well understood[4].

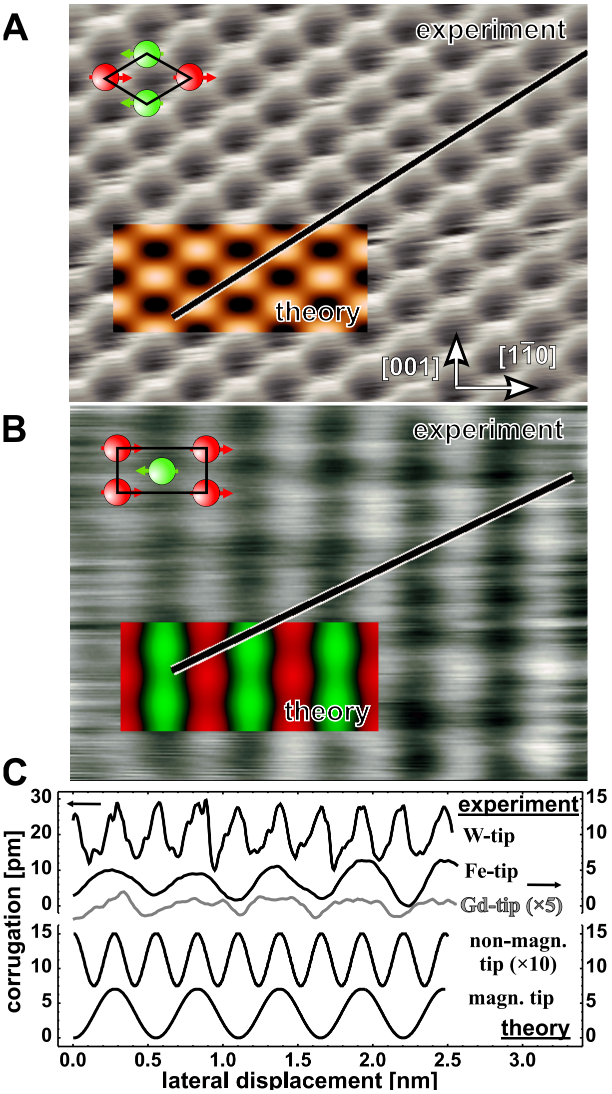

Figure 9.8: Comparison of experimental and theoretical STM-images of a Mn monolayer on W(110) with (a) a non-magnetic W- and (b) a magnetic Fe-tip. (c) Experimental and theoretical line sections for the images (a) and (b). The unit cell of the calculated magnetic ground state configuration is shown in (a) and (b) for comparison. Tunneling parameters for both images are $I_{\text{tun}} = 40$ nA and $U = -3$ mV. The image size is 2.7 nm × 2.2 nm.

In a second set of experiments different ferromagnetic tips were used. Since we know from the first-principles computations that the easy magnetization axis of the Mn monolayer on W(110) is in-plane, the experiment required a magnetic tip with a magnetization axis in the plane of the surface in order to maximize the effects. This condition is fulfilled by Fe-coated probe tips [132]. Fig. 9.8(b) shows an STM-image taken with such a tip. Periodic parallel stripes along the [001]-direction of the surface can be recognized. The periodicity along the [1$\bar{1}$0]-direction amounts to 4.5 ± 0.1 Å which corresponds well to the size of the magnetic c(2×2) unit-cell. The inset in Fig. 9.8(b) shows the calculated STM-image for the magnetic ground state, i.e. the

---

[4] The disagreement is related to the unknown atomic structure of the tip. A better quantitative agreement can be obtained by including more localized tip orbitals such as d_{z^2} whose corrugation amplitudes are much closer to experiment (see chapter 5).

c(2×2)-AFM configuration as discussed in Fig. 9.3(b). We find theory and experiment to give a consistent picture. Even the predicted weak constrictions of the stripes along the [001]-direction related to the pair of second smallest reciprocal lattice vectors of Fig. 9.6(e) are visible in the measurement. Again, experimental and theoretical data can be compared more quantitatively by drawing line-sections along the dense-packed $[1\bar{1}1]$-direction as indicated in Fig. 9.8(b). The result is plotted in Fig. 9.8(c). It reveals that the periodicity when measured with a Fe-coated probe is twice the nearest neighbor distance, i.e. 0.548 nm. The experimental corrugation amounts to 3 to 4 pm which is slightly below the corrugation expected from theory, $\Delta z(5\text{Å}) = 7$ pm at $V \approx 0$ V. In Fig. 9.9 the calculated corrugation amplitude is displayed as a function of the applied bias-voltage. The contributions from the majority and minority spin states are exactly the same except for the sign of the corrugation amplitude. In the present case the sign denotes that either the ferromagnetic or the antiferromagnetic Mn atom rows with respect to the tip magnetization are imaged as protrusions. Thus with a non-spinpolarized STM-tip the net corrugation amplitude of the stripe pattern vanishes, and the diamond shaped pattern of the chemical unit cell is observed. However, if the tip possesses a non-vanishing spin-polarization P_T the corrugation amplitude can be readily computed from the two spin contributions. This has been done for the case of $P_T = -0.4$ in Fig. 9.9. This value has been determined in earlier experiments [132]. There is a maximum in the corrugation amplitude at a voltage of about -0.5 V which is related to the edge of a surface state band of the Mn monolayer. In the next section it will be shown that it is also the cause of the possibility to image the magnetic structure at low bias-voltages, i.e. at the Fermi energy. In agreement with the expectation from the plot of the corrugation amplitude no qualitative bias-voltage dependence of the SP-STM image has been observed in the experiments which were performed at voltages between -100 meV and 0 meV.

In the calculation we assumed the magnetization axes of the sample and the probe tip to be collinear, i.e. $\cos\theta = \pm 1$. However, in the present experimental setup even for the case of $\theta = 0$, i.e. the tip magnetization lying perfectly in the surface plane, ϕ cannot be controlled and the alignment can be non-collinear, which might explain the discrepancy between theory and experiment. The strong dependence of the effect on the magnetization direction of the tip can be exploited to gain further information on the magnetization direction of the sample by using a tip which exhibits an easy magnetization axis which is *almost perpendicular*[5] to the one of the sample surface. This condition is fulfilled for a W-tip coated by 7 ± 1 ML Gd as we could show recently [27]. In Fig. 9.8(c) we have included a typical line-section as measured with a Gd-coated probe tip (grey line). Indeed, the corrugation amplitude was always much smaller than for Fe-coated tips and never exceeded 1 pm supporting the theoretical results that the easy axis of the Mn atoms is in-plane. Note, that the image still displays the stripe pattern characteristic of the magnetic superstructure as proposed

---

[5] The in-plane or out-of-plane magnetization direction of tips coated by thin films is governed by the interface and surface anisotropy of the film material, i.e. Fe or Gd, in contact with the most densely packed W-surface, i.e. W(110), which is formed at the tip apex after the thermal flash. To our experience, slight deviations from the ideal magnetization directions were frequently observed, probably caused by the curved shape of the tip.

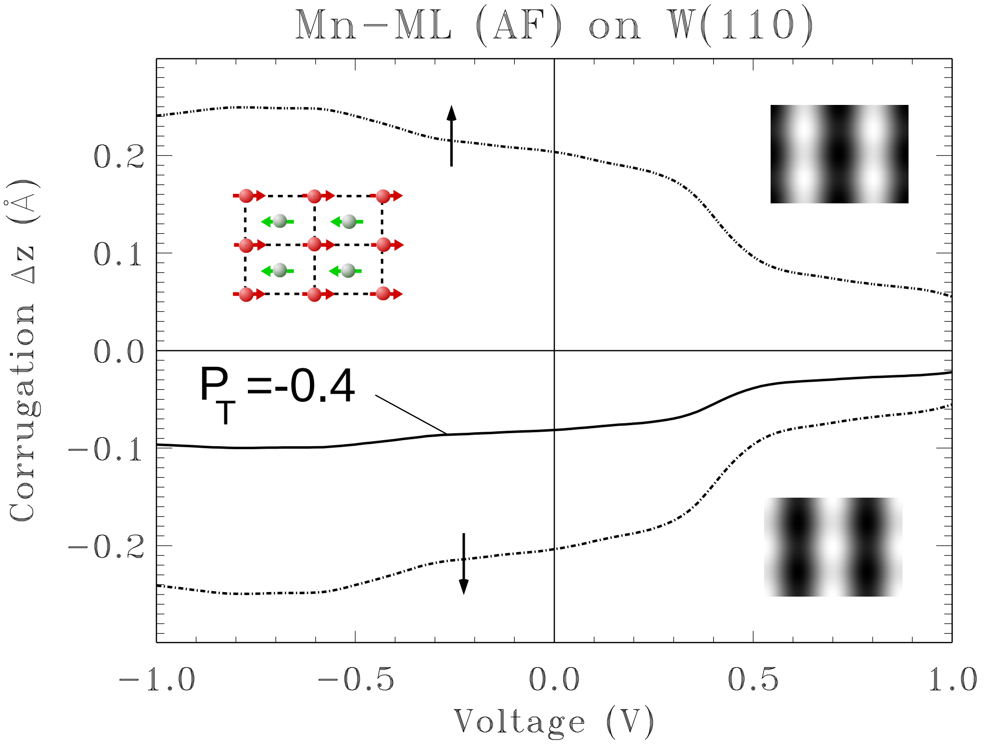

Figure 9.9: Calculated corrugation amplitude as a function of the applied bias-voltage for the c(2 × 2) antiferromagnetic configuration of the Mn-monolayer on W(110). The dotted and dashed-dotted curves denote the two spin contributions while the full line represents the total corrugation amplitude measured with a magnetic tip of spin-polarization $P_T = -0.4$. A positive (negative) corrugation amplitudes is related to imaging the ferromagnetic (antiferromagnetic) Mn atom rows with respect to the tip magnetization as protrusions. The insets show the unit cell of the c(2 × 2) antiferromagnetic configuration (upper left) and the calculated STM-images for $P_T > 0$ (upper right) and $P_T < 0$ (lower right).

by the discussion of Eq. (9.2) and (9.3) even for a small effective spin-polarization due to nearly orthogonal magnetization directions.

9.7 Correlation with the Electronic Structure

In section 9.4 we have discussed the reason for the possibility to image the magnetic superstructure on the basis of the exponential decay of the coefficients $I_{\mathbf{G}_{\|}^{n}}(z,\theta,V)$ in the vacuum. As the decay of the coefficients to a certain pattern, i.e. star function $\phi_s^{2D}(\mathbf{r}_{\|})$, of the STM image depends exponentially on the length of the corresponding reciprocal lattice vector $\mathbf{G}_{\|}^{s}$ the smallest vector will dominate the image. However, it must be kept in mind that the electronic structure of a specific sample enters into the coefficients. Therefore, it needs to be verified by first-principles calculations that there are actually contributions from electronic states to the pattern with the smallest reciprocal lattice vector. Otherwise the pattern corresponding to the next

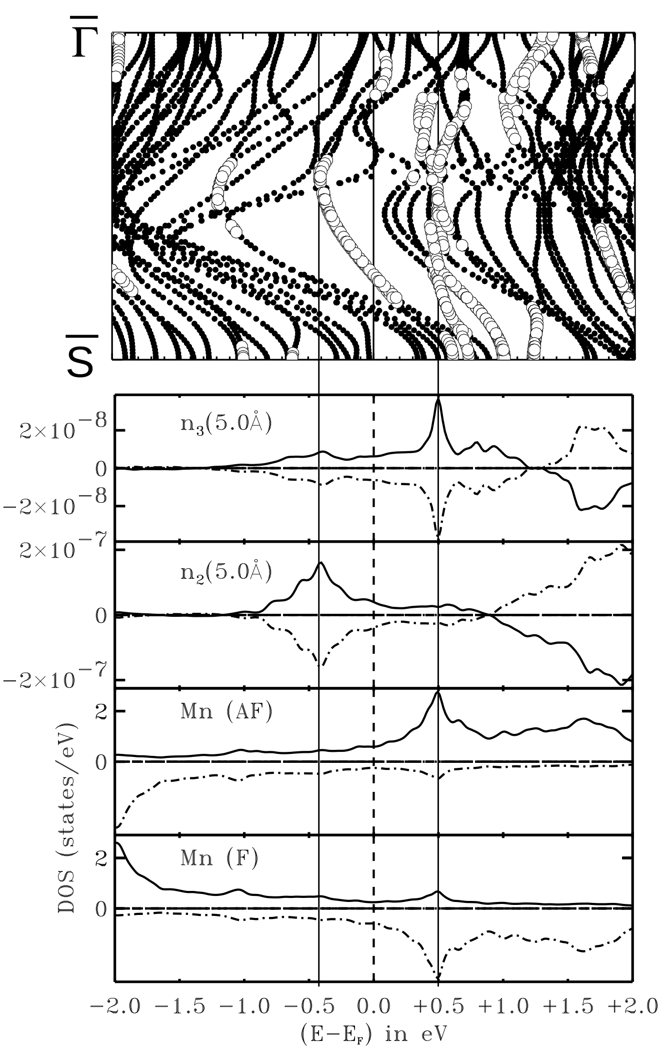

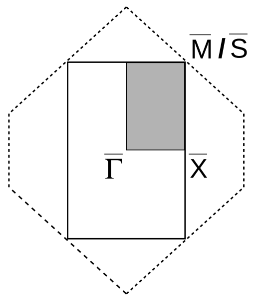

Figure 9.10: Comparison of the bandstructure, second and third star coefficient and the DOS of the ferro- and antiferromagnetic Mn atom of the Mn-monolayer on W(110). Full (dashed) lines in the DOS plots denote majority (minority) contributions. In the bandstructure states which are localized with more than 50 % in the Mn-monolayer and the vacuum region are marked by open circles. The bandstructure is shown for one spin contribution only since the other is identical. The two-dimensional Brillouinzone of the $c(2\times 2)$ unit cell is displayed in the upper panel by the full line while the one of the $p(1\times 1)$ unit cell is given by the dashed line.

larger reciprocal lattice vector will dominate the STM image. Thus in this section we will analyze in detail the bands responsible for the SP-STM image presented in the previous section. From our analysis it can be concluded that the effect should also be observable for a Cr-monolayer on W(110) and even with a slightly higher corrugation amplitude.

In Fig. 9.10 the electronic structure of the two magnetically inequivalent Mn atoms of the monolayer is compared in terms of their density of states and the bandstructure with the corresponding STM-images in terms of the two lowest star coefficients with non-constant patterns, i.e. the second (third) star coefficient corresponding to stripes along the short (long) side of the rectangular unit cell. The values of the star coefficients differ for the two spin directions only by their sign since the spin-summed electronic structure of both Mn atoms is identical. In the following we therefore focus on the majority contribution assuming that the magnetic STM-tip used favors this spin channel[6]. The (majority) second star coefficient $n_2(\epsilon)$ displays a distinc-

---

[6] The discussion can certainly also be applied to the minority states without a change of the result since both are identical due to the antiferromagnetic ground-state.

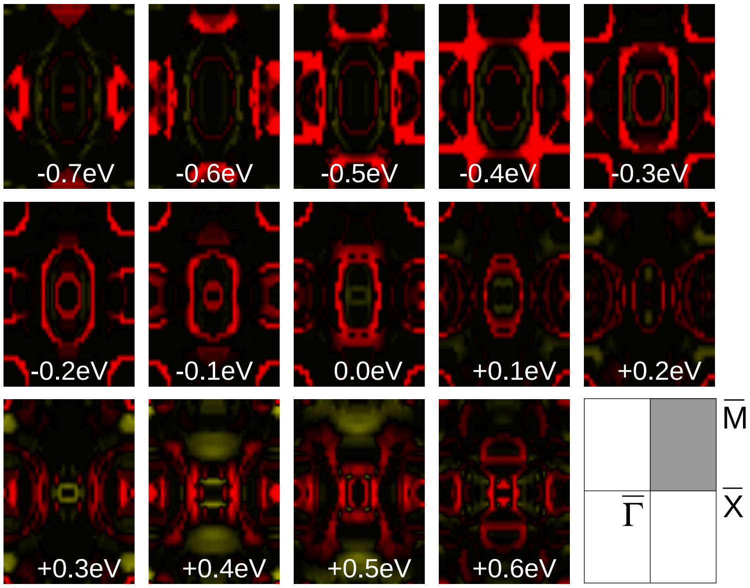

Figure 9.11: The majority second star coefficient as a function of the wave vector $\mathbf{k}_{\|}$ on a 512 point mesh in the irreducible part of the two-dimensional Brillouin zone. Energy intervals of 0.1 eV have been chosen and the energies are given relative to the Fermi energy. Red (yellow) marks positive (negative) coefficient values. The band edge of the surface state in $\bar{\Gamma}\bar{M}$-direction is clearly visible at $E = E_F - 0.4$ eV by its large contribution. From these plots one can conclude unambigiously that the surface state band is responsible for the SP-STM images.

tive maximum at an energy of about $E_F - 0.4$ eV. Correspondingly, the corrugation amplitude (Fig. 9.9) shows a maximum close to this bias-voltage. The peak position can be correlated with the edge of a surface state band, marked by open circles, along the $\bar{\Gamma}\bar{\text{M}}$-direction of the 2D-BZ. Note, that this direction remains unchanged when we backfold the bandstructure from the p(1×1) to the c(2×2) unit cell (see Fig. 9.10). Thus we see a close resemblance of this band with the one discussed in chapter 5 responsible for the bias-voltage dependent corrugation reversal on W(110) (compare Fig. 5.6). In the bandstructure of the Mn-monolayer on W(110) we additionally find its exchange-split partner with a band edge of about $E_F - 1.2$ eV and a very similar dispersion along the displayed high symmetry line. The value of the (majority) second star coefficient $(n_2^{\uparrow}(\epsilon))$ peak is positive and therefore the ferromagnetic Mn atom rows appear as protrusions in the SP-STM-image of the (majority) surface state band. The band possesses quite a large dispersion, and still dominates the SP-STM-image at the Fermi energy. Thus it is also responsible for the experimentally achieved magnetic resolution shown in the previous section. From Fig. 9.10 it cannot actually be concluded that the surface state band gives the predominant contribution although the correlation is already quite suggestive. Therefore, we present in Fig. 9.11 the contributions to the (majority) second star coefficient from different parts of two-dimensional Brillouin zone at various energies. From this plot we can clearly see the maximum value at an energy of $E = E_F - 0.4$ eV which is located right at the band edge of the surface state about midway between the $\bar{\Gamma}\bar{\mathrm{M}}$-direction. Also the dispersion of this band can be traced splitting into two branches, one which closes in around $\bar{\Gamma}$ and the other around $\bar{\mathrm{M}}$, until it vanishes at an energy of about $E = E_F + 0.2$ eV.

The third star coefficient $n_3(\epsilon)$ with values of a magnitude smaller than the second star coefficient displays a maximum in the unoccupied states at an energy of $E_F +$ 0.5 eV. Therefore the constrictions of the stripes along the [001]-direction should become more pronounced at positive bias-voltages near to the peak position. The correlation with strongly Mn located states is again marked by a line in Fig. 9.10. This very small effect has not been verified experimentally although the intensity of the constrictions varied considerably for SP-STM images taken at different tunneling conditions. At experimentally unreasonable large energies[7] above the Fermi energy the second star coefficient changes its sign since the exchange-split bands of the antiferromagnetic Mn atom then become dominant.

A single state of the surface state band is shown in Fig. 9.12. Obviously, there is a high localization in the Mn-monolayer and additionally in the first layer of the W(110)-substrate. This localization at the two top layers of the whole film is closely related to the surface states present at the pure W(110)-surface (compare the charge density plots in Fig. 5.10). The orbital character at the Mn atoms which are imaged as protrusions is d_{z^2} while it is d_{yz} for the other kind of Mn atoms. The corresponding SP-STM-image is also presented in Fig. 9.12 which makes the correlation with the cross-sections quite easy.

In conclusion, the specific electronic structure of the Mn-monolayer film on the W(110)-substrate leads to the possibility of imaging either the rows of ferro- or antiferromagnetic atoms as protrusions depending on the magnetization axis of the spin-polarized STM-tip. Notice the similarity of the surface state band with that of the W(110)-substrate only (see chapter 5) hinting at their close relation and the importance of the hybridization at the interface. As the ground-state configuration of a Cr-monolayer on W(110) is also c(2×2) antiferromagnetic the presence of a similar surface state band is expected. The calculation is actually in accordance with this expectation and since Cr possesses one electron less than Mn the surface state band edge shifts closer to the Fermi energy. Correspondingly also the maximum in the corrugation amplitude plot shifts towards zero bias-voltage (compare Fig. 9.9). Thus an even larger corrugation amplitude should be measurable but no experiments have been undertaken to verify this prediction. Still, there is a great potential in nanomagnetism for the application of the presented method of imaging the magnetic ground-state of ultra-thin magnetic films directly by SP-STM. Calculations carried out for related systems support this conviction (see for example the section on the STM images of the Cr and Mn monolayers on Fe(001) in the previous chapter). Even more complicated magnetic configurations like non-collinear spin-structures might be identified with the proposed approach in the future (see Fig. 10.1).

---

[7] Experimentally bias-voltages of ±0.5 V are commonly being used for atomic resolution images in order to achieve measurable corrugation amplitudes at tunneling currents which are handable by the electronics and do not destroy the tip.

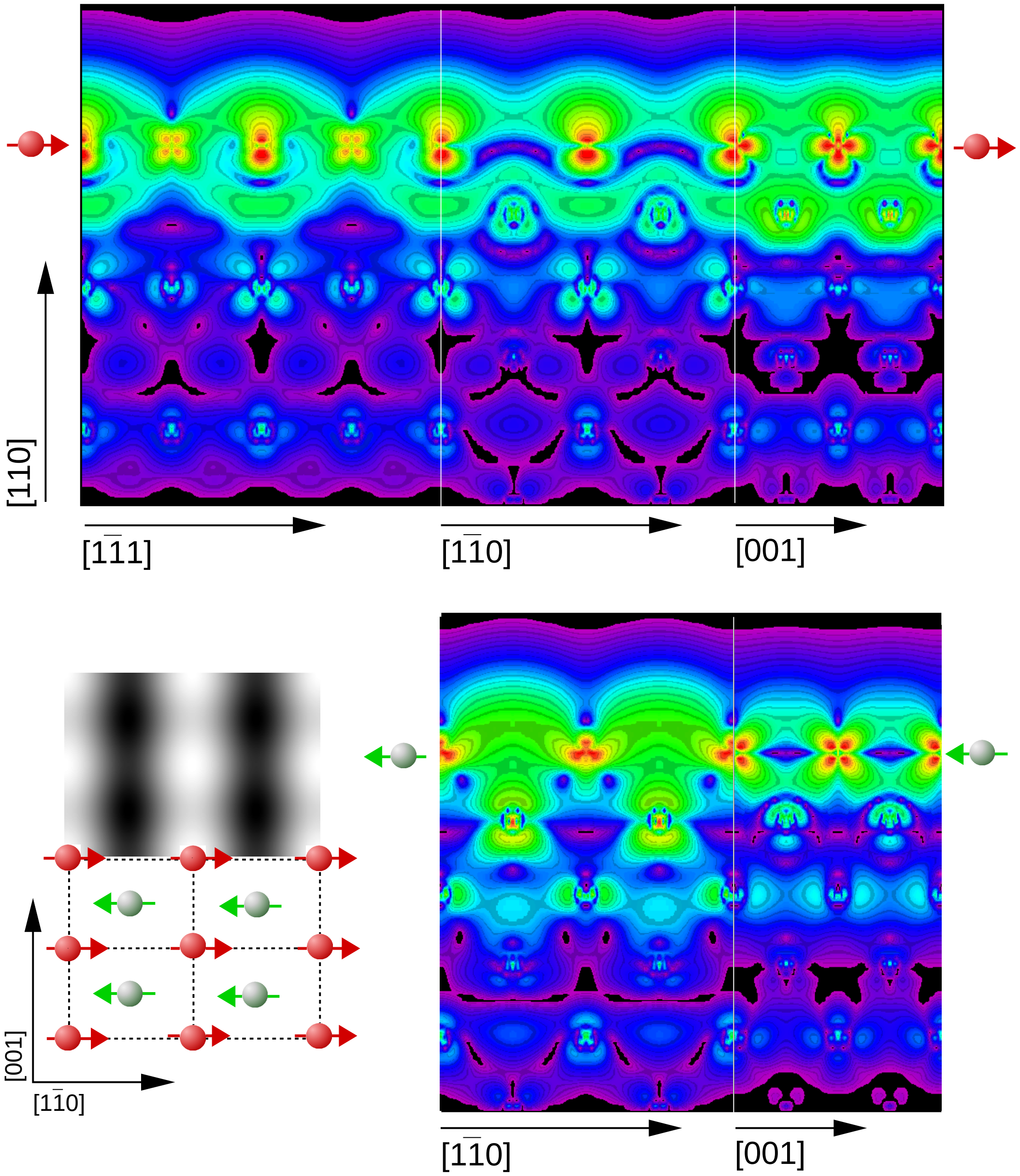

Figure 9.12: A single minority spin state of the surface band of the Mn-monolayer on W(110) responsible for the SP-STM image. The wave vector is $\mathbf{k}_{\parallel} = 0.6\,\bar{\Gamma}\bar{S}$ and the energy eigenvalue $\epsilon_{\nu\mathbf{k}_{\parallel}} = E_F - 0.25$ eV. In the upper (lower) panel cross-sections through the positions of the antiferromagnetic (ferromagnetic) Mn atom are displayed. In the lower left corner the corresponding SP-STM image for $P_T = 0.4$ is shown along with the surface structure.

Chapter 10

Summary

In this work a systematic study of the interpretation of scanning tunneling microscopy (STM) experiments on transition-metal surfaces and thin films on the atomic scale has been given for the first time. The combination of modern first-principles calculations applying the full-potential linearized augmented plane wave (FLAPW) method with the model of STM introduced by Tersoff and Hamann [6] and extended by Chen [11] has led to a number of surprising results. In contradiction to conventional wisdom the interpretation of STM images of transition-metal surfaces is far from trivial and cannot be performed on the basis of simple hard sphere models. The calculations have provided explanations for the unexpected outcome of several experiments and contain predictions for future experiments.

For the analysis of the calculated STM images an efficient method to compute corrugation amplitudes and to correlate features of the band structure with their contribution to the images has been developed. This method relies on the possibility to decompose the images into symmetrized plane waves, the two-dimensional star functions $\phi_s^{2D}(\mathbf{r}_\|)$. The contribution of every eigenstate of a surface to a certain star function s is given by an energy ϵ and wave vector $\mathbf{k}_\|$ dependent so-called star coefficient $n_s(\epsilon, \mathbf{k}_\|)$. As a result of the energy, wave vector, and star function dependent exponential decay of these star coefficients a selection rule for the most important contributions to a given star function can be derived. Thus only special parts of the two-dimensional Brillouin zone play a significant role for the different types of images. The direct comparison of the simple model with real first-principles calculations has demonstrated the validity of this argumentation.

A first application of this technique has been presented in chapter 5 dealing with the effect of a bias-voltage dependent corrugation reversal in atomic-resolution STM images of bcc-(110) transition-metal surfaces. One occurrence of anti-corrugation, i.e. the imaging of hollow sites as protrusions in an STM image, has already been observed and explained for experiments on Fe(001) and Cr(001) at small bias-voltages [115,116]. Here, the change from a normal image, i.e. where protrusions correlate with atom sites, to anti-corrugation with a variation of the applied bias-voltage has been predicted. The effect has been explained as a result of the competition between a surface state and a surface resonance band of the bcc-(110) transition-metal surfaces. It is of great importance to be aware of anti-corrugation and also of changes with the applied bias-voltage if one tries to deduce the adsorption site of deposited atoms from the STM images.

Another interesting aspect of the characterization of a surface by STM is chemical sensitivity, i.e. the ability to discriminate different chemical species from each other. Chemical sensitivity has been an important topic for a long time but still no general method is available to distinguish chemical species on the basis of an STM image. An example of the successful combination of first-principles calculations with STM experiments on a multi-component system, $CoSi_2(100)$, has been discussed in chapter 6. Counterintuitively, the STM image displays the Si surface atoms as protrusion for bias-voltages below +0.5 V and the Co atoms as protrusions above this voltage. On the basis of the excellent agreement between the calculation and the experiment a new model for the termination of the $CoSi_2(100)$-surface has been given with an inhomogeneous occupation of lattice sites.

While the feasibility of imaging even uncharged defects buried in semiconductor surfaces has been reported [96] conventional wisdom excludes this effect for metal surfaces due to the small screening length of electrons in metals. Thus only the symmetry of the surface layer should be observable with STM. This is in accordance with earlier STM experiments [93] deducing the occurrence of subsurface alloying indirectly while imaging only the structure of the surface layer. However, in chapter 7 another subsurface alloy has been studied, Ir in Cu(001), and for the first time the *direct imaging* of a buried transition-metal structure by STM has been demonstrated. The effect is related to the fact that STM probes an integration over the local density of states rather than the charge density. The dependence of such an effect on the specific electronic structure of the chemical components was deduced from the calculations. The results are in accordance with the earlier experiments but also reveal a wide class of transition-metals which should behave similar to Ir. Additionally, the possibility of imaging even deeper buried alloys has been explored. It turned out that the formation of quantum well states in these structures leads to oscillations in the corrugation amplitude. At small bias-voltages the value of the corrugation amplitude is higher than the resolution limit of STM. Thus the observation of deeply buried transition-metal structures seems possible. Experimentally such an effect has actually been demonstrated by imaging the famous (7×7)-Si(111) reconstruction beneath 100 Å of Pb [102]. However, the two-dimensional periodicity of this reconstruction is by far larger than that of the buried alloys taken under scrutiny here and it is a semiconductor-metal hybrid system rather than a pure metal system. To investigate if the direct imaging of deeply buried transition-metal structures in metal substrates is still feasible at the periodicities proposed here will be an experimental challenge in the future. The theoretically investigated system, Ir in Cu(001), appears to be an appropriate candidate also from the experimental point of view.

Today, there is a growing number of open questions in fundamental research as well as in technological applications of the magnetic-storage industry concerning the lateral magnetic order of surfaces and thin films on the nanometer scale. For example, complicated spin structures like spin-density waves, two-dimensional antiferromagnetism and non-collinear spin structures occur in thin film structures where ferromagnetic films are placed ontop of antiferromagnetic ones thus applying the exchange-bias effect. Such layered structures are relevant for example in read heads of hard disks. It is thus desirable to possess a tool that combines a resolution on the nanometer down to the atomic scale with magnetic sensitivity. The spin-polarized STM (SP-STM) is the appropriate method to achieve this goal [23–28].

As the SP-STM is still far from being routinely applied, we have started the theoretical investigation of the potential of STM in the field of atomic-scale magnetism in chapter 8 by studying the influence of the magnetic configuration of thin films on (non-spinpolarized) STM images and spectra. Cr and Mn on Fe(001) have been chosen as systems representative of the complex correlation of magnetic and structural properties. The calculated ST-spectra of the clean Fe(001)-surface and the $c(2 \times 2)$ CrFe surface alloy are in good agreement with experiments [66,94]. In the case of Cr monolayers on Fe(001) it should be possible to discriminate between the two magnetic configurations, which are nearly degenerate, on the basis of non-spinpolarized scanning tunneling spectroscopy (STS). For the Mn monolayers on Fe(001) the characteristic features are very close in energy and a distinction seems impossible. On the other hand, as the $c(2 \times 2)$ antiferrimagnetic configuration displays a $c(2 \times 2)$ pattern also in a (calculated) non-spinpolarized STM image one should be able to distinguish it from either the $p(1 \times 1)$ ferromagnetic or the $p(1 \times 1)$ layered antiferromagnetic configuration. In the case of Mn an even more complicated magnetic configuration with a $p(2 \times 2)$ unit cell has been proposed as the ground-state. However, non-spinpolarized STM images of this magnetic state will hardly help to distinguish it from the $c(2 \times 2)$ antiferrimagnetic configuration which is only by 7 meV per Mn atom unfavorable. The indistinguishability is due to the partial cancelation of majority and minority spin contributions leading to a $c(2 \times 2)$ pattern for the calculated STM images which is identical to the image of the competing $c(2 \times 2)$ antiferrimagnetic configuration.

Finally, in chapter 9 the potential of SP-STM to unravel the magnetic configuration of ultra-thin films on the atomic-scale has been explored in general, and the applicability of the approach has been demonstrated by experiments for a Mn-monolayer on W(110). By generalizing the Tersoff-Hamann model [6] to SP-STM and using the earlier introduced wave vector and star function dependent decay of star coefficients we have proved that SP-STM images with atomic resolution of a surface with chemically equivalent atoms display the two-dimensional magnetic superstructure rather than the chemical unit cell. The result is not just a small perturbation of the non-spinpolarized STM image but a complete domination of the image by the spin-polarized contribution. This aspect has been overlooked by theory up to now. The approach was applied to a Mn-monolayer on W(110). This system is a representative example of a two-dimensional antiferromagnet since nearest-neighbor Mn atoms couple antiferromagnetically in the ground-state as is deduced from the calculations. The occurrence of such a 2D antiferromagnetic configuration has first been predicted by Blügel *et al.* in 1988 [21] but unambiguous proof was missing so far. The Mn atoms of the monolayer are chemically equivalent and thus in a non-spinpolarized STM experiment an image was observed showing the diamond-shaped chemical unit cell. In the SP-STM images which were acquired using Fe and Gd-coated W-tips on the other hand a stripe pattern was found reflecting rows of ferromagnetic atoms that couple antiferromagnetic to neighboring rows. The experiment is in excellent

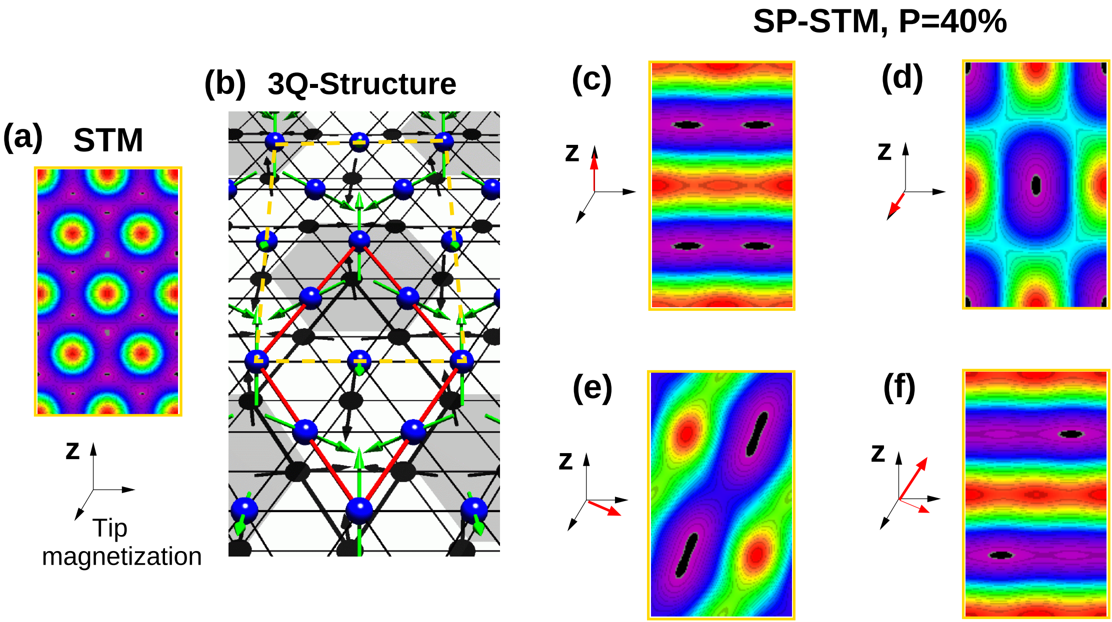

Figure 10.1: Example of the (future) potential of SP-STM to resolve complex non-collinear magnetic structures. A three-dimensional non-collinear magnetic ground-state occurs for a Mn-monolayer on a hexagonal lattice [133], shown in (b). (a) displays the expected STM image with a non-magnetic STM tip where the hexagonal chemical unit cell is seen. Calculated SP-STM images with a variation of the relative angle between the magnetization axis of tip and sample are shown in (c) to (e). As a result of the varying relative angle different patterns are observed. Since other magnetic configurations which are close in energy possess different magnetic unit cells a discrimination on the basis of the SP-STM images seems possible. (Calculated SP-STM images by courtesy of D. Wortmann.)

agreement with the prediction of the calculations. It is the first proof of 2D antiferromagnetism in monolayer magnetic films on non-magnetic substrates.

With this achievement the predictive power of both density functional theory and our approach to model STM has been confirmed. Demonstrating the feasibility to image the magnetic superstructure directly with SP-STM has opened the door to a comparison of state-of-the-art theoretical and experimental tools in the investigation of surface magnetism on the ultimate, the atomic-scale. As an example of the future potential of the introduced approach Fig.10.1 shows the calculated SP-STM images for a complex three-dimensional non-collinear spin structure of a Mn-monolayer on a hexagonal lattice [133]. In this case even different SP-STM images are expected depending on the relative angle between the magnetization axes of tip and sample.

In the future a number of questions concerning STM experiments on transition-metal surfaces remain to be answered. Although there have been some first-principles calculations concerning the electronic structure of non-magnetic transition-metal STM tips supported on a surface [53] to my knowledge there are no first-principles calculations for magnetically coated tips. To understand the influence of the material and the geometry on the electronic and magnetic properties will be of great importance. The key quantity to be determined is the spin-polarization of the tunneling electrons from such a tip. Also the orbital character of these spin-polarized electrons should be analyzed since there is still a dispute about the origin of the spin-polarization of the electrons. For example in the Tersoff-Hamann model s-wave functions are assumed for the tip states and s-electrons are most commonly held responsible for the major contribution to the tunneling current. However, the s-bands are only slightly spin-polarized in transition metals which leads to a contradiction to the rather large magnetic effects observed in the SP-STM experiments. Up to now only ferromagnetic materials like Fe and Gd have been used to coat STM tips. To explore whether antiferromagnets like Mn or Cr may have the same or even favorable properties concerning the use as SP-STM probes is another topic for future theoretical studies. The implementation of the full Bardeen approach treating the tip and the sample on an equal footing is closely related to the studies of tip properties. By calculating the tunneling current from the matrix elements of all possible transitions from tip to sample states the influence of particular tip states can be evaluated. However, a better quantitative description of the tunneling current on this basis requires additional knowledge of the geometric structure of the tip which needs to be provided by the experiments. Otherwise, the insight even with such an elaborate approach is quite limited due to the enormous number of possible tip configurations and their impact on the resulting tunneling current.

In conclusion, it has been shown that the influence of the electronic structure of transition-metal samples on STM experiments is much stronger than has been suspected by conventional wisdom. A number of surprising observations in STM experiments have been explained on the basis of the first-principles calculations performed within this work. Further, some predictions of the calculations remain to be verified experimentally in the future. All of our studies lead to the conclusion that a hard sphere model is by no means appropriate to understand STM experiments with atomic resolution on transition-metal surfaces. The developed approach to analyze and predict STM experiments combines the Tersoff-Hamann model of STM with the first-principles `FLEUR` code and provides fast insight into the correlation of electronic structure features and characteristic STM images. Although improvements like including the STM tip to the calculations are desirable in the future a great number of problems may still be tackled with the present method. By generalizing the Tersoff-Hamann model to SP-STM we have proved the feasibility to image magnetic superstructures on the atomic scale. This extends the use of STM from the exploration of the topological, chemical, and ferromagnetic structure of surfaces to the inherently much more difficult investigation of antiferromagnetic surfaces and surfaces with non-collinear spin structures with ultimate, atomic resolution.

Bibliography

[1] P. Grünberg, R. Schreiber, Y. Pang, M. B. Brodsky, and H. Sowers, Phys. Rev. Lett. **57**, 2442 (1986).

[2] G. Binnig und H. Rohrer, Helv. Phys. Acta **55**, 726 (1982).

[3] F. J. Giessibl, Science **267**, 68 (1995).

[4] Y. Sugawara, M. Ohta, H. Ueyama, and S. Morita, Science **270**, 1646 (1995).

[5] A. Messiah, *Quantenmechanik, Bd. 1* (de Gruyter, Berlin, 1991).

[6] J. Tersoff and D. R. Hamann, Phys. Rev. Lett. **50**, 1998 (1983).

[7] N. D. Lang, Phys. Rev. Lett. **55**, 230 (1985).

[8] N. D. Lang, Phys. Rev. B **34**, 5947 (1986).

[9] M. Tsukada, K. Kobayashi, N. Isshiki und H. Kageshima, Surf. Sci. Rep. **13**, 265 (1991).

[10] C. J. Chen, Phys. Rev. Lett. **65**, 448 (1990).

[11] C. J. Chen, *Introduction to Scanning Tunneling Microscopy* (Oxford University Press, Oxford, 1993).

[12] C. Noguera, in: Scanning Tunneling Microscopy III, Eds. R. Wiesendanger and H.-J. Güntherodt, Springer Ser. Surf. Sci., Vol. **29**, 51 (1993).

[13] G. Doyen, D. Drakova und M. Scheffler, Phys. Rev. B **47**, 9778 (1993).

[14] J. Cerdá, M. A. Van Hove, P. Sautet, and M. Salmeron, Phys. Rev. B **56**, 15885 (1997).

[15] S. Corbel, J. Cerdá, and P. Sautet, Phys. Rev. B **60**, 1989 (1999).

[16] J. Bardeen, Phys. Rev. Lett. **6**, 57 (1961).

[17] P. Hohenberg und W. Kohn, Phys. Rev. B **136**, 864 (1964).

[18] W. Kohn und L. J. Sham, Phys. Rev. B **140**, 1133 (1965).

[19] M. Levy, Phys. Rev. A **26**, 1200 (1982).

[20] M. Wuttig, Y. Gauthier, and S. Blügel, Phys. Rev. Lett. **70**, 3619 (1993).

[21] S. Blügel, M. Weinert, and P.H. Dederichs, Phys. Rev. Lett. **60**, 1077 (1988).

[22] M. C. Desjonqueres, and D. Spanjaard, in *Concepts in Surface Physics*, Springer Verlag (Heidelberg, 1996).

[23] R. Wiesendanger, H.-J. Güntherodt, G. Güntherodt, R. J. Gambino, and R. Ruf, Phys. Rev. Lett. **65**, 247 (1990).

[24] R. Wiesendanger, I.V. Shvets, D. Bürgler, G. Tarrach, H.J. Güntherodt, J.M.D. Coey, and S. Gräser, Science **255**, 583 (1992).

[25] S. F. Alvarado, Phys. Rev. Lett. **75**, 513 (1995).

[26] M. Bode, M. Getzlaff, and R. Wiesendanger, Phys. Rev. Lett. **81**, 4256 (1998).

[27] O. Pietzsch, A. Kubetzka, M. Bode, and R. Wiesendanger, Phys. Rev. Lett. 84, 5212 (2000).

[28] W. Wulfhekel and J. Kirschner, Appl. Phys. Lett. **75**, 1944 (1999).

[29] U. von Barth und L. Hedin, J. Phys. C. **5**, 1629 (1972).

[30] V. L. Moruzzi, J. F. Janak und A. R. Williams, *Calculated Electronic Properties of Metals* (Pergamon, New York, 1978).

[31] D. M. Ceperley und B. J. Adler, Phys. Rev. Lett. **45**, 566 (1980).

[32] S. H. Vosko, L. Wilk, and N. Nusair, J. Phys. C **5**, 1629 (1980).

[33] S. Blügel, *Bandmagnetismus II*, 24. Ferienkurs des Instituts für Festkörperforschung: *Magnetismus von Festkörpern und Grenzflächen*, Forschungszentrum Jülich (1993).

[34] R. Zeller, *Bandmagnetismus I*, 24. Ferienkurs des Instituts für Festkörperforschung: *Magnetismus von Festkörpern und Grenzflächen*, Forschungszentrum Jülich (1993).

[35] D. J. Singh, *Planewaves, Pseudopotenials and the LAPW Method* (Kluwer Academic Publishers, Boston, 1994).

[36] R. Pentcheva, *Ab–initio Rechnungen zum Zusammenhang zwischen Magnetismus und Struktur ultradünner Filme*, Diploma Thesis, Universität Köln (1996).

[37] P. Kurz, *Non-Collinear Magnetism of Ultrathin Magnetic Films*, Diploma Thesis, RWTH Aachen (1996).

[38] N. W. Ashcroft and N. D. Mermin, *Solid State Physics* (Saunders College Publishing, Cornell, 1978).

[39] J. C. Slater, Phys. Rev. **51**, 846 (1937).

[40] O. K. Andersen, Phys. Rev. B **12**, 3060 (1975).

[41] H. Krakauer, M. Posternak und A. J. Freeman, Phys. Rev. B **19**, 1706 (1979).

[42] E. Wimmer, H. Krakauer, M. Weinert und A. J. Freeman, Phys. Rev. B **24**, 864 (1981).

[43] M. Weinert, E. Wimmer und A. J. Freeman, Phys. Rev. B **26**, 4571 (1982).

[44] J. D. Jackson, *Classical Electrodynamics* (John Wiley & Sons, Berkeley 1975).

[45] O. Jepsen and O. K. Andersen, Solid State Commun. **9**, 1763 (1971).

[46] P. E. Blöchl, O. Jepsen, and O. K. Andersen, Phys. Rev. B **49**, 16223 (1994).

[47] S. L. Cunningham, Phys. Rev. B **10**, 4988 (1974).

[48] J. R. Oppenheimer, Phys. Rev. **13**, 66 (1928).

[49] S. Blügel, *Theorie der Rastertunnelmikroskopie*, 29. Ferienkurs des Instituts für Festkörperforschung: *Physik der Nanostrukturen*, Forschungszentrum Jülich (1998).

[50] G. Hörmandinger, Phys. Rev. B **49**, 13 897 (1994).

[51] A. L. Vázquez de Parga, O. S. Hernán, R. Miranda, A. L. Yeyati, N. Mingo, A. Martín-Rodero, and F. Flores, Phys. Rev. Lett. **80**, 357 (1998).

[52] S. Ohnishi und M. Tsukuda, Sol. State Comm. **71**, 391 (1989).

[53] W. A. Hofer, J. Redinger, and P. Varga, Solid State Comm. **113**, 245 (1999).

[54] J. V. Barth, H. Burne, G. Ertl und R. J. Behm, Phys. Rev. B **42**, 9307 (1990).

[55] S. Blügel, D. Pescia, and P. H. Dederichs, Phys. Rev. B **39**, 1392 (1989).

[56] H. J. Elmers, J. Hauschild, and U. Gradmann, Phys. Rev. B **59**, 3688 (1999).

[57] W. Sacks, G. Gauthier, S. Rousset, J. Klein, and M. A. Esrick, Phys. Rev. B **36**, 961 (1987).

[58] D. D. Chambliss and S. Chiang, Surf. Sci. Lett. **264**, L187 (1992).

[59] J. Tersoff and D. R. Hamann, Phys. Rev. B **31**, 805 (1985).

[60] R. M. Feenstra, J. A. Stroscio, J. Tersoff, and A. P. Fein, Phys. Rev. Lett. **58**, 1192 (1987).

[61] R. M. Feenstra, J. A. Stroscio, and A. P. Fein, Surf. Sci. **181**, 295 (1987).

[62] J. Dabrowski, H.–J. Müssig, and G. Wolff, Phys. Rev. Lett. **73**, 1660 (1994).

[63] R. B. Capaz, K. Cho, and J. D. Joannopoulos, Phys. Rev. Lett. **75**, 1811 (1995).

[64] Ph. Ebert, B. Engels, P. Richard, K. Schroeder, S. Blügel, C. Domke, M. Heinrich, and K. Urban, Phys. Rev. Lett. **77**, 2997 (1996).

[65] B. Voigtländer, V. Scheuch, H. P. Bonzel, S. Heinze and S. Blügel, Phys. Rev. B **55**, R13444 (1997).

[66] J. A. Stroscio, D. T. Pierce, A. Davies, R. J. Celotta und M. Weinert, Phys. Rev. Lett. **75**, 2960 (1995).

[67] A. Biedermann, O. Genser, W. Hebenstreit, M. Schmid, J. Redinger, R. Poudloucky, and P. Varga, Phys. Rev. Lett. **76**, 4179 (1996).

[68] V. M. Hallmark, S. Chiang, J. F. Rabolt, J. D. Swalen, and R. J. Wilson, Phys. Rev. Lett. **59**, 2879 (1987).

[69] J. Wintterlin, J. Wiechers, H. Brune, and T. Gritsch, H. Höfer and R. J. Behm, Phys. Rev. Lett. **62**, 59 (1989).

[70] Ch. Wöll, S. Chiang, R. J. Wilson, and P. H. Lippel, Phys. Rev. B **39**, 7988 (1989).

[71] R. J. Smith, C. Hennessy, M. W. Kim, C. N. Whang, M. Worthington and X. Mingde, Phys. Rev. Lett. **58**, 702 (1987).

[72] V. L. Moruzzi, J. F. Janak, A. R. Williams, Calculated Electronic Properties of Metals, Pergamon New York (1978).

[73] M. Bode, R. Pascal, and R. Wiesendanger, Surf. Sci. **344**, 185 (1995).

[74] R. H. Gaylord, K. H. Jeong, and S. D. Kevan, Phys. Rev. Lett. **62**, 2036 (1989). E. Rotenberg and S. D. Kevan, Phys. Rev. Lett. **80**, 2905 (1998).

[75] For a comparison of bandstructures and LDOS of different fcc and bcc transition metals see for example Ref. [72].

[76] We determined the minimum of the surface-state band for ferromagnetic bcc Fe(110) calculated at the experimental lattice constant of $a_0 = 5.43$ a.u. at -0.45 eV and -2.35 eV for the minority and majority states, respectively.

[77] D. Wortmann, *Interpretation of Scanning Tunneling Microscopy and Spectroscopy of Magnetic Metal Surfaces by Electron Theory*, Diploma Thesis, University of Dortmund (2000).

[78] R. M. Tromp, R. J. Hamers, and J. Demuth Phys. Rev. Lett. **55** 1303 (1985).

[79] A. Stroscio, R. M. Feenstra, and A. P. Fein, Phys. Rev. Lett. **57** 2579 (1989).

[80] R. J. Hamers, Phys. Rev. B **40** 1657 (1989).

[81] J. R. Jiminez, L. M. Hsiung, K. Rajan, and L. J. Schowalter, Appl. Phys. Lett. **57**(26) (1990) 2811.

[82] S. M. Yalisove, R. T. Tung, and D. Loretto, J. Vac. Sci. Technol. A **7** 1472 (1989).

[83] R. Stalder, C. Schwarz, H. Sirringhaus, and H. von Känel, Surf. Sci. **271** 355 (1992).

[84] This is important for the formation of buried silicide layers. S. Mantl and H. L. Bay, Appl. Phys. Lett. **61** (1992) 267.

[85] S. M. Yalisove, R. T. Tung, and J. L. Batstone Mat. Res. Soc. Symp. Proc. **116** 439 (1988).

[86] W. Weiß, U. Starke, K. Heinz, G. Ragelov, T. Fauster, and G. R. Castro, Surf. Sci. **347** 117 (1996).

[87] J. M. Gallego, R. Miranda, S. Molodtsov, C. Laubschat, and G. Kaindl, Surf. Sci. **239** 203 (1990).

[88] V. Scheuch, B. Voigtländer, and H. P. Bonzel, Surf. Sci. **372** 71 (1997).

[89] M. Schmid, H. Stadler, and P. Varga, Phys. Rev. Lett. **70**, 1441 (1993).

[90] L. Pleth Nielsen, F. Besenbacher, I. Steensgard, E. Lægsaard, C. Engdahl, P. Stoltze, K. W. Jacobsen, and J. K. Nørskov, Phys. Rev. Lett. **71**, 754 (1993).

[91] H. Röder, R. Schuster, H. Brune, and K. Kern, Phys. Rev. Lett. **71**, 2086 (1993).

[92] P. W. Murray, I. Stensgaard, E. Lægsaard, and F. Besenbacher, Phys. Rev. B **52**, R 14404 (1995).

[93] P. W. Murray, S. Thorshaug, I. Stensgaard, F. Besenbacher, E. Lægsaard, A. V. Ruban, K. W. Jacobsen, G. Kopodakis, and H. L. Skriver, Phys. Rev. B **55**, 1380 (1997).

[94] A. Davies, J. A. Stoscio, D. T. Pierce, and R. J. Celotta, Phys. Rev. Lett. **76**, 4175 (1996).

[95] P. T. Wouda, B. E. Nieuwenhuys, M. Schmid, and P. Varga, Surf. Sci. **359**, 17 (1996).

[96] For a review see: Ph. Ebert, Surf. Sci. Rep. **33**, 121 (1999).

[97] G. Gilarowski and H. Niehus, Surf. Sci. **436**, 107 (1999).

[98] H. Niehus, W. Heiland, and E. Taglauer, Surf. Sci. Rep. **17**, 578 (1993).

[99] *Binary alloy phase diagrams*, Ed. T. B. Massalski (AMS International, Materials Park, Ohio, 1990).

[100] S. H. Vosko, L. Wilk, and N. Nusair, Can. J. Phys. **58**, 1200 (1980).

[101] C. Carbone, E. Vescovo, O. Rader, W. Gudat, and W. Eberhardt, Phys. Rev. Lett. **71**, 2805 (1993).

[102] I. B. Altfeder, D. M. Chen, and K. A. Matveev, Phys. Rev. Lett. **80**, 4895 (1998).

[103] F. J. Himpsel, J. E. Ortega, G. J.Mankey, and R. F. Willis, Advances in Physics **47**, 511 (1998).

[104] S. Handschuh and S. Blügel, Solid State Comm. **105**, 633 (1998).

[105] A. Vega, S. Bouarab, H. Dreyssé, and C. Demangeat, Thin Solid Films **275**, 103 (1996). R. Q. Wu and A. J. Freeman, Phys. Rev. B **51**, 17131 (1995).

[106] O. Elmouhssine *et al.*, Phys. Rev. B **55**, R7410 (1997).

[107] T. G. Walker and H. Hopster, Phys. Rev. B **48**, 3563 (1993), *ibid* B **52**, 15691 (1995).

[108] S. Andrieu *et al.*, J. Magn. Magn. Mater. **165**, 191 (1997).

[109] S. Andrieu *et al.*, Phys. Rev. B **57**, 1985 (1998).

[110] R. Pfandzelter, T. Igel, and H. Winter, Surf. Sci. **389**, 317 (1997).

[111] Ch. Roth, Th. Kleeman, F. U. Hillebrecht, and E. Kisker, Phys. Rev. B **52**, 15691 (1995).

[112] S. Handschuh and S. Blügel, submitted to Phys. Rev. B.

[113] L. Pizzagalli *et al.*, J. Appl. Phys. **79**, 5834 (1996).

[114] B. Nonas, K. Wildberger, R. Zeller, and P. H. Dederichs, Phys. Rev. Lett. **80**, 4574 (1998).

[115] O. Genser, *Reine und Si-bedeckte Fe(001)-Oberflächen im Rastertunnelmikroskop: Begleitende Bandstrukturrechnungen*, Diploma Thesis, TU Wien (1995).

[116] M. Sporn, E. Platzgummer, M. Pinczolits, W. Hebenstreit, M. Schmid, W. Hofer and P. Varga, Surf. Sci. **396**, 78 (1998).

[117] R. Wu and A. J. Freeman, Phys. Rev. B **51**, 17131 (1995).

[118] T. Asada and S. Blügel, to be published.

[119] J.B. Kortright *et al.*, J. Magn. Magn. Mater. **207**, 7 (1999).

[120] G.A. Prinz, Science **282**, 1660 (1998).

[121] For a recent review see: J. Nogues, I. K. Schuller, J. Magn. Magn. Mater. **192**, 203 (1999).

[122] H. A. Dürr, E. Dudzik, S. S. Dhesi, J. B. Goedkoop, G. van der Laan, M. Belakhovsky, C. Mocuta, A. Marty, Y. Samson, Science **284**, 2166 (1999).

[123] F. U. Hillebrecht, H. Ohldag, U. Mick, M. Weiss, and J. Barth, submitted to Science.

[124] A. Scholl, J. Stöhr, J. Lüning, J. W. Seo, J. Fompeyrine, H. Siegwart, J.-P. Locquet, F. Nolting, S. Anders, E. E. Fullerton, M. R. Scheinfein, H. A. Padmore, Science **287**, 1014 (2000).

[125] S. Blügel and P. H. Dederichs, Europhys. Lett. **9**, 597 (1989).

[126] C. Krembel, M.C. Hanf, J.C. Peruchetti, D. Bolmont, and G. Gewinner, J. Magn. Magn. Mat. **93**, 529 (1991).

[127] J.E. Ortega and F.J. Himpsel, Phys. Rev. B **47**, 16441 (1993).

[128] G. Rangelov, H. D. Kang, J. Reinmuth, and M. Donath, Phys. Rev. B **61**, 549 (2000) and references therein.

[129] X. Nie, private communication.

[130] O. Pietzsch, A. Kubetzka, D. Haude, M. Bode, and R. Wiesendanger, Rev. Sci. Instr. **71**, 424 (2000).

[131] M. Bode, M. Hennefarth, D. Haude, M. Getzlaff, and R. Wiesendanger, Surf. Sci. **432**, 8 (1999).

[132] M. Bode, M. Getzlaff, and R. Wiesendanger, J. Vac. Sci. Technol. A **17**, 2228 (1999).

[133] Ph. Kurz, G. Bihlmayer, and S. Blügel, submitted to Phys. Rev. Lett.

Appendix A

Extension of the Tersoff-Hamann Model to SP-STM

In this section we present the extension of the Tersoff-Hamann model to spin-polarized STM (SP-STM) for the case of a ferromagnetic tip with a magnetization axis pointing along an arbitrary direction and a sample with an arbitrary, i.e. possibly non-collinear, spin-structure. The derivation given in the following leads to the general equation (Eq. (4.48)) for the spin-polarized tunneling current that has been mentioned in section 4.5 without proof.

As has been emphasized in section 4.5 the quantization axes of tip and sample do not in general coincide, i.e. are non-collinear. Thus we must transform the spin states to a global frame where the assumption of spin conservation can then be applied in a trivial manner, i.e. spin-up (down) states of the global frame can only tunnel into spin-up (down) states of the global frame. Without loss of generality we choose the local frame of the sample as the global frame of reference. Thus we will transform the states $|\nu\rangle$ of the tip which are diagonal in the spin-space with respect to the local quantization axis and are expressed as in section 4.5 by:

$$\Psi^T_{\nu\uparrow}(\mathbf{r}) = \psi^T_{\nu\uparrow}(\mathbf{r}) \begin{pmatrix} 1 \\ 0 \end{pmatrix} \quad \text{and} \quad \Psi^T_{\nu\downarrow}(\mathbf{r}) = \psi^T_{\nu\downarrow}(\mathbf{r}) \begin{pmatrix} 0 \\ 1 \end{pmatrix}. \tag{A.1}$$

The transformation from the local frame of the tip to the global frame is performed by applying a rotation in spin-space. Assuming that the quantization axis of the tip is defined by the polar angles (θ, ϕ) with respect to the global frame, the rotation matrix is given by:

$$U(\theta, \phi) = \begin{pmatrix} e^{-i\phi/2}\cos(\theta/2) & -e^{-i\phi/2}\sin(\theta/2) \\ e^{i\phi/2}\sin(\theta/2) & e^{i\phi/2}\cos(\theta/2) \end{pmatrix}. \tag{A.2}$$

States $\Psi^T_{\nu\uparrow}(\mathbf{r})$ and $\Psi^T_{\nu\downarrow}(\mathbf{r})$ of the tip are then given by:

$$\Psi^{T(g)}_{\nu\uparrow}(\mathbf{r}) = U(\theta, \phi)\Psi^T_{\nu\uparrow}(\mathbf{r}) = \psi^T_{\nu\uparrow}(\mathbf{r}) \begin{pmatrix} e^{-i\phi/2}\cos(\theta/2) \\ e^{i\phi/2}\sin(\theta/2) \end{pmatrix} \tag{A.3}$$

and

$$\Psi^{T(g)}_{\nu\downarrow}(\mathbf{r}) = U(\theta, \phi)\Psi^T_{\nu\downarrow}(\mathbf{r}) = \psi^T_{\nu\downarrow}(\mathbf{r}) \begin{pmatrix} -e^{-i\phi/2}\sin(\theta/2) \\ e^{i\phi/2}\cos(\theta/2) \end{pmatrix} \tag{A.4}$$

in the global frame. In the case of an arbitrary spin-structure the states $|\mu\rangle$ of the sample $\Psi^S_\mu(\mathbf{r})$ possess non-vanishing spin-up and spin-down components in the vacuum:

$$\Psi^S_\mu(\mathbf{r}) = \begin{pmatrix} \psi^S_{\mu\uparrow}(\mathbf{r}) \\ \psi^S_{\mu\downarrow}(\mathbf{r}) \end{pmatrix}. \tag{A.5}$$

The charge density $n_\mu(\mathbf{r})$ and the vector magnetization density $\mathbf{m}_\mu(\mathbf{r})$ of each state $|\mu\rangle$ can be calculated by:

$$n_\mu(\mathbf{r}) = \Psi^{S\dagger}_\mu(\mathbf{r})\Psi^S_\mu(\mathbf{r}) = |\psi^S_{\mu\uparrow}|^2 + |\psi^S_{\mu\downarrow}|^2 \tag{A.6}$$

and

$$\begin{aligned} \mathbf{m}_\mu(\mathbf{r}) &= \Psi^{S\dagger}_\mu(\mathbf{r})\,\boldsymbol{\sigma}\,\Psi^S_\mu(\mathbf{r}) && \text{(A.7)} \\ &= \left(\psi^S_{\mu\uparrow}\psi^{S*}_{\mu\downarrow} + \psi^{S*}_{\mu\uparrow}\psi^S_{\mu\downarrow}\,,\; i(\psi^S_{\mu\uparrow}\psi^{S*}_{\mu\downarrow} - \psi^{S*}_{\mu\uparrow}\psi^S_{\mu\downarrow})\,,\; |\psi^S_{\mu\uparrow}|^2 - |\psi^S_{\mu\downarrow}|^2\right), && \text{(A.8)} \end{aligned}$$

where the three components of $\boldsymbol{\sigma}$ are defined through the three Pauli spin matrices:

$$\boldsymbol{\sigma} = (\sigma_1, \sigma_2, \sigma_3). \tag{A.9}$$

In order to calculate the tunneling current within the Bardeen approach we use Eq. (4.11) for the transition between a state Ψ^S_μ of the sample and a state $\Psi^{T(g)}_\sigma(\mathbf{r})$ of the tip. Recall that the potential U_T of the tip enters into Eq. (4.11) which must not be confused with the rotation matrix in spin-space $U(\theta,\phi)$. Let us assume a spin-up state of the tip first. The corresponding (spin-polarized) matrix element $M_{\mu,\nu\uparrow}(\mathbf{R}_T,\theta,\phi)$ can be calculated from:

$$\begin{aligned} M_{\mu,\nu\uparrow}(\mathbf{R}_T,\theta,\phi) &= \langle\Psi^{T(g)}_{\nu\uparrow}|U_T|\Psi^S_\mu\rangle && \text{(A.10)} \\ &= \int_{\Omega_T} \Psi^{T(g)\dagger}_{\nu\uparrow} U_T \Psi^S_\mu\, dV && \text{(A.11)} \\ &= \int_{\Omega_T} (e^{i\phi/2}\cos(\theta/2), e^{-i\phi/2}\sin(\theta/2))\psi^{T*}_{\nu\uparrow} U_T \begin{pmatrix} \psi^S_{\mu\uparrow} \\ \psi^S_{\mu\downarrow} \end{pmatrix} dV && \text{(A.12)} \\ &= \int_{\Omega_T} dV \psi^{T*}_{\nu\uparrow} U_T \left[e^{i\phi/2}\cos(\theta/2)\psi^S_{\mu\uparrow} + e^{-i\phi/2}\sin(\theta/2)\psi^S_{\mu\downarrow}\right] && \text{(A.13)} \\ &= e^{i\phi/2}\cos(\theta/2)\int_{\Omega_T} dV \psi^{T*}_{\nu\uparrow} U_T \psi^S_{\mu\uparrow} + \\ &\quad\; e^{-i\phi/2}\sin(\theta/2)\int_{\Omega_T} dV \psi^{T*}_{\nu\uparrow} U_T \psi^S_{\mu\downarrow} && \text{(A.14)} \\ &= e^{i\phi/2}\cos(\theta/2) M_{\mu\uparrow,\nu\uparrow}(\mathbf{R}_T) + e^{-i\phi/2}\sin(\theta/2) M_{\mu\downarrow,\nu\uparrow}(\mathbf{R}_T). && \text{(A.15)} \end{aligned}$$

The (spin-polarized) matrix element $M_{\mu,\nu\downarrow}(\mathbf{R}_T,\theta,\phi)$ for a spin-down state of the tip can be calculated analogously. In the last line we have reduced the(spin-polarized) matrix element to a weighted sum of two matrix elements calculated from scalar wave functions which would totally determine the tunneling problem for the case of a collinear alignment of the magnetization axes of tip and sample. The weights express the rotation in spin-space while the matrix elements $M_{\mu\uparrow,\nu\uparrow}$ and $M_{\mu\downarrow,\nu\uparrow}$ can be computed analogously to the non-spinpolarized case. We can thus apply all the approximations introduced in chapter 4 in order to compute them. In the Tersoff-Hamann model which we use here the matrix elements are given by the value of the sample state at the position $\mathbf{R}_T$ of the tip. We can summarize the result to:

$$
\begin{aligned}
M_{\mu,\nu\uparrow}(...) &= -\frac{2\pi C_\uparrow \hbar^2}{\kappa_\uparrow m}\left[e^{i\phi/2}\cos(\theta/2)\psi^S_{\mu\uparrow}(\mathbf{R}_T) + e^{-i\phi/2}\sin(\theta/2)\psi^S_{\mu\downarrow}(\mathbf{R}_T)\right] && \text{(A.16)}\\
M_{\mu,\nu\downarrow}(...) &= -\frac{2\pi C_\downarrow \hbar^2}{\kappa_\downarrow m}\left[e^{-i\phi/2}\cos(\theta/2)\psi^S_{\mu\downarrow}(\mathbf{R}_T) - e^{i\phi/2}\sin(\theta/2)\psi^S_{\mu\uparrow}(\mathbf{R}_T)\right]. && \text{(A.17)}
\end{aligned}
$$

We assume that the spin-up and spin-down s-wave states can be characterized by the same decay constant $\kappa = \kappa_\uparrow = \kappa_\downarrow$ and the same coefficient $C = C_\uparrow = C_\downarrow$. Further, we assume that the density of states (DOS) of the spin-up $n_T^\uparrow(\epsilon)$ and spin-down $n_T^\downarrow(\epsilon)$ tip states is constant. For a magnetic tip the DOS of spin-up and spin-down states are non-equal. Inserting the matrix elements into the equation for the tunneling current, Eq. (4.14), leads to:

$$
\begin{aligned}
I(\mathbf{R}_T,\theta,\phi) &= \frac{2\pi e}{\hbar}\int d\epsilon\, g_{V,T}(\epsilon)\sum_\mu \delta(\epsilon_\mu - \epsilon)\times \\
&\quad \left[n_T^\uparrow |M_{\mu,\nu\uparrow}(...)|^2 + n_T^\downarrow |M_{\mu,\nu\downarrow}(...)|^2\right]. && \text{(A.18)}
\end{aligned}
$$

The last term in brackets can be evaluated by inserting the matrix elements (A.16) and (A.17):

$$
\begin{aligned}
[...] &= n_T^\uparrow\left[\cos^2(..)|\psi^S_{\mu\uparrow}|^2 + \sin^2(..)|\psi^S_{\mu\downarrow}|^2 + \cos(..)\sin(..)(e^{-i\phi}\psi^{S*}_{\mu\uparrow}\psi^S_{\mu\downarrow} + e^{i\phi}\psi^S_{\mu\uparrow}\psi^{S*}_{\mu\downarrow})\right] + \\
&\quad n_T^\downarrow\left[\sin^2(..)|\psi^S_{\mu\uparrow}|^2 + \cos^2(..)|\psi^S_{\mu\downarrow}|^2 - \cos(..)\sin(..)(e^{-i\phi}\psi^{S*}_{\mu\uparrow}\psi^S_{\mu\downarrow} + e^{i\phi}\psi^S_{\mu\uparrow}\psi^{S*}_{\mu\downarrow})\right],
\end{aligned}
$$

where we have suppressed the explicit dependence of the wave functions on the position of the tip $\mathbf{R}_T$ for brevity. Using the relation:

$$
\begin{aligned}
n_T n^S_\mu + m_T\cos\theta\, m^S_{\mu,z} &= 2\left[\cos^2(\theta/2)(n_T^\uparrow|\psi^S_{\mu\uparrow}|^2 + n_T^\downarrow|\psi^S_{\mu\downarrow}|^2) + \right.\\
&\quad \left.\sin^2(\theta/2)(n_T^\uparrow|\psi^S_{\mu\downarrow}|^2 + n_T^\downarrow|\psi^S_{\mu\uparrow}|^2)\right] && \text{(A.19)}
\end{aligned}
$$

[...] can be simplified to:

$$
\begin{aligned}
[...] &= \frac{1}{2}\left[n_T n^S_\mu + m_T\cos\theta\, m^S_{\mu,z} + m_T\sin\theta\,(e^{i\phi}\psi^S_{\mu\uparrow}\psi^{S*}_{\mu\downarrow} + e^{-i\phi}\psi^{S*}_{\mu\uparrow}\psi^S_{\mu\downarrow})\right] && \text{(A.20)}\\
&= \frac{1}{2}\left[n_T n^S_\mu + m_T\cos\theta\, m^S_{\mu,z} + m_T\sin\theta\,\big(\cos\phi\,(\psi^S_{\mu\uparrow}\psi^{S*}_{\mu\downarrow} + \psi^{S*}_{\mu\uparrow}\psi^S_{\mu\downarrow}) + \right.\\
&\quad \left. i\,\sin\phi\,(\psi^S_{\mu\uparrow}\psi^{S*}_{\mu\downarrow} - \psi^{S*}_{\mu\uparrow}\psi^S_{\mu\downarrow})\big)\right] && \text{(A.21)}\\
&= \frac{1}{2}\left[n_T n^S_\mu + m_T\big(\cos\theta\, m^S_{\mu,z} + \sin\theta\,(\cos\phi\, m^S_{\mu,x} + \sin\phi\, m^S_{\mu,y})\big)\right] && \text{(A.22)}\\
&= \frac{1}{2}\left[n_T n^S_\mu(\mathbf{R}_T) + \mathbf{m}_T\mathbf{m}^S_\mu(\mathbf{R}_T)\right], && \text{(A.23)}
\end{aligned}
$$

where we have made use of the definition of the charge and the vector magnetization density of a single sample state. Note, that the magnetization vector of the tip is defined in the global frame by the polar angles (θ, ϕ). Inserting this result into Eq. (A.18) leads to the general result of the tunneling current for an arbitrary spin-structure of the sample using a ferromagnetic tip:

$$I(\mathbf{R}_T, \theta, \phi) \quad = \quad \frac{4\pi^3 C^2 \hbar^3 e}{\kappa^2 m^2} \int d\epsilon \, g_{V,T}(\epsilon) \Big[n_T n_S(\mathbf{R}_T, \epsilon) + \mathbf{m}_T \mathbf{m}_S(\mathbf{R}_T, \epsilon) \Big], \qquad \text{(A.24)}$$

where we have introduced the local density of states $n_S(\mathbf{R}_T, \epsilon)$:

$$n_S(\mathbf{R}_T, \epsilon) = \sum_{\mu} \delta(\epsilon_\mu - \epsilon) \Psi_\mu^{S\dagger}(\mathbf{R}_T) \Psi_\mu^S(\mathbf{R}_T), \qquad \text{(A.25)}$$

and the local spin density of states $\mathbf{m}_S(\mathbf{R}_T, \epsilon)$:

$$\mathbf{m}_S(\mathbf{R}_T, \epsilon) = \sum_{\mu} \delta(\epsilon_\mu - \epsilon) \Psi_\mu^{S\dagger}(\mathbf{R}_T) \, \boldsymbol{\sigma} \, \Psi_\mu^S(\mathbf{R}_T). \qquad \text{(A.26)}$$

Appendix B

Publications and Conference Contributions

Publications

Journal Papers

- B. Voigtländer, V. Scheuch, H. P. Bonzel, S. Heinze, and S. Blügel. *Chemical Identification of Atoms at Multicomponent Surfaces on an Atomic Scale: CoSi*$_2$(100), Physical Review B **55**, R13444 (1997).

- S. Heinze, S. Blügel, R. Pascal, M. Bode, and R. Wiesendanger. *Prediction of Bias-Voltage-Dependent Corrugation Reversal for STM images of bcc (110) Surfaces: W(110), Ta(110) and Fe(110)*, Physical Review B **58**, 16432 (1998).

- T. Asada, G. Bihlmayer, S. Handschuh, S. Heinze, Ph. Kurz, and S. Blügel. *First-Principles Theory of Ultrathin Magnetic Films*, Journal of Physics C, **11**, 9347 (1999).

- S. Heinze, X. Nie, S. Blügel, and M. Weinert. *Electric-Field Induced Changes in STM Images of Metal Surfaces*, Chemical Physics Letters **315**, 167 (1999).

- S. Heinze, R. Abt, S. Blügel, G. Gilarowski, and H. Niehus. *STM-Images of Transition-Metal Structures buried below Noble-Metal Surfaces*, Physical Review Letters **83**, 4808 (1999).

- D. Wortmann, S. Heinze, G. Bihlmayer, and S. Blügel, *Interpreting STM-Images of the MnCu/Cu(100) Surface Alloy*, Physical Review B **62**, 2862 (2000).

- S. Heinze, M. Bode, A. Kubetzka, O. Pietzsch, X. Nie, S.Blügel, and R. Wiesendanger, *Real-Space Imaging of Antiferromagnetism on the Atomic Scale*, Science **288**, 1805 (2000).

Conference Contributions

Talks

- **15.03.1997** S. Heinze, M. Bode, R. Wiesendanger, and S. Blügel. *Simulation von STM-Experimenten für Fe/W(110)*, Spring meeting of the DPG, March 1997, Münster.

- **09.03.1998** S. Heinze and S. Blügel. *Theorie der Rastertunnelmikroskopie*, 29. Ferienkurs des Instituts für Festkörperforschung (Physik der Nanostrukturen), March 1998, Forschungszentrum Jülich.

- **26.03.1998** S. Heinze, S. Blügel, R. Pascal, M. Bode, and R. Wiesendanger. *Zusammenhang zwischen Oberflächenzuständen und Antikorrugation in STM-Bildern von Übergangsmetalloberflächen*, Spring meeting of the DPG, March 1998, Regensburg.

- **04.01.1999** S. Heinze and S. Blügel. *Theoretical Analysis of STM and STS of Thin Magnetic Films*, 211. WE-Heraeus Seminar (Magnetic Nanostructures), January 1999, Physikzentrum Bad Honnef.

- **25.03.1999** S. Heinze, X. Nie, S. Blügel, and M. Weinert. *Einfluß des elektrischen Feldes auf STM-Bilder von Metalloberflächen*, Spring meeting of the DPG, March 1999, Münster.

- **29.09.1999** S. Heinze, R. Wiesendanger, and S. Blügel. *Ab initio Bandstrukturrechnungen zum spin-polarisierten Tunneln*, Workshop on 'Magnetische Nanostrukturen: Physikalische Grundlagen und Anwendungen', Institute of Applied Physics, September 1999, University of Hamburg.

- **28.03.2000** S. Heinze, D. Wortmann, Ph. Kurz, X. Nie, S. Blügel, M. Bode, A. Kubetzka, O. Pietzsch, and R. Wiesendanger, *Ab initio Rechnungen zum spin-polarisierten Tunneln*, Spring meeting of the DPG, March 2000, Regensburg.

- **28.03.2000** S. Heinze, R. Abt, S. Blügel, G. Gilarowski, and H. Niehus, *STM-Bilder von vergrabenen Übergangsmetallstrukturen*, Spring meeting of the DPG, March 2000, Regensburg.

- **11.07.2000** S. Heinze, M. Bode, A. Kubetzka, O. Pietzsch, X. Nie, D. Wortmann, Ph. Kurz, S. Blügel, and R. Wiesendanger, *Real Space Imaging of Two-Dimensional Antiferromagnetism on the Atomic Scale*, 10th International Conference on Solid Films and Surfaces, July 2000, Princeton, N.J. , USA.

Posters

- **22.07.1997** M. Bode, R. Pascal, S. Heinze, S. Blügel, and R. Wiesendanger. *Nanostructural and Local Electronic Properties of Fe/W(110): Scanning Tunneling Spectroscopy and Ab Initio Calculations*, 9th International Conference on Scanning Tunneling Microscopy/Spectroscopy and Related Techniques, July 1997, Hamburg.

- **16.02.1998** S. Heinze and S. Blügel. *Theoretische Untersuchung zur STM und STS magnetischer Filme*, 187. WE-Heraeus Seminar (Spinabhängiger Transport), January 1998, Physikzentrum Bad Honnef.

- **21.09.1998** S. Heinze and S. Blügel. *Theoretical Analysis of STM and STS of Ultrathin Magnetic Films*, European Research Conference on Computational Physics for Nanotechnology, September 1998, Castelvecchio Pascoli, Italy.

- **05.01.1999** X. Nie, S. Heinze, M. Weinert, and S. Blügel. *Magnetic Surfaces under Static External Electric Fields'*, 211. WE-Heraeus Seminar (Magnetic Nanostructures), January 1999, Physikzentrum Bad Honnef.

- **19.07.1999** S. Heinze, S. Blügel, and R. Wiesendanger. *What can be learnt by non-spinpolarized Scanning Tunneling Microscopy about surface magnetism of Cr and Mn on Fe(001)?*, 10th International Conference on Scanning Tunneling Microscopy/Spectroscopy and Related Techniques, July 1999, Seoul, South Korea.

- **18.11.1999** S. Heinze, T. Asada, and S. Blügel. *Theoretical Analysis of STM and STS on Magnetic Thin Films*, 44th Annual Conference on Magnetism and Magnetic Materials, November 1999, San Jose, California, USA.

- **05.01.2000** S. Heinze, D. Wortmann, G. Bihlmayer, and S. Blügel. *Ab Initio Calculations of Tunneling through MgO Barriers on Fe(001)*, 228. WE-Heraeus Seminar (Metal-Nonmetal Structures for Magnetoelectronics), January 2000, Physikzentrum Bad Honnef.

- **14.02.2000** M. Bode, S. Heinze, A. Kubetzka, O. Pietzsch, X. Nie, S. Blügel, and R. Wiesendanger, *Spin-Polarized Scanning Tunneling Microscopy and Spectroscopy: Real-Space Observation of Magnetic Nanowires and a 2D Antiferromagnetic Monolayer*, 3rd Gordon Research Conference on Magnetic Nanostructures, Feburary 2000, Ventura, California, USA.

- **21.07.2000** S. Heinze, M. Bode, A. Kubetzka, D. Wortmann, Ph. Kurz, O. Pietzsch, X. Nie, S. Blügel, and R. Wiesendanger, *Real Space Imaging of Surface Antiferromagnetism on the Atomic Scale*, 2nd International Conference on Scanning Probe Spectroscopy, July 2000, Hamburg.

Seminar Talks

- **03.06.1997** S. Heinze and S. Blügel, *FLAPW-Rechnungen zu STM-Experimenten an Fe/W(110)*, Institut für Technische Elektrochemie, Technical University of Vienna, Austria.

- **03.05.1999** S. Heinze, R. Abt, and S. Blügel, *Interpretation von STM-Bildern von Übergangsmetallstrukturen auf der Basis der Elektronentheorie*, Institut für Oberflächenphysik und Atomstoßprozesse, Humboldt Universität zu Berlin.
- **19.01.2000** S. Heinze, *Interpretation of STM Experiments on Transition-Metal Structures by Ab Initio Calculations*, Research Institute for Materials, University of Nijmegen, Netherlands.
- **07.07.2000** S. Heinze, *Interpretation of STM Experiments on Transition-Metal Structures by ab initio Calculations*, IBM Research Division, T. J. Watson Research Center, Yorktown Heights, N.Y. , USA.

Danksagung

Am Ende dieser Arbeit ist es mir eine besondere Freude, mich bei allen zu bedanken, die durch Ihre Hilfe, Unterstützung, Förderung, Fürsprache, Engagement und Freundschaft einen grossen Beitrag zum Gelingen dieser Arbeit geleistet haben. Drei Jahre sind eine lange Zeit und dementsprechend kann eine Dankesliste nicht kurz ausfallen.

An erster Stelle sei Stefan Blügel genannt. Seine unglaubliche Motivation und seine freundschaftliche Betreuung haben mich immer wieder angespornt, wenn Hindernisse aufgetaucht sind. Ohne seine Förderung wären mir viele interessante Möglichkeiten vorenthalten geblieben, und ohne die Diskussionen mit ihm hätte ich viele Einblicke verpaßt. Ein Riesendankeschön für alles.

Bei Herrn Prof. Dr. R. Wiesendanger möchte ich mich für die große Freiheit im Hinblick auf die wissenschaftliche Arbeit als auch die Organisation aller Aufenthalte am Forschungszentrum Jülich bedanken. Weiterhin danke ich ihm für die hervorragenden Forschungsbedingungen in seiner Gruppe.

Herrn Prof. Dr. W. Eberhardt danke ich für die unkomplizierte Aufnahme und Freiheit zur Forschung am Institut für elektronische Eigenschaften des Forschungszentrums Jülich.

Für seine freundschaftliche Unterstützung, die lustige Arbeitsatmosphäre während aller meiner Jülichaufenthalte und die gelungene Konferenzrahmengestaltung danke ich Philipp Kurz ganz besonders. Sein erfahrener Blick für Tapeten war immer wertvoll.

Dunja Diederichs gilt ein besonders herzliches Dankeschön. Ihre und Philipps Gastfreundschaft haben die häufigen Jülichbesuche ermöglicht und dazu geführt, daß ich mich trotz der teilweise anstrengenden Fahrten immer darauf gefreut habe. Den bis auf die letzte Ecke gepackten Opel werde ich natürlich auch nicht vergessen.

Ein außerordentliches Dankeschön gilt Nils Eissfeldt, der während seiner Zeit am Forschungszentrum Jülich wesentlich zu der guten Atmosphäre beigetragen hat.

Auf Gustav Bihlmayers Hilfe zu verzichten, ist unmöglich, wenn man mit dem `FLEUR`-Code arbeitet. Bei Problemen hat er mir stets in seiner gelassenen Art unkompliziert und schnell geholfen und dafür und den Spaß, den man zusätzlich noch hatte, danke ich ihm herzlich.

Einen so begeisterten Diplomanden wie Daniel Wortmann mitzubetreuen, war mir eine Freude, und für seine vielfältigen Ideen und die wertvollen Diskussionen möchte ich mich bei ihm bedanken.

Robert Abt danke ich für seine gute Idee, sich einmal mit vergrabenen Legierungen zu beschäftigen und für nette Diskussionen, wenn sich unsere Arbeitszeiten doch einmal überschnitten haben.

Prof. Dr. Toshio Asada danke ich für die gute Zusammenarbeit bezüglich der $3d$-Übergangsmetalle auf Fe(001).

Desweiteren danke ich der ganzen Theoriegruppe am Forschungszentrum Jülich, als da sind bzw. waren Valerio Bellini, Bereshad Nonas, Alexander Settels, Phivos Mavropoulos, Nikos Papanicolaou, Xiliang Nie, Sean Clarke, Winfried Kromen, Dietrich Frielinghausen, Karsten Wildberger und Timo Korhonen, die zur erfolgreichen Gestaltung meiner Aufenthalte beigetragen haben und auch sonst immer eine Hilfe waren.

Besonders schön war nach langer Durststrecke der doch noch gemeinsam erzielte Erfolg mit Matthias Bode. Für sein großes Engagement und die vielen guten Diskussionen danke ich ihm besonders.

Oswald Pietzsch danke ich für das sorgsame Korrekturlesen der Arbeit, seine Aufmunterung beim Schreiben, die vielen freundschaftlichen Gespräche und die nette Zusammenarbeit. Desweiteren danke ich ihm, André Kubetzka und Matthias Bode für die phantastischen Messungen.

Meinem langjährigen Bürokollegen, Hendrik Hölscher, danke ich ganz besonders für viele wertvolle Tips, die gute Büroatmosphäre und die erhellenden Gespräche.

Allen Mitgliedern der Arbeitsgruppe Rastersensormethoden des Instituts für Angewandte Physik sei für die gute Arbeitsatmosphäre sowie für die Unterstützung gedankt.

Herrn Otto Büchner gilt mein Dank für seine Hilfe bei der Installation der Workstation in Jülich und der Konfiguration für die Wiedermitnahme nach Hamburg.

Herrn Prof. Dr. H. Niehus danke ich für die Einladung an sein Institut an der Humboldt Universität zu Berlin und die gute Zusammenarbeit.

Gerhard Gilarowski danke ich für die STM-Messungen an den vergrabenen Legierungen sowie die gute Kooperation.

Meinen Eltern danke ich für Ihre Förderung, Unterstützung und Aufmunterungen während der gesamten Zeit meiner Promotion. Ohne Ihre Großzügigkeit wären mein Forschungsaufenthalt in Jülich und die weiteren Besuche nicht so einfach zu organisieren gewesen.